Structural, chemical, and thermoelectric properties of Bi$_2$Te$_3$ Peltier materials: bulk, thin films, and superlattices

Dissertation
zur Erlangung des Grades eines Doktors
der Naturwissenschaften
der Fakultät für Mathematik und Physik
der Eberhard-Karls-Universität zu Tübingen

vorgelegt von

Nicola Peranio

aus Dunningen (Rottweil)
2008

Zusammenfassung

Thermoelektrische Materialien werden als Energiewandler zur Erzeugung elektrischer Energie aus Wärme und zur Peltierkühlung verwendet. In Peltierkühlern kommen bei Raumtemperatur bevorzugt Bi_2Te_3 Volumenmaterialien zum Einsatz, weil sie sich durch ihren großen Seebeck-Koeffizienten ($S \approx \pm 200 \, \mu V/K$), ihre große elektrische Leitfähigkeit ($\sigma \approx 1000 \, 1/\Omega \, cm$), ihre geringe (elektronische und Gitter-) Wärmeleitfähigkeit ($\lambda \approx 1.5 \, W/m \, K$) und ihren dementsprechend hohen thermoelektrischen Gütefaktor [$ZT = (S^2 \sigma / \lambda) \, T \approx 1$] bei $T = 300 \, K$ auszeichnen.

Thermoelektrische Quantentrog-Strukturen aus Bi_2Te_3 wie z.B. Übergitterstrukturen [künstliche Nanostrukturen (ans)] wurden von Hicks und Dresselhaus im Jahr 1993 vorgeschlagen. Im Jahr 1999 wurden von Venkatasubramanian Bi_2Te_3/Sb_2Te_3 Übergitterstrukturen (ans) mit spektakulären thermoelektrischen Gütefaktoren von $ZT > 2$ bei einer Periode von $6 \, nm$ hergestellt. Die ans zeigte im Vergleich zu den Volumenmaterialien einen erhöhten Wert für das Produkt $S^2 \sigma$ und eine geringere Gitterwärmeleitfähigkeit. Die reduzierte Gitterwärmeleitfähigkeit wurde auf die durch die ans induzierte strukturelle Unordnung und damit einer Reduktion der mittleren freien Weglänge der Phononen zurückgeführt. Die ans zeigte gegenüber den Volumenmaterialien einen deutlich größeren ZT-Wert und löste eine Entwicklung zur Herstellung von nanostrukturierten Materialien für thermoelektrische Anwendungen aus.

Bei der durch festkörperphysikalische Ansätze bestimmten Materialforschung an Thermoelektrika stellt man fest, dass die Verbesserung einer Transportgröße sich leicht nachteilig auf die anderen Größen auswirkt, weil sich die Transportkoeffizienten aus den allen gemeinsamen fundamentalen Parametern des Elektronen- und des Phononensystems ergeben. Der Seebeck-Koeffizient und die elektrische Leitfähigkeit hängen vor allem von der Dotierung und der chemischen Zusammensetzung ab, dagegen wird die Gitterwärmeleitfähigkeit stark von struktureller Unordnung auf der Nanometer-Skala bestimmt. Die Herausforderung besteht nun in der Synthese thermoelektrischer Materialien mit elektrischen Eigenschaften wie bei Einkristallen und, im Gegensatz dazu, thermische Eigenschaften wie bei amorphen Materialien. Kombinierte Struktur- und Transportmessungen und eine Diskussion der Ergebnisse sind zum Auffinden des Optimums zwischen diesen beiden Extremen, „electron crystal/phonon glass", nötig.

In der Literatur findet sich zu Bi_2Te_3 eine große Zahl an Transportmessungen, nur wenige Strukturanalysen, jedoch keine kombinierten Messungen. Eine offene Frage ist, warum bei Bi_2Te_3 Volumenmaterialien die Gitterwärmeleitfähigkeit so gering ist. Bei Voruntersuchungen mittels Transmissionselektronenmikroskopie (TEM) wurde in Bi_2Te_3 Volumenmaterialien eine Strukturmodulation [natürliche Nanostrukturen (nns)] mit einer Wellenlänge von $10 \, nm$ nachgewiesen. In dieser Arbeit wurde die nns auf ihre Natur hin untersucht und wird hinsichtlich ihrer Auswirkungen auf die Transportgrößen, insbesondere der Gitterwärmeleitfähigkeit, diskutiert.

Die Transmissionselektronenmikroskopie in Kombination mit energiedispersiver Röntgenspektrometrie (EDX) ist wegen ihrer unerreichten Ortsauflösung und ihrer hervorragenden Empfindlichkeit und Genauigkeit zur Messung mechanischer Spannungen und chemischer Zusammensetzungen das Mittel der Wahl für die Untersuchung der Beziehung Struktur-chemische Zusammensetzung-physikalische Eigenschaften von thermoelektrischen Materialien. In dieser Arbeit werden erstmals methodische Arbeiten dargestellt, die eine genaue Quantifizierung der chemischen Zusammensetzung und der mechanischen Spannungsfelder in Bi_2Te_3 und strukturell und chemisch ähnlich beschaffenen Verbindungen liefern.

Diese Arbeit lässt sich wie folgt unterteilen: (I) $Bi_2(Te, Se)_3$ und $(Bi, Sb)_2Te_3$ Volumenmaterialien, die durch das Bridgman Verfahren synthetisiert wurden und in kommerziell erhältlichen Peltierelementen verwendet werden. (II) Bi_2Te_3 Dünnfilme und $Bi_2Te_3/Bi_2(Te, Se)_3$ Übergitterstrukturen, die am Fraunhofer-Institut für Physikalische Messtechnik (IPM) hergestellt wurden. (III) Methodische Arbeiten zur TEM Probenpräparation, zur quantitativen chemischen Analyse mit hoher Genauigkeit durch EDX im TEM und zur Bildsimulation von Versetzungen und der nns im Rahmen der dynamischen Beugungstheorie.

(Ia) N-leitende $Bi_2(Te_{0.91}Se_{0.09})_3$ und p-leitende $(Bi_{0.26}Sb_{0.74})_{1.98}(Te_{0.99}Se_{0.01})_{3.02}$ Volumenmaterialien zeigten eine Textur mit Korngrößen von $1-10 \, \mu m$, die Atomzahlanteile von Te und Se im n-Typ Material betrugen $54.4 \, at. \%$ bzw. $5.5 \, at. \%$ und variierten um $\pm 0.5 \, at. \%$. Ein ähnliches Ergebnis ergab sich für das p-leitende Material bezüglich Sb und Bi. Die Stöchio-

metrieschwankungen im n-leitenden und p-leitenden Bi_2Te_3 waren auf der Submikrometer-Skala klein und nahmen bis auf $\pm 2\,at.\%$ auf größerer Längenskala zu. Die Messungen bestätigten das Ergebnis der wellenlängendispersiven Röntgenspektrometrie einer inhomogenen chemischen Zusammensetzung. Die Stöchiometrieschwankungen sind mit Schwankungen des Seebeck-Koeffizienten von $\pm 9\,\mu V/K$, gemessen in einer Seebeck-Mikrosonde, korreliert.

(Ib) Eine Strukturmodulation [natürliche Nanostruktur (nns)] wurde nachgewiesen und mittels Stereomikroskopie und Bildsimulation detailliert untersucht. In Dünnfilmen und Übergitterstrukturen wurde die nns ebenso nachgewiesen und ist daher ein allgemeines Charakteristikum für Bi_2Te_3 Materialien. Die nns erwies sich als ein reines, sinusförmiges Verschiebungsfeld mit (i) einem Verschiebungsfeldvektor in Richtung von $\langle 5, -5, 1\rangle$ mit einer Amplitude von etwa $10\,pm$ und (ii) einem Wellenvektor in Richtung von $\{1, 0, 10\}$ mit einer Wellenlänge von $10\,nm$. Bi_2Te_3 Proben, die unterschiedlichen Chargen bei vergleichbaren Herstellungsbedingungen entnommen wurden, zeigten eine unterschiedliche Charakteristik bezüglich der nns: es wurde entweder keine, eine oder zwei überlagerte nns beobachtet. Die nns ist in allen Teilen der Probe mit derselben Orientierung gegenwärtig. Die Bildung der nns erfordert entweder eine betimmte Stöchiometrie oder eine bestimmte thermische Vorgeschichte und ergibt sich aus der Neigung von Telluriden zur Bildung von amorphen Phasen. Ein geordnetes Netzwerk von Versetzungen mit Abständen von wenigen Nanometern und chemische Fluktuationen auf der Nanometerskala schieden als Ursache für die nns aus. Das Verschiebungsfeld der nns ist der mittleren Mikrostruktur überlagert und sollte die thermoelektrischen Eigenschaften wesentlich beeinflussen. Vor allem die Gitterwärmeleitfähigkeit sollte eine Reduktion aufgrund der Streuung von Phononen am Spannungsfeld der nns zeigen. Außerdem sollten infolge der nns ein- oder nulldimensionales Verhalten und anisotrope Transporteigenschaften bezüglich der Basalebene auftreten. Die Anzahl der nns und die thermoelektrischen Eigenschaften sollten sich durch die Wachstumsparameter der Materialien kontrollieren lassen.

(Ic) Im Bi_2Te_3 wurden Versetzungen in der Basalebene mit einer hohen Beweglichkeit bei Raumtemperatur beobachtet, was eine besondere physikalische Eigenschaft darstellt. Der Gleitprozess und die Wechselwirkungen der Versetzungen wurden erstmals analysiert und die Auswirkungen auf die thermoelektrischen Eigenschaften werden diskutiert. Der Gleitprozess wurde durch Heizen der Probe mit einem fokussierten Elektronenstrahl von $120\,keV$ ausgelöst, äußere mechanische Spannungen wurden nicht angelegt. Die Versetzungen waren in Bewegungsrichtung ausgebäumt und nur an der Oberfläche der Proben gepinnt. Stereomikroskopische Untersuchungen in Kombination mit Bildsimulationen ergaben Versetzungen in der Basalebene mit einer Dichte von $10^9\,cm^{-2}$ und Burgersvektoren vom Typ $\langle 1, 1, 0\rangle$. Videosequenzen von einzelnen gleitenden Versetzungen und von Gruppen von Versetzungen wurden aufgenommen. Frei stehende Versetzungen zeigten eine hohe Beweglichkeit in Richtung $\pm\langle 1, 1, 0\rangle$ bei einer Geschwindigkeit von $10 - 100\,nm/s$. Versetzungsdipole waren gepinnt und konnten nicht gleiten. Äquidistante, in der gleichen Gleitebene angeordnete Versetzungen zeigten eine kollektive Bewegung. In unterschiedlichen Gleitebenen übereinander gestapelte Versetzungen waren unbeweglich und wirkten als Hindernis für andere gleitende Versetzungen. Das Gleiten der Versetzungen wurde auf Restscherspannungen von etwa $10\,MPa$ zurückgeführt, wobei die Bewegungsrichtung vom Vorzeichen des Burgersvektors abhing. Die offensichtlichen anziehenden und abstoßenden Kräfte zwischen den Versetzungen begründen sich in den Kräften verbunden mit den elastischen Spannungsfeldern der Versetzungen.

Die Bedeutung der Streuung der Phononen an Versetzungen in Bi_2Te_3, begünstigt durch deren hohe Beweglichkeit und Dichte, wurde durch zwei Betrachtungen bestätigt. Zum einen ist bekannt, dass die Gitterwärmeleitfähigkeit durch die Streuung der Phononen am elastischen Spannungsfeld der Versetzungen reduziert wird. Die mittlere freie Weglänge der Phononen wurde auf etwa $800\,\mu m$ bei $3\,K$ abgeschätzt und stimmte mit publizierten Daten überein. Zum anderen sagt die Theorie der Versetzungs-Resonanz von Granato und Lücke eine Wechselwirkung zwischen Phononen und oszillierenden Versetzungen vorher. Die Absorption von Ultraschall durch Versetzungen wurde abgeschätzt und mit publizierten Daten verglichen.

(II) Bi_2Te_3 Dünnfilme und $Bi_2Te_3/Bi_2(Te_{0.88}Se_{0.12})_3$ Übergitterstrukturen (SLs) wurden mittels Molekularstrahlepitaxie (MBE) auf BaF_2 mit einer Periode von $12\,nm$ und $6\,nm$ am Fraunhofer IPM abgeschieden. Mittels der RHEED-Technik (reflection high-energy electron

diffraction) wurde Lagenwachstum nachgewiesen, mittels der Röntgenbeugung (XRD) wurden die Gitterparameter und SL-Perioden gemessen und ein epitaktisches Wachstum bestätigt. Die Transportgrößen in der Basalebene wurden an den Dünnfilmen und den SLs gemessen und ergaben für das Produkt $S^2\sigma$ Werte zwischen 28 und $35\,\mu\mathrm{W/cm\,K}^2$. Für die Gitterwärmeleitfähigkeiten wurden bei den Bi_2Te_3 Dünnfilmen $1.60\,\mathrm{W/m\,K}$ und bei einem $10\,\mathrm{nm}$ SL $1.01\,\mathrm{W/m\,K}$ ermittelt. Die besten Gütefaktoren ZT wurden bei den SLs erzielt, wobei die Werte geringer ausfielen als bei Volumenmaterialen. Für die Bi_2Te_3 Dünnfilme und die SLs ergaben sich Versetzungsdichten von etwa $2\times 10^{10}\,\mathrm{cm}^{-2}$. Die SLs zeigten Verbiegungen mit Amplituden von $30\,\mathrm{nm}$ ($12\,\mathrm{nm}$ SL) and $15\,\mathrm{nm}$ ($6\,\mathrm{nm}$ SL) bei einer Wellenlänge von $400\,\mathrm{nm}$. Außerdem wurden Versetzungen in Wachstumsrichtung (threading dislocations) mit einer Versetzungsdichte größer als $2\times 10^9\,\mathrm{cm}^{-2}$ beobachtet. Die Grenzflächen der Übergitterstrukturen sind besonders stark im Bereich dieser „threading dislocations" verbogen. Ungestörte Bereiche zeigten eine maximale laterale Ausdehnung von $500\,\mathrm{nm}$. Sowohl in Dünnfilmen als auch in den SLs wurden Strukturmodulationen [natürliche Nanostrukturen (nns)] mit einer Wellenlänge von $10\,\mathrm{nm}$ und einem Wellenvektor in Richtung $(1,0,10)$ beobachtet.

Die Mikro-/Nanostruktur wird maßgeblich von den Übergitterstrukturen, der nns und den Versetzungen in den Materialien bestimmt. Die hier erhaltenen Ergebnisse zeigen vielfältige mechanische Spannungen infolge der nns und der Versetzungen in den Proben auf, die bisher nicht erkannt und identifiziert wurden. Sie haben einen unmittelbaren Einfluss auf die Transportgrößen, vor allem auf die Gitterwärmeleitfähigkeit. In Dünnfilmen zeigten der Seebeck-Koeffizient und die elektrische Leitfähigkeit eine negative Korrelation, hingen von der Ladungsträgerdichte ab und zeigten keine klare Abhängigkeit dieser Größen von der Mikrostruktur.

(IIIa) Die TEM Probenpräparation der Volumenmaterialien und der Dünnfilme beinhaltete mechanisches Polieren und konventionelle Ionenstrahlätzung und war eine große Herausforderung. Bei den Dünnfilmen und Übergitterstrukturen schlugen die Standard-Präparationsmethoden aufgrund der Sprödigkeit des BaF_2 Substrates und der schwachen Bindung zwischen dem Bi_2Te_3 Dünnfilm und dem BaF_2 Substrat fehl und mussten modifiziert werden.

(IIIb) Erste EDX Spektren, die im Zeiss 912Ω TEM aufgenommen wurden, zeigten Artefakte in Form von Bi Röntgenstreustrahlung bei Messungen im Vakuum neben der Probe (hole-count). Eine Streustrahlungsblende wurde in die TEM Säule zur Absorption von Streustrahlung eingebaut. Mit Hilfe dieser Blende konnte eine quantitative chemische Analyse mit hoher Genauigkeit verwirklicht werden, basierend auf der Cliff-Lorimer Methode ohne Absorptionskorrektur. Durch diese Blende wurde die Zahl der Röntgenimpulse bei der „hole-count"-Messung um einen Faktor 5 und die Streuung der Daten um einen Faktor 4 reduziert. Die verbesserte Genauigkeit ist auch für andere Materialien bei der quantitativen EDX Analyse von großer Bedeutung. Dies wurde zum einen für den Hochtemperatur-Supraleiter $Bi_2Sr_2CaCu_2O_8$ und zum anderen für das Mineralsalz Hydroxyapatit $Ca_{10}(PO_4)_6OH_2$ demonstriert.

(IIIc) Die Bildsimulation wurde (i) zur Burgersvektoranalyse der Versetzungen und (ii) zur Analyse des Verschiebungsfeldvektors und des Wellenvektors der nns angewandt. Das Spannungsfeld der Versetzung wurde mit Hilfe des Integral-Formalismus von Barnett und Lothe berechnet, der auch auf piezoelektrische Materialien wie $BaTiO_3$ angewandt wurde. Die komplexen Amplituden des direkten und des abgebeugten Strahls wurden mit Hilfe der dynamischen Beugungstheorie von Howie and Whelan und unter Berücksichtigung von Absorptionseffekten berechnet. Die Rechenzeit pro Bild einer Versetzung wurde auf weniger als $10\,\mathrm{s}$ reduziert, der Programmiercode basierte auf MATLAB®.

Aufgrund der Ergebnisse dieser Arbeit sind folgende weiterführende Untersuchungen an Bi_2Te_3 Volumenmaterialien besonders wünschenswert: (a) Die Messung der Transportgrößen in drei unterschiedlichen Richtungen über einen weiten Temperaturbereich an Proben mit und ohne nns. (b) Die Berechnung der Transportgrößen, vor allem der Gitterwärmeleitfähigkeit, unter Berücksichtigung der Streuung der Phononen am Spannungsfeld der nns. (c) Systematische Untersuchungen zur Bildung der nns. Die Bildung der nns in den Bi_2Te_3 Materialien könnte mit der Neigung von Telluriden zur Bildung amorpher Phasen korreliert sein. Telluride werden daher bevorzugt bei wiederbeschreibbaren optischen Speichermedien (DVD) als Phasenwechsel-Materialien eingesetzt. In jüngster Zeit wurden in Bi_2Te_3-Sb_2Te_3 Verbindungen thermisch induzierte, reversible Glas-Kristall Phasenübergänge nachgewiesen. Aus diesem

Grund kann die nns auch als ein Zustand zwischen perfekt kristalliner und amorpher Phase angesehen werden, und ihre Bildung läßt sich eventuell durch die thermische Vorgeschichte der Probe steuern.

Auch andere thermoelektrische Materialien zeigen eine nns: In $AgPb_mSbTe_{2+m}$ Volumenmaterialien wurden chemische Modulationen auf der Nanometer-Skala (nns) mit einer Wellenlänge von $20 - 30\,nm$, eine geringe Gitterwärmeleitfähigkeit und ein spektakulärer thermoelektrischer Gütefaktor $ZT > 2$ nachgewiesen. $AgPb_mSbTe_{2+m}$ und Bi_2Te_3 zeigen ähnliche strukturelle Eigenschaften und demzufolge auch ähnliche Gitterwärmeleitfähigkeiten. Die methodischen Verbesserungen, die in dieser Arbeit gewonnen wurden, können auch auf die $AgPb_mSbTe_{2+m}$ Volumenmaterialien übertragen werden. Insbesondere betrifft dies die strukturelle Analyse einer nns im TEM und ihre quantitative chemische Analyse durch EDX im TEM.

Beide Arten von Nanostrukturen, künstliche (ans) und natürliche (nns) Nanostrukturen, führten in einer großen Zahl von thermoelektrischen Materialien zu einer geringen Gitterwärmeleitfähigkeit, was sich gewinnbringend auf den thermoelektrischen Gütefaktor ZT auswirkte. Die Ursache ist die durch die ans und nns induzierte strukturelle Unordnung und die damit verbundene Reduktion der mittleren freien Weglänge der Phononen. Die ans und die nns sind der Schlüssel zur Erhöhung der ZT-Werte nach Jahrzehnten der Stagnation und stehen daher aktuell bei der Forschung und bei den Anwendungen im Mittelpunkt.

Summary

Thermoelectric materials are used for power-generation and solid-state refrigeration devices. At room temperature, Bi_2Te_3 bulk materials are widely used Peltier materials since they are known for their large thermopower ($S \approx \pm200\,\mu V/K$), large electrical conductivity ($\sigma \approx 1000\,1/\Omega\,cm$), low (electronic and lattice) thermal conductivity ($\lambda \approx 1.5\,W/m\,K$), and thereby a high thermo-electric figure of merit [$ZT = (S^2\sigma/\lambda)\,T \approx 1$] at $T = 300\,K$.

Thermoelectric quantum well systems such as superlattices [artificial nanostructure (ans)] based on Bi_2Te_3 were proposed by Hicks and Dresselhaus in 1993. In 1999, Venkatasubramanian manufactured Bi_2Te_3/Sb_2Te_3 superlattices (ans) with a period of 6 nm and a spectacular thermoelectric figure of merit of $ZT > 2$. The ans yielded an increased power factor $S^2\sigma$ and a low lattice thermal conductivity compared to bulk materials. The reduced lattice thermal conductivity was attributed to a reduction of the phonon mean free path due to the structural disorder introduced by the ans. The ans showed a significantly increased ZT compared to bulk materials and was a boost for the synthesis of nanostructured materials for thermoelectric applications.

The research on thermoelectric materials is based on solid state physics which predicts that it is difficult to improve one transport coefficient without changing the others in an unfavourable way. The reason is that the transport coefficients are determined by common fundamental parameters of the electron and phonon systems. The thermopower and the electrical conductivity particularly depend on the doping level and the chemical composition, whereas the lattice thermal conductivity is sensitive to structural disorder on the nanometer scale. The challenge is to synthesise thermoelectric materials with electrical properties of crystalline materials and, in contradiction, thermal properties of amorphous materials. Combined measurements, i.e., transport and structural investigations on the same samples, and a discussion of the results are required to find the optimum between these two extremes, i.e., electron crystal/phonon glass.

In Bi_2Te_3, in the literature there are a large number of published measurements of transport properties, a small number of structural analyses, however no data of combined measurements. It is still an open question, why the lattice thermal conductivity of bulk Bi_2Te_3 is so small. Preliminary investigations by transmission electron microscopy (TEM) yielded a structural modulation [natural nanostructure (nns)] with a wavelength of 10 nm in bulk Bi_2Te_3. In this work, the nature of the nns was analysed and the correlations to the transport coefficients, particularly the lattice thermal conductivity, is discussed.

Transmission electron microscopy combined with energy dispersive X-ray spectrometry (EDX) is the method of choice for a study of the correlations between structure, chemical composition, and physical properties in thermoelectric materials. Particularly, stress fields and chemical compositions can be analysed at an unrivalled lateral resolution, a high sensitivity, and a high accuracy. In this work, experimental methods will be presented for the first time, yielding an accurate quantitative analysis of the chemical composition and of stress fields in Bi_2Te_3 and in compounds with similar structural and chemical microstructures.

This work can be subdivided as follows: (I) $Bi_2(Te, Se)_3$ and $(Bi, Sb)_2Te_3$ bulk materials synthesised by the Bridgman technique, which are used in commercially available Peltier devices. (II) Bi_2Te_3 thin films and $Bi_2Te_3/Bi_2(Te, Se)_3$ superlattices manufactured at the Fraunhofer-Institut für Physikalische Messtechnik (IPM). (III) Experimental methods, i.e., TEM specimen preparation, high-accuracy quantitative chemical analysis by EDX in the TEM, and image simulations of dislocations and the nns according to the two-beam dynamical diffraction theory.

(Ia) N-type $Bi_2(Te_{0.91}Se_{0.09})_3$ and p-type $(Bi_{0.26}Sb_{0.74})_{1.98}(Te_{0.99}Se_{0.01})_{3.02}$ bulk materials showed a texture and grain sizes of $1 - 10\,\mu m$, the mole fractions of Te and Se were 54.4 at. % and 5.5 at. % and varied by ±0.5 at. % for n-type material. A similar behaviour was found for Sb and Bi in p-type material. The variation in stoichiometry was smaller on the sub-micro-meter scale and increased to ±2 at. % with increasing length scale for both, n-type and p-type Bi_2Te_3. Measurements in the TEM confirmed the inhomogeneous chemical composition found by wavelength dispersive X-ray spectrometry. The variations in stoichiometry are correlated to variations in the thermopower by $\pm9\,\mu V/K$ measured in a Seebeck scanning microprobe.

(Ib) A structural modulation [natural nanostructure (nns)] was found and was analysed in detail by stereomicroscopy and by image simulation. This nns was also observed in thin films and superlattices and turned out to be of general character for Bi_2Te_3 materials. The nns was found to be a pure sinusoidal displacement field with (i) a displacement vector parallel to $\langle 5, -5, 1 \rangle$ and an amplitude of about $10\,pm$ and (ii) a wave vector parallel to $\{1, 0, 10\}$ and a wavelength of $10\,nm$. Bi_2Te_3 samples from different batches produced under similar conditions showed different characteristics with respect to the nns: none, one, or two superimposed nns were observed. The nns is present in all parts of the sample with the same orientation. The formation of the nns is either bound to a certain stoichiometry range or to the thermal history and is related to the tendency of Te-compounds to form amorphous phases. An ordered network of dislocations a few nanometers apart and chemical fluctuations on the nanometer scale as origins of the nns were ruled out. The displacement field of the nns is superimposed to the average structure and should significantly affect the thermoelectric properties. Particularly, the lattice thermal conductivity should be decreased due to phonon scattering on the strain field of the nns. Also, the nns should yield a one-dimensional or zero-dimensional behaviour and anisotropic transport coefficients in the basal plane. The number of nns and thereby the thermoelectric properties might be controlled by the growth parameters.

(Ic) In Bi_2Te_3, dislocations in the basal plane with a high mobility at room temperature were found, which is a unique physical property. The motion and the interactions of the gliding dislocation were analysed for the first time and the influence on the thermoelectric properties is discussed. The motion was induced by heating with a focused electron beam at $120\,keV$. External stresses were not applied. The dislocations were bowed out in the direction of motion and were only pinned at the surface of the samples. Stereomicroscopy investigations combined with image simulations yielded basal plane dislocations with a density of $10^9\,cm^{-2}$ and Burgers vectors $\langle 1, 1, 0 \rangle$. Video sequences showing the glide of single dislocations and of groups of dislocations were recorded. Free standing dislocations showed a high mobility in $\pm \langle 1, 1, 0 \rangle$ direction at a velocity of $10 - 100\,nm/s$. Dislocation dipoles were pinned and did not glide. Dislocations equidistantly arranged within the same glide plane showed a collective movement. Dislocations piled up in different glide planes were fixed and acted as barriers for other gliding dislocations. The motion of dislocations was attributed to residual shear stresses, estimated to $10\,MPa$, and their directions depended on the sign of the Burgers vector. Attractive and repulsive forces of dislocations directly visualise the forces due to the elastic strain fields of the dislocations.

The relevance of phonon scattering on dislocations in Bi_2Te_3, particularly due to their high mobility and density, was confirmed by two inspections. First, dislocations are known to decrease the lattice thermal conductivity due to phonon scattering on the elastic strain field. The phonon mean free path was estimated to about $800\,\mu m$ at $3\,K$ and agreed with published data. Second, the dislocation resonance theory of Granato and Lücke predicts an interaction between phonons and dislocations acting as oscillating strings. The attenuation of ultrasound due to dislocations was estimated and was compared with published data.

(II) Bi_2Te_3 thin films and $Bi_2Te_3/Bi_2(Te_{0.88}Se_{0.12})_3$ superlattices (SLs) were epitaxially grown by molecular beam epitaxy (MBE) on BaF_2 substrates with a period of $12\,nm$ and $6\,nm$ at the Fraunhofer IPM, respectively. Reflection high-energy electron diffraction (RHEED) confirmed a layer-by-layer growth, X-ray diffraction (XRD) yielded the lattice parameters and SL periods and proved epitaxial growth. The basal plane transport coefficients were measured and the thin films and SL had power factors between 28 and $35\,\mu W/cm\,K^2$. The lattice thermal conductivity varied between $1.60\,W/m\,K$ for Bi_2Te_3 thin films and $1.01\,W/m\,K$ for a $10\,nm$ SL. The best figures of merit ZT were achieved for the SL; however, the values are slightly smaller than in bulk materials. In the Bi_2Te_3 thin film and SL the dislocation density was found to be $2 \times 10^{10}\,cm^{-2}$. Bending of the SL with amplitudes of $30\,nm$ ($12\,nm$ SL) and $15\,nm$ ($6\,nm$ SL) and a wavelength of $400\,nm$ was determined. Threading dislocations were found with a density greater than $2 \times 10^9\,cm^{-2}$. The superlattice interfaces are strongly bent in the region of the threading dislocations, undisturbed regions had a maximum lateral size of $500\,nm$. Thin films and SL showed a structural modulation [natural nanostructure (nns)] with a wavelength of $10\,nm$ and a wave vector parallel to $(1, 0, 10)$.

The microstructure/nanostructure is governed by the superlattice, the nns, and the dislocations that are present in the films. The results obtained here showed a significant amount of stress in the samples, induced by the nns and the dislocations, which were still not noticed and identified. The stress fields directly affect the transport coefficients, particularly the lattice thermal conductivity. In thin films, the thermopower and the electrical conductivity were found to be negatively correlated, depend on the charge carrier density, and no clear dependence of the two quantities on the microstructure could be found.

(IIIa) TEM specimen preparation of the bulk materials and of the thin films included mechanical polishing and conventional ion milling and was a significant challenge. For thin films and superlattices, the standard preparation procedure failed and had to be modified due to the brittleness of the BaF_2 substrate and the weak bonding between the Bi_2Te_3 thin film and the BaF_2 substrate.

(IIIb) Preliminary EDX spectra obtained in the Zeiss 912Ω TEM yielded artifacts due to Bi spurious X-rays and hole-counts significantly beyond zero. A stray aperture was inserted in the TEM to absorb the stray radiation. With this aperture inserted a high-accuracy quantitative chemical analysis was established, based on the Cliff-Lorimer method without absorption correction. The hole-counts decreased by a factor of 5 and the scatter of data decreased by a factor of 4 due to this aperture. The improved accuracy of the quantitative EDX analysis is also for other compounds of great importance. This was demonstrated on the high-T_C superconductor $Bi_2Sr_2CaCu_2O_8$ and the mineral salt hydroxyapatite $Ca_{10}(PO_4)_6OH_2$.

(IIIc) Image simulation was used to analyse (i) the Burgers vector of dislocations and (ii) the displacement vector and the wave vector of the nns. The strain field of the dislocations was calculated according to the integral formalism of Barnett and Lothe and was also applied to piezoelectric materials such as $BaTiO_3$. The complex amplitudes of the direct beam and of the diffracted beam were calculated according to the two-beam dynamical diffraction theory of Howie and Whelan under consideration of absorption effects. The computing time for one image of a dislocation could be reduced to less than $10\,s$, the simulation was implemented in MATLAB®.

On the basis of our experimental results following investigations on bulk Bi_2Te_3 are highly recommended in future: (a) Transport measurements in three different directions over a wide temperature range on samples with and without a nns. (b) Calculations of the transport coefficients, particularly of the lattice thermal conductivity, under consideration of phonon scattering on the strain field of the nns. (c) Systematic investigations of the formation of the nns. The formation of the nns in Bi_2Te_3 could be related to the ability of Te-compounds to easily form glasses. Therefore, Te-compounds are widely used for rewritable phase-change optical recording applied in optical data storage systems like digital versatile disks (DVD). Recently, thermally induced reversible glass-crystal phase changes were also found in Bi_2Te_3-Sb_2Te_3 compounds. For this, the nns might be regarded as an intermediate state between pure crystalline and amorphous and might be controlled by the thermal history of the sample.

Other thermoelectric materials also showed a nns: $AgPb_mSbTe_{2+m}$ bulk materials showed chemical modulations on the nanometer scale (nns) with a wavelength of $20-30\,nm$, a low lattice thermal conductivity, and a spectacular thermoelectric figure of merit of $ZT > 2$. Therefore, $AgPb_mSbTe_{2+m}$ and Bi_2Te_3 have common structural features and their lattice thermal conductivities are in a similar range. The improved experimental methods yielded in this work, particularly structural analysis of a nns in a TEM and its quantitative chemical analysis by EDX in the TEM, can also be transferred to $AgPb_mSbTe_{2+m}$ bulk materials.

Both kinds of nanostructures, artificial (ans) and natural (nns) nanostructures, yielded in a large number of thermoelectric materials a low lattice thermal conductivity which was beneficial for the thermoelectric figure of merit ZT. The reason is a reduction of the phonon mean free path due to the structural disorder introduced by the ans and the nns. The ans and the nns are the key to an increased ZT after several decades of stagnancy, and therefore are currently a main topic of research and application.

Chapter preview

Chapter 1 is an introduction to macroscopic and microscopic thermoelectricity. The thermoelectric figure of merit of a Peltier device will be given in dependence of the transport coefficients. The advantages of microcoolers compared to conventional coolers will be explained. For bulk semiconductors and for $2D$ quantum well systems, the dependence of the electronic transport coefficients on fundamental parameters of the electron and phonon systems according to the band theory of solids and the Boltzmann equation will be shown. General criteria for high-performance thermoelectric materials will be given. Finally, general properties of bulk Bi_2Te_3 and preliminary results obtained in our samples will be presented.

Chapter 2 is dedicated to dislocations. The strain field of dislocations in elastically isotropic crystals will be given and its influence on the lattice thermal conductivity and on diffraction contrast observed in the TEM will be explained. Gliding and oscillating dislocations were observed in bulk Bi_2Te_3. The motion of the dislocations is determined by forces which could be due to (i) image forces close to free surfaces, (ii) residual shear stresses in the sample, and (iii) due to the interaction between the dislocations. Finally, the Granato-Lücke theory of dislocation resonance will be presented.

In Chapter 3 the structure and composition of the bulk samples will be specified and an overview of the experimental techniques used in this work will be given.

In Chapter 4 first the improvements of the EDX analysis in the TEM will be presented which were obtained by inserting a stray aperture for absorbing stray radiation in the column of the TEM. Results of the quantitative chemical analysis by EDX in the TEM obtained in bulk Bi_2Te_3 and other model materials will be shown and discussed.

Chapter 5 is dedicated to the structural modulations (nns) observed in bulk Bi_2Te_3. A detailed model for the nns will be given and discussed. Possible reasons for the formation of the nns and its influence on the thermoelectric properties will be discussed.

Chapter 6 shows the results obtained in Bi_2Te_3 based thin films and superlattices. First, the structure and composition of the samples, the MBE growth parameters, and the experimental techniques will be specified. Second, the preliminary measurements by RHEED and XRD, and the measurements of the thermoelectric properties will be presented. TEM specimen preparation of thin films and superlattices was demanding and therefore was also included in this work. Finally, the TEM results obtained on cross-sectional and plan view samples will be shown and discussed.

Chapter 7 presents stereomicroscopy results and video sequences obtained on gliding dislocations in bulk Bi_2Te_3. The results were analysed with respect to the Burgers vector and the line direction of the dislocations, forces on dislocations, and residual shear stresses in the sample. An estimation for the phonon mean free path and ultrasound attenuation in dependence of the measured dislocation density will given and discussed.

Chapter 8 is about image simulation of strain fields in crystals, implemented in MATLAB®. First, the equations for the strain field of dislocations in elastically anisotropic crystals according to Barnett and Lothe will be given. Second, the basic principles used for a fast image simulation will be explained. Results obtained on dislocations in aluminium and β-brass used as reference materials will be shown. Finally, image simulation was applied to dislocations and the nns found in bulk Bi_2Te_3.

Finally, in the Appendix new results obtained in bulk Bi_2Te_3 will be presented. The MATLAB® code for image simulation of dislocations will be presented in detail.

Contents

Chapter 1

Thermoelectricity

1.1 Macroscopic thermoelectricity and thermoelectric refrigerators

1.1.1 Conventional coolers and thermoelectric figure of merit

Thermoelectric materials are used for power-generation and solid-state refrigeration devices. The challenge is to synthesise high-performance thermoelectric materials and to develop highly-efficient devices through ingenious material engineering. The applications which are currently in the field of interest are (i) direct conversion of waste heat into electrical energy, particularly for the automotive industry, (ii) power generators for deep space missions, (iii) miniaturised coolers for computers, infrared detectors, electronics, and optoelectronics. The main topics of research are (a) high-temperature bulk materials such as skutterudites, clathrates, half-Heusler alloys, complex chalcogenides, and ceramic oxides, (b) bulk materials with structural and/or compositional modulations on the nanometer scale, (c) and nanoengineered quantum well systems such as quantum dots, nanowires, and superlattices. An overview of state-of-the-art applications and research is given in References [1–3].

Thermoelectric refrigerators based on isotropic solids were described in detail by Goldsmid [4] and will be the central topic of this section. For an understanding of the basic function of such devices several fundamental effects have to be considered; which are Ohm's law ($j = \sigma\,E$), the Seebeck effect ($E = S\frac{dT}{dx}$), the Peltier effect ($j_Q = \Pi\,j$), Fourier's law ($j_Q = -\lambda\frac{dT}{dx}$), and the Joule effect, where j is the electrical current density, j_Q is the heat current density, E is the electric field, T is the temperature, $\frac{dT}{dx}$ is a temperature gradient, σ is the electrical conductivity, λ is the thermal conductivity, S is the thermopower, and Π is the Peltier coefficient. According to the Kelvin-Onsager relation the Peltier coefficient is related to the thermopower by $\Pi = S\,T$. For semiconductors, the sign of the thermopower and of the Peltier coefficient depend on the type of the majority charge carriers, being negative for n-type and positive for p-type semiconductors.

A schematic drawing of a single-couple refrigerator with two branches which consist of a p-type and a n-type semiconductor is shown in Figure 1.1(a). The bottom of the thermocouple is kept to a constant temperature T_{H}. In the p-type branch the electrical current I and the heat current I_{Q} due to the Peltier effect are parallel, whereas in the n-type branch both currents are anti-parallel. Therefore, the top of the thermocouple is cooled to a temperature T_{C}. A commercially available conventional cooler is shown in Figure 1.1(b). In such modules many single thermocouples are connected electrically in series and act thermally in parallel.

The potential of a material for thermoelectric application or the potential of thermoelectric devices are determined by the thermoelectric figure of merit Z or by the related dimensionless figure of merit $ZT = Z \cdot T$ [4, chap. 1.3]. The thermoelectric figure of merit Z determines in a large part the maximum temperature difference $\Delta T = (T_{\mathrm{H}} - T_{\mathrm{C}})_{\mathrm{max}}$, the maximum cooling power q_{C} at the cold side, and the maximum coefficient of performance COP. The calculation
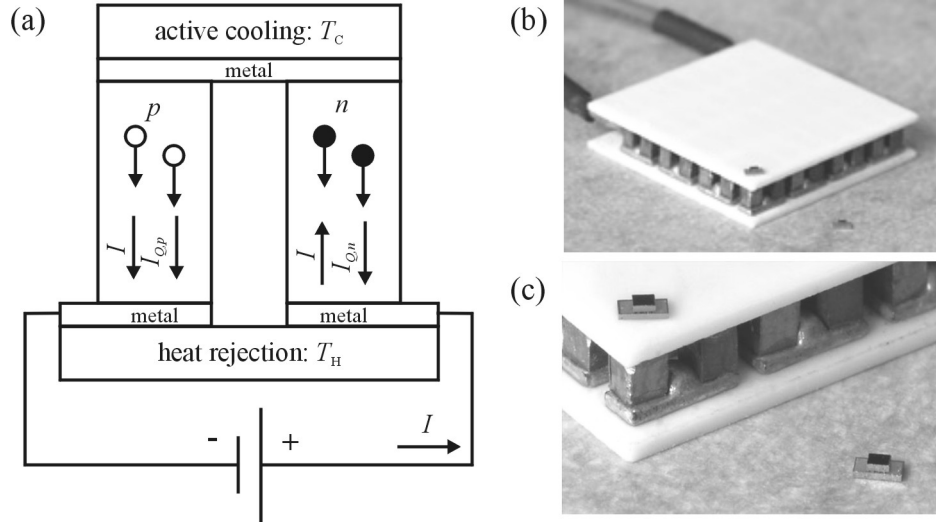
Figure 1.1 (a) Model of a single-couple thermoelectric refrigerator. (b) Conventional cooler. (c) Micropelt's microcooler with a size of about $5\,\text{mm} \times 5\,\text{mm} \times 0.5\,\text{mm}$ on top of a conventional cooler.

of these quantities can be simplified by assuming that (i) there is no contact resistance between the metal links and the thermoelements, (ii) the metal links have zero resistance, (iii) there is no thermal resistance between the thermocouple and the heat source and heat sink, (iv) there are no radiation effects, and (v) the transport coefficients are independent of the temperature.

$$\Delta T = \frac{1}{2}\, Z\, T_{\text{C}}{}^2 \,=\, \frac{1}{2\,Z} \left(\sqrt{2\, Z\, T_{\text{H}} + 1} - 1 \right)^2 , \tag{1.1a}$$

$$q_{\text{C}} = K \left\{ \frac{1}{2}\, Z\, T_{\text{C}}{}^2 - (T_{\text{H}} - T_{\text{C}}) \right\} , \tag{1.1b}$$

$$COP = \frac{T_{\text{C}}}{T_{\text{H}} - T_{\text{C}}} \frac{\sqrt{1 + \frac{1}{2}\, Z\, (T_{\text{H}} + T_{\text{C}})} - \frac{T_{\text{H}}}{T_{\text{C}}}}{\sqrt{1 + \frac{1}{2}\, Z\, (T_{\text{H}} + T_{\text{C}})} + 1} . \tag{1.1c}$$

The thermoelectric figure of merit Z of the thermocouple is given by

$$Z = \frac{S^2}{K\, R} , \tag{1.2a}$$

$$S = S_p - S_n , \tag{1.2b}$$

$$R = \rho_p \frac{L_p}{A_p} + \rho_n \frac{L_n}{A_n} , \tag{1.2c}$$

$$K = \lambda_p \frac{A_p}{L_p} + \lambda_n \frac{A_n}{L_n} , \tag{1.2d}$$

where S is the total thermopower, R is the electrical resistance, and K is the thermal conductance of the thermocouple. These quantities depend on the transport coefficients $S_{p,n}$, $\rho_{p,n} = 1/\sigma_{p,n}$, $\lambda_{p,n}$, of the cross-section areas $A_{p,n}$, and of the lengths $L_{p,n}$ of both branches.

1.1.2   Chip spot cooling by Bi₂Te₃ based microcoolers

Future microprocessors require a higher packaging density and a higher processor speed, which leeds to an increased heat flux of up to $300\,\text{W/cm}^2$. Therefore, the thermal management issues of power microelectronics has to be solved. One solution are Peltier microcoolers which were

suggested and discussed with respect to the main technological problems by Fleurial [5]. Complete microcoolers based on thin film technology in combination with microsystem technology [6] are manufactured by Micropelt GmbH [7] in collaboration with the Fraunhofer Institut für Physikalische Messtechnik (IPM) [8] and Infineon Technologies AG (Fig. 1.1(c)).

The cooling power density q_{C} of an ideal Peltier refrigerator is proportional to the thermal conductance K (Eq. 1.1) and thereby inversely proportional to the leg length L (Eq. 1.2). At room temperature, current $\mathrm{Bi_2Te_3}$ based coolers with a leg length of about $2\,\mathrm{mm}$ reach a cooling power density of about $5\,\mathrm{W/cm^2}$. Microcoolors with a film thickness of $20\,\mu\mathrm{m}$ would reach a cooling power density of about $500\,\mathrm{W/cm^2}$, which is sufficient for future demands. However, for decreasing leg lengths the metal/semiconductor contact resistance can not be neglected and should be about $10^{-10}\,\Omega\mathrm{m^2}$ [6] to preserve the cooling power density. Finally, due to the high heat fluxes high thermal conductive substrates are necessary.

1.2 Microscopic thermoelectricity

1.2.1 Thermoelectric figure of merit for single materials

The criterion for the selection of a material for a thermocouple is to maximise the thermoelectric figure of merit of the device. It is convenient to define the thermoelectric figure of merit for a single material as

$$Z = \frac{S^2\,\sigma}{\lambda} = \frac{S^2\,\sigma}{\lambda_{\mathrm{latt}} + \lambda_{\mathrm{el}}}\,. \tag{1.3}$$

Therefore, a good thermoelectric material requires a large thermopower S, a large electrical conductivity σ, and a low thermal conductivity λ, which is the sum of the lattice thermal conductivity λ_{latt} and the electronic thermal conductivity λ_{el}. Particularly, semiconductors achieve these requirements, as will be shown. Also, the difference of the thermopowers should be as large as possible (Eq. 1.2). Therefore, p-type and their n-type counterpart semiconductors are used for the branches.

Only small increases of the thermoelectric figure of merit could be achieved in the last decades. The reason is, that the thermopower S, the electrical conductivity σ, and the thermal conductivity λ depend on each other and it is difficult to improve one transport coefficient without significantly changing the others in an unfavourable way. The transport coefficients are determined by more fundamental parameters of the electron and phonon systems; which are the charge carrier density n, the electron mobility μ, the electron scattering rate or relaxation time τ, the Debye temperature θ_{D}, and the phonon mean free path l_{ph}. In the next two sections the calculation of the transport coefficients for isotropic crystals following the textbooks of Goldsmid [4, chap. 2] and of Ziman [9], will be presented. General criteria for the selection or the optimization of a thermoelectric material will be discussed [4, chap. 3].

1.2.2 Lattice thermal conductivity

The lattice thermal conductivity can be calculated as

$$\lambda_{\mathrm{latt}} = 1/3\,C\,v\,l_{\mathrm{ph}} \tag{1.4}$$

according to transport theory for isotropic solids [9, page 259], where C is the total specific heat, v is the velocity of sound, and l_{ph} is the phonon mean free path. The total specific heat can be determined by the Debye model, where θ_{D} is the Debye temperature, z is the number of atoms per unit cell, $\frac{N}{V}$ is the number of unit cells per volume, and k_{B} is the Boltzmann's constant [9, page 54],

$$C = 9\,k_{\mathrm{B}}\,z\,\frac{N}{V}\left(\frac{T}{\theta_{\mathrm{D}}}\right)^3 \int_0^{\frac{\theta_{\mathrm{D}}}{T}} \frac{y^4 e^y}{(e^y - 1)^2}\,dy\,. \tag{1.5}$$

At high temperatures $T > \theta_\mathrm{D}$, the specific heat tends to $3\,k_\mathrm{B}\,z\,\frac{N}{V}$ [9, page 54] being constant, and therefore the lattice thermal conductivity is determined by the phonon mean free path. Phonon-phonon scattering is dominant at high temperatures, particularly due to Umklapp-processes. Leibfried and Schlömann derived under consideration of the Lindemann melting formula for the lattice thermal conductivity

$$\lambda_\mathrm{latt} \propto \left(T_\mathrm{M}^{\frac{3}{2}}\, \rho^{\frac{2}{3}}\, A^{-\frac{7}{6}} \right)\,\frac{1}{T}\,, \tag{1.6}$$

where T_M is the melting point, ρ is the mass density, and A is the mean atomic weight (Ref. [9, pages 58 and 296] and Ref. [4, chap. 3.4.1]). The phonon mean free path and thereby the lattice thermal conductivity decreases inversely proportional to the temperature. The first factor is determined by material parameters and decreases for increasing mean atomic weight.

At low temperatures $T \ll \theta_\mathrm{D}$, the specific heat increases with T^3 [9, page 54],

$$C = \frac{12\pi^4}{5} k_\mathrm{B}\, z\, \frac{N}{V} \left(\frac{T}{\theta_\mathrm{D}} \right)^3\,. \tag{1.7}$$

For an ideal crystal the phonon mean free path l_ph would be limited only by the size of the sample, since phonon scattering on the crystal surfaces is the dominating scattering mechanism [9, chap. 11]. Therefore, the lattice thermal conductivity would have the same temperature dependence as the specific heat.

However, in a real crystal the phonon mean free path l_ph would be limited also by phonon scattering on point defects and on extended crystals defects such as grain boundaries and dislocations [9, chap. 6 and 8]. Particularly, the dependence of the lattice thermal conductivity on the dislocation density will be discussed in more detail in Chapter 2.4.1. In solid solutions, alloy scattering also offers the possibility to reduce the lattice thermal conductivity [9, chap. 6 and 8]. Finally, the dependence of the lattice thermal conductivity on structural disorder was nicely demonstrated for single crystalline Si thin films and other model materials [10]. Particularly, hole-conducting Bi_2Te_3/Sb_2Te_3 superlattices with a period of 6 nm showed a decreased lattice thermal conductivity and spectacular thermoelectric figure of merit of $ZT = 2.4$ at 300 K [11–13].

In summary, some general criteria can be derived for high performance thermoelectric materials [4, chap. 3.4]. A low lattice thermal conductivity and thereby a large thermoelectric figure of merit is found for

High-ZT criterion (i) bulk materials of high mean atomic weight (Eq. 1.6),

High-ZT criterion (ii) bulk materials with a high structural disorder,

High-ZT criterion (iii) alloyed bulk materials,

High-ZT criterion (iv) thin films and superlattices.

1.2.3   Electronic transport coefficients

Bulk semiconductors

The thermopower S, the electrical conductivity σ, and the electronic thermal conductivity λ_el of crystalline solids can be determined by using the band theory of solids and the linearised Boltzmann equation [9, chap. 7 and 10]. Only the expressions for an isotropic semiconductor with a simple, parabolic band will be given here. For the calculation of the quantities the carrier energy $\varepsilon = E - E_\mathrm{L}$ ($\varepsilon = E_\mathrm{V} - E$) and the Fermi energy $\zeta = E_\mathrm{F} - E_\mathrm{L}$ ($\zeta = E_\mathrm{V} - E_\mathrm{F}$) are measured with respect to the bottom of the conduction band E_L (with respect to the top of the valence band E_V).

$$\sigma = n\,e\,\mu\,, \tag{1.8a}$$

$$S = \pm\frac{k_{\mathrm{B}}}{e}\left\{\frac{1}{k_{\mathrm{B}}\,T}\frac{\langle\tau(\varepsilon)\,\varepsilon\rangle}{\langle\tau(\varepsilon)\rangle} - \frac{\zeta}{k_{\mathrm{B}}\,T}\right\}\begin{cases} + & \text{for holes} \\ - & \text{for electrons} \end{cases}, \tag{1.8b}$$

$$\lambda_{\mathrm{el}} = L\,T\,\sigma\,, \tag{1.8c}$$

$$n = \int\limits_0^\infty D(\varepsilon)\,f^0(\varepsilon)\,d\varepsilon\,, \tag{1.8d}$$

$$\mu = \frac{e}{m}\,\langle\tau(\varepsilon)\rangle\,, \tag{1.8e}$$

$$\langle\tau(\varepsilon)\rangle = \frac{\frac{2}{3}\int\limits_0^\infty \tau(\varepsilon)\,\varepsilon\left(-\frac{\partial f^0}{\partial \varepsilon}\right)D(\varepsilon)\,d\varepsilon}{\int\limits_0^\infty D(\varepsilon)\,f^0(\varepsilon)\,d\varepsilon}\,, \tag{1.8f}$$

$$L = \frac{1}{(k_{\mathrm{B}}\,T)^2}\left[\frac{\langle\tau(\varepsilon)\,\varepsilon^2\rangle}{\langle\tau(\varepsilon)\rangle} - \left\{\frac{\langle\tau(\varepsilon)\,\varepsilon\rangle}{\langle\tau(\varepsilon)\rangle}\right\}^2\right]\left(\frac{k_{\mathrm{B}}}{e}\right)^2\,, \tag{1.8g}$$

$$\langle\tau(\varepsilon)\,\varepsilon^n\rangle = \frac{\frac{2}{3}\int\limits_0^\infty \tau(\varepsilon)\,\varepsilon^{n+1}\left(-\frac{\partial f^0}{\partial \varepsilon}\right)D(\varepsilon)\,d\varepsilon}{\int\limits_0^\infty D(\varepsilon)\,f^0(\varepsilon)\,d\varepsilon}\,. \tag{1.8h}$$

These expressions differ in their appearance from the expressions given in the textbooks of Ziman [9, chap. 10] and Goldsmid [4, chap. 2.4], but are similar to the results of the Drude model including the Wiedemann-Franz law. However, there are some differences to the Drude model: (i) m is the effective mass of the conduction electrons. (ii) The carrier density n depends on the density of states $D(\varepsilon)$ and the Fermi energy ζ through the unperturbed Fermi distribution function $f^0(\varepsilon)$. (iii) The carrier mobility μ depends on the average relaxation time $\langle\tau(\varepsilon)\rangle$. (iv) The thermopower S and the Lorenz number L depend on a weighted average of the total heat energy $\langle\varepsilon - \zeta\rangle$ transported by a carrier.

For a parabolic band the density of states is given by $D(\varepsilon) = \frac{1}{2\pi^2}\left(\frac{2m}{\hbar^2}\right)^{\frac{3}{2}}\sqrt{\varepsilon}$. In the simplest case the relaxation time can be expressed by $\tau(\varepsilon) = \tau_0\,\varepsilon^r$, where τ_0 and r are constants. Particularly, the scattering exponent r depends on the electron scattering process and is equal to $-\frac{1}{2}$ for acoustic phonon scattering and equal to $\frac{3}{2}$ for scattering on ionised impurities [4, chap. 3.3.1]. Due to these simplifications all quantities are determined by the Fermi-Dirac integrals $F_m(\eta)$ [4, chap. 2.4], which can be expressed in terms of the reduced energy $\xi = \varepsilon/(k_{\mathrm{B}}\,T)$ and reduced Fermi energy $\eta = \zeta/(k_{\mathrm{B}}\,T)$.

$$F_m(\eta) = \int\limits_0^\infty \xi^m\,f^0(\xi,\eta)\,d\xi\,, \tag{1.9a}$$

$$f^0(\xi,\eta) = \frac{1}{e^{(\xi-\eta)}+1}\,, \tag{1.9b}$$

$$\langle\tau(\varepsilon)\,\varepsilon^n\rangle = \tau_0\,(k_{\mathrm{B}}\,T)^{r+n}\frac{2}{3}\frac{(r+n+\frac{3}{2})\,F_{r+n+\frac{1}{2}}}{F_{\frac{1}{2}}}\,. \tag{1.9c}$$

The final result for an isotropic semiconductor with a simple, parabolic band is

$$\sigma = n\,e\,\mu\,, \tag{1.10a}$$

$$S = \pm\frac{k_{\mathrm{B}}}{e}\left\{\frac{(r+\frac{5}{2})\,F_{r+\frac{3}{2}}}{(r+\frac{3}{2})\,F_{r+\frac{1}{2}}} - \eta\right\}\begin{cases} + & \text{for holes} \\ - & \text{for electrons} \end{cases}, \tag{1.10b}$$

$$\lambda_{\mathrm{el}} = L\,T\,\sigma\,, \tag{1.10c}$$
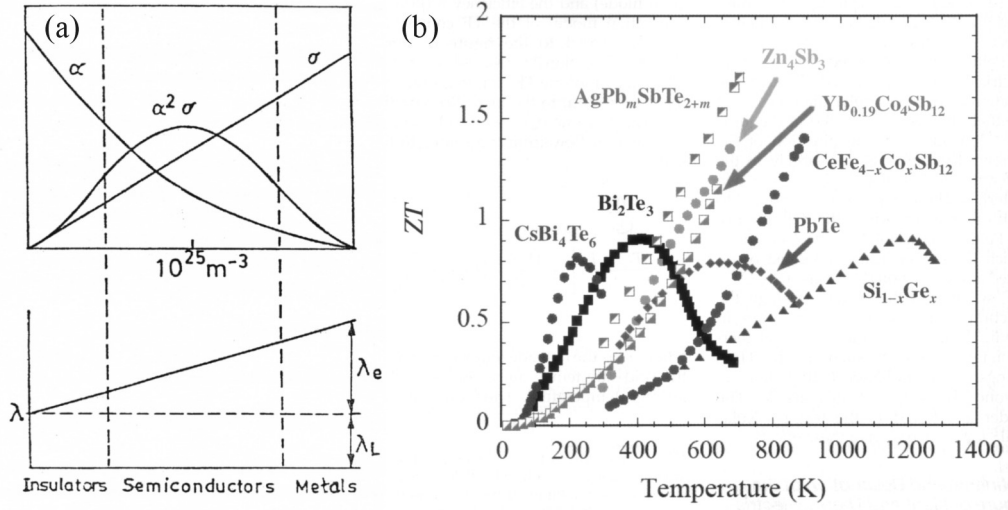
Figure 1.2 (a) Schematic drawing of the thermopower α, the electrical conductivity σ, the power factor $\alpha^2 \sigma$, the lattice thermal conductivity λ_L, and the electronic thermal conductivity λ_e in dependence of the carrier density [14, page 44]. (b) Thermoelectric figure of merit ZT in dependence of the temperature for various bulk thermoelectric materials [1, page 190].

$$n = \frac{1}{2\pi^2} \left(\frac{2m}{\hbar^2} k_B T \right)^{\frac{3}{2}} F_{\frac{1}{2}} \, , \tag{1.10d}$$

$$\mu = \frac{e}{m} \left\langle \tau(\varepsilon) \right\rangle , \tag{1.10e}$$

$$\left\langle \tau(\varepsilon) \right\rangle = \tau_0 \left(k_B T \right)^r \frac{2}{3} \frac{\left(r + \frac{3}{2} \right) F_{r+\frac{1}{2}}}{F_{\frac{1}{2}}} \, , \tag{1.10f}$$

$$L = \left[\frac{\left(r + \frac{7}{2} \right) F_{r+\frac{5}{2}}}{\left(r + \frac{3}{2} \right) F_{r+\frac{1}{2}}} - \left\{ \frac{\left(r + \frac{5}{2} \right) F_{r+\frac{3}{2}}}{\left(r + \frac{3}{2} \right) F_{r+\frac{1}{2}}} \right\}^2 \right] \left(\frac{k_B}{e} \right)^2 \, , \tag{1.10g}$$

$$ZT = \frac{\left(S \frac{e}{k_B} \right)^2 F_{\frac{1}{2}}}{\frac{1}{B} + L \left(\frac{e}{k_B} \right)^2 F_{\frac{1}{2}}} \overset{(r=0)}{=} \frac{\left(\frac{5 F_{\frac{3}{2}}}{3 F_{\frac{1}{2}}} - \eta \right)^2 F_{\frac{1}{2}}}{\frac{1}{B} + \left[\frac{7 F_{\frac{5}{2}}}{3 F_{\frac{1}{2}}} - \left\{ \frac{5 F_{\frac{3}{2}}}{3 F_{\frac{1}{2}}} \right\}^2 \right] F_{\frac{1}{2}}} \, , \tag{1.10h}$$

$$B = \frac{\left(\frac{k_B}{e} \right)^2 T \sigma}{\lambda_{\text{latt}} F_{\frac{1}{2}}} = \frac{1}{2\pi^2} \left(\frac{2m}{\hbar^2} k_B T \right)^{\frac{3}{2}} \left(\frac{k_B}{e} \right)^2 \frac{T e \mu}{\lambda_{\text{latt}}} \, . \tag{1.10i}$$

All quantities depend on the reduced Fermi energy η through the Fermi-Dirac integrals $F_m(\eta)$. Therefore, the Fermi energy has to be altered for increasing the thermoelectric figure of merit ZT. The Fermi energy itself depends on the temperature and the density of donors and acceptors.

On the basis of these equations some general criteria can be derived for high performance thermoelectric materials [4, chap. 3.1-3.3].

High-ZT criterion (v) The principal dependence of the transport coefficients on the carrier density is shown in Figure 1.2(a) for acoustic phonon scattering ($r = -\frac{1}{2}$). The thermopower S decreases with increasing carrier density n, whereas the electrical conductivity σ increases with increasing carrier density n. Therefore, the power factor $S^2 \sigma$ and the thermoelectric figure of merit ZT show a maximum for a carrier density of about

$10^{19}\,\text{cm}^{-3}$. This diagram also shows that only extrinsic semiconductors are suitable for thermoelectric applications with large ZT, whereas for insulators the electrical conductivity σ and for metals the thermopower S would be too small.

High-ZT criterion (vi) Figure 1.2(b) shows the thermoelectric figure of merit ZT in dependence of the temperature for various high-ZT bulk materials. This figure shows, that a ZT value of about 1 usually is the highest observed value. Also, each material is only suitable for a certain temperature range. Particularly, Bi_2Te_3 shows a high ZT at $300\,\text{K}$ and is therefore widely used for Peltier devices at room temperature .

High-ZT criterion (vii) The carrier density n can be altered by doping. The carrier density depends on the impurity density and on the impurity level. The impurity level $E_{\text{D,A}}$ of the donors (D) and acceptors (A) depends on the dielectric constant ϵ_r of the host material according to $E_{\text{D,A}} \propto \epsilon_r^{-2}$. Therefore, doped materials with a high dielectric constant ϵ_r yield a high carrier density.

High-ZT criterion (viii) The material should have a minimum thermopower of about $160\,\mu\text{V/K}$. This value can be derived by assuming a figure of merit $ZT = 1$, a vanishing lattice thermal conductivity $\lambda_{\text{latt}} = 0$, and a Lorenz number $L = L_0$ equal to that of metals.

High-ZT criterion (ix) The figure of merit increases for an increasing dimensionless material parameter B ($\propto m^{\frac{3}{2}}\mu$). Therefore, a high carrier mobility μ and a high effective mass m would be favourable. However, for acoustic phonon scattering the carrier mobility is proportional to $T^{-\frac{3}{2}}m^{-\frac{5}{2}}$, and thereby the material parameter B would be inversely proportional to the effective mass m. Therefore, materials with small effective masses are required.

High-ZT criterion (x) For isotropic crystals the material parameter B is in a large part determined by intrinsic properties and offers no possibility for optimizing ZT. However, for anisotropic crystals there might be differences of the carrier mobility μ and thereby the material parameter B with respect to the current direction. Therefore, the current should flow along the direction of highest mobility.

High-ZT criterion (xi) Material with more complex band structures offer additional possibilities [4, chap. 3.3.2]. For multivalley semiconductors the material parameter B increases linearly with the number of valleys N_{V}. For materials with nonparabolic bands the effective mass m depends on the energy, yielding larger carrier mobilities for narrow-gap semiconductors. However, if the band gap is too small, the thermoelectric figure of merit decreases drastically due to minority carrier effects.

Multi-quantum-well systems

A new approach to an increased thermoelectric figure of merit are multi-quantum-well structures, which were proposed by Hicks and Dresselhaus in 1993 [15]. Particularly, low-dimensional structures based on Bi_2Te_3 superlattices (SLs) are predicted to have an increased thermoelectric figure of merit compared to bulk material [15]. The calculations of Hicks and Dresselhaus for 2D thermoelectricity are based on several assumptions. (i) A simple-band, narrow-gap 2D quantum well with layer thickness a is embedded in a wide-gap semiconductor. (ii) The electrons only occupy the lowest subband of the quantum well. (iii) There is no tunnelling through the wide-gap semiconductor. (iv) The wide-gap semiconductor does not contribute to the conduction.

The calculations of the transport coefficients in a direction parallel to the multilayers are analogous to the calculations for 3D bulk materials. The energy dispersion relation $\varepsilon(\mathbf{k})$ and thereby the density of states $D(\varepsilon)$ are changed due to the reduced dimensions (Eq. 1.8). The transport coefficients still depend on the Fermi-Dirac integrals $F_m(\eta^*)$ (Eq. 1.9). However,

Table 1.1 In-plane thermoelectric properties of n-type and p-type Bi_2Te_3 bulk materials at $300\,K$ [14]: carrier density n, carrier mobility μ, electrical conductivity σ, thermopower S, power factor $S^2\sigma$, thermal conductivity λ, lattice thermal conductivity λ_{latt}, thermoelectric figure of merit $ZT = (S^2\sigma/\lambda)\,T$.

Composition	n $(10^{19}$ $cm^{-3})$	μ $(cm^2/$ $Vs)$	σ $(1/\Omega\,cm)$	S $(\mu V/K)$	$S^2\sigma$ $(\mu W/$ $cm\,K^2)$	λ $(W/m\,K)$	λ_{latt} $(W/m\,K)$	ZT
Bi_2Te_3	2.00	160	513	227	26	1.73	1.53	0.46
$(Bi_{0.25}Sb_{0.75})_2Te_3$	3.34	177	781	225	40	1.37	1.07	0.87
$Bi_2(Te_{0.95}Se_{0.05})_3$	4.00	150	901	-223	45	1.59	1.15	0.85

the reduced Fermi energy has to be redefined and Fermi-Dirac integrals $F_m(\eta^*)$ with different indices m have to be used compared to bulk material.

$$\eta^* = \eta - \frac{1}{k_B\,T}\frac{\hbar^2}{2m}\frac{\pi^2}{a^2}\,, \tag{1.11a}$$

$$ZT \overset{(r=0)}{=} \frac{\left(\frac{2\,F_1}{F_0} - \eta^*\right)^2 F_0}{\frac{1}{B} + \left[\frac{3\,F_2}{F_0} - \left\{\frac{2\,F_1}{F_0}\right\}^2\right] F_0}\,, \tag{1.11b}$$

$$B = \frac{1}{2\pi}\left(\frac{2m}{\hbar^2}\,k_B\,T\right)\left(\frac{k_B}{e}\right)^2 \frac{T\,e\,\mu}{\lambda_{latt}}\frac{1}{a}\,. \tag{1.11c}$$

The most significant difference between 2D quantum wells and 3D bulk materials is a redefinition of the material parameter B (Eq. 1.10), which is additionally inversely proportional to the layer thickness a [15]. Therefore, an additional general criterion can be derived for high performance thermoelectric materials.

High-ZT criterion (xii) Thin 2D quantum wells show an increased material parameter B and thereby an increased thermoelectric figure of merit compared to bulk materials.

1.3   Thermoelectricity in Bi_2Te_3, preliminary results, and aim of this work

1.3.1   General and thermoelectric properties of bulk Bi_2Te_3

An overview of the thermoelectric properties and material parameters of Bi_2Te_3 is given in the textbooks of Goldsmid [4], Rowe [2, 14], and in Reference [16]. Bi_2Te_3 has a rhombohedral crystal symmetry with space group $R\bar{3}m$. The lattice parameters of the pseudo-hexagonal unit cell are $a = 0.438\,nm$ and $c = 3.05\,nm$ [17]. The pseudo-hexagonal unit cell consists of a layered structure with three five-layer-groups with the sequence $Te^1 - Bi - Te^2 - Bi - Te^1$ with weak $Te^1 - Te^1$ bondings [4, 14]. The band-structure can be described by a six-valley model [4] with a band gap of $E_G = 0.16\,eV$ [16]. The impurity levels are close to the conduction band or valence band due to a large dielectric constant of $\epsilon_r = 85$ [16]. The thermoelectric properties of n-type and p-type bulk materials measured parallel to the basal plane (in-plane) are summarised in Table 1.1. The thermoelectric figure of merit is by a factor of 2 higher for a current direction parallel to the basal plane compared to a current direction parallel to the c axis [14, 18]. The reasons are a smaller carrier mobility and a smaller thermal conductivity in a direction parallel to the c axis, possibly due to the weak $Te^1 - Te^1$ bondings.

Bi_2Te_3 is known for its large thermopower ($S \approx 200\,\mu V/K$), large electrical conductivity ($\sigma \approx \pm 1000\,1/\Omega\,cm$), low thermal conductivity ($\lambda \approx 1.5\,W/m\,K$), and high thermoelectric figure of merit ($ZT \approx 1$) at room temperature. At higher temperatures, the thermopower and thereby the figure of merit decreases drastically due to increasing minority carrier effects,

particularly in a narrow-gap semiconductor such as Bi_2Te_3 (Fig. 1.2(b)). Since Bi_2Te_3 is a compound of high mean atomic weight and low melting point $T_M = 858\,K$ [16], the lattice thermal conductivity is also small (Eq. 1.6). The reason for the high thermopower is that pure Bi_2Te_3 is an extrinsic p-type semiconductor with a nearly optimum high acceptor concentration (Table 1.1). Tellurium diffuses out during growth, yielding (i) a nonstoichiometric maximum melting composition and (ii) Bi_{Te}-anti-site defects which act as acceptors [4, 14, 18].

The thermoelectric figure of merit of Bi_2Te_3 was further improved by doping and alloying. Particularly, electron-conducting $Bi_2(Te_{1-x}Se_x)_3$ and hole-conducting $(Bi_{1-x}Sb_x)_2Te_3$ alloys yielded the highest ZT values at room temperature (Table 1.1). The effect of alloying is (i) an increase of the carrier density and thereby electrical conductivity (Eq. 1.10) and (ii) a reduction of the lattice thermal conductivity due to alloy scattering (Table 1.1). A simultaneous reduction of the carrier mobility and thereby electrical conductivity due to impurity scattering is moderate compared to the reduction of lattice thermal conductivity (Table 1.1). In summary, these solid solutions show an increased thermoelectric figure of merit (Table 1.1).

1.3.2 Preliminary results in bulk Bi_2Te_3

It is still an open question, why the lattice thermal conductivity of Bi_2Te_3 bulk is so small. In the literature there are a large number of published measurements of transport properties; however, there are a small number of structural analyses and virtually no data of combined measurements, i.e., transport and structural investigations on the same samples. In some publications, particularly if ambiguous results are presented, assumptions on the possible microstructures are given; e.g., it was concluded from lattice thermal conductivity measurements in bulk Bi_2Te_3 that there should be dislocations which scatter the phonons without proving their existence [19]. There are a few measurements of the transport coefficients in dependence of the grain size [20–22] and one measurement of the transport coefficients in dependence of the dislocation density [23]. A direct proof for the absorption of phonons by dislocations in Bi_2Te_3 was given by ultrasound absorption measurements depending on the dislocation density [23]. Only a few TEM studies on extended defects in bulk Bi_2Te_3 [24–27] but no quantitative chemical analysis by EDX in the TEM were reported in the literature. With respect to its chemical microstructure Bi_2Te_3 was assumed to be a solid solution with homogeneous stoichiometry.

In general, Te compounds tend to be structurally highly complex on the nanometer scale. In $Bi_2Te_3Ge_x$ single crystals structural and/or compositional modulations with a wave length of about $10 - 20\,nm$ were found [27]. Particularly, thermoelectric $AgPb_mSbTe_{2+m}$ bulk materials also showed chemical modulations with a wave length of $20 - 30\,nm$, a low lattice thermal conductivity, and a spectacular thermoelectric figure of merit of of $ZT = 2.2$ at $800\,K$ [28–31]. In the following, these intrinsic structural or chemical modulations on the nanometer scale are referred to as natural nanostructures (nns), whereas the superlattice structure is referred to as artificial nanostructure (ans). The structural disorder introduced by the ans and the nns most likely yields a reduced phonon mean free path and thereby a reduced lattice thermal conductivity, which is beneficial for the thermoelectric figure of merit.

The microstructure of n-type and p-type Bi_2Te_3 bulk materials was analysed. The samples were synthesised by the Bridgman technique and were obtained from commercially available Peltier devices of Peltron GmbH [32]. Quantitative chemical analysis by wavelength dispersive X-ray spectrometry (WDX) in an electron probe microanalyser (EPMA) yielded a fairly large variation in stoichiometry on the micrometer scale [33]. TEM investigations yielded gliding dislocations with a dislocation density of $10^9\,cm^{-2}$ and a structural modulation (nns) with a wavelength of $10\,nm$ [34]. It was suggested that the nns might be caused by chemical inhomogeneities on the nanometer scale [34]. One aim of this work was to find out more about the nature of the nns. Three models were assumed and inspected by TEM on Bi_2Te_3 bulk materials and will be discussed. The wavelength of the nns and the period of the ans are of the same order of magnitude [35, 36]. Since the ans clearly reduced the lattice thermal conductivity, a significant scattering of phonons on the strain field of the nns should occur and will be discussed. A second aim was to study the gliding dislocations in more detail. The high mobility and density of the dislocations should be relevant for phonon scattering and will be discussed.

1.3.3 Preliminary results in Bi$_2$Te$_3$ based thin films and superlattices

Hole-conducting Bi$_2$Te$_3$/Sb$_2$Te$_3$ suerlattices (SLs) epitaxially grown on GaAs substrates by metallorganic chemical vapor deposition (MOCVD) with a period of 6 nm showed a spectacular thermoelectric figure of merit of $ZT = 2.4$ at 300 K [11–13]. An also impressive figure of merit of $ZT = 3$ at 550 K was achieved for PbSeTe/PbTe quantum-dot SLs epitaxially grown by molecular beam epitaxy (MBE) [37]. The predictions of Hicks and Dresselhaus (Chap. 1.2.3) and the increased ZT in SLs were a boost for the synthesis of nanostructured materials for thermoelectric applications [10].

Electron-conducting Bi$_2$(Te$_{1-x}$, Se$_x$)$_3$/Bi$_2$(Te$_{1-y}$, Se$_y$)$_3$ SLs were epitaxially grown by MBE on BaF$_2$ substrates at the Fraunhofer-Institut für Physikalische Messtechnik (IPM) [8] in collaboration with Infineon Technologies AG. They yielded figures of merit close to those in bulk materials [38–40]. Microstructural analyses are required to explain the poor enhancement of ZT in thin films and SLs with respect to bulk. The aim is (1) to image directly the SL and to study their structural quality, (2) to image dislocations by their strain contrast, and (3) to study interactions of the SL with defects, particularly dislocations. The natural nanostructures are also present in our samples. The superposition of the two nanostructures, the ans and the nns, and their influence on the lattice thermal conductivity are of particular interest.

Chapter 2

Dislocations

2.1 Introduction

In this chapter the nature of dislocations, their influence on the transport coefficients, and their analysis by diffraction contrast in the TEM will be discussed. The textbooks of Hirth and Lothe about the theory of the dislocations [41], of Ziman about transport properties of solids [9], and of Williams and Carter about transmission electron microscopy [42] were used as references.

A dislocation is a one dimensional crystal defect, yielding a bending of the lattice planes close to the dislocation core. Therefore, the dislocation is surrounded by a strain field, which will be given in this chapter for an elastically isotropic crystal. Other dislocation related properties such as stress field, strain energy, and forces on dislocations will be discussed also.

The strain field of a dislocation is of crucial role for both, transport coefficients and imaging by diffraction contrast in the TEM. Particularly at low temperatures, scattering of the phonons on the strain field of the dislocation is dominant and determines the lattice thermal conductivity and ultrasound attenuation. For a qualitative understanding, diffraction contrast in the TEM observed on dislocations in elastically isotropic materials will be explained. In chapter 8, the quantitative analysis of dislocations by diffraction contrast in the TEM will be presented. This includes (i) the numerical calculation of the strain field of the dislocations under consideration of the anisotropic elastic properties and (ii) the simulation of two-beam images.

2.2 Strain field, stress field, and line energy of dislocations

2.2.1 Elementary properties of dislocations treated in the continuum theory

A model of an edge dislocation is shown in Figure 2.1(a) [41, chap. 1.3]. According to this model the crystal was cut above the core of the dislocation into two pieces and an extra half-plane of atoms was inserted. The unit vector parallel to the dislocation core is referred to as line direction $\mathbf{t}$. Close to the dislocation core the atoms are displaced from their lattice positions, i.e., the lattice planes are bent (Fig. 2.1(a)). In general, the dislocation core represents a boundary of a slipped region. The Burgers vector $\mathbf{b}$ is a lattice vector and describes the strength of the displacements in the slipped region, or in other words, the deviation of the disturbed crystal structure from an ideal crystal structure. For an edge dislocation the Burgers vector is perpendicular to the line direction ($\mathbf{b} \perp \mathbf{t}$), for a screw dislocation these quantities would be parallel ($\mathbf{b} \parallel \mathbf{t}$). For a mixed dislocation the Burgers vector can be resolved in an edge component $\mathbf{b}_\mathrm{e}$ and a screw component $\mathbf{b}_\mathrm{s}$, which are given by

$$\mathbf{b} = \mathbf{b}_\mathrm{s} + \mathbf{b}_\mathrm{e}\,, \tag{2.1a}$$

$$\mathbf{b}_\mathrm{s} = (\mathbf{b} \cdot \mathbf{t})\,\mathbf{t}\,, \tag{2.1b}$$

$$\mathbf{b}_\mathrm{e} = \mathbf{t} \times (\mathbf{b} \times \mathbf{t})\,. \tag{2.1c}$$

The strain field and stress field of a dislocation beyond its core can be calculated by linear, anisotropic elasticity theory (continuum theory) [41, chap. 2.2]. In the following the absence of internal torques, net torques, and of body forces are assumed. According to Hooke's law the stresses σ_{ij} depend linearly on the strains ϵ_{kl}, which are related to the derivatives of the displacement field $\mathbf{u}(\mathbf{x})$.

$$\sigma_{ij} = c_{ijkl}\,\epsilon_{kl} = c_{ijkl}\,\frac{\partial u_k}{\partial x_l} \quad \text{(Hooke's law)}\,, \tag{2.2a}$$

$$\epsilon_{kl} = \frac{1}{2}\left(\frac{\partial u_k}{\partial x_l} + \frac{\partial u_l}{\partial x_k}\right)\,. \tag{2.2b}$$

Only 21 components of the 81 components of the tensor of the elastic constants c_{ijkl} are independent due to the symmetry of the stress tensor and the strain tensor, and due to the conservation of energy. Therefore, the elastic constants can be considered as components of a symmetric 6×6 matrix c_{mn}. The pairs of indices (i, j) and (k, l) were replaced by single indices m and n, according to the transformation scheme $(1, 1) \rightarrow 1$, $(2, 2) \rightarrow 2$, $(3, 3) \rightarrow 3$, $(2, 3)$ or $(3, 2) \rightarrow 4$, $(3, 1)$ or $(1, 3) \rightarrow 5$, and $(1, 2)$ or $(2, 1) \rightarrow 6$. This transformation scheme can be expressed mathematically compact by using the Kronecker's delta function δ_{ij}.

$$\sigma_{ij} = \sigma_{ji}\,, \tag{2.3a}$$

$$\epsilon_{ij} = \epsilon_{ji}\,, \tag{2.3b}$$

$$c_{ijkl} = c_{jikl} = c_{ijlk} = c_{klij}\,, \tag{2.3c}$$

$$c_{mn} = c_{nm}\,, \tag{2.3d}$$

$$m = 0.5\,(i + j)\,\delta_{ij} + [9 - (i + j)](1 - \delta_{ij})\,, \tag{2.3e}$$

$$n = 0.5\,(k + l)\,\delta_{kl} + [9 - (k + l)](1 - \delta_{kl})\,. \tag{2.3f}$$

The crystal symmetries further reduce the number of independent elastic components. For isotropic and cubic crystals the matrices c_{mn} have the same structure. However, for cubic crystals the elastic constants c_{11}, c_{12}, and c_{44} are all independent constants, whereas for elastically isotropic crystals c_{44} additionally equals to $\frac{1}{2}(c_{11} - c_{12})$.

$$c_{mn} = \begin{pmatrix} c_{11} & c_{12} & c_{12} & 0 & 0 & 0 \\ c_{12} & c_{11} & c_{12} & 0 & 0 & 0 \\ c_{12} & c_{12} & c_{11} & 0 & 0 & 0 \\ 0 & 0 & 0 & c_{44} & 0 & 0 \\ 0 & 0 & 0 & 0 & c_{44} & 0 \\ 0 & 0 & 0 & 0 & 0 & c_{44} \end{pmatrix}\,. \tag{2.4}$$

Some further important quantities are the shear modulus μ, the Poisson's ratio ν, and the anisotropy ratio A [41, chap. 2.4]. Particularly, the anisotropy ratio A equals to 1 for isotropic crystals and might differ from 1 for anisotropic crystals.

$$\mu = c_{44}\,, \tag{2.5a}$$

$$\nu = \frac{c_{12}}{c_{12} + c_{12}}\,, \tag{2.5b}$$

$$A = \frac{2c_{44}}{c_{12} - c_{12}}\,. \tag{2.5c}$$

2.2.2   Plain strain solutions for isotropic crystals

The stress field, and thereby the displacement field and the strain field, is determined by an equilibrium condition [41, chap. 2.2]. The differential equations for the stress fields have to be solved under consideration of the Burgers circuit as boundary condition [41, chap. 1.3]. The Burgers vector **b** is given by a line integral, taken in a right-handed sense relative to the line direction **t**, of the displacement field **u** around the dislocation (Fig. 2.1(b)).

$$\frac{\partial}{\partial x_i}\sigma_{ij} = c_{ijkl}\frac{\partial^2 u_k}{\partial x_i \partial x_l} = 0\,, \tag{2.6a}$$

$$\mathbf{b} = \oint_C \frac{\partial \mathbf{u}}{\partial l}\,dl\,. \tag{2.6b}$$

This definition of the Burgers circuit corresponds to the **SF**/RH convention: A closed Burgers circuit is first carried out in a right-handed sense (RH) in a perfect crystal. The same Burgers circuit is then carried out in the disturbed crystal. The Burgers vector **b** is defined as the vector **SF** from start S to finish F, which is required to close the latter circuit.

In the following paragraphs, the solutions for the displacement field **u** and the strain field $\frac{\partial \mathbf{u}}{\partial x_l}$ of a dislocation in an elastically isotropic crystal will be presented, using more advanced theories instead of the solutions usually presented in textbooks and lectures. For anisotropic crystals the displacement field of a dislocation was calculated by Eshelby [43], Stroh [44, 45], and by Barnett and Lothe [46]. Plane strain solutions are required for a dislocation; i.e., the displacement field, the strain field, and the stress field, should not vary in line direction [41, chap. 2.5]. For this, Stroh [45] introduced arbitrary orthonormal plane basis vectors **m** and **n** defined by

$$\mathbf{t} = \mathbf{m} \times \mathbf{n}\,. \tag{2.7}$$

Eshelby showed that the "Ansatz" for the displacement field has to be of the form

$$\mathbf{u} = \mathbf{A}\,f(\mathbf{m}\cdot\mathbf{x} + p\,\mathbf{n}\cdot\mathbf{x})\,. \tag{2.8}$$

The coefficient p and the vector **A** are determined by Equations 2.6. The numerical calculation of the quantities p and **A** for anisotropic crystals was solved by Stroh [44] and by Barnett and Lothe [46] and will be the main topic in Chapter 8.1. As mentioned above, the displacement field should not vary in line direction, i.e., the displacement field should be invariant for translations $a\,\mathbf{t}$ parallel to the line direction **t**, where a is an arbitrary factor. Since $\mathbf{m}\cdot\mathbf{t} = 0$ and $\mathbf{n}\cdot\mathbf{t} = 0$ holds, it can be easily shown that the plain strain property is valid, i.e.,

$$\mathbf{u}(\mathbf{x}) = \mathbf{u}(\mathbf{x} + a\,\mathbf{t})\,. \tag{2.9}$$

At this point Barnett and Lothe [46] expressed the solutions in terms of cylinder coordinates r and θ (Fig. 2.1(c)), which were defined as follows: (i) The radius r is the shortest distance of the point **x** from the dislocation core (Fig. 2.1(c)). (ii) The plane basis vectors **m** and **n** were chosen to fulfill the conditions $\mathbf{m}\cdot\mathbf{x} = r$ and $\mathbf{n}\cdot\mathbf{x} = 0$. (iii) The azimuth angle θ was defined by the rotation of arbitrary fixed orthonormal plane basis vectors $\mathbf{m}_0$ and $\mathbf{n}_0$ in a right-handed sense around the dislocation core into the plane basis vectors **m** and **n** (Fig. 2.1(c)).

$$r = \sqrt{(\mathbf{m}_0\cdot\mathbf{x})^2 + (\mathbf{n}_0\cdot\mathbf{x})^2}\,, \tag{2.10a}$$

$$\tan(\theta) = \frac{\mathbf{n}_0\cdot\mathbf{x}}{\mathbf{m}_0\cdot\mathbf{x}}\,, \tag{2.10b}$$

$$\mathbf{m} = \cos(\theta)\,\mathbf{m}_0 + \sin(\theta)\,\mathbf{n}_0\,, \tag{2.10c}$$

$$\mathbf{n} = -\sin(\theta)\,\mathbf{m}_0 + \cos(\theta)\,\mathbf{n}_0\,. \tag{2.10d}$$

For edge dislocations or mixed dislocations, the convenient choice for the fixed plane basis vectors is given by

$$\mathbf{m}_0 = \frac{\mathbf{b}_e}{|\mathbf{b}_e|}\,, \tag{2.11a}$$
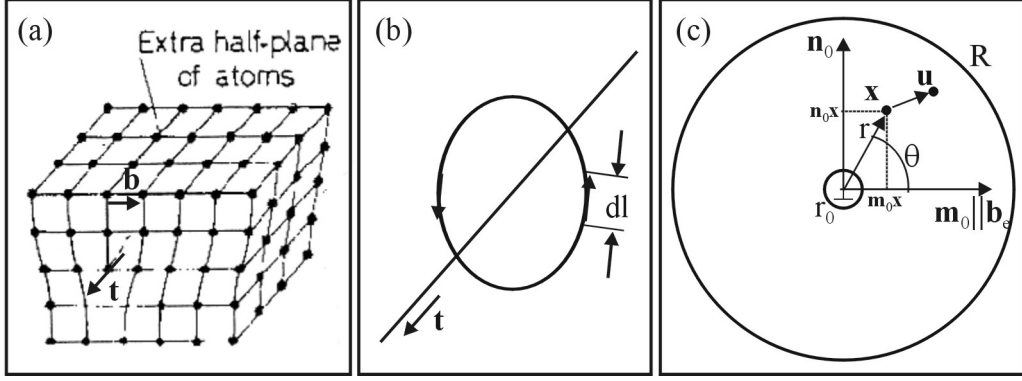
Figure 2.1 (a) Model of an edge dislocation with Burgers vector **b** and line direction **t**. (b) Definition of the Burgers vector by a Burgers circuit according to the **SF**/RH convention. (c) Schematic drawing of an edge dislocation. The line direction points out of the paper sheet. The characteristic quantities for the calculation of the strain field $\frac{\partial \mathbf{u}}{\partial x_l}$ and the line energy E_{L} are the displacement vector **u**, the cylinder coordinates r and θ, the plane basis vectors $\mathbf{m}_0$ and $\mathbf{n}_0$, the core radius r_0, and R being half the distance between two dislocations.

$$\mathbf{n}_0 = \mathbf{t} \times \mathbf{m}_0 , \tag{2.11b}$$

where $\mathbf{b}_e$ is the edge component of the Burgers vector **b** (Eq. 2.1).

The displacement field **u** of a dislocation in an elastically isotropic crystal is well known (Ref. [47, page 31] and Ref. [41, pages 60 and 78]),

$$\mathbf{u}(r,\theta) = \frac{1}{2\pi} \left[\mathbf{b}\,\theta + \mathbf{b}_e \frac{\sin(2\theta)}{4\,(1-\nu)} - (\mathbf{t} \times \mathbf{b}) \left\{ \frac{1-2\nu}{4\,(1-\nu)} \ln\left(r^2\right) + \frac{\cos(2\theta)}{4\,(1-\nu)} \right\} \right] . \tag{2.12}$$

However, the strain field $\frac{\partial \mathbf{u}}{\partial x_l}$ expressed in terms of the cylinder coordinates r and θ is commonly not reported in textbooks.

$$\frac{\partial \mathbf{u}}{\partial x_l}(r,\theta) = \frac{1}{2\pi}\frac{1}{r}\left(m_l\,\mathbf{s}_{\mathrm{m}} + n_l\,\mathbf{s}_{\mathrm{n}}\right) , \tag{2.13a}$$

$$\mathbf{s}_{\mathrm{m}} = -(\mathbf{t} \times \mathbf{b})\frac{1-2\nu}{2\,(1-\nu)} , \tag{2.13b}$$

$$\mathbf{s}_{\mathrm{n}} = \mathbf{b} + \mathbf{b}_e\frac{\cos(2\theta)}{2\,(1-\nu)} + (\mathbf{t} \times \mathbf{b})\frac{\sin(2\theta)}{2\,(1-\nu)} . \tag{2.13c}$$

This notation corresponds to the solutions of Barnett and Lothe [46]. The solution for the strain field of a dislocation in an anisotropic crystal only differ with respect to the vectors $\mathbf{s}_{\mathrm{m}}$ and $\mathbf{s}_{\mathrm{n}}$, which have to be calculated numerically [46].

In summary, the displacement field, the strain field, and the stress field of a dislocation show following fundamental properties:

Dislocation property (i) The displacement field, the strain field, and the stress field show plain strain properties and are proportional to the Burgers vector.

Dislocation property (ii) The displacement field, the strain field, and the stress field can be expressed in terms of cylinder coordinates r and θ.

Dislocation property (iii) The strain field and the stress field are inversely proportional to the radius r.

Dislocation property (iv) The strain field and the stress field can be resolved in a factor only depending on the radius r and a factor only depending on the azimuth angle θ.

For a qualitative understanding of diffraction contrast in the TEM screw dislocations shall only be considered. Simple, well known expressions are obtained [41, page 60]. For the calculations it was further assumed that the line direction is parallel to the z axis, i.e., $\mathbf{b} = [0, 0, b]$, $\mathbf{m}_0 = [1, 0, 0]$, and $\mathbf{n}_0 = [0, 1, 0]$.

$$\mathbf{u}(r, \theta) = \mathbf{b}\, \frac{\theta}{2\pi}\,, \tag{2.14a}$$

$$\frac{\partial \mathbf{u}}{\partial x_l}(r, \theta) = \mathbf{b}\, \frac{1}{2\pi} \frac{n_l}{r}\,, \tag{2.14b}$$

$$\sigma_{23} = \frac{\mu\, b}{2\pi} \frac{\cos(\theta)}{r}\,, \tag{2.14c}$$

$$\sigma_{31} = -\frac{\mu\, b}{2\pi} \frac{\sin(\theta)}{r}\,, \tag{2.14d}$$

$$\sigma_{12} = \sigma_{11} = \sigma_{22} = \sigma_{33} = 0\,. \tag{2.14e}$$

2.2.3 Line energy

A unit volume element is deformed by a differential strain $d\epsilon_{ij}$ [41, chap. 2.2], i.e., stresses σ_{ij} do a differential work on the cube faces by an amount

$$dw = \sigma_{ij}\, d\epsilon_{ij} = c_{ijkl}\, \epsilon_{kl}\, d\epsilon_{ij}\,. \tag{2.15}$$

The line energy $E_{\mathrm{L}} = W/L$ of an infinite dislocation is defined by the strain energy stored per unit length, in a region bounded by cylinders of radius r_0 and R, where r_0 is core radius and R is half the distance between the dislocations [41, page 63] (Fig. 2.1(c)). The line energy of a dislocation in an isotropic crystal is given by

$$E_{\mathrm{L}} = \frac{\mu\, b^2}{4\pi} \left(\cos^2 \beta + \frac{\sin^2 \beta}{1 - \nu} \right) \ln \left(\frac{R}{r_0} \right)\,, \tag{2.16}$$

where μ is the shear modulus (Eq. 2.5), ν is the Poisson's ratio (Eq. 2.5), and β is the angle between the line direction $\mathbf{t}$ and the Burgers vector $\mathbf{b}$ [41, page 91].

Dislocation property (v) The line energy increases with $|\mathbf{b}|^2$. Therefore, dislocations with Burgers vectors b which correspond to shortest lattice vectors are energetically favourable.

Dislocation property (vi) The line energy depends on the line direction $\mathbf{t}$ and on the material constants.

In face centred cubic structures and hexagonal structures Burgers vectors of the type $\mathbf{b} = \frac{1}{2}\langle 1, 1, 0 \rangle$ and $\mathbf{b} = \langle 1, 0, 0 \rangle$ would be energetically favourable, respectively. However, the line energy also depends on the line direction. Since the Poisson's ratio ν (Eq. 2.5) is usually smaller than one, the line energy of screw dislocations ($\beta = 0°$) is smaller than the line energy of edge dislocations ($\beta = 90°$) or mixed dislocations ($\beta < 90°$) for both, face centred cubic and hexagonal structures. However, for trigonal crystals such as Bi$_2$Te$_3$ the line energy of screw dislocations in the basal plane might not be the smallest one and will be discussed in Chapter 8.3.4.

2.3 Gliding dislocations and forces on dislocations

2.3.1 Gliding dislocations

In Bi$_2$Te$_3$ gliding dislocations can be easily observed in the TEM and were analysed in detail with respect to the glide plane, velocity, forces due to residual stresses in the sample, and interactions between dislocations.

The glide plane normal $\mathbf{G}$ of a dislocation is given by $\mathbf{b} \times \mathbf{t}$ (Fig. 2.2(a)). For a screw dislocation the glide plane normal would be indetermined. Any plane for which $\mathbf{b}$ is a zone axis is a possible glide plane for screw dislocations [41, page 26]. The temperature T has to be increased and/or an external shear stress σ has to be applied to start and maintain gliding. Therefore, gliding is a thermally activated process. An activation energy $U(\sigma)$ has to be overcome and yields a dislocation velocity law $v = v_0 \exp\{-U(\sigma)/k_\mathrm{B}\,T\}$ [48, page 261]. The dislocation velocity depends strongly on the applied shear stress, which was nicely demonstrated for LiF crystals [49] (Fig. 2.2(b)).

2.3.2   Images forces close to free surfaces

The elastic forces $F_\mathrm{L} = F/L$ per unit length on dislocations are virtual forces representing the change of free energy of the system with displacement of the dislocation [41, page 65]. This forces could be due to (i) the attractive image forces close to free surfaces, (ii) applied shear stresses, and (iii) the interaction between two dislocations. The following expressions for the elastic forces were derived for infinite dislocations in isotropic crystals.

For the calculation of image forces on screw dislocation and edge dislocations the dislocations are assumed to be in a distance R from the surface, the line direction being parallel to the surface, and the slip plane being normal to the free surface (Fig. 2.2(c)) [41, pages 69 and 88]. The maximum radius of the strain field, and thereby the line energy, is limited by R. The line energy decreases for decreasing distance R (Eq. 2.16). This corresponds to an attractive force acting on the dislocation towards the free surface. The force per unit length is given by

$$F_\mathrm{L} = \frac{\mu\,b^2}{4\pi\,R} \quad \text{(screw dislocation)}\,, \tag{2.17a}$$

$$F_\mathrm{L} = \frac{\mu\,b^2}{4\pi\,(1-\nu)\,R} \quad \text{(edge dislocation)}\,. \tag{2.17b}$$

2.3.3   Forces due to applied shear stresses

A shear stress σ_{yz} shall be externally applied to a sample with a screw or an edge dislocation being parallel to the z axis (Fig. 2.2(d)) [41, pages 68 and 81]. The external shear stress works on the dislocation, yielding a force parallel to the x direction. Particularly, the direction of the force and thereby the direction of motion depends on the sign of the Burgers vector $\mathbf{b}$.

$$(\mathbf{F}_\mathrm{L})_x = \sigma_{yz}\,b\,. \tag{2.18}$$

The effect of the external stress σ could also be, that the dislocations is bowed out if the dislocation is pinned at its ends, e.g., pinned at the surface or at point defects (Fig. 2.2(a)). The bending radius r of the dislocation is determined by the equilibrium of stretching due to the external stress σ and shortening for minimizing the line energy E_L of the dislocation [48, pp. 249-250].

$$r = \frac{E_\mathrm{L}}{\sigma\,b}\,. \tag{2.19}$$

2.3.4   Forces between two parallel straight dislocations

Forces between two parallel dislocations $(\mathbf{b}_1, \mathbf{t})$ and $(\mathbf{b}_2, \mathbf{t})$ are of interest. Attractive and repulsive forces between the dislocations can be best explained for the simplest cases (a) $\mathbf{b}_1 = \mathbf{b}_2$ and (b) $\mathbf{b}_1 = -\mathbf{b}_2$, i.e., the Burgers vectors of the dislocations only differ in their signs. In general, there is a superposition of the strain fields of both dislocations. At large distances, there is effectively no overlap of both strain fields. Therefore, the total line energy would be given by $E_\mathrm{L} = E_\mathrm{L1} + E_\mathrm{L2} = 2\,E_\mathrm{L1}$, where E_L1 and $E_\mathrm{L2} = E_\mathrm{L1}$ are the line energies of both single dislocations (Eq. 2.16). At short distances, there is a strong overlap of the strain fields of both dislocations. Therefore, the dislocation system can be regarded as one single dislocation with a total Burgers vector $\mathbf{b} = \mathbf{b}_1 + \mathbf{b}_2$, yielding (a) $\mathbf{b} = 2\,\mathbf{b}_1$ and (b) $\mathbf{b} = 0$, respectively. The total
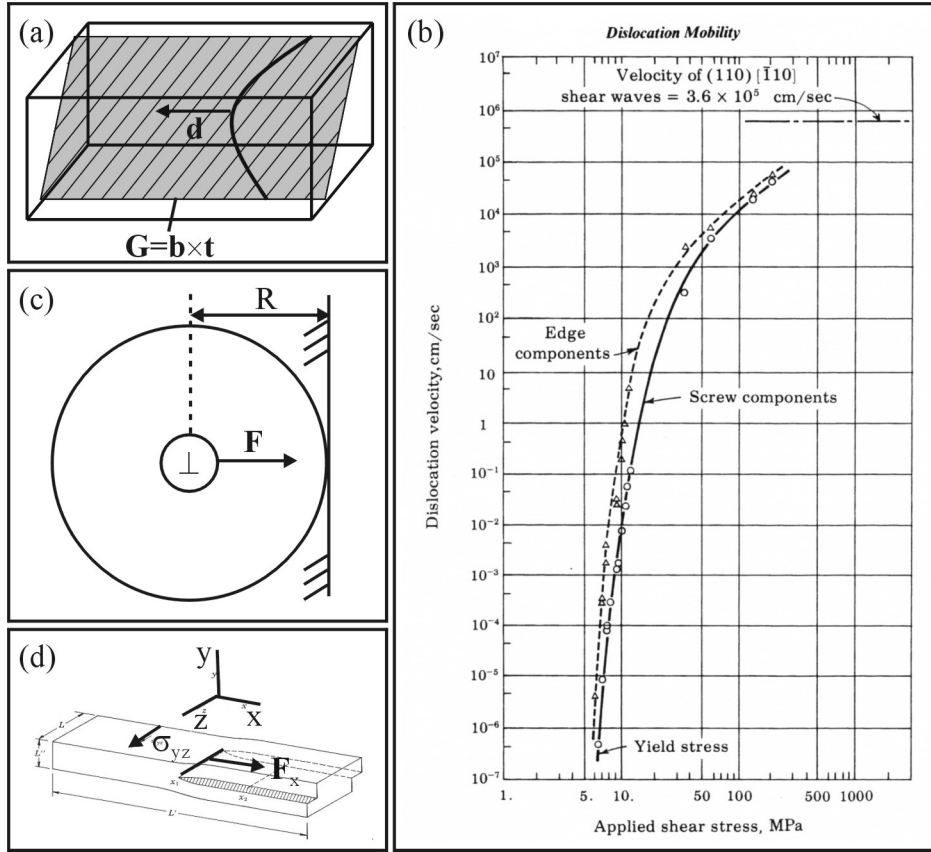
Figure 2.2 (a) Model of a gliding dislocation, where **G** is the glide plane and **d** is the direction of motion. (b) Dislocation velocity versus applied shear stress for LiF crystals [49]. (c) Attractive image forces on dislocations close to a free surface. (d) Gliding of a dislocation induced by an externally applied shear stress.

line energy would be given by (a) $E_L = 4\,E_{L1}$ and (b) $E_L = 0$, respectively. In summary, the total line energy (a) increases at short distances for Burgers vectors having the same signs and (b) decreases at short distances for Burgers vectors having opposite signs. This corresponds to repulsive and attractive forces between the dislocations, respectively.

The calculation of the force per unit length between two parallel dislocations is shown in more detail in the textbook of Hirth and Lothe [41, chap. 5.2]. Cylinder coordinates were introduced with the first dislocation as the origin and the second dislocation at (R, θ), where R is the distance between the dislocations. The force per unit length can be resolved in a radial component F_R/L and an angle depended component F_θ/L, which are given by

$$F_R/L = \frac{\mu}{2\pi\,R}(\mathbf{b}_1 \cdot \mathbf{t})(\mathbf{b}_2 \cdot \mathbf{t}) + \frac{\mu}{2\pi\,(1-\nu)\,R}\left[(\mathbf{b}_1 \times \mathbf{t}) \cdot (\mathbf{b}_2 \times \mathbf{t})\right], \qquad (2.20a)$$

$$F_\theta/L = \frac{\mu}{2\pi\,(1-\nu)\,R^3}\left[(\mathbf{b}_1 \cdot \mathbf{R})\left\{(\mathbf{b}_2 \times \mathbf{R}) \cdot \mathbf{t}\right\} + (\mathbf{b}_2 \cdot \mathbf{R})\left\{(\mathbf{b}_1 \times \mathbf{R}) \cdot \mathbf{t}\right\}\right], \qquad (2.20b)$$

where **R** is the distance vector between the dislocations.

2.4   Lattice thermal conductivity and ultrasound attenuation

2.4.1   Lattice thermal conductivity

The lattice thermal conductivity depends on the phonon mean free path l_{ph} according to transport theory for isotropic solids (Chap. 1.2.2). At low temperatures, in a real crystal the phonon mean free path would be limited by phonon scattering on extended crystals defects. Particularly, phonons can be scattered on the strain field of dislocations, which was concluded from measurements on samples with different amount of cold work [9, page 325]. An overview of the calculation of the phonon mean free path is given in the textbook of Ziman [9, chap. 6.4, 8.5, and 8.9]. For dislocations in isotropic crystals, the average phonon mean free path at low temperatures [9, page 325] is given by

$$l_{\text{ph}} = 0.455 \, (\gamma^2 \, b^2 \, k_{\text{D}})^{-1} \frac{1}{N_{\text{D}}} \frac{\theta_{\text{D}}}{T} \,. \tag{2.21}$$

The phonon mean free path is inversely proportional to the dislocation density N_{D}, i.e., the phonon mean free path decreases with increasing dislocation density N_{D}. The other quantities are the Debye temperature θ_{D}, the Grüneisen constant γ, the Burgers vector $\mathbf{b}$, the Debye radius $k_{\text{D}} = \left(6\pi^2 \frac{N}{V}\right)^{\frac{1}{3}}$, and the number of unit cells per volume $\frac{N}{V}$. Finally, under consideration of Equations 1.4, 1.7, and 2.21 the lattice thermal conductivity at low temperatures is given by

$$\lambda_{\text{latt}} = 0.599 \, k_{\text{B}} \, z \, \left(\frac{k_{\text{D}}}{\gamma \, b}\right)^2 v \, \frac{1}{N_{\text{D}}} \left(\frac{T}{\theta_{\text{D}}}\right)^2 \,. \tag{2.22}$$

2.4.2   Ultrasound attenuation

Phonons are scattered on the static strain field of the dislocations. However, dislocations are also able to glide under applied shear stresses. Particularly, this motion can be induced by the stress field correlated to phonons or ultrasonic waves. Besides a uniform motion, dislocations can be bowed out and oscillate if they are pinned by impurities or at the surface. Elastic waves will be generated by gliding or oscillating dislocations, and therefore an incident ultrasonic wave will be inelastically scattered, i.e., elastic waves will be attenuated.

The attenuation of ultrasound by dislocations was described by Granato and Lücke [50–52]. Their theory of dislocation resonance assumed a dislocation with Burgers vector $\mathbf{b}$, being fixed between pinning centres at a distance L, and exposed to a periodic external stress $\sigma(\omega) = \sigma_0 \, e^{i\omega t}$ with angular frequency ω (Fig. 2.3(a)). The dislocations were considered as damped vibrating strings and the equation of motion for the dislocation displacement $y(x,t)$ is given by

$$A \, \frac{\partial^2 y}{\partial t^2} + B \, \frac{\partial y}{\partial t} - C \, \frac{\partial^2 y}{\partial x^2} = b \, \sigma(\omega) \,. \tag{2.23}$$

The effective dislocation mass per unit length A is determined by a rod at the dislocation core with radius b and mass density ρ. The damping force per unit length B arises from drag due to interaction with phonons, electrons, and due to re-radiation of elastic waves [51]. The damping force depends on the number of atoms per unit cell z, the shear wave velocity v_t, the lattice constant a, the temperature T, and the Boltzmann's constant k_{B} [53]. Finally, the dislocation line energy C in a bowed-out dislocation depends on the shear modulus μ and the Poisson's ratio ν (Eq. 2.5).

$$A = \pi \, \rho \, b^2 \,, \tag{2.24a}$$

$$B = \left(\frac{3 \, k_B \, z}{10 \, v_t \, a^2}\right) T \,, \tag{2.24b}$$

$$C = \frac{2 \, \mu \, b^2}{\pi(1 - \nu)} \,. \tag{2.24c}$$
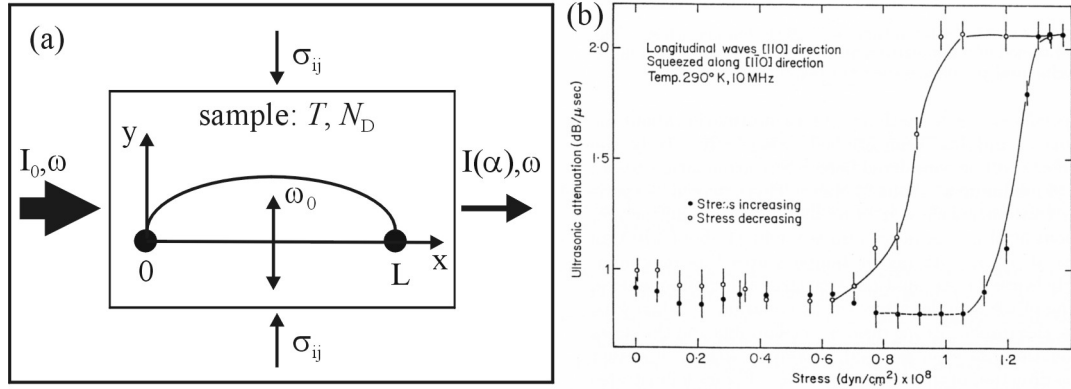
Figure 2.3 (a) Model of an oscillating dislocation with resonance frequency ω_0 and principle of ultrasound attenuation. The attenuation $\alpha(\omega)$ is measured in dependence of the ultrasound frequency ω. The dislocation configuration (density N_D, length L) can be changed by application of a stress σ_{ij}. (b) Stress dependence of ultrasound attenuation measured on HgTe [54].

Ultrasound attenuation experiments measure the attenuation $\alpha(\omega)$ and velocity of sound $v(\omega)$ of the incident ultrasound in dependence of its frequency ω (Fig. 2.3(a)). A related quantity is the decrement $\triangle(\omega) = 2\pi\alpha(\omega)\frac{v(\omega)}{\omega}$ which is given by

$$\Delta(\omega) = \Omega\,\Delta_0\,N_\mathrm{D}\,L^2\,f\left(\frac{\omega}{\omega_0}, D\right)\,, \tag{2.25a}$$

$$f\left(\frac{\omega}{\omega_0}, D\right) = \frac{\frac{\omega}{\omega_0}\big/D}{\left[1 - \left(\frac{\omega}{\omega_0}\right)^2\right]^2 + \left(\frac{\omega}{\omega_0}\big/D\right)^2}\,. \tag{2.25b}$$

The decrement Δ depends on (a) the dislocation density N_D, (b) the length L of the dislocation or of its oscillating segments, and (c) the frequency response $f(\frac{\omega}{\omega_0}, D)$, determined by the normalised damping constant D and the ratio of the frequency ω to the resonance frequency ω_0 of the dislocation. Ω is an orientation factor and Δ_0 is a constant.

$$\omega_0 = \frac{\pi}{L}\sqrt{\frac{C}{A}}\,, \tag{2.26a}$$

$$D = \omega_0\,\frac{A}{B}\,, \tag{2.26b}$$

$$\Delta_0 = \frac{8\,\mu\,b^2}{\pi^3\,C}\,. \tag{2.26c}$$

The effects of dislocations on ultrasound attenuation were nicely demonstrated on HgTe [54]. The attenuation was first measured on an annealed sample in a frequency range between $10\,\mathrm{MHz}$ and $300\,\mathrm{MHz}$ at a temperature of $4.2\,\mathrm{K}$. The attenuation showed a maximum at $240\,\mathrm{MHz}$ and its dependence on the frequency corresponded to the frequency response factor $f\left(\frac{\omega}{\omega_0}, D\right)$. In a second experiment, the sample was compressed at right angles to the direction of sound (Fig. 2.3(b)) in a stress range of $0 - 1.4\,\mathrm{MPa}$, the temperature was $290\,\mathrm{K}$, and the ultrasound frequency was $10\,\mathrm{MHz}$. The attenuation showed a hysteresis in dependence of the applied stress (Fig. 2.3(b)). The crystals were plastically deformed, i.e., the configuration of the dislocations were changed. This confirmed the dependence of the attenuation on the dislocation density N_D and their lengths L, since an external stress field changes the microstructure.

2.5 Diffraction contrast and image simulation

2.5.1 Diffraction contrast

Two-beam conditions are used for imaging of dislocations and other extended crystal defects by diffraction contrast in a TEM [42, chap. 13], i.e., the direct beam is diffracted by one lattice plane only with reciprocal lattice vector $\mathbf{g}$. The complex amplitudes of the direct beam T and the diffracted beam S can be calculated according to the two-beam dynamical diffraction theory of Howie and Whelan [55, 56]. This theory is based on the column approximation, i.e., there is no interaction of the electrons in neighboured columns [42, chap. 13]. In each column, the amplitudes of the direct beam and the diffracted beam change simultaneously with specimen thickness z since they are coupled according to a linear first-order differential equation [47, chap. 2.3],

$$\begin{pmatrix} \frac{dT}{dz} \\ \frac{dS}{dz} \end{pmatrix} = \frac{\pi}{\xi_{\mathbf{g}}} \begin{pmatrix} -N & [i-A] \\ [i-A] & [-N+2\,i\,w'] \end{pmatrix} \begin{pmatrix} T \\ S \end{pmatrix}. \tag{2.27}$$

The intensities of the direct beam and diffracted beam are given by

$$I_{\mathrm{T}}(z) = T(z)\,\overline{T(z)}\,, \tag{2.28a}$$

$$I_{\mathrm{S}}(z) = S(z)\,\overline{S(z)}\,. \tag{2.28b}$$

Absorptions effects are considered by the absorption coefficients N (normal) and A (anomalous). Diffraction effects are considered by the parameter $w'(z)$ which is related to (i) the extinction distance $\xi_{\mathbf{g}}$ corresponding to the Bragg reflection $\mathbf{g}$, (ii) the excitation error s or the dimensionless excitation error w, representing the deviation of the crystal orientation from the exact Bragg position, (iii) the strain field $\frac{\partial \mathbf{u}}{\partial x_l}$ of the extended crystal defect, and (iv) the displacement function $\beta(z)$, representing the bending of the diffracting lattice plane $\mathbf{g}$ in direction of the plane normal.

$$w' = w + \xi_{\mathbf{g}}\,\beta(z)\,, \tag{2.29a}$$

$$w = \xi_{\mathbf{g}}\,s\,, \tag{2.29b}$$

$$\beta(z) = \frac{\partial}{\partial z}(\mathbf{g} \cdot \mathbf{u}) = \mathbf{g} \cdot \frac{\partial \mathbf{u}}{\partial z}\,. \tag{2.29c}$$

For an ideal crystal ($\beta = 0$) without absorption effects ($A = N = 0$) well known solutions are obtained for the intensities [42, chap. 13],

$$I_{\mathrm{S}}(z) = \left(\frac{\pi z}{\xi_{\mathbf{g}}}\right)^2 \frac{\sin^2(\pi z\,s_{\mathrm{eff}})}{(\pi z\,s_{\mathrm{eff}})^2} = 1 - I_{\mathrm{T}}(z)\,, \tag{2.30a}$$

$$s_{\mathrm{eff}} = \sqrt{s^2 + \xi_{\mathbf{g}}^{-2}}\,, \tag{2.30b}$$

where s_{eff} is the effective excitation error. The wavelength is determined by the extinction distance $\xi_{\mathbf{g}}$. These solutions are also referred to as "Pendellösung" fringes or thickness fringes observed in wedge-shaped TEM samples [42, chap. 23].

For real crystals, diffraction contrast is determined by the strain field of the extended crystal defect, i.e., the displacement function $\beta(z)$ yields local changes of the excitation error s (Eq. 2.29) and thereby local changes of the amplitudes of the direct beam and the diffracted beam (Eq. 2.27). For a screw dislocation in an isotropic crystal the displacement field is given by $\mathbf{b}\,\frac{\theta}{2\pi}$ (Eq. 2.14). Therefore, for two-beam conditions with $\mathbf{g} \cdot \mathbf{b} = 0$ and thereby $\beta(z) = 0$ and assuming an elastically isotropic crystal there would be no additional diffraction contrast. The reason is, that for a screw dislocation lattice planes with the plane normal $\mathbf{g}$ being perpendicular to the Burgers vector $\mathbf{b}$ are not bent.

2.5.2 Image simulation of crystals having strain fields

The $\mathbf{g} \cdot \mathbf{b} = 0$ criterion for dislocations being out of contrast can be used for determination of the Burgers vector. However, this criterion is only partially valid for edge dislocations and completely fails in elastically anisotropic crystals. Therefore, image simulation is required for anisotropic crystals. Image simulation includes (i) the calculation of the strain field $\frac{\partial \mathbf{u}}{\partial x_l}$ and thereby the displacement function $\beta(z)$ (Eq. 2.29) and (ii) the numerical integration of the Howie-Whelan equations (Eq. 2.27).

The calculation of the strain field of a dislocation was solved by Stroh [44, 45] and by Barnett and Lothe [46]. A fast calculation of electron micrographs based on the Stroh formalism and implemented in FORTRAN was presented by Head [47]. The aim of this work was to compute electron micrographs of dislocations based on the integral formalism of Barnett and Lothe implemented in MATLAB® and will be presented in Chapter 8. The advantage of the integral formalism and of MATLAB® is a reduction of the computing time compared to Head [47]. Finally, two-beam images of structural modulations (nns) found in Bi_2Te_3 were also simulated (Chap. 8.3.3).

Usually, the Howie-Whelan equations (Eq. 2.27) can be solved only numerically due to the local changes of the strain field (Eq. 2.29). For numerical integration the specimen has to be separated in columns and slices, and the strain field is assumed to be constant within each slice. For each column, the amplitudes (T_{n+1}, S_{n+1}) in slice $(n+1)$ have to be calculated under consideration of the Howie-Whelan equations (Eq. 2.27) and the boundary condition that the amplitudes (T_n, S_n) in the previous slice (n) are already known. The boundary condition on top of the sample is $(T_1, S_1) = (1, 0)$. A high-precision numerical integration method is the Runge-Kutta method, which was used by Head [47]. In this work, another method was used; the differential equations were transformed by an "Ansatz" into algebraic equations and the algebraic equations were solved (Eq. 2.30). For both methods, the amplitudes are transformed from slice (n) to slice $(n+1)$ by matrices (K_n) according to

$$\begin{pmatrix} T_{n+1} \\ S_{n+1} \end{pmatrix} = (K_n) \begin{pmatrix} T_n \\ S_n \end{pmatrix} , \tag{2.31a}$$

$$\begin{pmatrix} T(z) \\ S(z) \end{pmatrix} = \cdots (K_3)(K_2)(K_1) \begin{pmatrix} T_1 \\ S_1 \end{pmatrix} , \tag{2.31b}$$

due to the linear character of the Howie-Whelan equations. The transformation matrices (K_n) depend in a large part on the displacement function $\beta(z)$, and particularly are independent of the amplitudes (App. C.5).

Chapter 3

Experimental for bulk materials

The samples were n-type $Bi_2(Te_{0.91}Se_{0.09})_3$ and p-type $(Bi_{0.26}Sb_{0.74})_{1.98}(Te_{0.99}Se_{0.01})_{3.02}$ bulk materials synthesised by the Bridgman technique (Table 3.1), which were obtained from commercially available Peltier devices [32]. About 10 samples were conventionally prepared for TEM analysis by grinding, polishing, or dimpling, and finally by Ar^+-ion milling at $4\,kV$. The c axis was lying in the plane of the TEM samples.

Variations in stoichiometry were analysed by energy dispersive X-ray spectrometry (EDX) on two n-type samples (samples N1 and N2) and on two p-type samples (samples P1 and P2) (Table 3.1). It will be shown that the TEM sample thickness, i.e., $100\,\mu m$ for dimpled samples and $30\,\mu m$ for polished samples, has a strong influence on the obtained hole-count spectra. The structural modulations [natural nanostructure(nns)] were analysed by stereomicroscopy and image simulation on three n-type samples (samples N3, N4, and N5) and one p-type sample (sample P3) (Table 3.1). Finally, gliding dislocations were analysed by stereomicroscopy, video analysis, and image simulation on sample P4 (Table 3.1).

A Zeiss 912Ω TEM was used with a LaB_6 gun operated at $120\,kV$ and with a point resolution of $0.37\,nm$ (Fig. 3.1). The microscope is equipped with (i) a Köhler illumination system, (ii) an OMEGA filter, (iii) a side entry EDX detector of Oxford Instruments for chemical analysis with an energy resolution of $132\,eV$ at the Mn K_α line, (iv) a low-background, liquid nitrogen cooling, double-tilt holder with a tilting range of $\pm 60°/\pm 30°$, (v) a CCD-camera of SIS (14-bit, 1024×1024 pixel), and (vi) a video-CCD-camera of Sony (8-bit, 768×576 pixel).

The stereomicroscopy technique included: (i) tilting of the same specimen region by angles up to $\pm 60°$ to various orientations and (ii) imaging of the strain fields by diffraction contrast with strongly excited Bragg reflections $\mathbf{g} = \{0, 0, 15\}, \{-1, 0, 5\}, \{1, 0, 10\}$, or $\{1, 1, 0\}$. Particularly, the nns can be imaged with strongly excited $\{-1, 0, 5\}$ reflections [34–36, 57]. Image simulation was applied, which required two numerical calculations: (i) the strain field of the dislocations and of the nns and (ii) the amplitudes of the direct beam and the diffracted beam according to the two-beam dynamical diffraction theory (Ref. [42, chap. 13] and [55]).

For the stereomicroscopy experiments Kikuchi maps are indispensable and were constructed for Bi_2Te_3 by stereographic projection [58, page 28] of the poles on the basal plane (Fig. 3.2). Kikuchi maps are used as road maps and allow in combination with the analysis of the diffraction patterns a precise determination of the beam direction and the foil normal, which have to be known for image simulation. Figure 3.3 shows an overview Kikuchi map, the tilting experiments for the analysis of the nns and of gliding dislocations are labelled by arrows. In Appendix B more detailed Kikuchi maps are given (Fig. B.1 and B.2).

The dislocations were analysed with respect to dislocation density, Burgers vector, line direction, glide plane, and line energy. The accuracy of the measurement of the line directions is about $\pm 10°$. The Burgers vectors $\mathbf{b}$ were determined according to the $\mathbf{g} \cdot \mathbf{b} = 0$ criterion for dislocations being out of contrast [56]. This method could be applied because Bi_2Te_3 has almost isotropic elastic properties, the anisotropy ratio being $A = 1.17$ [41, chap. 2.4] calculated from the elastic constants c_{ij} [59]. Image simulation was applied for a exact analysis of the Burgers vectors. The strain field and the line energy were calculated under consideration of the

Table 3.1 Composition and TEM preparation of the investigated Bi_2Te_3 samples for the EDX analysis, the analysis of the nns, and the analysis of gliding dislocations.

Sample	Composition	TEM preparation
	EDX	
N1	$Bi_2(Te_{0.91}Se_{0.09})_3$	Dimpling ($100\,\mu m$)
N2	$Bi_2(Te_{0.91}Se_{0.09})_3$	Polishing ($30\,\mu m$)
P1	$(Bi_{0.26}Sb_{0.74})_{1.98}(Te_{0.99}Se_{0.01})_{3.02}$	Dimpling ($100\,\mu m$)
P2	$(Bi_{0.26}Sb_{0.74})_{1.98}(Te_{0.99}Se_{0.01})_{3.02}$	Polishing ($30\,\mu m$)
	nns	
N3	$Bi_2(Te_{0.91}Se_{0.09})_3$	Polishing ($30\,\mu m$)
N4	$Bi_2(Te_{0.91}Se_{0.09})_3$	Polishing ($30\,\mu m$)
N5	$Bi_2(Te_{0.91}Se_{0.09})_3$	Polishing ($30\,\mu m$)
P3	$(Bi_{0.26}Sb_{0.74})_{1.98}(Te_{0.99}Se_{0.01})_{3.02}$	Dimpling ($100\,\mu m$)
	Gliding dislocations	
P4	$(Bi_{0.26}Sb_{0.74})_{1.98}(Te_{0.99}Se_{0.01})_{3.02}$	Dimpling ($100\,\mu m$)

Table 3.2 Cliff-Lorimer k factors as used by the software (INCA®, Oxford Instruments) for $120\,keV$ electrons ("theoretical") and after calibration by EPMA for Bi_2Te_3 and Bi-2212 samples ("calibrated"). Te served as reference element.

	Z	X-ray line	Energy (keV)	Theoretical	Calibrated
Ca	20	$K_{\alpha 1}$	3.692	0.959	1.04 ± 0.11
Cu	29	$K_{\alpha 1}$	8.048	1.457	1.19 ± 0.05
Se	34	$K_{\alpha 1}$	11.222	2.071	2.15 ± 0.21
Sr	38	$K_{\alpha 1}$	14.165	2.629	2.23 ± 0.20
Sb	51	$L_{\alpha 1}$	3.605	1.890	2.02 ± 0.07
Te	52	$L_{\alpha 1}$	3.769	1.961	1.961
Bi	83	$L_{\alpha 1}$	10.839	3.083	2.17 ± 0.11

anisotropic elastic properties according to the integral formalism of Barnett and Lothe [46].

The characteristic quantities of the nns are the wave vector $\mathbf{q}$ and the displacement vector $\mathbf{u}$. The wavelength of the wave vector was obtained from the fringe spacing in the two-beam images of the nns and its direction was determined in the corresponding diffraction patterns. The direction of the displacement vector was calculated according to the $\mathbf{g} \cdot \mathbf{u} = 0$ criterion for a displacement field being out of contrast [56]. The exact amplitude of the displacement vector was determined by comparison of experimental and simulated images with respect to their diffraction contrast $(I_{max} - I_{min})/(I_{max} + I_{min})$, where I is the intensity.

The chemical composition was first determined by wavelength dispersive X-ray spectrometry (WDX) in an electron probe microanalyser (EPMA) [33] and then by EDX in the TEM [60, 61]. Additionally, electron energy-loss spectra (EELS) were acquired in the TEM to verify the local thickness of the sample in terms of the electron mean free path (mfp). The Cliff-Lorimer method [62] was applied for quantitative chemical analysis by EDX, and the Cliff-Lorimer k factors were calibrated such that the mean values of the mole fractions corresponded to those of the EPMA results [33] (Table 3.2).

The acquisition conditions for the EDX spectra were an acquisition time of $120\,s$, a spot size of $63\,nm$, a detector take-off angle of $20°$, and a specimen tilt angle of $15°$. The integrated counts N of the Bi $L_{\alpha 1}$, Te $L_{\alpha 1}$, and Sb $L_{\alpha 1}$ peaks were larger than $20\,000$ for EDX spectra acquired in thick specimen regions ($> 0.4\,mfp$), yielding a minimum statistical error of $\sigma_N/N = 0.7\%$ (Poisson statistics) for the determination of the local mole fractions. In thin specimen regions ($< 0.4\,mfp$) the integrated counts of the Bi $L_{\alpha 1}$ and Te $L_{\alpha 1}$ peaks were larger than 5000 and the statistical error was $\sigma_N/N = 1.4\%$. For the determination of variations in stoichiometry within individual grains and in the entire sample mean mole fractions c, standard deviations σ_c, and relative errors σ_c/c were calculated.
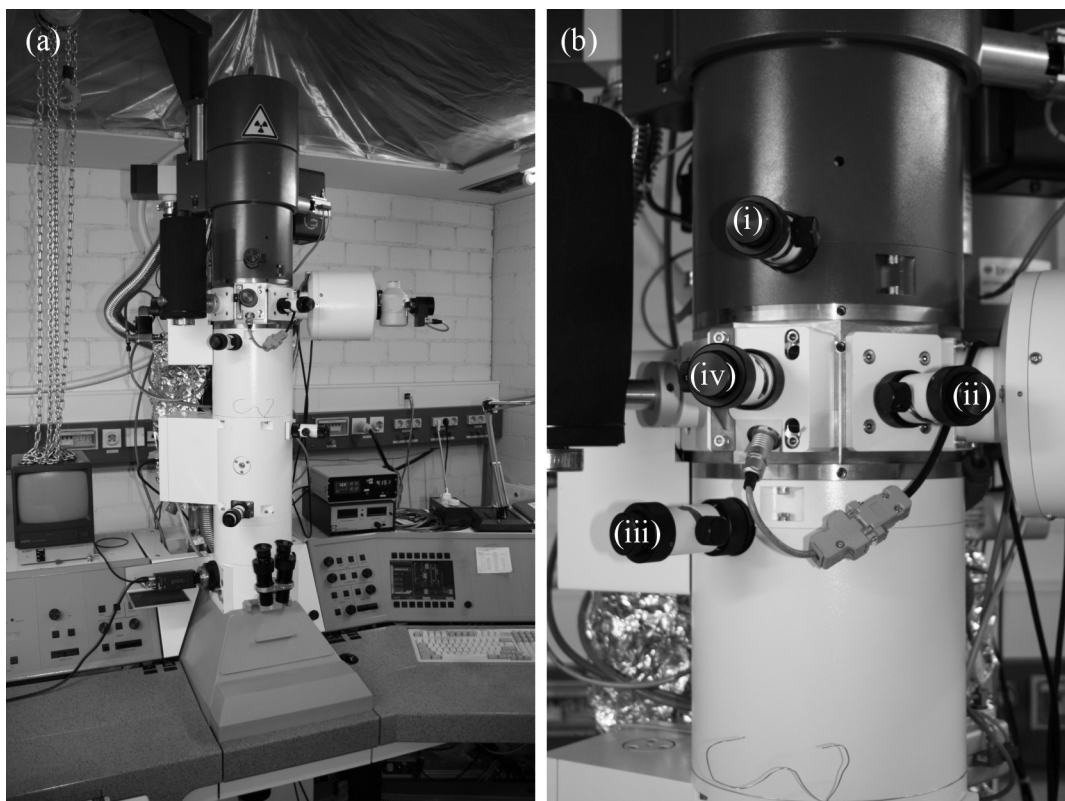
Figure 3.1 (a) The Zeiss 912Ω TEM and (b) a magnified image showing (i) the condenser aperture, (ii) the objective aperture, (iii) the selected area aperture, and (iv) the stray aperture for elimination of the "hole-count" artifact.
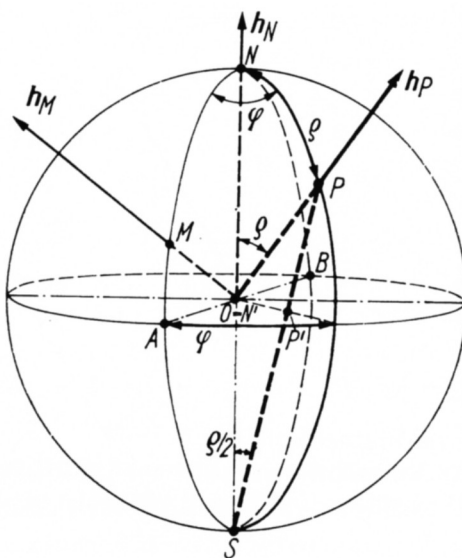
Figure 3.2 Construction of a Kikuchi map by stereographic projection [58, page 28]. The pole-direction $\mathbf{h}_P$ and its corresponding point P on the pole sphere is projected into the point P' in the basal plane. In Bi_2Te_3, the pole N and the pole A correspond to the $[0,0,1]$ and $[1,0,0]$ directions, respectively. For image simulation, the pole directions were specified by their Miller indices $[u,v,w]$ or by polar coordinates (φ, ρ).

Figure 3.3 Overview Kikuchi map for Bi_2Te_3. The Kikuchi map was used as a road map for the tilting experiments in the TEM. The $[0,0,1]$ pole in the centre correspond to the North-Pole (Fig. 3.2). The poles in the basal plane such as $[1,0,0]$ are on the outer circle (equator line). The arrows show the tilting experiments for samples N3, N4, N5, P3, and P4.

Chapter 4

Bulk: Quantitative EDX microanalysis

4.1 Introduction

There are a few studies by transmission electron microscopy (TEM) on extended structural defects in Bi_2Te_3 [24–26] but no quantitative chemical analysis by energy dispersive X-ray spectrometry (EDX) in the TEM reported in the literature. With respect to its chemical microstructure Bi_2Te_3 was assumed to be a solid solution with homogeneous stoichiometry. However, quantitative chemical analysis by wavelength dispersive X-ray spectrometry (WDX) in an electron probe microanalyser (EPMA) yielded a fairly large variation in stoichiometry on the micrometer scale [33]. On the other hand, TEM investigations yielded a structural modulation on the nanometer scale [34, 63]. It was suggested that the structural modulation might be caused by chemical inhomogeneities on the nanometer scale [34]. The lateral resolution of the WDX method is only $1\,\mu$m and too large for yielding meaningful results. EDX spectrometry in the TEM is the method of choice due to its higher lateral resolution of less than $50\,$nm for a TEM with a thermal emitter and about $1\,$nm for a TEM with a field emission gun.

Over the last years, EDX spectrometry has also emerged as a method for quantitative chemical analysis of light elements found in, e.g., biological samples, since by introducing ultrathin detector windows the analysis of light elements down to C, O, and B ($Z = 5$) is now possible [64–66]. The quantitative chemical analysis of heavy elements like Bi ($Z = 83$) is also demanding. It is well known (Ref. [42, chap. 33] and Ref. [67–72]) that spurious X-rays are generated at various sections of the microscope or sample and might reach the EDX detector and yield artifacts. Spurious X-rays (characteristic and continuum X-rays) of the sample can be generated by uncollimated electrons and by X-ray fluorescence, the latter being generated by the electron beam. The artifact can be reduced by thick apertures of high atomic number located at the second condenser lens [67] or at the anticontaminator [71], by preparation of thin TEM samples [67], by design of the specimen holder [71, 72], and by limiting the field of view of the X-ray detector [71]. These points were already implemented in the Zeiss 912Ω TEM, however, did not solve the problem satisfactorily.

Materials such as Bi_2Te_3 or Bi_2O_3 [73] are particularly susceptible to stray radiation since their heavy element Bi absorbs more strongly than the other elements of the compound. Therefore, the hole-count artifact is stronger than in other systems and considerably reduces the accuracy of the measurements below an acceptable and relevant level. In this chapter it will be reported how this artifact was further suppressed yielding a quantitative chemical analysis with high accuracy.

Chemical microanalysis of Bi compounds is of great interest because of (i) the outstanding physical properties of these compounds and (ii) the stoichiometry range the crystal structures of these compounds have. Considering the importance and outstanding properties of Bi_2Te_3 as a thermoelectric material or the $Bi_2Sr_2Ca_{n-1}Cu_nO_{4+2n}$ compounds as a superconducting ma-

terial, little is known and has been published on the chemical composition of these compounds. Recently, new Te-phases such as $AgPb_mSbTe_{2+m}$ bulk materials with outstanding thermoelectric and structural properties were found [28, 29]. EDX in the TEM on such compounds will be necessary to correlate physical properties with chemical composition.

4.2   Results

4.2.1   Elimination of stray radiation

Stray radiation in the TEM can be verified by hole-count measurements, for which the electron beam is positioned in the vacuum close to the edge of the sample and an EDX spectrum is acquired [67]. The X-ray counts obtained in such a spectrum are called "hole-counts" and are artifacts. This is demonstrated for sample N1. The electron probe was positioned (1) at a hole close to the edge of the specimen, (2) at a thin region 100 nm away from the edge of the sample, and (3) at a thicker region at a distance 250 nm away from the edge (Fig. 4.1). The acquisition time was the same for all three spectra. Note that the intensities of the X-ray lines are not proportional to the specimen thickness. Therefore, the obtained mole fraction ratios depend on the position of the measurements. In thick specimen regions the Te $L_{\alpha 1}$ peak is larger than the Bi $L_{\alpha 1}$ peak, whereas in thin specimen region the Bi $L_{\alpha 1}$ peak is larger. The hole-count spectrum shows strong Bi L X-ray peaks and the intensity of the Bi $L_{\alpha 1}$ line is 31% of the value measured at a thin specimen region.

Uncollimated electrons might hit the specimen at thick outer parts of the sample and, thereby, produce spurious X-rays. In sample P1 spectra were acquired (1) at a hole, (2) at an electron transparent region at the edge of the sample, and (3) at a thick region, i.e., a not transparent region (Fig. 4.2). The spectra were normalised with respect to the Bi $L_{\alpha 1}$ lines. Spectrum 2 is a conventional EDX/TEM spectrum whereas hole-count spectrum 1 and spectrum 3 are almost identical and differ significantly from spectrum 2.

In hole-count spectra the Bi $L_{\alpha 1}$ peak was found to be larger than the Te $L_{\alpha 1}$ peak. It is a characteristic feature of the artifact, that the peaks of high energy X-ray lines of the heavy elements are larger than the low energy X-ray lines of the lighter elements. Therefore, the quantitative analysis in thin specimen regions yielded a too large mole fraction of Bi, i.e., 64 at. % instead of 40 at. % in spectrum 2 of sample N1. For improving the accuracy of the analysis the Bi $L_{\alpha 1}$ spurious X-rays had to be reduced and the intensity of the Bi $L_{\alpha 1}$ hole-count should decrease to 1% or less of the value measured at a thin specimen region. In the following, the ratio of the Bi $L_{\alpha 1}$ counts measured less than 100 nm away from the edge of the sample and at a hole under identical acquisition conditions is referred to as the Bi $L_{\alpha 1}$ hole-count ratio. The Bi $L_{\alpha 1}$ hole-count ratio should be 100 or larger for a high-accuracy analysis.

A Mo stray aperture (Fig. 4.3(a)) with a diameter of 200 μm was inserted close to and above the anticontaminator, i.e., 5.6 mm above the specimen. This aperture can be inserted and removed like the objective aperture. This aperture prevents stray radiation hitting the specimen without limiting the field of view of the electron beam. Figure 4.3(b) shows two hole-count spectra acquired in sample N1 without and with inserted stray aperture. With inserted stray aperture the intensity of spurious X-rays was drastically reduced. For sample P1 the Bi $L_{\alpha 1}$ spurious X-rays could be reduced by a factor of 8 yielding a Bi $L_{\alpha 1}$ hole-count ratio of 42 (Table 4.1).

Usually, to assess the amount of stray radiation in a an analytical TEM a NiO thin film mounted on a 200-mesh Mo-grid is used [74, 75]. Two spectra were acquired under identical acquisition conditions on a commercially available NiO test specimen (Plano GmbH). The specimen was inserted with the film facing the electron beam, and the electron beam was positioned at the centre of a mesh. The first spectrum was acquired on the NiO film and the second at a hole of a nearby mesh without a film. The Ni $K_{\alpha 1}$ and Mo $K_{\alpha 1}$ integrated counts were determined from both spectra. Two different Ni $K_{\alpha 1}$/Mo $K_{\alpha 1}$ count ratios were determined that characterise the quality of the EDX measurements; (i) a film-count ratio, where both counts were obtained from the first spectrum and (ii) a hole-count ratio, where the Ni $K_{\alpha 1}$

and the Mo $K_{\alpha1}$ counts were obtained from the first and second spectrum, respectively. The Ni $K_{\alpha1}$/Mo $K_{\alpha1}$ film-count ratio increased from 3.0 without to 6.6 with inserted stray aperture (Table 4.1). The Ni $K_{\alpha1}$/Mo $K_{\alpha1}$ hole-count ratio is a more sensitive performance figure for column radiation and increased from 5.1 without to 45 with inserted stray aperture (Table 4.1). The hole-count measurement also showed a reduction of the Mo $K_{\alpha1}$ spurious X-rays by a factor of 8.7 and a change of the Mo $K_{\alpha1}$/Mo $L_{\alpha1}$ count ratio from 4.3 without to 39.7 with inserted stray aperture.

Hole-count artifacts can also be reduced by preparing thinner samples. The thickness of the sample has to be expressed in terms of the electron and X-ray mean free paths [67]. The mean free path in Bi_2Te_3 is estimated to $9\,\mu$m for 120 keV electrons [76] and to $21\,\mu$m and $492\,\mu$m for 20 keV and 120 keV X-rays, respectively [77, 78]. Up to now, only measurements on dimpled samples were presented, which have a thickness of about $100\,\mu$m. Hole-count measurements were carried out on sample N2, which was entirely polished to a thickness of $30\,\mu$m. Without stray aperture a Bi $L_{\alpha1}$ hole-count ratio of 9.3 was found, which is an improvement by a factor of 3 compared to the dimpled sample P1 (Table 4.1). With the stray aperture inserted the spurious X-rays were further decreased by a factor of 5 yielding a Bi $L_{\alpha1}$ hole-count ratio of 43 (Table 4.1).

4.2.2 Quantitative chemical analysis of Bi_2Te_3

Bulk materials

First, the improved accuracy of the EDX analysis due to the stray aperture had to be verified. Second, the goal of the EDX analysis was (i) to find the length scale of chemical inhomogeneities and (ii) a possible correlation to a structural modulation (Fig. 4.4) [34, 63]. The results are summarised in tables and are presented as Se-Te correlation diagrams for n-type $Bi_2(Te, Se)_3$ and as Bi-Sb correlation diagrams for p-type $(Bi, Sb)_2Te_3$. Particularly, the scatter of data is of interest. All spectra were acquired in specimen regions thicker than 0.4 mfp but thin enough such that absorption of the Te $L_{\alpha1}$ and Sb $L_{\alpha1}$ lines is still small. The reason is, that the mean free path of X-rays in Bi_2Te_3 is estimated to $10\,\mu$m for the Bi $L_{\alpha1}$ line and $1\,\mu$m for the Te $L_{\alpha1}$ line [77, 78], which is large compared to a typical specimen thickness of 100 nm.

Seven spectra were acquired within an area of $1\,\mu$m^2 of a n-type sample without and with inserted stray aperture (Table 4.2, Fig. 4.5). A mole fraction of 52.8 ± 0.8 at. % Te and of 53.9 ± 0.2 at. % Te was obtained without and with inserted stray aperture, respectively.

With inserted stray aperture at a different grain, seven spectra were acquired on n-type $Bi_2(Te, Se)_3$ within an area of $1\,\mu$m^2 and yielded a mole fraction of 54.1 ± 0.5 at. % Te (Table 4.3). More than 60 spectra were acquired in an extended area larger than $100\,\mu$m^2. An average mole fraction of 54.4 ± 1.3 at. % Te (Table 4.3) and a negative correlation between Te and Se (Fig. 4.6(a)) was obtained in large areas. The same type of measurements on p-type $(Bi, Sb)_2Te_3$ yielded a mole fraction of 29.6 ± 0.2 at. % Sb within an area of $1\,\mu$m^2. In areas larger than $100\,\mu$m^2 an average mole fraction of 29.8 ± 0.8 at. % Sb (Table 4.3) and a negative correlation between Bi and Sb (Fig. 4.6(b)) was obtained.

Te-depletion in thin specimen areas

The stray aperture was inserted and EDX spectra were acquired on a freshly prepared n-type $Bi_2(Te, Se)_3$ TEM sample. Spectra were acquired along a line perpendicular to the edge and the specimen thickness was measured by EELS. Figure 4.7 shows the mole fraction in dependence of the position (specimen thickness). The mole fraction of Te drops significantly at a thickness of less than 0.4 mfp. More than 10 spectra were acquired in thin specimen regions of less than 0.4 mfp yielding a mole fraction of 48.4 ± 5.2 at. % Te (Table 4.4) and no correlation between Se and Te (Fig. 4.8(a)). The same type of measurements on p-type $(Bi, Sb)_2Te_3$ yielded a mole fraction of 53.6 ± 4.6 at. % Te (Table 4.4) and no correlation between Bi and Sb (Fig. 4.8(b)). Therefore, a Te-depletion exists in both samples at thin specimen areas.
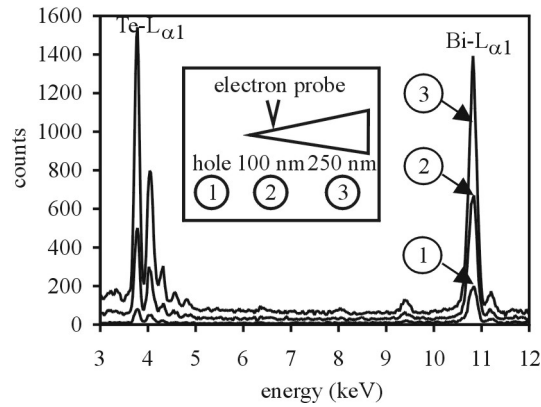
Figure 4.1 EDX spectra of sample N1 acquired (1) as hole-count and (2,3) at electron transparent regions with increasing specimen thickness. The insert shows the positions of the EDX measurements.
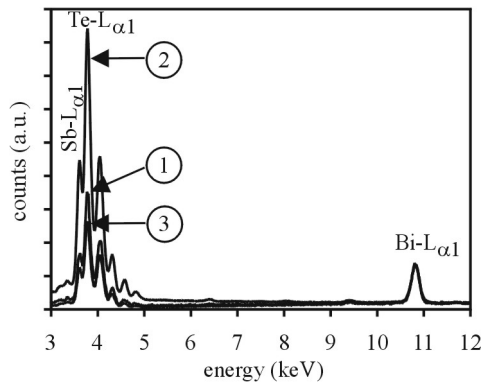
Figure 4.2 EDX spectra of sample P1 acquired (1) as hole-count, (2) at an electron transparent, and (3) a non electron transparent region. The spectra were normalized with respect to the Bi $L_{\alpha 1}$ lines.
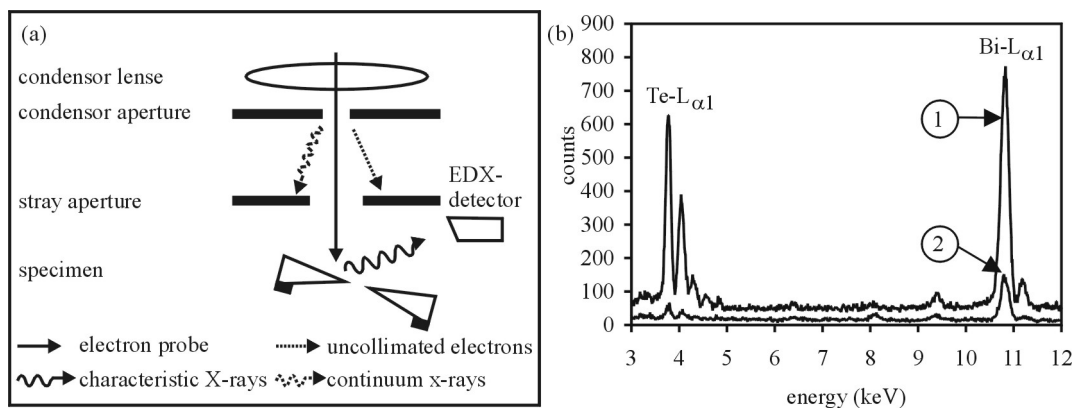
Figure 4.3 (a) Schematic drawing of the stray aperture configuration positioned slightly above the sample. (b) Hole-count EDX spectra of sample N1 acquired (1) without and (2) with inserted stray aperture. Identical acquisition conditions were used for both spectra.

Table 4.1 Effect of the stray aperture and sample preparation on the film-count and hole-count ratio. A high performance corresponds to a large ratio.

Sample	Sample preparation	Performance figure	Without aperture	With aperture
NiO film	200-mesh Mo grid	Ni $K_{\alpha 1}$/Mo $K_{\alpha 1}$ film-count ratio [a]	3.0	6.6
NiO film	200-mesh Mo grid	Ni $K_{\alpha 1}$/Mo $K_{\alpha 1}$ hole-count ratio [b]	5.1	45
Sample P1	Dimpled	Bi $L_{\alpha 1}$ hole-count ratio [c]	3.5	42
Sample N2	Polished	Bi $L_{\alpha 1}$ hole-count ratio [c]	9.3	43
Bi-2212	Polished	Bi $L_{\alpha 1}$ hole-count ratio [c]	25	127
HAP film	200-mesh Cu grid	Ca $K_{\alpha 1}$/Cu $K_{\alpha 1}$ film-count ratio [a]	0.6	6.1

[a]Both counts were measured on the film. [b]The Ni $K_{\alpha 1}$ count was measured on the film and the Mo $K_{\alpha 1}$ count was measured at a hole under identical acquisition conditions. [c]The Bi $L_{\alpha 1}$ counts were measured close to the edge of the sample and at a hole under identical acquisition conditions.
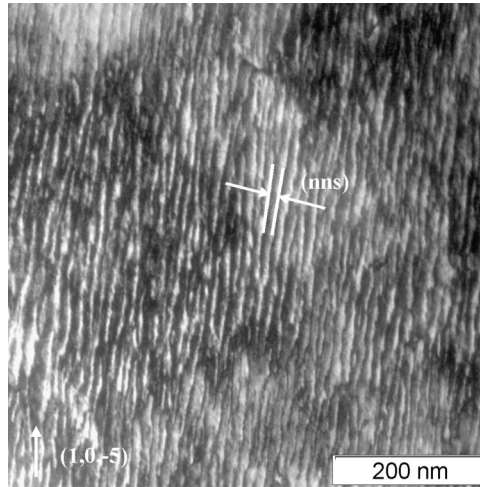
Figure 4.4 $(1, 0, -5)$ dark field image for imaging a structural modulation (nns) with a wavelength of $10\,\text{nm}$ in n-type Bi_2Te_3.

4.2.3 Quantitative chemical analysis of other systems

Quantitative chemical analysis by EDX in the TEM on TEM foils and on powders is a standard technique. The improvement of the accuracy by using the stray aperture is demonstrated on a high-T_C superconductor $Bi_2Sr_2CaCu_2O_{8+\delta}$ (Bi-2212) and on nano hydroxyapatite (HAP) $Ca_{10}(PO_4)_6OH_2$ powders on Cu-grids, HAP being a main component of bones and teeth.

Similar to Bi_2Te_3, Bi-2212 contains the heavy element Bi and shows large variations in stoichiometry [79]. Although this compound has fascinating physical properties and is structurally complex, only a few systematic studies have been published on the chemical composition of these materials. First, hole-count measurements were carried out on a polished bulk TEM sample. With inserted stray aperture the spurious X-rays could be decreased by a factor of 4 yielding an improvement of the Bi $L_{\alpha 1}$ hole-count ratio from 25 to 127 (Fig. 4.9(a), Table 4.1). Variations in stoichiometry were determined by 3 measurements in an area smaller than $1\,\mu\text{m}^2$ and 30 measurements in an area larger than $100\,\mu\text{m}^2$ (Table 4.5) and are shown in a Ca-Cu correlation diagram (Fig. 4.9(b)). Variations in stoichiometry are by a factor of 5 smaller on the sub-micrometer scale.

A powder of nano HAP was dispersed on a holey carbon film on top of a 200-mesh Cu-grid. EDX spectra of the nano powder particles at the centre of a mesh were acquired. Without stray aperture the Cu $K_{\alpha 1}$ spurious peak is the largest peak in the spectrum (Fig. 4.10(a)). With inserted stray aperture the Cu $K_{\alpha 1}$ spurious peak was reduced by a factor of 10 (Fig. 4.10(b)), i.e., the Ca $K_{\alpha 1}$/Cu $K_{\alpha 1}$ film-count ratio being 0.6 without and 6.1 with inserted stray

Figure 4.5 Se-Te correlation diagrams obtained in a thicker region ($> 0.4\,\mathrm{mfp}$) of n-type $\mathrm{Bi_2(Te, Se)_3}$ within an area of $1\,\mu\mathrm{m^2}$ (a) without and (b) with inserted stray aperture.

Table 4.2 Mole fractions obtained in a thicker region ($> 0.4\,\mathrm{mfp}$) of n-type $\mathrm{Bi_2(Te, Se)_3}$ within an area of $1\,\mu\mathrm{m^2}$ with and without stray aperture.

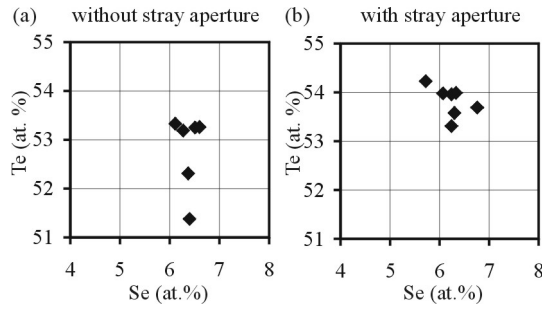|	Without aperture			With aperture		
	Bi	Te	Se	Bi	Te	Se
c (at. %)	40.8	52.8	6.4	39.9	53.9	6.2
σ_c (at. %)	0.8	0.8	0.2	0.2	0.2	0.3
σ_c/c (%)	1.9	1.5	2.7	0.6	0.4	5.5

aperture (Table 4.1). The quantitative chemical analysis yielded mole fractions of 63 at. % Ca and 37 at. % P without stray aperture and of 59 at. % Ca and 41 at. % P with stray aperture [80], which is very close the expected composition. Therefore, for chemical analysis of powders on Cu grids, the effect of the stray aperture is most significant among the samples studied in this paper.

4.3   Discussion

4.3.1   Quantitative EDX microanalysis of $\mathrm{Bi_2Te_3}$ materials

No correlations between chemical inhomogeneities and the nns

The quantitative chemical analysis by EPMA on p-type $\mathrm{(Bi, Sb)_2Te_3}$ yielded a negative correlation between Sb and Bi with a variation in stoichiometry of about $1 - 1.5$ at. % [33]. The same behaviour was found for Se and Te in n-type $\mathrm{Bi_2(Te, Se)_3}$ [33]. Therefore, Sb can be substituted for Bi and Se for Te in p-type and n-type samples, respectively. Both samples are inhomogeneous on the micrometer scale. Diffraction contrast experiments in the TEM yielded in both samples a structural modulation with a wavelength of 10 nm (Fig. 4.4) [34, 63]. This structural modulation is referred to as natural nanostructure (nns) [63].

With the stray aperture inserted the average Te mole fraction was found to be equal to the nominal composition and the scatter of data could be reduced by a factor of 4 (Table 4.2). Also, line scans at varying sample thickness yielded smaller variations of the determined mole fractions. The relative error of $\sigma_c/c = 1\%$ for Te found on the sub-micrometer scale (Table 4.3) is due to (i) a statistical error of $\sigma_N/N = 0.7\%$ and (ii) due to absorption of the low-energy X-ray lines.

The effect of absorption of X-ray lines on the scatter of data will be discussed in detail only for the material which is most strongly affected by absorption, i.e., n-type $\mathrm{Bi_2(Te, Se)_3}$. A line scan at distances between 200 nm and 800 nm away from the edge of the sample yielded a maximum scatter of data of 1.6%. However, no clear absorption effect was observed, i.e., a reduction of the Te mole fraction for increasing specimen thickness (Fig. 4.7). For a wedge-shaped sample the specimen thickness should increase from 90 nm to 355 nm, respectively. On
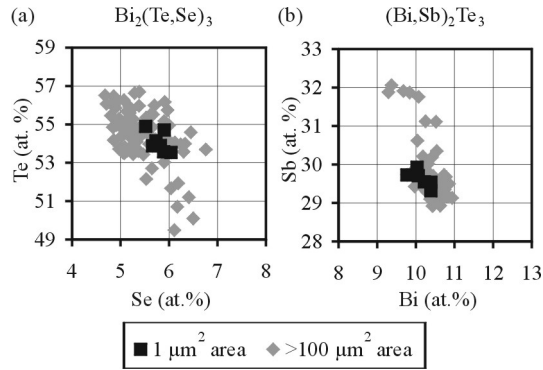
Figure 4.6 Se-Te and Sb-Bi correlation diagrams obtained in thick regions (> 0.4 mfp) of (a) n-type $Bi_2(Te, Se)_3$ and (b) p-type $(Bi, Sb)_2Te_3$, within an area of $1\ \mu m^2$ (black squares) and an area larger than $100\ \mu m^2$ (grey diamond). The stray aperture was inserted.

Table 4.3 Mole fractions obtained in thick regions (> 0.4 mfp) of n-type $Bi_2(Te, Se)_3$ and p-type $(Bi, Sb)_2Te_3$ within an area of $1\ \mu m^2$ and an area larger than $100\ \mu m^2$. The stray aperture was inserted.

| | $Bi_2(Te, Se)_3$ | | | | | | $(Bi, Sb)_2Te_3$ | | | | | |
| | Area $< 1\ \mu m^2$ | | | Area $> 100\ \mu m^2$ | | | Area $< 1\ \mu m^2$ | | | Area $> 100\ \mu m^2$ | | |
	Bi	Te	Se	Bi	Te	Se	Bi	Sb	Te	Bi	Sb	Te
c (at. %)	40.1	54.1	5.8	40.1	54.4	5.5	10.1	29.6	60.2	10.4	29.8	59.9
σ_c (at. %)	0.5	0.5	0.2	1.1	1.3	0.5	0.2	0.2	0.2	0.3	0.8	0.6
σ_c/c (%)	1.1	1.0	3.0	2.8	2.4	8.7	2.4	0.7	0.3	3.1	2.6	1.0

the basis of the mass absorption coefficients [77, 78] the absorption correction factors ACF_{TeBi} [42, chap. 35] for the k factor of the Te $L_{\alpha1}$ line should be 5% and 23%, respectively. Therefore, for the line scan shown in Figure 4.7 a reduction of the Te mole fraction was expected from nominal 54.4 at. % to 53 at. % at a distance of 200 nm and to 49 at. % at a distance of 800 nm away from the edge. The reason for the absence of absorption effects in this line scan might be a deviation from the ideal wedge shape and thereby an overestimation of the sample thickness. Line scans on the other Bi-based samples yielded similar results. Therefore, X-ray absorption effects cannot account for the large scatter in stoichiometry found for these materials.

In n-type $Bi_2(Te, Se)_3$ in areas smaller than $1\ \mu m^2$ the variation in stoichiometry of Te and Se was found to be about 0.5 at. % (Table 4.3), which is 2-3 times smaller compared to EPMA results [33]. The variations in stoichiometry increased by a factor of 2 in areas larger than $100\ \mu m^2$ (Table 4.3), which is in agreement with the EPMA results [33]. The negative correlation between Te and Se is due to cross substitution of these two elements. A corresponding behaviour was found in p-type $(Bi, Sb)_2Te_3$ with respect to Bi and Sb. Both, n-type $Bi_2(Te, Se)_3$ and p-type $(Bi, Sb)_2Te_3$ are more homogeneous on the sub-micrometer scale.

A structural modulation (nns) was found in n-type $Bi_2(Te_{0.91}Se_{0.09})_3$ and p-type $(Bi_{0.26}Sb_{0.74})_2Te_3$ bulk materials [34, 63], Bi_2Te_3 thin films and $Bi_2Te_3/Bi_2(Te_{0.88}Se_{0.12})_3$ superlattices epitaxially grown on BaF_2 substrates [35, 36, 57]. Therefore, the nns is of general character for Bi_2Te_3 materials. A main topic of the EDX analysis was to find a correlation between the nns and chemical modulations on the nanometer scale. A spot size of 63 nm is too large, and a microscope with a better lateral resolution would be required for this problem. However, on the basis of our experimental findings a relation of the nns to chemical inhomogeneities is unlikely for several reasons. (i) The nns was also found in epitaxially grown pure Bi_2Te_3 thin films [35, 36, 57]. Therefore, alloying and subsequent precipitation alone cannot be the origin of the nns. (ii) The EDX measurements in the TEM on n-type and p-type bulk materials yielded smaller variations in stoichiometry on the sub-micrometer scale, which is not
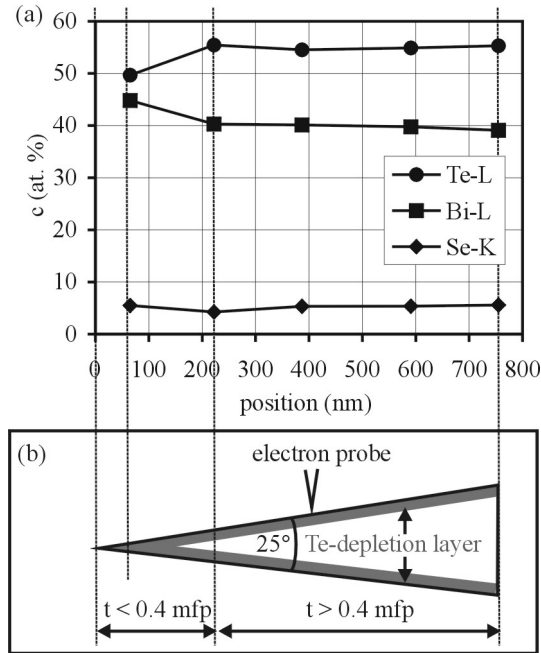
Figure 4.7 (a) EDX line scan obtained in n-type $Bi_2(Te, Se)_3$ with increasing sample thickness t. The stray aperture was inserted. (b) Illustration of a Te depletion layer (grey) in the wedge-shaped TEM samples.

expected if the modulation with its 10 nm wavelength would be induced by chemical inhomogeneities. (iii) The crystallographic features (wavelength and direction of the wave vector) of the nns were found to be independent of the chemical composition, i.e., the Se and Sb mole fraction [35, 36, 57, 63]. This is in contradiction to natural nanostructures found in other Te-phases such as $AgPb_mSbTe_{2+m}$ ($m = 6 - 18$) bulk materials [28, 29] and $Bi_2Te_3Ge_x$ ($x = 0.1 - 0.88$) crystals [27]. In these materials the nns was related to compositional fluctuations on the nanometer scale, since the direction and wavelengths of the wave vectors depended on the Te and Ge mole fraction, respectively. A detailed analysis by diffraction contrast experiments and image simulation on n-type and p-type Bi_2Te_3 bulk materials yielded a pure structural modulation, i.e., a displacive modulation with a wavelength of 10 nm and an amplitude of about 10 pm, as the origin of the nns [63].

Te-depletion in thin layers

With inserted stray aperture in specimen regions thinner than 0.4 mfp both, n-type and p-type Bi_2Te_3, showed a relative Te-depletion of more than 10% (Table 4.4, Fig. 4.7(a)). No correlations were found between Se and Te and between Bi and Sb, respectively (Fig. 4.8). Te-depletion is about one order of magnitude larger than the statistical error of the measurement of $\sigma_N/N = 1.4\%$. It is known that in n-type and in p-type Bi_2Te_3 materials Te is depleted at surfaces [22] and the results might be explained by a Te-depletion layer on surfaces (Fig. 4.7(b)). In thin specimen regions this Te-depletion layer yields a larger fraction of the volume analysed by EDX. Therefore, Te-depletion is strongest in thin specimen regions and less significant in thicker regions.
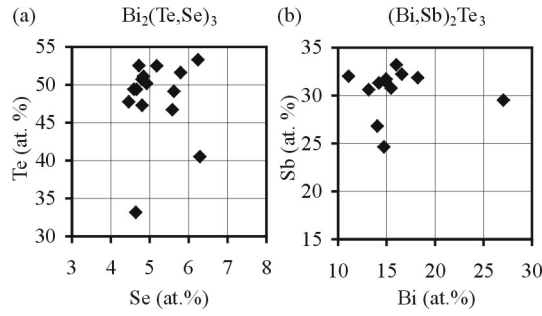
Figure 4.8 Se-Te and Sb-Bi correlation diagrams obtained in thin regions ($< 0.4\,\mathrm{mfp}$) of (a) n-type $Bi_2(Te, Se)_3$ and (b) p-type $(Bi, Sb)_2 Te_3$. The stray aperture was inserted.

Table 4.4 Mole fractions obtained in thin regions ($< 0.4\,\mathrm{mfp}$) of (a) n-type $Bi_2(Te, Se)_3$ and (b) p-type $(Bi, Sb)_2 Te_3$. The stray aperture was inserted.

	$Bi_2(Te, Se)_3$			$(Bi, Sb)_2 Te_3$		
	Bi	Te	Se	Bi	Sb	Te
c (at. %)	46.5	48.4	5.1	15.9	30.5	53.6
σ_c (at. %)	5.3	5.2	0.6	3.9	2.5	4.6
σ_c/c (%)	11.4	10.8	11.8	24.8	8.1	8.5

The TEM samples investigated here were freshly prepared, so Te-depletion is a fast process and was completed when sample preparation, i.e., ion milling, was finished. EDX measurements in the TEM on epitaxially grown thin films and superlattices yielded no Te-depletion in thin specimen regions [35, 36, 57]. Therefore, Te-depletion is not a general character of $Bi_2 Te_3$ materials but only appeared in bulk samples prepared as thin foils. However, Te-depletion has to be checked and considered if present. Quantitative chemical analysis by EDX in the TEM could only be performed in specimen regions thicker than $0.4\,\mathrm{mfp}$ (Fig. 4.7). Further, the application of high-resolution TEM analysis is restricted since it is performed on thin specimen regions. Finally, Te-depletion could be a limiting factor when going from bulk materials to nanostructures, since the thermoelectric figure of merit sensitively depends on the chemical composition.

Thin films and superlattices

EPMA combined with EDX in the TEM on p-type and n-type $Bi_2 Te_3$ bulk materials served for a recalibration of the Cliff-Lorimer k factors. Particularly, the k factor of the Bi $L_{\alpha1}$ line was too large by 30% (Table 3.2). These changes enabled direct EDX analysis in the TEM of $Bi_2 Te_3$ thin films and $Bi_2 Te_3/Bi_2(Te, Se)_3$ superlattices epitaxially grown on BaF_2 substrates [35, 36, 57].

The stray aperture also preserves the lateral resolution of the EDX measurements. With inserted stray aperture the acquired spectra only contain characteristic X-ray lines which were generated at the position of the electron probe but no additional counts generated by uncollimated electrons at other specimen regions. This was particularly import for the measurements, since thin film and substrate differ in composition but contain elements with X-ray lines at almost the same energy (Te $L_{\beta1}$ at $4.30\,\mathrm{keV}$, Ba $L_{\alpha1}$ at $4.47\,\mathrm{keV}$).

Figure 4.9 EDX results of a high-T_C superconductor $Bi_2Sr_2CaCu_2O_8$ (Bi-2212). (a) Hole-count spectra acquired (1) without and (2) with inserted stray aperture. Identical acquisition conditions were used for both spectra. (b) Ca-Cu correlation diagram obtained within an area of $1\,\mu m^2$ (black squares) and within an area larger than $100\,\mu m^2$ (grey diamond). The stray aperture was inserted.

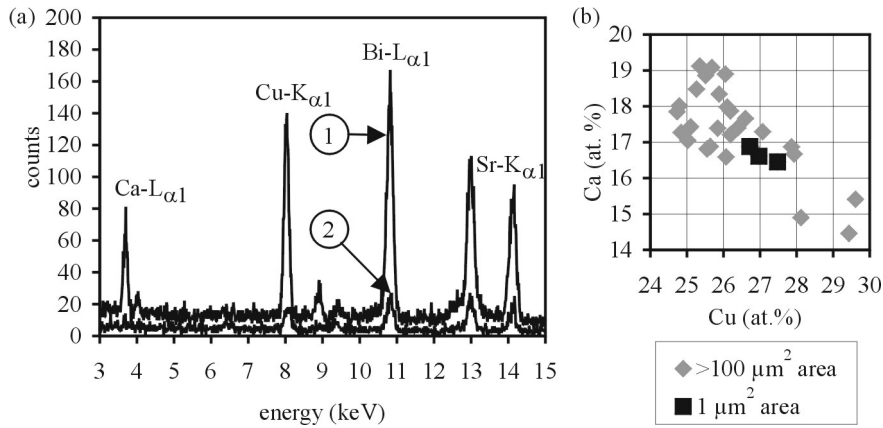**Table 4.5** Mole fractions obtained for Bi-2212 within an area of $1\,\mu m^2$ and an area larger than $100\,\mu m^2$. The stray aperture was inserted.

	Area $< 1\,\mu m^2$				Area $> 100\,\mu m^2$			
	Ca	Cu	Sr	Bi	Ca	Cu	Sr	Bi
c (at. %)	16.6	27.1	23.7	32.6	17.3	26.4	24.7	31.6
σ_c (at. %)	0.2	0.4	0.2	0.2	1.1	1.3	1.2	1.2
σ_c/c (%)	1.3	1.4	0.9	0.6	6.5	4.8	4.9	3.9

4.3.2   Elimination of uncollimated electrons

EDX spectra of powder particles mounted on 200-mesh Cu-grids yielded Cu $K_{\alpha 1}$ spurious X-ray peaks (Fig. 4.10). Therefore, the stray radiation hits the TEM sample at least $50\,\mu m$ away from the electron probe, particularly in the non electron transparent outer parts of the TEM sample. With respect to Bi_2Te_3, hole-count spectra and spectra obtained in these non electron transparent regions were almost identical (Fig. 4.2). Therefore, uncollimated electrons are the reason for the observed spurious X-rays in the hole-count spectra. In Bi_2Te_3, the relatively large Bi $L_{\alpha 1}$ peak in the hole-count is due to a stronger absorption of the lower energy Te $L_{\alpha 1}$ line in non electron transparent specimen regions.

The small Mo $K_{\alpha 1}$/Mo $L_{\alpha 1}$ count ratio of 4.3 obtained without stray aperture on a hole of a mesh of the NiO test specimen indicates uncollimated electrons as the predominant origin of column radiation. With inserted stray aperture the Mo $K_{\alpha 1}$ spurious X-rays were drastically reduced by a factor of 8.7. Therefore, the stray aperture absorbs the uncollimated electrons. The remaining Mo spurious X-ray peaks are due to stray X-rays, since the Mo $K_{\alpha 1}$/Mo $L_{\alpha 1}$ count ratio increased to about 40 which is a typical value for this type of column radiation [74, 75].

The Ni $K_{\alpha 1}$/Mo $K_{\alpha 1}$ film-count ratios were found to be 3 without and 6.6 with inserted stray aperture (Table 4.1). Typical analytical microscopes showed values lying in a range between 3 and 10 [75]. Therefore, on the basis of the Ni $K_{\alpha 1}$/Mo $K_{\alpha 1}$ film-count ratios, it is not clear whether the improvement of the performance is good enough for Bi-based systems.

Bi_2Te_3 and Bi-2212, both systems contain Bi and are particularly susceptible to stray radiation. For these materials the Bi $L_{\alpha 1}$ hole-count ratio is significant and was used as performance figure for column radiation. For a quantitative chemical analysis the intensity of the Bi $L_{\alpha 1}$ hole-count should be less than 1% of the value measured at a thin specimen region, i.e., the
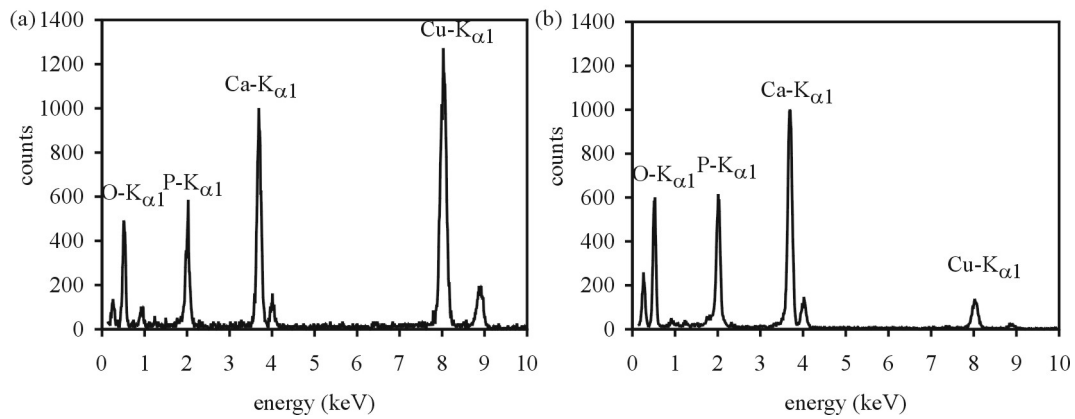
Figure 4.10 EDX-Spectra of hydroxyapatite $Ca_{10}(PO_4)_6OH_2$ acquired (a) without and (b) with inserted stray aperture.

Bi $L_{\alpha 1}$ hole-count ratio should be larger than 100. For Bi-2212 the Bi $L_{\alpha 1}$ hole-count ratio was larger than 100 (Table 4.1). For Bi_2Te_3 the Bi $L_{\alpha 1}$ hole-count ratio could only be increased to 42 (Table 4.1). In specimen regions thicker than 0.4 mfp, i.e., at distances larger than 200 nm away from the edge (Fig. 4.7), the Bi $L_{\alpha 1}$ hole-count ratio increases to values larger than 100. In summary, the stray aperture allows high-accuracy quantitative EDX analysis independent of sample preparation, since the artifact could be reduced significantly also for dimpled TEM samples and Cu-grids (Table 4.1).

In conclusion, the hole-count artifact in a Zeiss 912Ω TEM could be drastically reduced by introducing a stray aperture. With the stray aperture inserted a high-accuracy EDX analysis in the TEM combined with a sub-micrometer lateral resolution is available. These improvements combined with an ultrathin detector window and a digital pulse processor enables a quantitative chemical analysis on samples with elements distributed over a wide range in the periodic table.

Chapter 5

Bulk: Structural modulations (nns)

5.1 Results

5.1.1 Texture and gliding dislocations

The quantitative chemical analysis by EPMA yielded variations in stoichiometry in n-type and p-type samples [33]. The p-type samples showed a substitution of Sb for Bi with a variation in stoichiometry of about $1 - 1.5$ at. %. The same behaviour was found for Se and Te in n-type material [33]. EDX measurements in the TEM yielded a variation in stoichiometry of about $0.5 - 1$ at. % on the submicrometer scale and of about 2 at. % in areas larger than $100 \, \mu m^2$ [60, 61].

The lattice parameters were measured by X-ray diffraction (XRD) [22] and by analysis of the TEM diffraction patterns (Table 5.1). All samples showed a strong texture and grain sizes between $1 \, \mu m$ and $10 \, \mu m$ divided by small-angle grain boundaries. Investigations on n-type and p-type samples yielded dislocation densities of about 10^9 cm^{-2} [33]. These dislocations showed a high mobility of $10 - 100$ nm/s when the sample was heated by an electron beam with a large illumination angle. The gliding dislocations were analysed in detail in p-type materials and results will be reported elsewhere [81]. Stereomicroscopy investigations yielded edge dislocations with Burgers vector $[1, 1, 0]$ and the basal plane being the glide plane [81].

5.1.2 N-type sample with one nns

In sample N3, a structural modulation [natural nanostructure (nns)] was imaged with the sample close to the $[5, -5, 1]$ orientation (Fig. 5.1(a)), which is at an intermediate projection between the a and the c axis. A sinusoidal strain contrast appeared in two-beam cases with strongly excited $(-1, 0, 5)$ reflection (Fig. 5.2(a)) and disappeared with strongly excited $(0, 1, 5)$ reflection (Fig. 5.2(b)). The fringes showed a wavelength of about 10 nm (Fig. 5.2(a)) and a wave vector parallel to $(1, 0, 10)$ (Fig. 5.1(b)). Line scans obtained from images of the nns and a $Bi_2Te_3/Bi_2(Te_{0.88}Se_{0.12})_3$ superlattice [artificial nanostructure (ans)] [36] with a period of 12 nm are shown in Figure 5.3(a). The intensity profile of the ans is of almost perfect sinusoidal shape, whereas the intensity profile of the nns is irregularly sinusoidal with alternating amplitude and wavelength. The nns yielded a diffraction contrast $(I_{max} - I_{min})/(I_{max} + I_{min})$ of about 25%, where I is the intensity. The Fourier transformed images (FT) of the two-beam images of the nns and the ans are shown in Figures 5.3(b) and 5.3(c), respectively. The FT of the nns only shows first order reflections with a full width at half maximum (FWHM) of 0.03 1/nm (Fig. 5.3(b)), whereas the FT of the ans also yields third order reflections with a FWHM of 0.01 1/nm (Fig. 5.3(c)).

Table 5.1 Lattice parameters of Bi_2Te_3 bulk materials measured by X-ray diffraction (XRD) and transmission electron microscopy (TEM).

Method	a (nm)	c (nm)
	Bi_2Te_3 [a]	
XRD [a]	0.43835	3.0487
	$Bi_2(Te_{0.91}Se_{0.09})_3$ (samples N3, N4, and N5)	
XRD [b]	0.4366	3.0774
TEM [c]	0.436 ± 0.004	3.05 ± 0.02
	$(Bi_{0.26}Sb_{0.74})_{1.98}(Te_{0.99}Se_{0.01})_{3.02}$ (sample P3)	
XRD [b]	0.4254	3.0597
TEM [c]	0.430 ± 0.004	3.05 ± 0.01

[a]Ref. [17]. [b]Ref. [22]. [c]This work.

Dislocations were found and analysed in structurally modulated Bi_2Te_3. Dislocations marked by arrows can be seen in Figure 5.2(b), where the nns is out of contrast. The nns shows no bending due to dislocations (Fig. 5.2(a)). These dislocations showed a high mobility when the sample was heated by an focused electron beam and moved with a velocity of about 100 nm/s. The gliding dislocations are bowed out in the direction of motion and are pinned at the surfaces (Fig. 5.2(b)).

5.1.3 *N*-type sample with two superimposed nns

In sample N4, the analysed grain was initially in a $[5, -5, 1]$ orientation. A nns with a wavelength of 10 ± 2 nm could be imaged with strongly excited $(-1, 0, 5)$ reflection (Fig. 5.4(a)), which is referred to as nns(1) (Table 5.2). The same specimen region was imaged with a strongly excited $(0, 1, 5)$ reflection (Fig. 5.4(b)). The nns(1) is out of contrast and a second structural modulation appeared with a wavelength of 11 ± 3 nm, which is referred to as nns(2) (Table 5.2). The fringes of nns(2) are not as straight as the fringes of nns(1) (Fig. 5.4(a) and 5.4(b)). The superposition of both structural modulations is shown in Figures 5.4(c) and 5.4(d).

Stereomicroscopy was then applied to analyse both structural modulations in more detail. The sample was tilted towards an orientation parallel to the a axis and towards an orientation closer to the c axis, i.e., towards the $[0, -1, 0]$ and $[-5, -10, 2]$ poles (Fig. 5.1(b) and 5.1(c)). Both nanostructures, nns(1) and nns(2), were imaged at various tilt angles under $(-1, 0, 5)$ and $(0, 1, 5)$ two-beam conditions, respectively. The wavelengths of both nns showed no strong dependence on the relative tilt angle, e.g., the relative tilt angle between the images Fig. 5.4(a) and 5.4(c) and between Fig. 5.4(b) and 5.4(c) were $34°$ and $47°$, respectively. This indicates that the nns is a three-dimensional rather than a two-dimensional crystal defect. In a first approximation the displacement field of the nns can be understood as $\mathbf{u}(\mathbf{r}) = \mathbf{u}_0 \, sin(\mathbf{q} \cdot \mathbf{r})$, where $\mathbf{q}$ is the wave vector and $\mathbf{u}_0$ is the direction of the displacement vector. Two-beam images with other reflections were also acquired. Particularly, those reflections are of interest for which the nns is out of contrast since they allow one to determine the direction of the displacement field (Table 5.2). The wavelengths and directions of the wave vectors and the direction of the displacement vectors of nns(1) and nns(2) are summarised in Table 5.2.

5.1.4 *N*-type sample without a nns

In sample N5, no nns was found at all. This sample was initially in a $[5, -5, 1]$ orientation and was then tilted in a $[-10, -5, 1]$ orientation. These two poles contain all three equivalent $\{-1, 0, 5\}$ reflections, i.e., $(-1, 0, 5)$, $(0, 1, 5)$, and $(-1, 1, 5)$. Two-beam images were acquired with each of these three reflections, but no fringe contrast appeared. The analyses of 10 TEM samples yielded a frequency of observation of 50% for none or one nns. Only in sample N4 were two superimposed nns found.
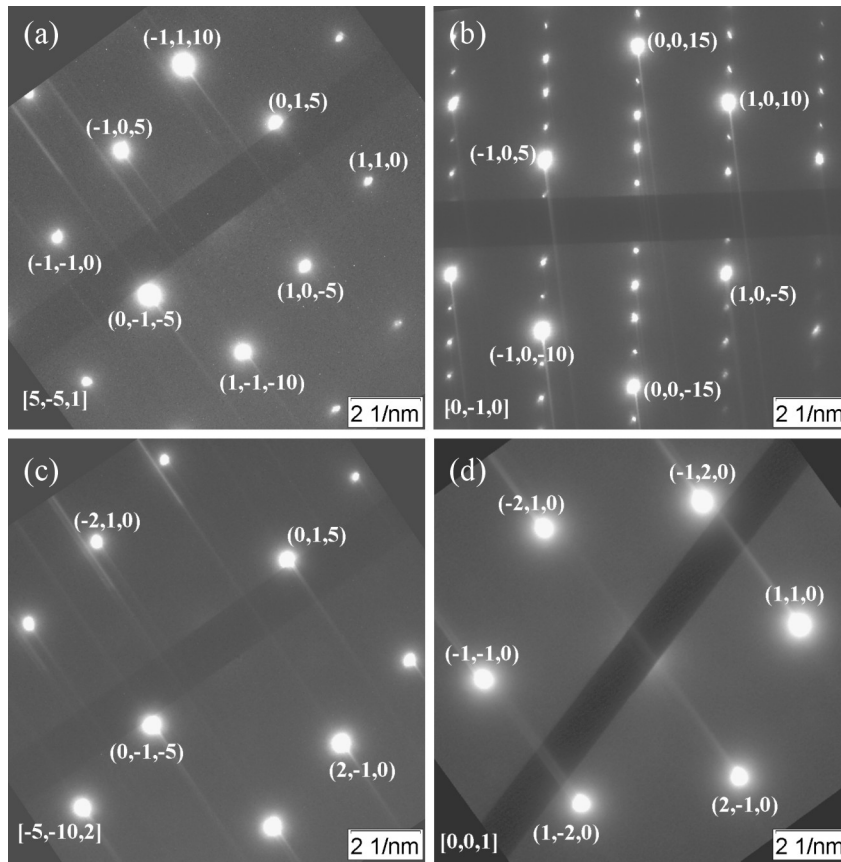
Figure 5.1 TEM diffraction patterns obtained in Bi_2Te_3 in the orientations (a) $[5, -5, 1]$, (b) $[0, -1, 0]$, (c) $[-5, -10, 2]$, and (d) $[0, 0, 1]$.
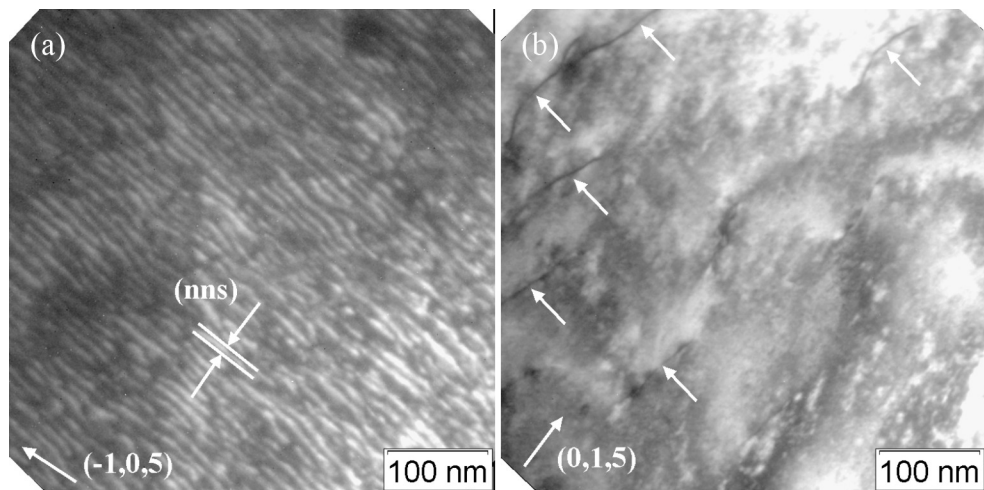
Figure 5.2 Two beam images of an area of sample N3. (a) $(-1, 0, 5)$ dark field image for imaging a nns. (b) $(0, 1, 5)$ bright field image, the nns is out of contrast and single dislocations (arrows) started to glide when the sample was heated by an focused electron beam. The dislocation are bowed out in the direction of motion.
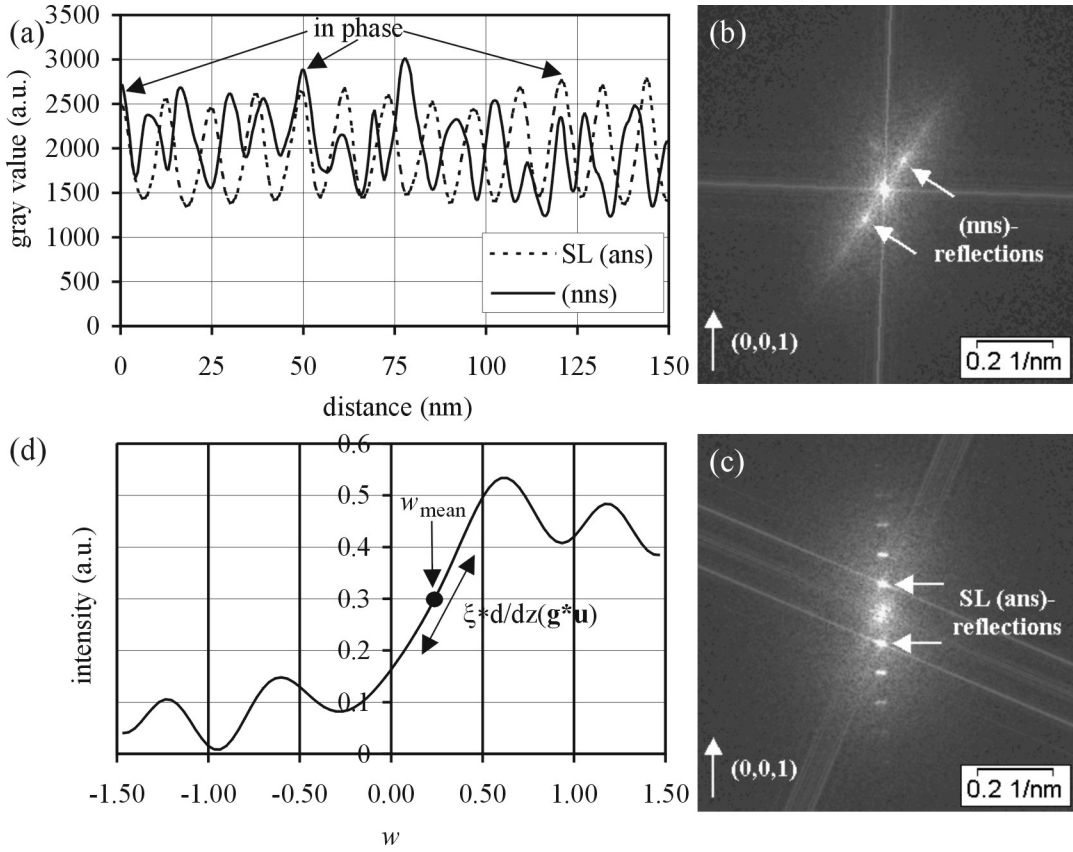
Figure 5.3 (a) Intensity profiles obtained from a dark field image of the nns and a bright field image of a $Bi_2Te_3/Bi_2(Te_{0.88}Se_{0.12})_3$ superlattice (SL) with a period of 12 nm. (b) FT of an image of a nns and (c) FT of an image of a 12 nm SL (ans). (d) Intensity of a direct electron beam in dependence of the dimensionless excitation error $w = s \cdot \xi_{\mathbf{g}}$.

5.1.5 P-type sample with one nns

In sample P3 a nns with a wavelength of 15 ± 4 nm was found. As usual, two-beam images were primarily acquired with the sample close to the $[5, -5, 1]$ orientation. In contradiction to sample N4, the nns is out of contrast under $\mathbf{g} = (-1, 0, 5)$ two-beam condition (Fig. 5.5(a)) and shows strong contrast for $\mathbf{g} = (0, 1, 5)$ (Fig. 5.5(b)). Stereomicroscopy yielded the same displacement vector and wave vector as for nns(2) in sample N4 (Table 5.2). The dislocations visible in Figure 5.5(a) were found to be in the basal plane.

The specimen region shown in Figures 5.5(a) and 5.5(b) was then tilted to orientations parallel to the c axis and parallel to the basal plane, i.e., parallel to $[0, 0, 1]$ and $[1, -1, 0]$. The wavelength of the nns showed no strong dependence on the relative tilt angle. The analysis of the nns in an orientation parallel to the c axis is particularly important since the number of nns can be directly determined. For this, in this orientation two-beam images and weak beam dark-field images were acquired using all three equivalent $\{1, 1, 0\}$ reflections, i.e., $(1, 1, 0)$, $(-2, 1, 0)$ and $(-1, 2, 0)$ (Fig. 5.1(d)).

The nns could be imaged under a $\mathbf{g} = (1, 1, 0)$ two-beam condition (Fig. 5.5(c)) and was out of contrast for $\mathbf{g} = (-2, 1, 0)$ (Fig. 5.5(d)). Finally, $(1, -2, 0)$ $\mathbf{g}/3\mathbf{g}$ weak beam dark-field images were acquired at a lower (Fig. 5.5(e)) and a higher magnification (Fig. 5.5(f)). For this imaging condition two superimposed fringe contrast patterns were observed. The fringes running in diagonal direction are due to the nns. The horizontal fringes are a new observation and showed a wavelength of 9 ± 3 nm. These horizontally orientated fringes were not regarded

as a second nns superimposed to the structure, since they could only be imaged (i) in certain orientations such as $[0, 0, 1]$ and $[1, -1, 0]$ and (ii) by using the weak beam technique instead of two-beam conditions. The stereomicroscopy results indicate that for the displacement field of the nns a second wave vector has to be considered. In summary, the analysis of the sample P3 in $[0, 0, 1]$ orientation yielded only one nns.

5.1.6 Formation, stability, and long-range order of the nns

Originally, sample P3 was a sample without a nns. However, after additional ion etching a nns was present in the entire sample. Further experiments were carried out to analyse the stability of the nns in sample P3. The structural modulation showed no changes due to electron beam induced heating, even for a focused electron beam with a spot size of $100\,\mathrm{nm}$ and after a time of $15\,\mathrm{min}$. Also, the nns showed no changes after in situ cooling with liquid nitrogen. Finally, the sample was reanalysed after 5 months, the nns was still present and showed identical properties. Our results indicate that Bi_2Te_3 exhibits properties of a phase change material. The nns can be switched on and off reversibly depending on the thermal history of the sample.

For all samples, the structural modulations showed a uniform character in the entire sample: (i) The nns is extended over the entire grain and (ii) could be observed in all sections of the sample. (iii) The nns showed the same displacement vector and wave vector in adjacent grains and in grains several $100\,\mu\mathrm{m}$ apart from each other.

5.2 Discussion

5.2.1 Imaging by diffraction contrast and general character of the nns

A structural modulation (nns) was found in n-type $Bi_2(Te_{0.91}Se_{0.09})_3$ and p-type $(Bi_{0.26}Sb_{0.74})_{1.98}(Te_{0.99}Se_{0.01})_{3.02}$ bulk materials synthesised by the Bridgman technique [34] and in epitaxially grown n-type Bi_2Te_3 thin films and in $Bi_2Te_3/Bi_2(Te_{0.88}Se_{0.12})_3$ superlattices [35, 36, 57]. The nns is of general character for Bi_2Te_3 materials, since in all these materials the wavelength was found to be $10\,\mathrm{nm}$ and the wave vector parallel to $\{1, 0, 10\}$. The nns showed no bending due to dislocations, superlattices, or a second nns in the sample. Therefore, the nns is perfectly superimposed to the average structure and is structurally very stable.

The nns can be imaged by diffraction contrast, the contrast is due to the sinusoidal strain field of the nns. Under $\{-1, 0, 5\}$ two-beam conditions strong contrast is observed and the nns is out of contrast for reflections perpendicular to $\{-1, 0, 5\}$ (Table 5.2, Fig. 5.1). The contrast can be explained by the two-beam dynamical diffraction theory of electron diffraction (Ref. [42, chap. 13] and [55]) and the Howie-Whelan equations will be applied to simulate the contrast for a crystal with a displacement field considering anomalous absorption. The intensity of the direct beam at the exit surface was calculated for a perfect Bi_2Te_3 crystal in dependence of the dimensionless excitation error w and is shown in Figure 5.3(d) ($\mathbf{g} = \{-1, 0, 5\}$, extinction distance $\xi_{\mathbf{g}} = 33.4\,\mathrm{nm}$, anomalous absorption coefficient A $= 0.1$, specimen thickness $85\,\mathrm{nm}$). The imaging conditions used for the analysis of the nns and for standard analysis of dislocations was identical, i.e., two-beam conditions with $w \approx 0.2-0.3$ in bright field and $w = 0$ in dark field. It is well known that for these imaging conditions the contrast changes sensitively if bending of the lattice planes occurs. The strain field of the structural modulation yields local variations of the dimensionless excitation error w through the product $\xi_{\mathbf{g}} \cdot \frac{\partial}{\partial z}(\mathbf{g} \cdot \mathbf{u})$ [56] (Fig. 5.3(d)), $\mathbf{u}$ being the displacement field of the nns.
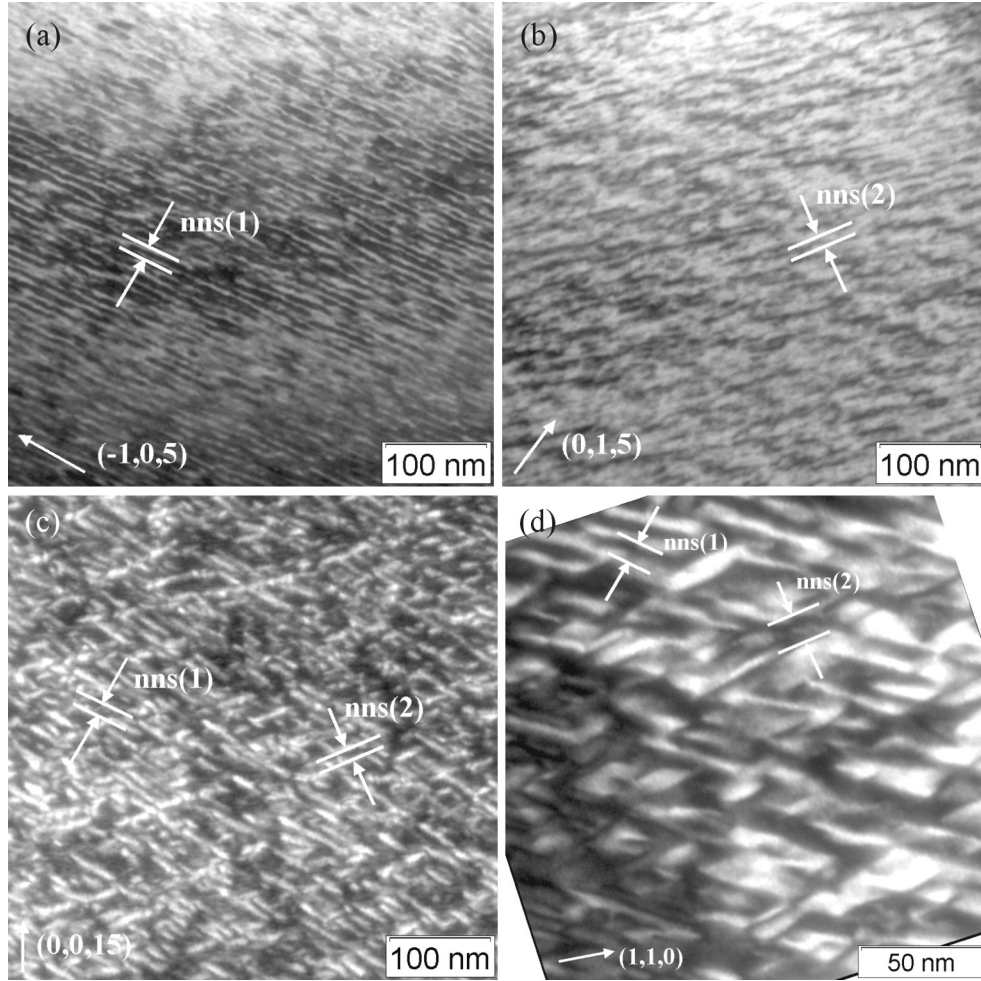
Figure 5.4 Two-beam images acquired of an area of sample N4, showing the superposition of two structural modulations, nns(1) and nns(2): (a) $(-1, 0, 5)$ bright field image, (b) $(0, 1, 5)$ bright field image, (c) $(0, 0, 15)$ dark field image, and (d) $(1, 1, 0)$ bright field image.

Table 5.2 Wavelengths λ, direction of the wave vectors $\mathbf{q}$, and direction of the displacement vectors $\mathbf{u}_0$ of the nns observed in sample N4 and sample P3 according to sinusoidal model $\mathbf{u}(\mathbf{r}) = \mathbf{u}_0 \sin(\mathbf{q} \cdot \mathbf{r})$ for its displacement field. The displacement vector $\mathbf{u}_0$ was calculated according $\mathbf{g} \cdot \mathbf{u}_0 = 0$ for the displacement field being out of contrast.

	λ	$\mathbf{q}$	nns out of contrast for reflection $\mathbf{g}$?				$\mathbf{u}_0$
	(nm)		$(-1, 0, 5)$	$(0, 1, 5)$	$(1, 0, 10)$	$(0, -1, 10)$	
nns(1) in sample N4	10 ± 2	$(1, 0, 10)$ [a]	No	Yes	Yes	No	$[-10, -5, 1]$
nns(2) in sample N4	11 ± 3	$(0, -1, 10)$ [b]	Yes	No	No	Yes	$[5, 10, 1]$
nns in sample P3	15 ± 4	$(0, -1, 10)$ [c]	Yes	No	No	Yes	$[5, 10, 1]$

[a] $\mathbf{q} = (1, 0, 10)$, [b] $\mathbf{q} = (3, -4, 25)$, and [c] $\mathbf{q} = (-1, 0, 5)$ determined by image simulation.
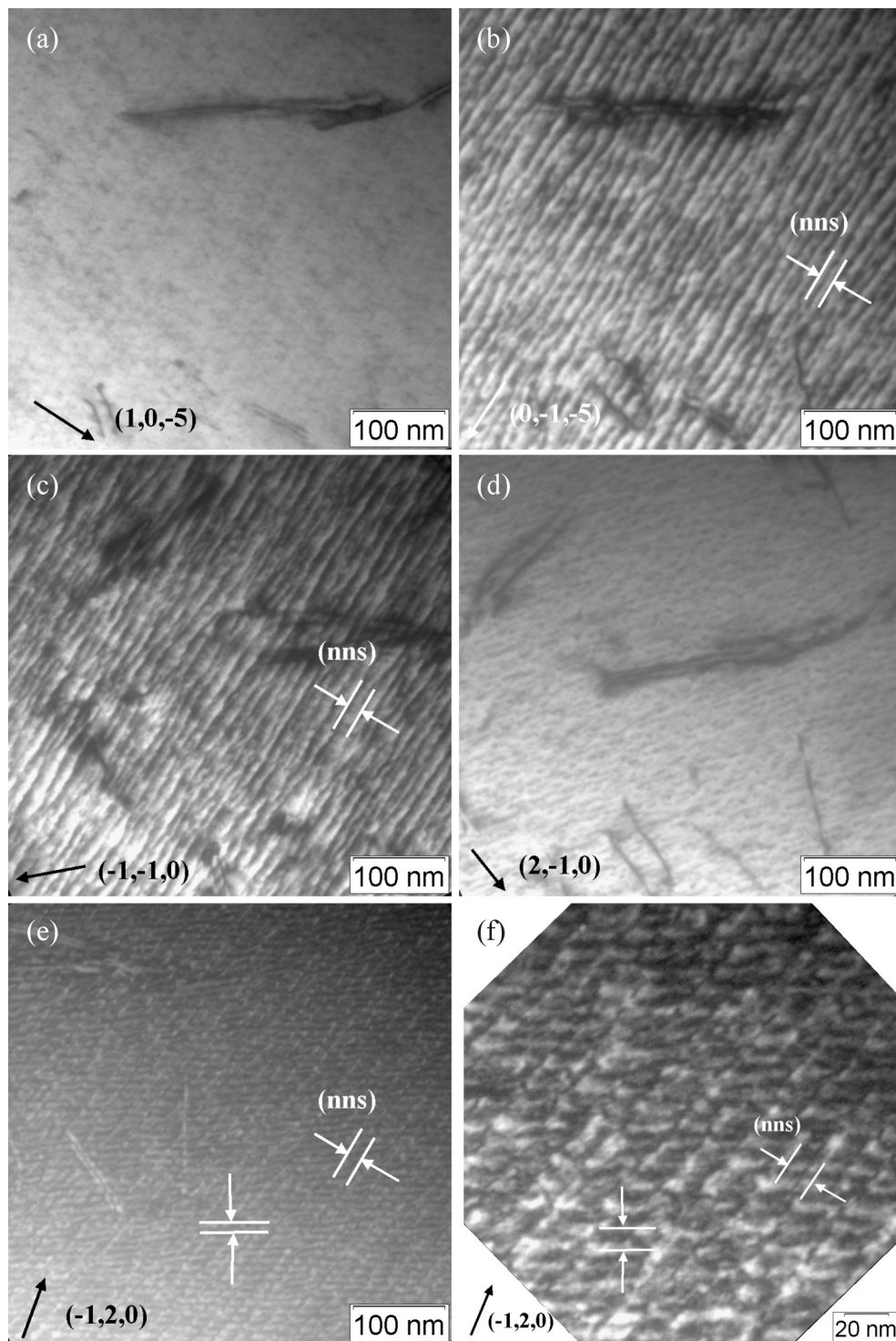
Figure 5.5 Two-beam images of an area of sample P3 in orientations (a) - (b) close to $[5, -5, 1]$ and (c)-(f) close to the c axis:. (a) $(1, 0, -5)$ bright field image. The nns is out of contrast. (b) $(0, 1, 5)$ dark field image for imaging a nns. (c) $(-1, -1, 0)$ dark field image with diffraction contrast. (d) $(2, -1, 0)$ bright field image, the nns is out of contrast. (e) and (f): $(-1, 2, 0)$ **g**/3**g** weak beam dark-field images showing a superposition of two fringe contrast patterns.

5.2.2   Model for the nns

The origin of the sinusoidal strain field of the nns could be due to (i) a pure displacive modulation related to a thermodynamic structural instability, (ii) a chemical modulation, or (iii) an ordered network of dislocations a few nanometers apart. These three models will be discussed.

The intensity profile of the nns is of approximately sinusoidal shape (Fig. 5.3(a)). Therefore, the displacement field $\mathbf{u}(\mathbf{x})$ and thereby the strain field of the nns should also be of approximately of sinusoidal shape. A simplified model for the displacement field is $\mathbf{u}(\mathbf{x}) = \mathbf{u}_0 \sin(\mathbf{q} \cdot \mathbf{x} + \phi)$, $\mathbf{u}_0$ being the displacement vector, $\mathbf{q}$ being the wave vector, and ϕ being the phase of the modulation (Fig. 5.6(a)). The wavelength and the direction of the wave vector can be determined from the fringe spacing in the two-beam images and from the diffraction patterns, respectively. The direction of the displacement vector $\mathbf{u}_0$ was calculated according to the $\mathbf{g} \cdot \mathbf{u} = 0$ criterion for displacement fields being out of contrast, values are given in Table 5.2. As an example, in Figure 5.4 nns(1) was out of contrast for the reflections $\mathbf{g}_1 = (1, 0, 10)$ and $\mathbf{g}_2 = (0, 1, 5)$ and the direction of the displacement vector $\mathbf{u}_0$ was calculated as $\mathbf{g}_1 \times \mathbf{g}_2 = [-10, -5, 1]$ (Table 5.2). In general, the displacement vector was found to be parallel to $\langle 5, -5, 1 \rangle$ (Table 5.2), the wave vector parallel to $\{1, 0, 10\}$ (Table 5.2), and the wave vectors being perpendicular to the displacement vectors. Therefore, the nns might be regarded as a frozen transverse phonon mode.

For determining the amplitude of the displacement field of the nns it was assumed to be given by $\mathbf{u}(\mathbf{x}) = \mathbf{u}_0 \sin(\mathbf{q} \cdot \mathbf{x})$. Without image simulation, an amplitude of $|\mathbf{u}_0| \approx 2\,\mathrm{pm}$ was estimated as follows: The intensity of the direct beam is about 0.3 for an excitation error $w \approx 0.2 - 0.3$ (Fig. 5.3(d)). The local excitation error w is altered by ± 0.1 through the product $\xi_{\mathbf{g}} \cdot \frac{\partial}{\partial z}(\mathbf{g} \cdot \mathbf{u})$, which has a maximum of $\frac{2\pi}{\lambda} \xi_{\mathbf{g}} \, \mathbf{g} \cdot \mathbf{u}_0$, λ being the wavelength of the nns. Therefore, the intensity of the direct beam varies between 0.2 and 0.4 (Fig. 5.3(d)). This corresponds to a diffraction contrast of 33%, which is close to the value of 25% determined by line scans of the nns (Fig. 5.3(a)). A detailed analysis by image simulation yielded higher amplitudes of about $10 - 20\,\mathrm{pm}$ and refined values for the wave vectors (Table 5.2). Electron diffraction on thicker samples yields an averaging of the displacement field, i.e., only a larger amplitude of the displacement field could explain the observed contrast. Finally, the image simulations also showed only small variations of the fringe spacing in dependence of the tilt angle, which is in agreement with the experimental findings. This was surprising bat can also be explained as an averaging effect of the electron diffraction.

The simple sinusoidal model for the displacement field is helpful but is oversimplifying the displacement field for three reasons: (i) The line scans obtained on images of the nns yielded intensity profiles only approximately of sinusoidal shape (Fig. 5.3(a)). (ii) The FT of the nns yielded reflections which are smeared out (Fig. 5.3(b)), higher order reflections did not appear in the FT (Fig. 5.3(c)). (iii) In sample P3 only one nns was found. However, in orientations parallel to the c axis (Fig. 5.5(e) and 5.5(f)) or parallel to the basal plane a superposition of two fringe contrast patterns was observed.

The FT of two-beam images of the nns indicate a spectrum of wave vectors rather than a defined wave vector. The model of a sinusoidal displacement field can be extended by introducing local changes (i) of the phase ϕ, (ii) of the wavelength, and (iii) the direction of the wave vector. Furthermore, the analysis of sample P3 gives strong evidence for the presence of a second wave vector with a wavelength of approximately $10\,\mathrm{nm}$ (Fig. 5.5(e) and 5.5(f)). The second fringe contrast pattern could be best imaged by weak beam dark-field images. This indicates a smaller amplitude of the displacement field along the second wave vector.

Chemical modulations as the origin of the nns can be ruled out on the basis of our experimental findings for several reasons: (i) The nns was found in epitaxially grown pure Bi_2Te_3 thin films [36, 57]. Therefore, alloying and subsequent precipitation alone cannot be the origin of the nns. (ii) The nns was also found in n-type Se alloyed and p-type Sb alloyed bulk materials. The EDX measurements in the TEM on both type of bulk materials yielded smaller variations in stoichiometry on the submicrometer scale than on the micrometer scale [60, 61]. (iii) The crystallographic features, wave vector and displacement vector, of the nns were found to be independent of the chemical composition, i.e., the Se and Sb mole fractions. This is in
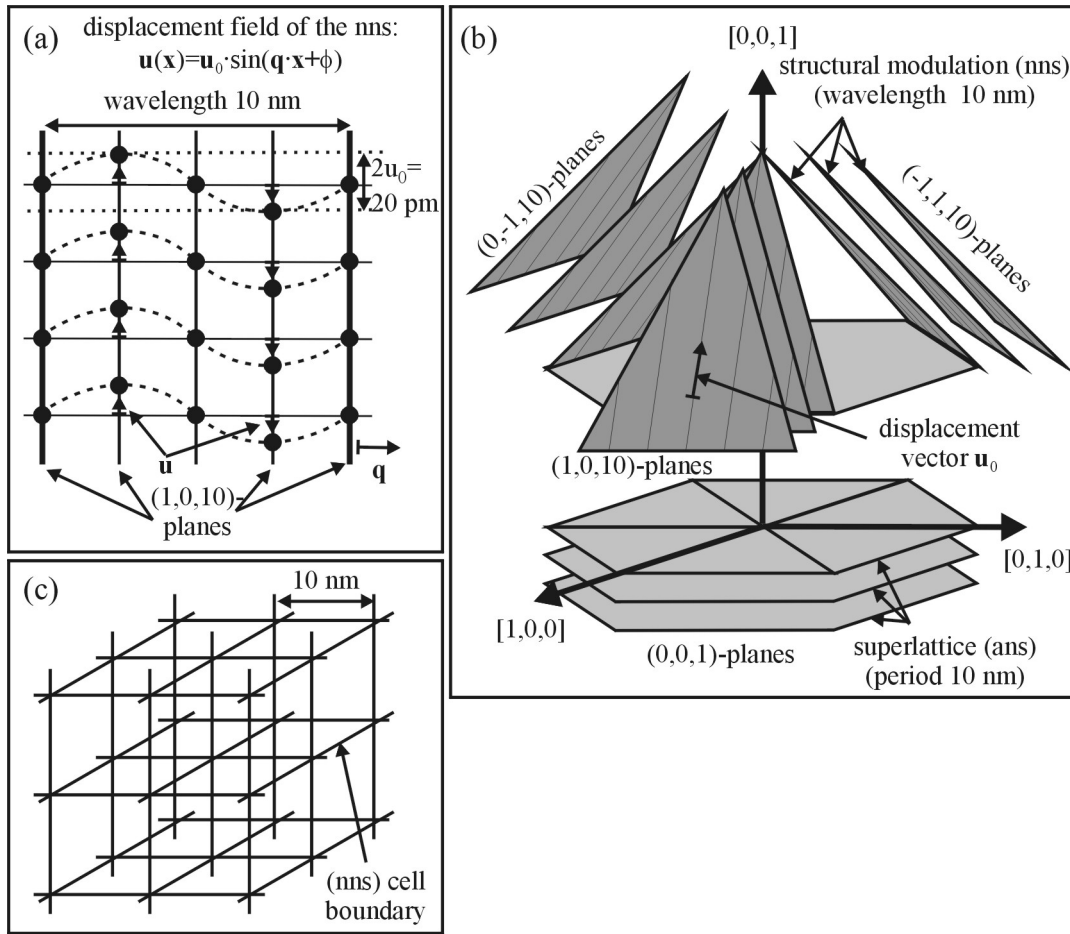
Figure 5.6 (a) Simplified structure model of the nns shown in cross section with viewing direction parallel to the $(1, 0, 10)$ planes. A sinusoidal displacement field is superimposed to the crystal structure. (b) Arrangement of the structural modulations (nns) and a superlattice structure (ans) in Bi_2Te_3 materials. (c) The superposition of three nns defines a $10\,nm \times 10\,nm \times 10\,nm$ unit cell in which phonons are localized.

contraction to natural nanostructures found in $AgPb_mSbTe_{2+m}$ bulk materials [28, 29] and $Bi_2Te_3Ge_x$ crystals [27]. In these materials the nns was related to compositional fluctuations on the nanometer scale since the direction and wave lengths of the wave vectors depended on the composition.

Finally, also an ordered network of dislocations a few nanometer apart as the origin of the displacement field can be ruled out for two reasons:

(i) Under the hypothesis of dislocations being the origin of the nns(1) and nns(2), their Burgers vectors and line directions were determined from the experimental data and were found to point out of the basal plane (Table 5.3). However, dislocations with Burgers vectors pointing out of the basal plane are energetically unfavourable for this highly anisotropic structure with a large lattice parameter c of $3.05\,nm$. Therefore, an ordered network of dislocations cannot be the reason for the observed sinusoidal strain field and the nns in general. The line energies for dislocations in the basal plane found by TEM in p-type Bi_2Te_3 bulk [81] were calculated according to Barnett and Lothe [46]. Line energies were also calculated for hypothetical dislocations forming the nns(1) and nns(2) in sample N4 and are summarised in (Table 5.3). The line energies for the dislocations of the nns would be 10 times larger compared to dislocations in the basal plane.

Table 5.3 Elastic line energies of dislocations in the basal plane observed in Bi_2Te_3 and of hypothetical dislocations forming nns(1) and nns(2) in sample N4. A dislocation distance of $10\,\mu m$ and a dislocation core radius equal to the lattice parameter a were assumed.

Network	Burgers vector **b**	Line direction **t**	Line energy (eV/nm)
Basal plane [a]	$[1, 1, 0]$	$[2.7, -1, 0]$	26
nns(1)	$1/3[-10, -5, 1]$	$[-9.9, -8.2, 1]$	310
nns(2)	$1/3[5, 10, 1]$	$[27.0, 23.9, 1]$	304

[a]Ref. [81].

Table 5.4 TEM results with respect to the observation of a nns in Bi_2Te_3 materials in dependence of the composition, structure, and growth technique.

Sample	Growth technique	nns observed ?	Reference
$Bi_2(Te_{0.91}Se_{0.09})_3$, bulk	Bridgman	Yes	This work
$(Bi_{0.26}Sb_{0.74})_{1.98}(Te_{0.99}Se_{0.01})_{3.02}$, bulk	Bridgman	Yes	This work
Bi_2Te_3, thin film	MBE	Yes	[36, 57]
$Bi_2Te_3/Bi_2(Te_{0.88}Se_{0.12})_3$ superlattice	MBE	Yes	[35, 36]
Bi_2Te_3, bulk	Bridgman	Yes	[27]
Bi_2Te_3/Sb_2Te_3 superlattice	MOCVD	No	[12]
Bi_2Te_3, bulk	Normal crystallization	No	[24]
Bi_2Te_3, bulk	Czochralski	No	[25]

(ii) In samples showing the characteristic contrast of the nns, individual dislocations were gliding in situ in the basal plane when the samples were heated by a focused electron beam (Fig. 5.2(b)). No pinning of these dislocations by the nns was observed. Since the fringe contrast of the nns is parallel to $\{1, 0, 10\}$, the dislocations generating the displacement field of the nns should lie in these planes. The basal plane and the $\{1, 0, 10\}$ planes intersect; therefore there should be a reaction between the gliding dislocations in the basal plane and the dislocations of the nns on the $\{1, 0, 10\}$ planes, gliding should be blocked by dislocation reactions. However, this was not observed.

Therefore, from all our experimental findings a pure displacive modulation was found to be the most appropriate model for the nns. Its formation will be discussed in the next section.

5.2.3 Formation of the nns

Our investigations showed the presence of nns in n-type and p-type bulk materials [34] and in epitaxially grown n-type thin films and superlattices [35, 36, 57]. There are several other TEM investigations on bulk materials [24–27] and on epitaxially grown Bi_2Te_3/Sb_2Te_3 superlattices [12] reported in the literature, but only one [27] also yielded a structural modulation. Since the nns yields easily recognisable diffraction contrast for almost any strongly excited reflections with $\mathbf{g} \cdot \mathbf{u} \neq 0$ it is assumed that in the samples reported in the literature the nns might not be present. Table 5.4 gives an overview about the presence of a nns for the various samples and their growth techniques studied in this paper.

Our results on bulk samples, thin films, and superlattices showed that the formation of the nns is independent of the composition, structure, and growth technique (Table 5.4). However, the frequency of observation of a nns in our samples was only 50%. In bulk materials, fairly large variations in stoichiometry on the micrometer scale were found [33]. Therefore, the formation of the nns could be bound to a certain stoichiometry range.

Another explanation could be that the formation of the nns depends on the thermal history of the samples. The formation of the nns could also be related to the ability of Te-compounds to form glasses. Therefore, they are widely used for rewritable phase-change optical recording applied in optical data storage systems like digital versatile disks (DVD) [82]. These phase-

changes were observed in situ by TEM induced by heating with the electron beam at an energy of 120 keV [83]. Recently, thermally induced reversible glass-crystal phase changes were also found in Bi_2Te_3-Sb_2Te_3 compounds [84]. Therefore, the formation of the nns probably is sensitive on the cooling rate. An indication for this assumption is the observation, that in sample P3 a nns appeared after additional ion milling. The electron diffraction patterns gave no indication for an amorphous state. However, the nns might be regarded as an intermediate state between pure crystalline and amorphous and its presence might be controlled by the thermal history of the sample.

The uniform structure of the nns, extending over the entire sample with the same orientation, possibly corresponds to a configuration of minimum energy. Measurements of the enthalpy of formation of the solid compound of Bi_2Te_3 yielded a large scatter of data in the literature with values of about $-6\,kJ/mol$, $-16\,kJ/mol$, and $-38\,kJ/mol$ [85]. These three different values probably correspond to the formation of none, one, and two nns.

5.2.4 Correlation between the nns and thermoelectric properties

The nns represents a significant structural disorder due to an amplitude of about $10\,pm$ of the displacement field and its wavelength of about $10\,nm$. Therefore, there should be a dominant contribution of phonon scattering on the strain field of the nns.

The nns is a volume effect and breaks the trigonal symmetry of the crystal. This might also affect the thermoelectric properties. In general, in Bi_2Te_3 materials the transport coefficients are anisotropic with respect to the c axis and the basal plane. The presence of a nns might break the isotropy in the basal plane. Measurements of the thermopower S, electrical conductivity σ, and thermal conductivity λ in three different directions might yield three different values. Such an effect was observed in $Bi_{0.5}Sb_{1.5}Te_3$ bulk materials doped with $2\,at.\%\,I$ [18]. The ratios of the transport coefficients at room temperature obtained by measurements in two perpendicular directions along the basal plane were found to be $S_{11}^{I}/S_{11}^{II} = 1.1$, $\sigma_{11}^{I}/\sigma_{11}^{II} = 4.7$, and $\lambda_{11}^{I}/\lambda_{11}^{II} = 0.9$.

In n-type and p-type superlattices (ans) [11–13, 38] the lattice thermal conductivity decreased most likely due to phonon scattering on SL interfaces. The superlattice layers were parallel to the basal plane (Fig. 5.6(b)). Phonon propagation is particularly suppressed in the direction perpendicular to the basal plane. The nns is superimposed to the average structure with wave vector parallel to $\{1, 0, 10\}$. Schematic drawings of (a) the nns in a cross-sectional view along the $\{1, 0, 10\}$ planes and (b) the orientation of the ans and nns in the crystal are shown in Figures 5.6(a) and 5.6(b). Phonons should be scattered on the strain field of the nns, particularly at directions perpendicular to the $\{1, 0, 10\}$ planes. Therefore, phonon transport should be two-dimensional, favourably parallel to the $\{1, 0, 10\}$ planes, if one nns is present. If there are two nns, phonon transport should be one-dimensional. Finally, the superposition of three structural modulations restricts phonon propagation to unit cells with a size of $10\,nm \times 10\,nm \times 10\,nm$, yielding a localization of the phonons (Fig. 5.6(c)).

For Bi_2Te_3 the lattice thermal conductivity on samples with a nns and without a nns might yield significant differences and could explain the scatter of data in the literature [86, 87]. Cubic $AgPb_mSbTe_{2+m}$ bulk materials also showed the presence of a nns, yielding a low lattice thermal conductivity, and a high thermoelectric figure of merit ZT [28, 29].

Chapter 6

Thin films and superlattices

6.1 Experimental

Bi_2Te_3 is a rhombohedral layered structure with three five-layer-groups with the sequence $Te^1 - Bi - Te^2 - Bi - Te^1$ and space group $R\bar{3}m$. The pseudo-hexagonal lattice parameters [17] are $a = 0.438$ nm and $c = 3.05$ nm (Table 6.1). Barium fluoride is a face centred cubic structure [88] with space group $Fm\bar{3}m$ and lattice parameter $a = 0.620$ nm (Table 6.1). The lattice mismatch between the $(1, 1, 1)$-planes of BaF_2 and the basal plane of Bi_2Te_3 is 0.045% at room temperature.

The investigated samples (Table 6.2) were Bi_2Te_3 thin films (samples TF01 and TF02) and $Bi_2Te_3/Bi_2(Te_{0.88}Se_{0.12})_3$ symmetric superlattices (SL) with periods of 12 nm (sample SL12) and 6 nm (sample SL06). The film thicknesses were $1\,\mu$m. The thin films and SL were epitaxially grown on single crystal $(1, 1, 1)$-BaF_2 substrates by molecular beam epitaxy (MBE) at substrate temperatures between 290 °C and 336 °C, a flux ratio $Bi/(Te + Se) = 5/12$, and a growth rate of about $0.4\,\mu$m/h [39, 40]. MBE growth of Bi_2Te_3 thin films was carried out in a custom built machine and a commercial one (EPI 930). The surface roughness was measured by reflection high-energy electron diffraction (RHEED) and by atomic force microscopy (AFM). The chemical composition was measured by energy dispersive X-ray spectrometry (EDX) in a scanning electron microscope (SEM) [39, 40]. X-ray diffraction (XRD) and high resolution XRD (HRXRD) were used for determination of the epitaxial relations, the lattice parameters, and the SL periods.

The in-plane transport coefficients were measured at room temperature [38]. The van der Pauw method was applied to measure the electrical conductivity, the carrier density, and carrier mobility. Thermopower was measured by conventional methods. The thermal conductivity was measured by a bridge method [89].

Table 6.1 Lattice parameters measured by XRD and TEM.

Sample	Method	a (nm)	c (nm)
Bulk materials			
Bi_2Te_3	XRD [a]	0.43835	3.0487
BaF_2	XRD [b]	0.61964	
Thin films and superlattices			
TF01 [c]	XRD [d]	0.4375 ± 0.0005	3.0554 ± 0.0005
TF01/TF02 [c]	TEM	0.437 ± 0.005	3.03 ± 0.04
SL12 [c]	TEM	0.437 ± 0.007	3.05 ± 0.02
SL06 [c]	TEM	0.444 ± 0.001	3.04 ± 0.01

[a]Ref. [17]. [b]Ref. [88]. [c]Table 6.2. [d]Ref. [39, 40].

Table 6.2 Structure, composition, and growth parameters of the epitaxially grown thin films and superlattices (SLs).

Sample	Composition	Substrate temperature ($^\circ$C)	Film thickness (nm)	SL period (nm)
		Thin films		
TF01	Bi_2Te_3	290	1000	
TF02	Bi_2Te_3	325	1000	
TF03	$Bi_2(Te_{0.94}Se_{0.06})_3$	290	1000	
TF01	Bi_2Te_3	290	180	
		Symmetric $Bi_2(Te_{1-x}Se_x)_3/Bi_2(Te_{1-y}Se_y)_3$-SL		
SL20	$x = 0/y = 0.12$	290	1000	20
SL12	$x = 0/y = 0.12$	336	1000	12
SL12/2	$x = 0.06/y = 0.12$	290	1000	12
SL10	$x = 0/y = 0.12$	290	1000	10
SL06	$x = 0/y = 0.12$	336	1000	6

Plan view samples and cross-sectional TEM samples were prepared. Specimen preparation was demanding due to (i) the brittleness of the BaF_2 substrate and (ii) the poor adhesion between the epitaxially grown films and the BaF_2 substrate. The standard procedure for TEM sample preparation had to be modified [57]. Because of the delamination of the film, film and substrate could be prepared only separately for TEM. The BaF_2 substrates were glued between Si and $BaTiO_3$ dummies. For the films we glued a Si dummy on top of the film and then removed the BaF_2 substrate completely. The conventional thinning procedure was applied to the $Si\|BaF_2\|BaTiO_3$ and $Bi_2Te_3\|Si$ composites. This includes mechanical grinding and polishing down to a thickness of $10 - 15\,\mu$m followed by Ar^+-ion milling in a Gatan Duo Mill® machine.

For a structural analysis at the different steps of the TEM sample preparation we used a scanning electron microscope JEOL-JSM-6500F-FEG operated at 25 kV. A Zeiss 912Ω TEM at 120 kV having a point resolution of 0.37 nm was used for the structural and chemical analysis. Two-beam images with strongly excited $(0,0,l)$ reflections and high-resolution images were acquired to study the superlattice [artificial nanostructure (ans)]. Dislocations were imaged under two-beam conditions by diffraction contrast in the TEM and image simulation was applied for analysing the contrast. The same imaging conditions were used for imaging a structural modulation [natural nanostructure (nns)], particularly useful are $\{-1,0,5\}$ reflections for this case [34, 57, 63]. The energy selecting aperture (ΔE $= 20$ eV) of the OMEGA filter was used to avoid background from inelastically scattered electrons.

The microscope is equipped with an EDX detector for chemical analysis with an energy resolution of 132 eV at the Mn K line. The acquisition time for EDX was 120 s and a spot size of 32 nm was used. The Cliff-Lorimer method [62] was applied for quantitative chemical analysis. The Cliff-Lorimer k factors were user defined such that the mean values of the mole fraction ratios of n-type $Bi_2(Te, Se)_3$ and p-type $(Bi, Sb)_2Te_3$ bulk materials measured by EDX in the TEM corresponded to measurements by electron probe microanalysis (EPMA) [33, 60]. The intensities of the Bi L and Te L lines were at least 20 000 counts to yield a minimum statistical error of 0.7%(Poisson statistics) for a quantitative analysis.

6.2 MBE growth and structural characterization

The RHEED measurements confirmed a layer-by-layer growth at substrate temperatures above $280\,^\circ$C. In Bi_2Te_3 thin films a Te mole fraction of 60 at. % was found by EDX in a SEM. The roughness of BaF_2 substrates and Bi_2Te_3 thin films with a film thickness of 180 nm was analysed by AFM in dependence of the substrate temperature. Freshly cleaved BaF_2 substrates showed monoatomic steps on the surface. Smooth Bi_2Te_3 surfaces were obtained at a substrate temper-

Table 6.3 Surface and layer roughnesses of Bi_2Te_3 thin films and superlattices (SLs) measured by AFM and TEM.

Sample	Film thickness (nm)	Method	Height (nm)	Width (nm)
TF04	180	AFM	9	1000
SL12	1000	TEM	30	400
SL06	1000	TEM	15	400

ature of $280\,°C$, whereas at $290\,°C$ triangular pyramidal structures appeared. The pyramidal structures were build up by layers with a step height of $1\,nm$, a total height of $9\,nm$, and a width of $1\,\mu m$ (Table 6.3). The XRD measurements (Fig. 6.1(a)) yielded that the $\{0,0,l\}$ planes and $\langle 1,0,0 \rangle$ directions of the Bi_2Te_3 thin films were parallel to the $\{1,1,1\}$ planes and $\langle 1,1,0 \rangle$ directions of the BaF_2 substrate. From the layer-by-layer growth and the orientation relationship between substrate and film it was concluded that the growth is epitaxial. Thin films and SL showed lattice parameters of about $a = 0.4375\,nm$ and $c = 3.0554\,nm$ (Fig. 6.1(a), Table 6.1). The lines showed a full width at half maximum (FWHM) of $0.2°$. HRXRD on sample SL06 yielded a period of $6.3 \pm 0.5\,nm$. HRXRD diffraction patterns of a sample with a SL period of $10\,nm$ (sample SL10, Table 6.2) and sample SL06 are shown in Figure 6.1(b) and 6.1(c). The $(0,0,33)$ reflection is labelled as SLR0. Both spectra show first order SL reflections (SLR1). The intensity ratio SLR1/SLR0 are 0.13 for sample SL10 and 0.05 for sample SL06. The second order SL reflections SLR2 disappeared in sample SL06, indicating a poor long range order.

6.3 Thermoelectric properties

The in-plane transport coefficients at room temperature [38] are summarised in Table 6.4. The electrical conductivity, carrier density, carrier mobility, thermopower, and thermal conductivity λ were measured. The lattice thermal conductivity $\lambda_{latt} = \lambda - \lambda_{el}$ and the thermoelectric figure of merit ZT were calculated. The electronic part of the thermal conductivity λ_{el} was calculated according to the Wiedemann-Franz law with a Lorenz number of $1.3 \times 10^{-8}\,W\,\Omega\,K^{-2}$ [38, 90]. The properties of $Bi_2Te_{3+0.63}$ and $Bi_2(Te_{0.94}Se_{0.06})_3$ bulk materials with maximum figure of merit [14], Bi_2Te_3 and $Bi_2(Te_{0.94}Se_{0.06})_3$ thin films and finally $Bi_2Te_3/Bi_2(Te_{0.88}Se_{0.12})_3$-SL with periods between 6 and $20\,nm$, are given for comparison. For the SL with a period of $12\,nm$ the average Se content was varied between 0.06 and 0.09. The thin films and SL showed carrier densities between 2.8×10^{19} and $4.4 \times 10^{19}\,cm^{-3}$, carrier mobilities of about $110\,cm^2/V\,s$, electrical conductivities of $400 - 1000\,1/\Omega\,cm$ and power factors between 28 and $35\,\mu W/cm\,K^2$. The lattice thermal conductivity varied between $1.60\,W/m\,K$ for Bi_2Te_3 thin films and $1.01\,W/m\,K$ for a SL with a period of $10\,nm$.

6.4 TEM sample preparation

6.4.1 BaF_2 cross-sectional samples

The conventional procedure of specimen preparation failed for BaF_2 substrates. The samples disrupted completely into small pieces during polishing and grinding below a thickness of $100\,\mu m$. Thinning the samples by dimpling technique yielded similar results.

To overcome these problems, we sandwiched the BaF_2 substrate between two stable dummies and proceeded with cross-sectional preparation. Even if the BaF_2 sample disrupts during polishing, the pieces are held between the dummies and can further be polished and thinned. We used a Si and a $BaTiO_3$ dummy, Si is readily available from waver material and $BaTiO_3$ is used as thermistor material (PTC devices) and comes as discs of $10\,mm$ in diameter and $3\,mm$ thickness. The preparation consisted of three stages; (i) building the $Si\|BaF_2\|BaTiO_3$

Table 6.4 In-plane thermoelectric properties of n-type Bi_2Te_3 bulk materials, thin films and symmetric superlattices (SLs) at 300 K: average Se content x_{av}, SL period d_{SL}, carrier density n, carrier mobility μ, electrical conductivity σ, thermopower S, power factor $S^2\sigma$, thermal conductivity λ, lattice thermal conductivity λ_{latt}, and thermoelectric figure of merit $ZT = (S^2\sigma/\lambda)\,T$.

Sample	x_{av}	d_{SL} (nm)	n (10^{19} cm^{-3})	μ (cm^2/ Vs)	σ (1/Ω cm)	S (μV/K)	$S^2\sigma$ (μW/ cm K^2)	λ (W/ m K)	λ_{latt} (W/ m K)	ZT
					Bulk materials					
Bulk1 [a]	0		2.3	212	1000	-240	58	2.02	1.70	0.87
Bulk1 [b]	0.05		4.0	150	901	-223	45	1.59	1.15	0.87
					Thin films and superlattices					
TF01	0				1008	-167	28	1.87	1.48	0.45
TF02	0		3.3	120	670	-201	27	1.87	1.67	0.44
TF03	0.06		3.4		444	-208	19	1.50	1.33	0.48
SL20	0.06	20	4.4	110			32	1.42	1.12	0.57
SL12/2	0.09	12	4.2				35		1.07	0.75
SL12	0.06	12			394	-251	25			
SL10	0.06	10	4.0	100	639	-204	27	1.25	1.01	0.60
SL06	0.06	6	2.8	110	540	-219	26			

[a]$Bi_2Te_{3+0.63}$, Ref. [14]. [b]$Bi_2(Te_{0.95}Se_{0.05})_3$, Ref. [14].

composite structure, (ii) cutting pieces out of the composite suitable for the TEM holder with a specimen diameter of 3 mm, and (iii) thinning the TEM sample to electron transparency. The final sample thickness after mechanical grinding and polishing was 25 μm. Finally, the sample was glued on a 3 mm diameter aluminium ring and was ion etched from both sides. We chose 4 kV, 0.25 mA, an angle of 12.5°, and cooling with liquid nitrogen as operating parameters. After $8 - 16$ h ion etching a hole in the Si appeared and got larger with further ion etching until it reached the BaF_2 substrate. SEM images of the cross-sectional sample showed a hole in the Si dummy whereas the $BaTiO_3$ dummy retained its original shape (Fig. 6.2(a)). In the middle of the sample to the left and right side the 200 μm thick BaF_2 substrate disrupted in several small pieces but is still sandwiched between the two dummies (Fig. 6.2(b)). Electron transparent regions are close to the hole in the Si dummy. All BaF_2 pieces in the centre are lost.

Two different dummies had to be used for the composite structure due to the differences in ion etching rates. BaF_2 is an insulating material. BaF_2 charges up during ion milling so that the ion beam is deflected, resulting in a low etching rate. We thinned the substrate to a lateral thickness of at least 200 μm to keep the etching time as short as possible and to raise the stability of the composite structure. The small thickness is also of advantage for TEM analysis since this prevents charging effects during the examination. The $BaTiO_3$ dummy has the lowest etching rate and is therefore the backbone of our composite structure. The etching rate of Si is the highest of all three materials which allows a controlled ion milling starting in the Si dummy and extending towards the BaF_2 substrate.

6.4.2 Bi_2Te_3 thin film cross-sectional and plan view samples

Bi_2Te_3 thin films were prepared in both, plan view and cross section. The brittleness of the BaF_2 substrate turned out to be a severe obstacle, but also the adhesion of the film to the substrate was poor and the films delaminated after cutting pieces with a wire saw. We observed a partial separation of the Bi_2Te_3 thin film from the BaF_2 substrate (Fig. 6.2(c)). The SEM image shows that some fractions of the Bi_2Te_3 thin film are completely separated and bent away from the substrate. We concluded that it is possible to remove larger and intact pieces of the thin film from the substrate.
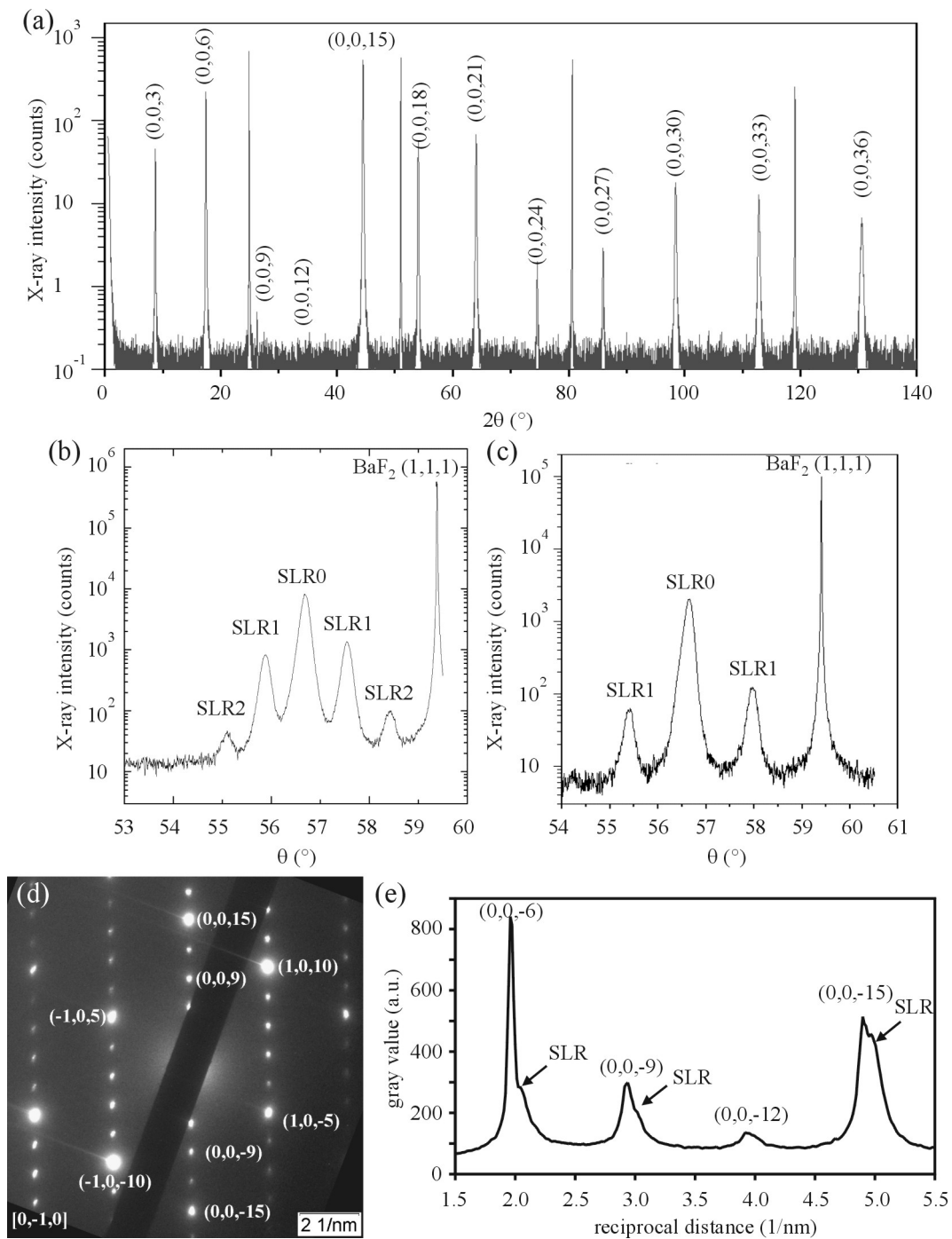
Figure 6.1 (a) XRD spectrum of sample TF01. HRXRD spectra of the samples (b) SL10 and (c) SL06. The $(0,0,33)$ reflection labelled as SLR0, SLR1 and SLR2 are first order and second order SL reflections. (d) TEM diffraction pattern of a cross section of sample SL12 and (e) line scan along the $(0,0,l)$ reflections and SL reflections (SLR).
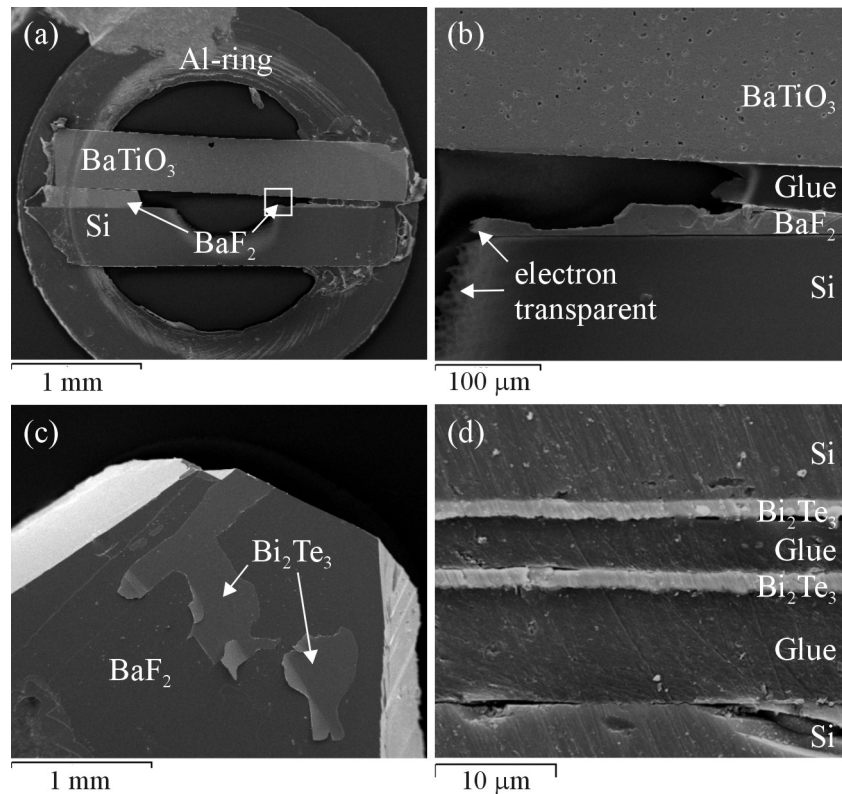
Figure 6.2 SEM images: (a) and (b) BaF_2 cross-sectional TEM sample. (a) Overview image and (b) magnified image of the region marked by a white square. (c) BaF_2 substrate partially covered with Bi_2Te_3 thin film and some loose pieces. (d) Bi_2Te_3 cross-sectional TEM sample before ion etching.

For plan view preparation we glued a Si dummy onto the Bi_2Te_3 thin film and then removed the BaF_2 substrate completely. The procedure started by gluing a polished $450\,\mu$m thick Si dummy with M-Bond 610® on top of the film. The dummy should completely cover the thin film. The dummy was pressed against the thin film between two brass pistons. This step ensures a planar and close contact of the thin film to the dummy. Finally, the BaF_2 substrate was removed from the thin film in an ultrasonic bath or by tweezers. For the further preparation it is crucial that the substrate and the glue are completely removed. The $Bi_2Te_3\|Si$ composite could now be used for plan view preparation. This was done by standard procedure as outlined above. The electron transparent parts of the Bi_2Te_3 thin film were free of Si and glue and the etching time of 1 h is quite short due to the similar high and etching rates of both materials.

Cross-sectional preparation was carried out by cutting the $Bi_2Te_3\|Si$ composites into pieces of $3\,\text{mm} \times 3\,\text{mm}$. A second polished Si dummy with the same dimensions was glued on top of the thin film. The further preparation steps for this $Si\|Bi_2Te_3\|Si$ composite were the same as described for BaF_2 cross-sectional samples. After ion etching from both sides for 4 h the sample was ready for TEM investigations. It is also possible to glue two $Bi_2Te_3\|Si$ composites with the thin films facing against each other and to proceed with the cross-sectional preparation (Fig. 6.2(d)). For such a composite structure it is unambiguous at which side of the thin film the substrate originally was.

In general, the BaF_2 substrate was completely removed from the thin film. Only some small pieces of BaF_2 with a size of a few nanometer were found by EDX in the TEM. The film thicknesses in the electron transparent regions were always found to be $1\,\mu$m, i.e., the original film thickness. Therefore, we concluded that the delamination of the film occurs at the interface or at the first atomic layers of the Bi_2Te_3 thin film. One drawback of our preparation

Table 6.5 Statistics on dislocations in Bi_2Te_3 bulk materials, thin films, and superlattices.

Sample	Dislocation type or plane	Dislocation density (cm^{-2})	Dislocation distance (nm)	Always observed	Dislocation network
		Bulk materials			
n/p-type Bi_2Te_3 [a]	Basal plane	1×10^9	320	Yes	Irregular
BaF_2 substrate [b]	$(1,1,1)$	$< 1\times10^8$	> 1000		Irregular
		Thin films and superlattices			
TF01/TF02	Basal plane	2×10^{10}	70	Yes	Irregular
TF01/TF02	Nonbasal plane	1×10^{11}	30	No	Parallel
TF01/TF02 [b]	Threading dislocation	1×10^9	320	Yes	
SL12	Basal plane	2×10^{10}	70	Yes	Irregular
SL12	Threading dislocation	2×10^9	220	Yes	
SL06	Threading dislocation	2×10^9	220	Yes	

[a]Ref. [33, 81]. [b]Ref. [57].

method is that it was not possible to study the interfaces between the substrate and the thin film. Investigations on Bi_2Te_3 superlattices grown on GaAs [12] did not report problems during preparation due to weak bondings between the substrate and the thin film or within the film.

6.5 Structural and chemical analysis by TEM

6.5.1 BaF_2 substrates and Bi_2Te_3 thin films

The TEM investigations were carried out on $(1,1,1)$ orientated BaF_2 substrates. Figure 6.3(a) shows a small-angle grain boundary between two grains. The grain boundary is inclined to the electron beam so that individual dislocations 25 nm apart are visible. The grains had a size of several micrometers. There were also individual dislocations within the grains with a density of less than $10^8 \, cm^{-2}$ (Table 6.5).

The chemical composition of the films was measured by EDX in the TEM and yielded mole fraction ratios of 39.4 at. % Bi and 60.6 at. % Te (Table 6.6). Images of a plan view sample TF02 (Fig. 6.3(b)) and a cross section of sample TF01 in $[0,-1,0]$ orientation (Fig. 6.3(c) and 6.3(d)) were acquired. The type of dislocations, the dislocation density and distance, the frequency of observation, and the network type are summarised in Table 6.5. The plan view measurements yielded two types of dislocation networks. The first network consists of dislocations crossing at large angles forming an irregular network with a dislocation density of $2 \times 10^{10} \, cm^{-2}$. The second network consists of almost parallel dislocations running in diagonal direction of the image (Fig. 6.3(b)). The dislocations are 30 nm apart, yielding a density of $1 \times 10^{11} \, cm^{-2}$. Two-beam images of the cross-sectional sample with strongly excited $(1,0,10)$ reflection yielded v-shaped threading dislocations with a dislocation density of $1 \times 10^9 \, cm^{-2}$ (Fig. 6.3(c)) [57]. Figure 6.3(d) is a $(-1,0,5)$ dark field image acquired close to the BaF_2/Bi_2Te_3 interface. A sinusoidal diffraction contrast appeared in the Bi_2Te_3 thin film with fringes inclined by an angle of about $30°$ to the growth direction. This contrast is due to a sinusoidal strain field referred to as a nns. The nns has a wavelength of about 10 ± 3 nm (Table 6.7) and a wave vector parallel to $(1,0,10)$. A line scan in the dark field image of the nns yielded a contrast $(I_{\max} - I_{\min})/(I_{\max} + I_{\min})$ equal to 0.15 (Table 6.7).

Table 6.6 Chemical composition measured by EDX in the TEM.

Sample	Bi (at. %)	Te (at. %)	Se (at. %)
TF01/TF02	39.4 ± 1.1	60.6 ± 1.1	
SL12	40.0 ± 1.2	56.3 ± 1.2	3.7 ± 0.9
SL06	39.3 ± 0.9	57.1 ± 1.0	3.5 ± 0.6

Table 6.7 Wavelengths of the nns, periods of the SL (ans), and contrast of the nns and ans.

Sample	Modulation	Period or wavelength (nm)	Contrast $(I_{max} - I_{min})/(I_{max} + I_{min})$
TF01	nns	10 ± 3	0.15
SL12	ans	12.0 ± 0.5	0.25
SL12	nns	10 ± 2	0.25
SL06	ans	6.2 ± 0.5	0.15
SL06	nns	8 ± 2	0.25
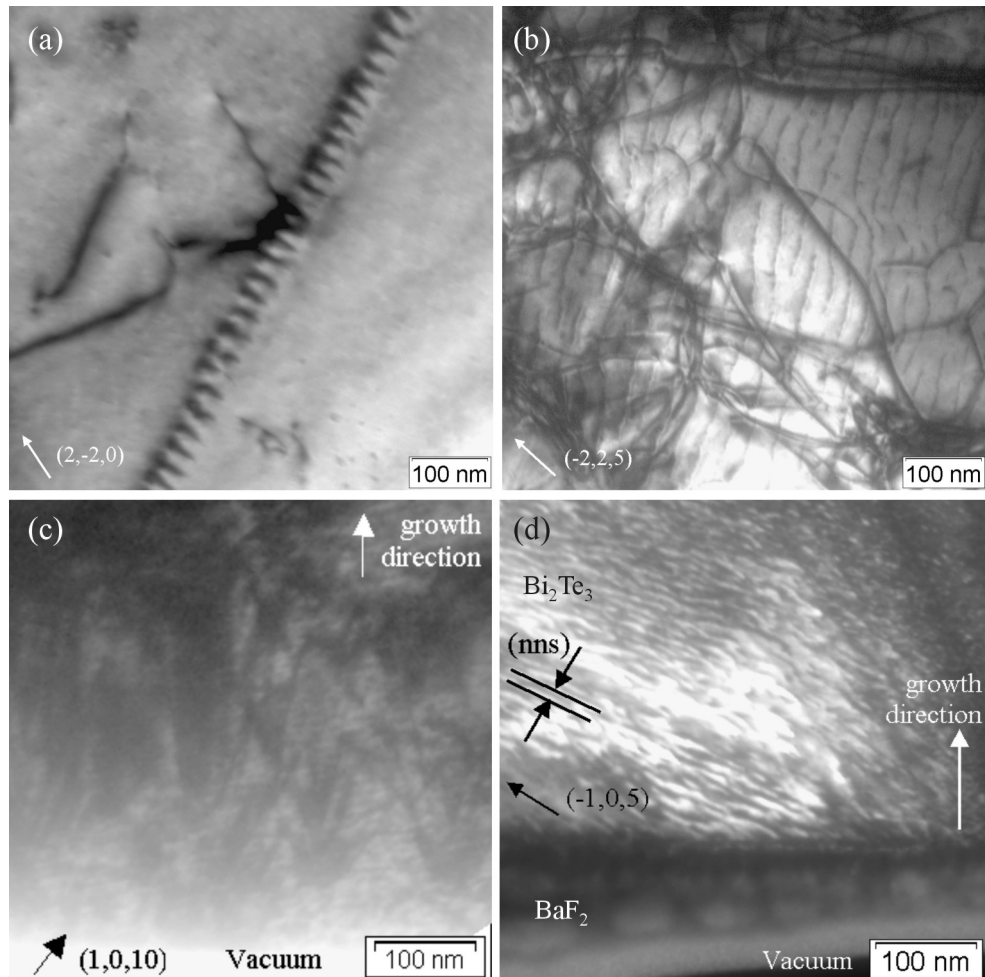
Figure 6.3 (a) $(2,-2,0)$ bright field image of BaF_2. (b) $(-2,2,5)$ bright field image of a plan view sample TF02. (c) $(1,0,10)$ bright field image and (d) $(-1,0,5)$ dark field image of a cross section of sample TF01.
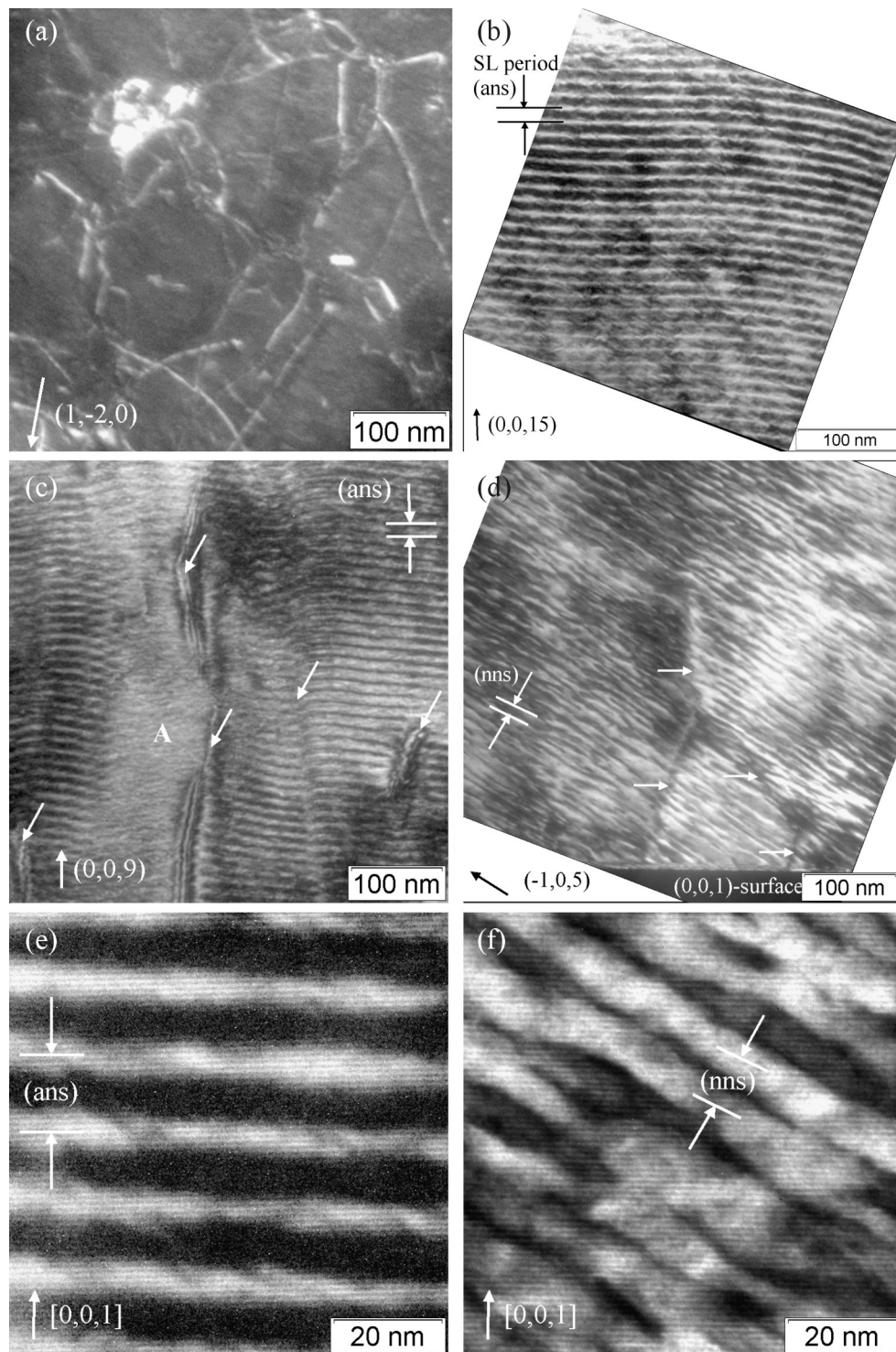
Figure 6.4 Images of sample SL12: (a) $(1, -2, 0)$ **g/3g** weak beam image of a plan view sample. (b)-(e) Cross sections with imaging conditions for imaging the ans and nns. (b) $(0, 0, 15)$ bright field image of the SL structure without threading dislocations. (c) $(0, 0, 9)$ dark field image of the SL with threading dislocations (arrows) and a region A without SL. (d) $(-1, 0, 5)$ dark field image of the nns with threading dislocations (arrows). (e) High resolution image of the ans with strongly excited $(0, 0, l)$ reflections. (f) High resolution image of the nns with strongly excited $(-1, 0, 5)$ reflection.
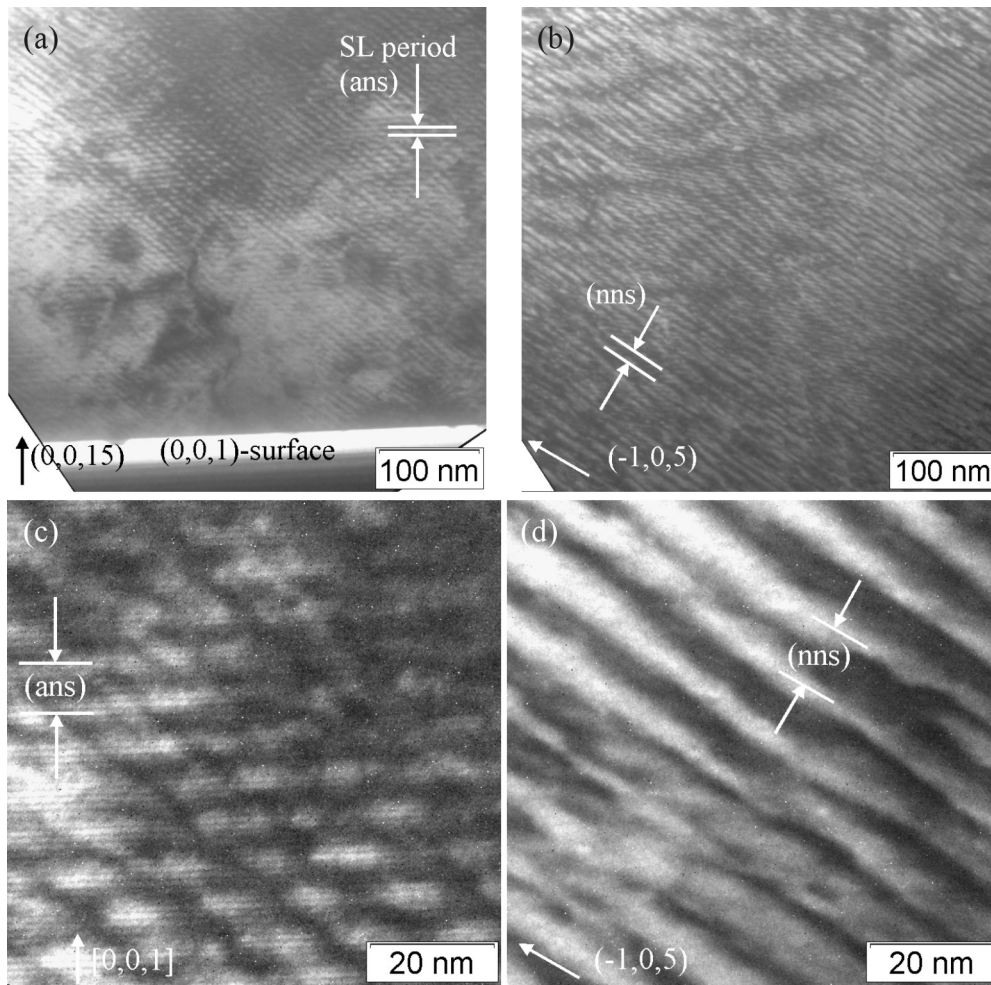
Figure 6.5 Cross sections of sample SL06 with imaging conditions for imaging the ans and nns: (a) $(0, 0, 15)$ bright field image of the SL structure ans. (b) $(-1, 0, 5)$ dark field image of the nns. (c) High resolution image of the ans with strongly excited $(0, 0, l)$ reflections. (d) $(-1, 0, 5)$ bright field image of the (nns) at high magnification.

6.5.2   12 nm superlattice

The chemical composition of the films was investigated in cross section by EDX and yielded mole fraction ratios of $40\,\mathrm{at.\,\%}$ Bi, $56.3\,\mathrm{at.\,\%}$ Te, and $3.7\,\mathrm{at.\,\%}$ Se (Table 6.6). The images of a plan view sample show a network of irregularly arranged dislocations with a dislocation density of $2 \times 10^{10}\,\mathrm{cm}^{-2}$ (Fig. 6.4(a), Table 6.5). The bright spot in the upper left corner is a region with a high dislocation density of $10^{11}\,\mathrm{cm}^{-2}$. A diffraction pattern of a $[0, -1, 0]$ oriented cross-sectional sample was acquired (Fig. 6.1(d)). The fundamental $(0, 0, l)$, $(-1, 0, 5)$, and $(1, 0, 10)$ reflections can be seen. A line scan along the $(0, 0, l)$ reflections yielded SL reflections and a periodicity of $13 \pm 1\,\mathrm{nm}$ (Fig. 6.1(e)). An overview of a dislocation-free region of the SL structure is shown in Figure 6.4(b). A SL period of $12 \pm 0.5\,\mathrm{nm}$ and a contrast of 0.25 was found (Table 6.7). The SL is slightly bent with an amplitude of $30\,\mathrm{nm}$ and a wavelength of $400\,\mathrm{nm}$ (Table 6.3). Dislocation-free regions have a maximum lateral size of $500\,\mathrm{nm}$. Strained regions with threading dislocations parallel to the growth direction were also observed. The SL is bent by several degrees close to threading dislocations (Fig. 6.4(c)). In regions close to threading dislocations the contrast of the SL almost disappeared (region A in Fig. 6.4(c)). The density of threading dislocations was about $2 \times 10^{9}\,\mathrm{cm}^{-2}$. The structural modulation (nns) is shown in

Figure 6.4(d) within a region with threading dislocations. The fringes are inclined by an angle of about 30° to the growth direction and have a wavelength of 10 ± 2 nm and a contrast of 0.25. The structural modulations (nns) is not bent due to threading dislocations. High resolution images of the ans (Fig. 6.4(e)) and the nns (Fig. 6.4(f)) were acquired within regions without threading dislocations. The (003) lattice fringes can be seen with a lattice spacing of about 1 nm. The fringe contrast of both nanostructures, the ans and nns, appears straight; there is no bending of the ans due to the nns and vice versa. Finally, line scans across the images of the ans and nns are shown in Figure 5.3(a). The intensity profile of the ans is of almost perfect sinusoidal shape, whereas the intensity profile of the nns is irregularly sinusoidal with alternating amplitude and wavelength.

6.5.3 6 nm superlattice

The chemical composition of the film measured in cross sections by EDX yielded mole fraction ratios of 39.3 at. % Bi, 57.1 at. % Te, and 3.5 at. % Se (Table 6.6). Figures 6.5(a) and 6.5(b) show an overview of the SL and of the structural modulation within a dislocation-free region. Both images show a chessboardlike contrast pattern. The structural modulation (nns) is inclined by an angle of about 35° to the growth direction. The intensity profiles yielded a SL period of 6.2 ± 0.5 nm and a contrast of 0.15 for the ans and a wavelength of 8 ± 2 nm and a contrast of 0.25 for the nns. The SL is slightly bent with an amplitude of 15 nm and a wavelength of 400 nm (Table 6.3). However, strongly bent regions of the SL were observed when threading dislocations were present. The density of threading dislocations was 2×10^9 cm^{-2}. The high-resolution images of the SL (ans) (Fig. 6.5(c)) and the structural modulation (nns) (Fig. 6.5(d)) were acquired within regions without threading dislocations. The fringe contrast of both nanostructures appears straight; there is no bending of the ans due to the nns and vice versa.

6.6 Discussion

6.6.1 Artificial (ans) and natural (nns) nanostructures

Images of the SL with strongly excited $(0, 0, l)$ reflections showed strong contrast for the SL layers. The contrast of the SL (ans) is due to interference of the fundamental reflections of the Bi$_2$Te$_3$ and the SL reflections. The contrast depends on the local specimen thickness and defocus. RHEED measurements confirmed an epitaxial layer-by-layer growth at a substrate temperature above 280 °C. The SL period determined by HRXRD and TEM were in agreement with each other. The EDX measurements in the TEM confirmed the nominal composition, particularly the average Se content of the SL. However, the lateral resolution of the EDX in the TEM was not sufficient to measure the chemical composition in separate SL layers.

The striking microstructural feature is the presence of a nns. The correlated sinusoidal strain field could be imaged by diffraction contrast with strongly excited $\{-1, 0, 5\}$ reflections. The structural modulation (nns) was unambiguously identified in the epitaxially grown thin films and SL and was also identified in p-type and n-type Bi$_2$Te$_3$ bulk materials [34, 63]. Therefore, the nns is of general character for Bi$_2$Te$_3$ materials, independent of the growth technique and doping level. In all samples the wavelength is about 10 nm and the wave vector is parallel to $\{1, 0, 10\}$, the fringes are tilted with respect to the $(0, 0, l)$ planes by an angle of $30° - 35°$. However, the diffraction contrast intensity profiles of the nns were only approximately of sinusoidal shape. This indicates local changes of the amplitude, the wavelength, and the phase of the displacement field. No bending of the nns due to dislocations or superlattices is observed, the nns is perfectly superimposed to the average structure. The nature of the structural modulation was analysed in detail in n-type and p-type bulk materials [63] and was found to be a pure structural modulation. Chemical modulations due to alloying and subsequent precipitation can be ruled out, since the nns was also found in pure Bi$_2$Te$_3$ thin films. A network of dislocations a few nanometers apart as an origin of the strain field could also be ruled out by investigations on bulk materials.

6.6.2   Bending and extended defects in the SL structure

Dislocation-free regions of the SL showed bending with a wavelength of 400 nm and amplitudes of 30 nm for SL12 and 15 nm for SL06, respectively. For both SLs the bending amplitude is 2.5 times larger than the SL period. This slight bending is in agreement with AFM surface roughness measurements (Table 6.3). The film and layer roughness is correlated with the substrate temperature. Smooth surfaces were only found at 280 °C, whereas surface roughness increased at higher temperature. However, the substrate temperature during thin film growth was chosen to be 290 °C for optimizing the power factor $S^2\sigma$ and thereby the thermoelectric figure of merit of the films [40]. Bending of the SL was most pronounced close to threading dislocations.

TEM showed dislocation-free regions of the SL with a lateral size of less than 500 nm, which is significantly smaller than the film thicknesses. In X-ray diffraction the $(0,0,l)$ reflections showed a FWHM of 0.2°. According to the Scherrer formula [91] a grain size of 80 nm parallel to $[0,0,1]$ can be calculated. This grain size (size of coherent scattering regions) is ten times smaller than the film thicknesses. The nns contributes to the reflection broadening in X-ray diffraction patterns and might explain the differences between TEM and XRD.

Threading dislocations were found in thin films and SL with the same density of about $10^9\,\mathrm{cm}^{-2}$. The cross-section images show strong bending of the SL close to threading dislocations. Usually, the stress field of strained-layered SL cause bending of threading dislocations [92]. Threading dislocations and bending of the SL was not reported for p-type SL [12]. The SL disappeared close to one threading dislocation (Fig. 6.4(c)) and an alloyed region has formed. Threading dislocations might be generated due to the lattice mismatch between the substrate and the epitaxially grown film and should be of edge type. The line direction has a large component parallel to the growth direction and the Burgers vector should be parallel to the basal plane. Close to threading dislocation the planes are bent and therefore the local lattice parameters change. Threading dislocations change the local growth rate and surface steps or even a complete disorder will be introduced in the SL.

A lattice parameter misfit of 0.045% was calculated for Bi_2Te_3 thin films on BaF_2 substrates. The XRD measurements of Bi_2Te_3 thin film TF01 showed that lattice parameter a was 0.2% smaller and lattice parameter c 0.2% larger with respect to Bi_2Te_3 bulk materials. This indicates that the film is under compressive stress, which is in agreement with the positive lattice parameter misfit. From the lattice parameter misfit a misfit dislocation density of $10^8\,\mathrm{cm}^{-2}$ and a dislocation distance of 970 nm can be estimated. Misfit dislocations could not be analysed due to the poor adhesion between the epitaxially grown films and the BaF_2 substrate, the films delaminated during TEM specimen preparation.

TEM of plan view samples yielded irregular arranged dislocations and parallel dislocations with a density of $2 \times 10^{10}\,\mathrm{cm}^{-2}$ (Table 6.5). Similar dislocations networks were found in n-type and p-type bulk materials and analysed with respect to their Burgers vectors, line directions, and line energy [33, 81]. It is assumed that they are identical with the networks observed in the thin films and SL. The dislocation density is two orders of magnitude larger than that (i) expected from the BaF_2-Bi_2Te_3 misfit and (ii) the dislocation density in the BaF_2 substrates. Also, the dislocation density is one order of magnitude larger than in bulk samples.

Finally, the intensity ratios SLR1/SLR0 of SL reflections found by HRXRD is 2.6 times smaller for sample SL06 compared to sample SL10. This indicates a reduced quality of the short period superlattice, which might be due to three reasons: (i) The SL smeares out during MBE growth due to diffusion, which is more significant in short period SL. (ii) TEM showed in both SLs slightly bent SL layers. (iii) TEM showed a chessboardlike contrast pattern in sample SL06 due to an either ordered demixing of Te and Se in the basal plane or an ordered rearrangement of the structural modulation of the nns.
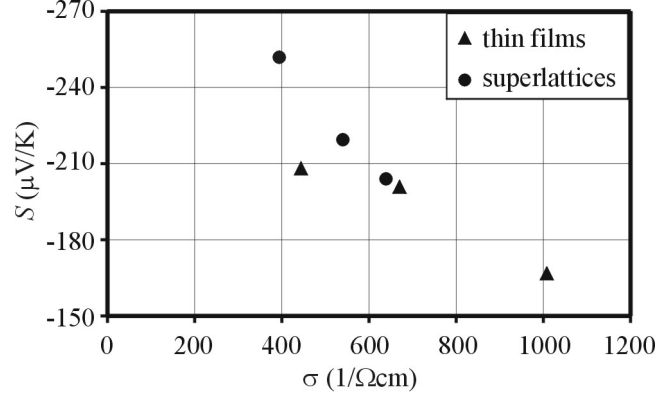
Figure 6.6 Correlation diagram for the thermopower S and the electrical conductivity σ for the epitaxially grown thin films and superlattices.

Table 6.8 Lattice thermal conductivity λ_{latt} and phonon mean free path l_{ph} at $300\,\mathrm{K}$ for Bi_2Te_3 and other model materials in dependence of structural disorder. $(\perp c)/(\parallel c)$ indicate λ_{latt} perpendicular/parallel to the c axis. l_{ph} was calculated as $\lambda_{\mathrm{latt}} = 1/3\,\rho\,c\,v\,l_{\mathrm{ph}}$ with mass density ρ, specific heat c, and average velocity of sound v. The specific heat was determined by the Debye model: Debye temperature θ_{D} and number of atoms N per unit cell with volume V.

Sample	Structure	λ_{latt} (W/m K)	l_{ph} (nm)
	Bi_2Te_3		
$Bi_2Te_3(2)$ [a]	Bulk, single crystal, $(\perp c)$	1.4	2.1
$Bi_2Te_3 - 1500$nm [b]	Thin film, polycrystalline, film thickness $1.5\,\mu$m, grain size $300\,$nm, $(\perp c)$	1.2	1.8
$Bi_2Te_3 - 1000$nm (Sample TF01 [c])	Thin film, single crystal, film thickness $1\,\mu$m, (nns), wavelength $10\,$nm, $(\perp c)$	1.48	2.2
$Bi_2Te_3 - SL10$nm [d] (Sample SL10 [c])	$10\,$nm SL, single crystal, film thickness $1\,\mu$m, (nns), wavelength $10\,$nm, $(\perp c)$	0.81[d] 1.01[c]	1.2 1.5
	Si		
Si [e]	Bulk, single crystal	155	43
Si-1600nm [f]	Thin film, single crystal, film thickness $1.6\,\mu$m	95	26
Si-20nm [g]	Thin film, single crystal, film thickness $20\,$nm	22	6.7
	SiO_2		
SiO_2 crystal [h]	Bulk, single crystal, $(\parallel c)$	3.8	1.3
SiO_2 glass [i]	Bulk, glass	1.7	0.7
	$Bi_{1.4}Pb_{0.6}Sr_2Ca_2Cu_3O_{10}$		
Bi-2223 [j]	Bulk, polycrystalline, grain size $50\,$nm, incommensurately modulated structure, wavelength $5\,$nm	0.7	0.5

[a]Ref. [19, 87, 93]. [b]Ref. [93, 94]. [c]This work and Ref. [93]. [d]This work and Ref. [39, 93].
[a-d]($\rho = 7.86\,\mathrm{g/cm^3}$, $c = 153\,\mathrm{J/kg\,K}$, $v = 1650\,\mathrm{m/s}$, $\theta_{\mathrm{D}} = 165\,\mathrm{K}$, $N/V = 0.30 \times 10^{23}\,\mathrm{cm^{-3}}$).
[e]Ref. [95, 96]. [f]Ref. [96, 97]. [g]Ref. [96, 98].
[e-g]($\rho = 2.39\,\mathrm{g/cm^3}$, $c = 710\,\mathrm{J/kg\,K}$, $v = 6400\,\mathrm{m/s}$, $\theta_{\mathrm{D}} = 640\,\mathrm{K}$, $N/V = 0.50 \times 10^{23}\,\mathrm{cm^{-3}}$).
[h]Ref. [99] ($\rho = 2.65\,\mathrm{g/cm^3}$, $c = 715\,\mathrm{J/kg\,K}$, $v = 4400\,\mathrm{m/s}$, $\theta_{\mathrm{D}} = 550\,\mathrm{K}$, $N/V = 0.80 \times 10^{23}\,\mathrm{cm^{-3}}$).
[i]Ref. [99] ($\rho = 2.22\,\mathrm{g/cm^3}$, $c = 715\,\mathrm{J/kg\,K}$, $v = 4160\,\mathrm{m/s}$).
[j]Ref. [100, 101] ($\rho = 3.48\,\mathrm{g/cm^3}$, $c = 442\,\mathrm{J/kg\,K}$, $v = 2930\,\mathrm{m/s}$, $\theta_{\mathrm{D}} = 220\,\mathrm{K}$, $N/V = 0.18 \times 10^{23}\,\mathrm{cm^{-3}}$).
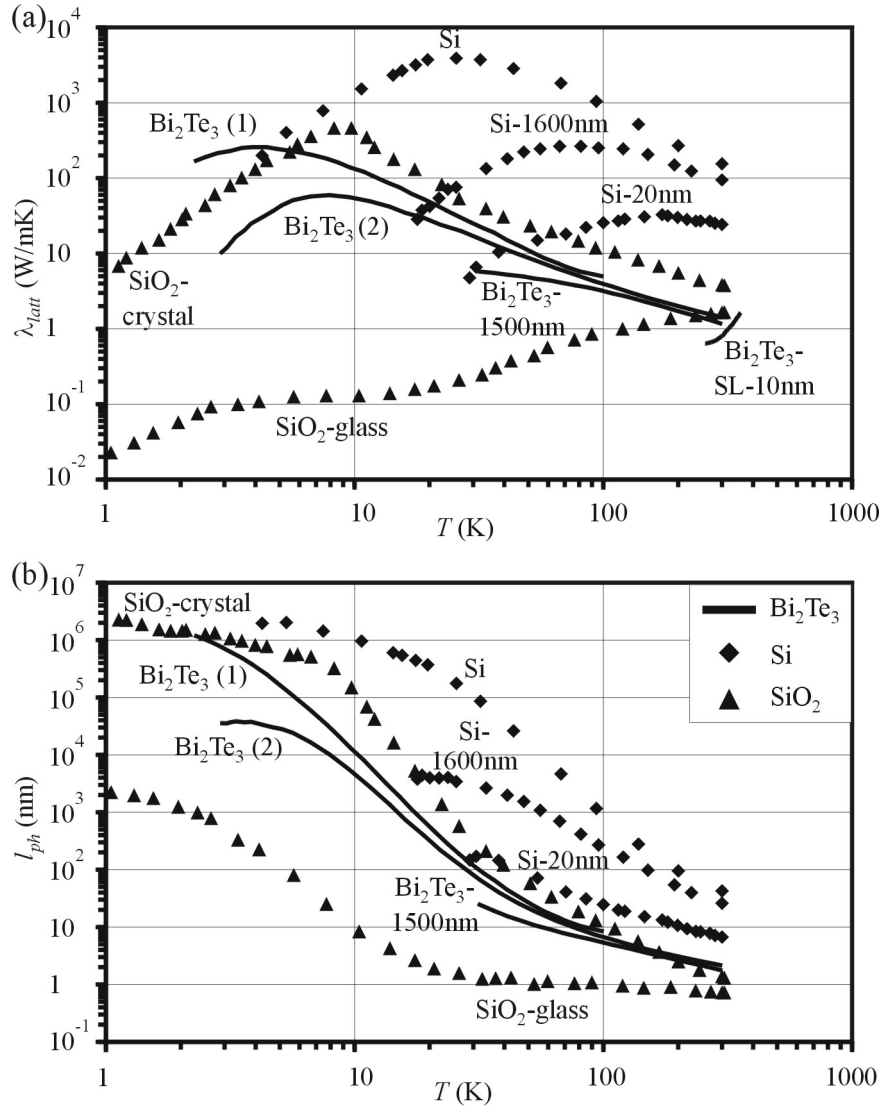
Figure 6.7 Temperature dependence of (a) the lattice thermal conductivity λ_{latt} and (b) the calculated phonon mean free path l_{ph} for Bi_2Te_3, Si, and SiO_2 materials with different amounts of structural disorder (Table 6.8): Bi_2Te_3 bulk (Bi_2Te_3 (1) see Ref. [86, 93], Bi_2Te_3 (2) see Ref. [19, 87, 93]), Bi_2Te_3 thin film with a thickness of $1.5\,\mu$m (Bi_2Te_3-1500nm see Ref. [93, 94]), $Bi_2Te_3/Bi_2(Te_{0.88}Se_{0.12})_3$ SL with a period of $10\,$nm (Bi_2Te_3-SL-10nm see Ref. [39]), Si bulk (see Ref. [95, 96]), Si thin films with a thickness of $1.6\,\mu$m (Si-1600nm see Ref. [96, 97]) and $20\,$nm (Si-20nm see Ref. [96, 98]), and crystalline and amorphous SiO_2 (see Ref. [99]).

6.6.3 Correlation between structural and thermoelectric properties

At $300\,\text{K}$ the thermal conductivity of Bi_2Te_3 thin films and SL were found to be $1.1 - 1.7$ times smaller than in bulk (Table 6.4). However, also the power factors were reduced by factor of 2. Therefore, the thermoelectric figure of merit ZT of the thin films and SL did not increase with respect to bulk samples.

The electrical conductivity and thermopower in thin films and SL showed a negative correlation (Table 6.4, Fig. 6.6). The reduction of the power factor can be correlated to a reduced carrier mobility [38]. Our results do not show a clear dependence of these two quantities on the microstructure. Possibly, the reduction of the power factor is correlated to the density of threading dislocations. A reduction of the threading dislocation density by introducing buffer layers could enhance ZT.

The lattice thermal conductivity is a transport quantity that sensitively reflects the structural disorder. Structural disorder particularly on the nanometer scale significantly decreases the phonon mean free path and thereby the lattice thermal conductivity. In thin films investigated in this work the lattice thermal conductivity is reduced because of three reasons. (1) Phonons are more strongly scattered on surfaces due to the small thicknesses of the films. (2) The thermal conductivity of SL is reduced by a factor of 1.3 compared to single layer thin films and bulk materials with the same average Se content. Also, the thermal conductivity decreases with decreasing SL period; therefore, superlattices yield an enhanced scattering of phonons. In SL the reduction of the thermal conductivity overcompensates the reduction of the power factor and yields a better ZT compared to thin films [38]. For the $10\,\text{nm}$ SL (thickness $1\,\mu\text{m}$) the lattice thermal conductivity was measured in a temperature range between $250\,\text{K}$ and $350\,\text{K}$ [39]. The lattice thermal conductivity decreases with decreasing temperature (Fig. 6.7, Bi_2Te_3-SL-10nm) which is a characteristic feature for materials with high structural disorder. (3) Samples SL12 and SL12/2 only differed with respect to the average Se content, SL films with higher average Se content show a reduced thermal conductivity [38]. This can be attributed to an increased alloy scattering of the phonons.

Bi_2Te_3 is known for its low lattice thermal conductivity of about $1.5\,\text{W/m\,K}$. In this paragraph we would like to discuss the possible reasons for the small lattice thermal conductivity of bulk Bi_2Te_3. Bi_2Te_3 single crystals show lattice thermal conductivities such as materials with high structural disorder (Table 6.8, Fig. 6.7). The nns represents a significant structural disorder and has to be considered as the most promising reason. Doped Si [95–98, 102], SiO_2 single crystals and glass [99], and the high-T_C superconductor $Bi_{1.4}Pb_{0.6}Sr_2Ca_2Cu_3O_{10}$ (Bi-2223) [100, 101] serve as model materials to illustrate the effects of structural disorder. For Bi-2223 only the normal state properties are considered in this work. For these materials the lattice thermal conductivity λ_{latt} and the corresponding phonon mean free path l_{ph} at room temperature are given in Table 6.8, the temperature dependence can be seen in Figure 6.7. Both values, λ_{latt} and l_{ph}, depend on the microstructure of the materials, particularly at low temperatures. The phonon mean free path was calculated as $\lambda_{\text{latt}} = 1/3\rho\,c\,v\,l_{\text{ph}}$ according to transport theory for isotropic solids, where ρ is the mass density, c is the specific heat, and v is the velocity of sound. The lattice thermal conductivity of single crystalline materials such as Si and SiO_2 (Fig. 6.7) shows a sharp peak at low temperatures and a phonon mean free path of about $1\,\text{mm}$; phonon scattering on the crystal surfaces is the dominating scattering mechanism. The effect of structural disorder can best be seen when going from Si single crystals to single crystalline thin films. The phonon mean free path decreases by one to four orders of magnitude depending on the film thickness and the peak of the lattice thermal conductivity decreases by two orders of magnitude and shifts towards higher temperatures. This behaviour could be explained by additional phonon scattering on surfaces and interfaces [98]. When going from crystalline SiO_2 to amorphous SiO_2 a dramatic decrease of the lattice thermal conductivity is found due to structural disorder. On the other hand, Bi-2223 is (i) a layered structure, (ii) consists of Bi planes, (iii) exhibits an incommensurately modulated structure [103, 104], and therefore has common structural features also found in Bi_2Te_3. The atomic positions of the crystal can be described by an average structure, on which a sinusoidal displacement field is superimposed with a wavelength of about $2 - 5\,\text{nm}$. Bi-2223 and Bi_2Te_3 have common structural

features and their lattice thermal conductivities are in a similar range. The incommensurately modulated structure of Bi-2223 corresponds to the nns in Bi_2Te_3, yielding a decrease of the lattice thermal conductivity.

In Bi_2Te_3 materials no systematic microstructural investigations can be found in the literature despite the importance of the material for thermoelectric applications. Also, only few measurements of the lattice thermal conductivity cover a wide temperature range, i.e., single crystals (Bi_2Te_3 (1) [86] and Bi_2Te_3 (2) [19, 87]) measured in the basal plane. In these measurements the small phonon mean free paths could not be explained by phonon surface scattering, Umklapp processes, and isotope scattering alone over the entire temperature range [19]. Therefore, it was assumed that the increased phonon scattering was due to dislocations [19]. The lattice thermal conductivity could be further decreased in polycrystalline Bi_2Te_3 thin films [94] with a thickness of $1.5\,\mu m$ (Bi_2Te_3-1500nm) and a grain size of about $300\,nm$ due to additional phonon scattering on grain boundaries.

However, in Bi_2Te_3 thin films the lattice thermal conductivity could only be reduced by a factor of 2 with respect to bulk at room temperature. In other model materials artificially introduced structural disorder yielded a reduction of one or several orders of magnitude. The reason is most likely the structural modulation (nns) and the presence of dislocations in bulk Bi_2Te_3. The displacement field of the nns is correlated to a sinusoidal strain field which should significantly scatter phonons due to its amplitude and wavelength of $10\,nm$ which is of the same order of magnitude as the SL period. In a recent publication [28] a similar (nns) structure was imaged by TEM in $AgPb_mSbTe_{2+m}$ bulk materials. Also this material yields a small lattice thermal conductivity and a high thermoelectric figure of merit ZT. A more detailed analysis showed the structural complexity of other Te compounds [29]. Crystalline Te compounds are known to be easily transferred in an amorphous state and are used in, e.g., phase change materials for various applications [84]. The nns might be regarded as an intermediate state between pure crystalline and amorphous and might be the key for the small thermal conductivity and large thermoelectric figure of merit of Bi_2Te_3.

Chapter 7

Bulk: Gliding dislocations

7.1 Results

7.1.1 Stereomicroscopy (Tomography)

The microstructure of p-type $(\mathrm{Bi}, \mathrm{Sb})_2\mathrm{Te}_3$ was investigated by conventional TEM [33]. The sample showed a strong texture with grain sizes of $1 - 10\,\mu\mathrm{m}$ divided by small-angle grain boundaries. The dislocation density was found to be $10^9\,\mathrm{cm}^{-2}$ and dislocations in the basal plane showed a high mobility. The motion was induced by heating the sample by an electron beam with a large illumination angle. External stresses were not applied. The gliding dislocations were also found in n-type $\mathrm{Bi}_2(\mathrm{Te}, \mathrm{Se})_3$ [63]. The stereomicroscopy technique (Fig. 3.3) was applied to determine (a) the Burgers vector, line direction, glide plane, and the direction of motion of individual dislocations, and (b) the spatial arrangement of groups of dislocations in p-type $\mathrm{Bi}_2\mathrm{Te}_3$ (Table 3.1, sample P4). Figure 7.1 shows four two-beam images of the same specimen region at various orientations. The sample was tilted by up to 90° from an orientation close to the c axis (Fig. 7.1(a), 7.1(b), and 7.1(c)) to an orientation parallel to the a axis (Fig. 7.1(d)). Details of the sample orientations are given in Table 7.1. In this specimen region the motion of (i) free standing dislocations, (ii) equidistant dislocations in the same glide plane, and (iii) dislocation pileups were analysed.

(i) Figures 7.1(a) and 7.1(b) show the sample before and after $2\,s$ of heating by a focused electron beam, respectively. There are free standing dislocations with a high mobility of $20 - 50\,\mathrm{nm/s}$. The stereomicroscopy investigations yielded mixed dislocations with Burgers vector $[1, 1, 0]$, line direction $[2.7, -1, 0]$, and the basal plane as glide plane with direction of motion $-[1, 1, 0]$. The Burgers vector was determined by using the $\mathbf{g} \cdot \mathbf{b} = 0$ criterion for dislocations being out of contrast and by image simulation. The dislocations first bowed out in the direction of motion and then started to glide.

(ii) Figures 7.1(a) and 7.1(b) also yielded a group of equidistant dislocations which showed a collective movement with the same direction of motion as the free standing dislocations. The dislocations kept a minimum distance of $80\,\mathrm{nm}$. In a sample orientation parallel to the a axis the dislocations turned out to glide on the same $(0, 0, \mathrm{l})$ plane (Fig. 7.1(d), Table 7.1).

(iii) Finally, Figures 7.1(c) and 7.1(d) show a second type of groups of dislocations, which were not able to glide. In a sample orientation closer to the c axis these dislocations appear as bundles of dislocations (Fig. 7.1(c), Table 7.1). In an orientation parallel to the a axis the dislocations turned out to be piled up on different $(0, 0, \mathrm{l})$ planes at a distance of $30 - 80\,\mathrm{nm}$ (Fig. 7.1(d), Table 7.1).

7.1.2 Video sequences and analysis

The sample was in an orientation close to $[5, -5, 1]$, which is at an intermediate projection between the a axis and the c axis (Table 7.1). Video sequences of free standing dislocations, of groups of dislocations, and of dislocation dipoles were recorded. The video sequences were

analysed in slow motion, i.e., frame by frame at a frame rate of 25 frames per second. This allowed the post-analysis of processes which were to fast or to complex for human eyes, and therefore were not recognised during acquisition. Particularly, the interaction in groups of dislocations were of interest. For this, distances between the dislocations and their velocities (Table 7.2) were measured. The figures show a poor quality due to the low dynamical range of the video camera. Also, optimised two-beam conditions could not be applied since most of the dislocations glided away too fast.

Figure 7.2 shows free standing dislocations at various times. At the beginning dislocations can be seen bowed out in opposite directions with a radius of about 100 nm (Fig. 7.2(0s)). The dislocations started to move in opposite directions but with the same velocity of about 50 nm/s (Table 7.2) when the sample was heated by a focused electron beam. During the entire glide process the dislocations were bowed out, therefore the dislocations are only pinned at the surface. The motion is rather a hopping process than a continuous process. The following two frames show the gliding dislocations after 19 s (Fig. 7.2(19s)) and at the end after 48 s (Fig. 7.2(48s)). In each frame the total length of the dislocations increased compared to the previous frame. Therefore, the dislocations moved towards thick specimen regions. The dislocations could glide until they reached a dislocation pileup (Fig. 7.2(48s)). The motion stopped at distance of about 175 nm in front of the dislocation pileup and the free standing dislocations got straight.

Figure 7.3 shows a group of equidistant dislocations gliding in the same plane. The dislocations showed a collective movement with a velocity of less than 10 nm/s (Table 7.2), keeping a minimum distance of about 50 nm between to neighboured dislocations.

The last video sequences show (a) the formation of a dislocation dipole (Fig. 7.4(0s), 7.4(0.6s), and 7.4(0.7s)) and (b) an oscillating dipole (Fig. 7.4(5.2s), 7.4(14.4s), and 7.4(14.6s)). Both processes are very fast and required a frame by frame analysis.

At the beginning of the formation of a dislocation dipole a free standing dislocation (i) bowed out at started to glide slowly at a velocity of 20 nm/s towards another free standing dislocation (ii) (Fig. 7.4(0s) and 7.4(0.6s)). At a distance of 200 nm between both dislocations the velocity of dislocation (i) accelerated to more than $1\,\mu$m/s (Table 7.2) and stopped its motion close to dislocation (ii) (Fig. 7.4(0.7s)). The motion of the dislocation (i) during the last moments of the formation of the dipole fast too fast to be recorded by the video camera. Only weak traces are visible at the places where the dislocation was pinned at the surface (Fig. 7.4(0.7s)).

A few seconds later at the same specimen region an oscillating dipole (iii) could be observed (Fig. 7.4(5.2s), 7.4(14.4s), and 7.4(14.6s)). The dipole (iii) bowed out slowly by 50 nm within 6.8 s and kept its shape for 2.4 s (Fig. 7.4(5.2s) and 7.4(14.4s)). During this time of maximum bending another nearby free standing dislocation (iv) glided away (Fig. 7.4(14.4s)). Immediately after this, the dipole snapped back within 0.2 s (Fig. 7.4(14.6s)).

7.2 Discussion

7.2.1 Thermally induced gliding and elastic forces

The high mobility of the dislocations in Bi_2Te_3 at room temperature is a unique physical property and was reported several times [24, 25, 33]. Stereomicroscopy yielded mixed dislocations and the basal plane being the glide plane, which was expected for a hexagonal material such as Bi_2Te_3. Free standing dislocations, dislocations in the same glide plane, and dislocation pileups were unambiguously identified by stereomicroscopy. The motion had not to be induced by external shear stresses or by heating of the sample beyond room temperature. Only an activation energy had thermally to be overcome by a focused electron beam to start and maintain motion. The dislocation velocity increased for larger illumination angles and thereby higher temperatures. The dislocations were bowed out in the direction of motion and were only pinned at the surface. Obviously, there are no pinning centres such as impurities since the gliding dislocations showed no zig-zag shape.

Table 7.1 Sample orientations applied for the various micrographs and video sequences.

Micrograph	Nearest pole	Angle to c axis
Fig. 7.1(a) and Fig. 7.1(b)	$[-5, -10, 2]$	$32°$
Fig. 7.1(c)	$[5, -5, 1]$	$51°$
Fig. 7.1(d)	$[1, 0, 0]$	$90°$
Fig. 7.2, Fig. 7.3, Fig. 7.4	$[5, -5, 1]$	$51°$
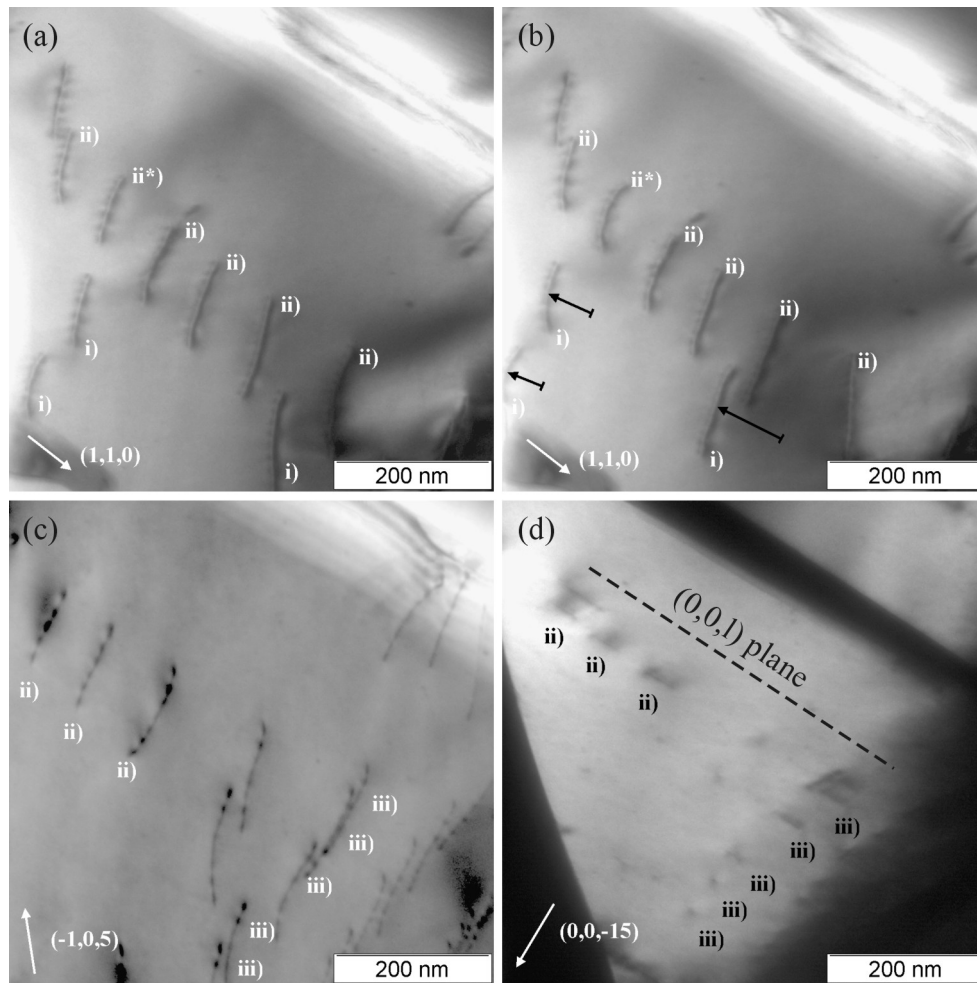
Figure 7.1 (a) $(1, 1, 0)$, (b) $(1, 1, 0)$, (c) $(-1, 0, 5)$, and (d) $(0, 0, -15)$ bright field images of the same specimen region. Images (a), (b), and (c) were acquired in a sample orientation close to the c axis, and image (d) in an orientation parallel to the a axis (Table 7.1). Images (a) and (b) were recorded before and after $2\,s$ heating by a focused electron beam, respectively. (i) Free standing dislocations with a high mobility. The dark arrows indicate the position of the dislocations before and after heating. (ii) Equidistant dislocations in the same glide plane. (ii*) Dislocation bowed out by 15 nm after heating. (iii) Dislocations piled up in different $(0, 0, l)$ planes.

Table 7.2 Velocity of the gliding dislocations for various processes.

Process	Velocity (nm/s)
Formation of dipoles	> 1000
Free standing dislocations	$10 - 100$
Equidistant dislocations in the same glide plane	< 10
Dislocation pileups and dipoles	0
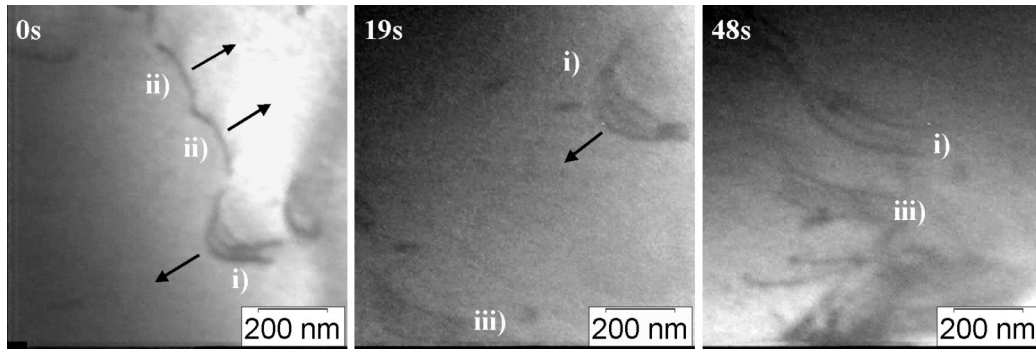
Figure 7.2 Video sequences of free standing dislocations (i) and (ii) at different times, gliding in opposite directions. The motion of dislocations (i) stopped in front of a dislocation pileup (iii).
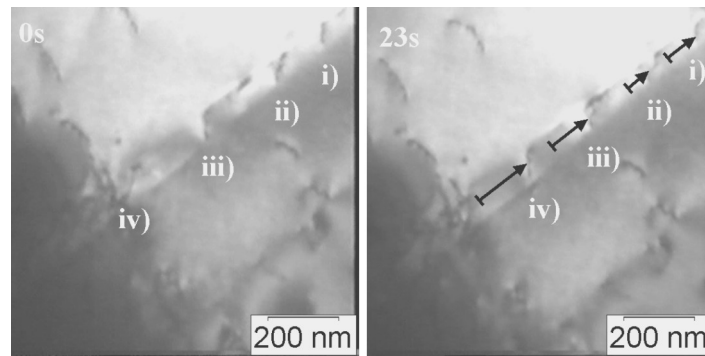
Figure 7.3 Video sequences of equidistant gliding dislocations in the same plane. The arrows indicate the positions of the dislocations (i)-(iv) before and after heating.

The direction of motion is determined by elastic forces acting on the dislocations. The origin of these forces [41] could be (i) attractive image forces close to free surfaces, (ii) residual or externally applied shear stress, and (iii) the interaction between two dislocations. The video sequences visualised each type of these forces. (i) Dislocations were observed which moved towards the edge of the sample until they disappeared. (ii) Figure 7.2(a) showed dislocations moving in opposite directions. It is known that for residual or external shear stresses the direction of motion depends on the sign of the Burgers vector [41]. Therefore, the dislocations differed in the sign of their Burgers vectors. (iii) Attractive and repulsive forces between two dislocations depend on the signs of their Burgers vectors [41]. The video sequences showing equidistant dislocations in the same glide plane (Fig. 7.3) and dislocations moving towards dislocation pileups (Fig. 7.2(b) and 7.2(c)) visualise repulsive forces between dislocations with identical Burgers vectors. The repulsive forces reduced the mobility of dislocations in the same glide plane (Table 7.2). Also, dislocation pileups acted as barriers for free standing dislocations (Fig. 7.2(b) and 7.2(c)). The formation of the dipole (Fig. 7.4(0s), 7.4(0.6s), and 7.4(0.7s))
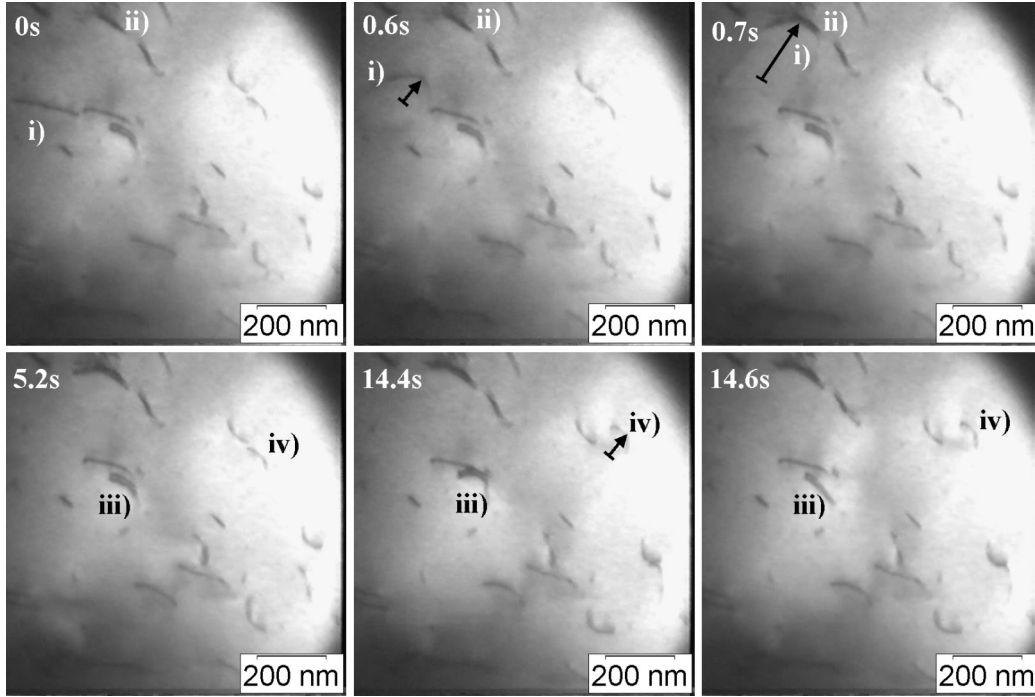
Figure 7.4 Video sequences showing (a) the formation of a dislocation dipole from free standing dislocations (i) and (ii) and (b) an oscillating dipole (iii). The oscillating dipole first bowed out slowly by 50 nm within 6.8 s, kept its shape for 2.4 s, and snapped back after dislocation (iv) glided away.

can be explained by attractive forces between two dislocations which differed in the signs of their Burgers vector. Particularly, the attraction between both dislocations explains the strong increase of the dislocation velocity (Table 7.2). Finally, in regions of high dislocation density the glide process depends on the local arrangement of all dislocations at the various times (Fig. 7.4). The glide process has similarity to the stop and go movement in a traffic jam.

7.2.2 Residual shear stresses

Forces due to residual shear stresses on dislocations are more dominant in Bi_2Te_3 than image forces close to free surfaces because a large number of dislocations were observed, moving away from the edge of the sample towards thick specimen regions (Fig. 7.2(b) and 7.2(c)). The residual shear stresses σ can be estimated from dislocation configurations showing equilibrium of forces. For elastically isotropic crystals expressions were derived for the elastic forces F_L per unit length [41]. The formulas given in Reference [41] can be applied because Bi_2Te_3 has almost isotropic elastic properties, the anisotropy ratio being 1.17 [41, chap. 2.4] calculated from the elastic constants c_{ij} [59]. The calculations assume a shear modulus $\mu = 2.74 \times 10^{10}$ Pa and a Poisson's ratio $\nu = 0.24$ [41, chap. 2.4], and finally edge dislocations with Burgers vector $\mathbf{b} = [1,1,0]$, line direction $\mathbf{l} = [1,-1,0]$, and direction of motion $\langle 1,1,0 \rangle$. Three examples will be given.

(i) Figure 7.2(c) showed gliding dislocations stopped by a dislocation pileup at a distance of $R = 175$ nm. The driving force is the residual shear stress given by $F_L = \sigma\, b$ [41, page 81], whereas the repulsive force between two parallel straight edge dislocations is given by $F_L = \frac{\mu\, b^2}{2\pi\,(1-\nu)\,R}$ [41, page 123]. In equilibrium, a residual shear stress of $\sigma = 14 \times 10^6$ Pa can be calculated.

(ii) A dislocation was observed at a distance $R = 300$ nm away from the edge of the sample, gliding very slowly "backwards" towards the edge of the sample. The bending of the dislocation

Table 7.3 Lattice thermal conductivity λ_{latt} of n-type Bi_2Te_3 measured at $3\,K$ parallel to the basal plane. The phonon mean free path l_{ph} was calculated as (a) $\lambda_{\text{latt}} = 1/3\,C\,v\,l_{\text{ph}}$ and (b) $l_{\text{ph}} = 0.455\,(\gamma^2\,b^2\,k_D)^{-1}\,\frac{1}{N_D}\,\frac{\theta_D}{T}$ for a dislocation density of $N_D = 10^9\,\text{cm}^{-2}$. Material parameters [16]: $C = 574\,\text{J/K}\,\text{m}^3$ at $T = 3\,K$, $v = 1650\,\text{m/s}$, $\theta_D = 165\,K$, $z = 5$, $\frac{N}{V} = 0.06 \times 10^{23}\,\text{cm}^{-3}$, $\gamma = 1.49$, $b = 0.438\,\text{nm}$, and $k_D = 7.05\,\text{nm}^{-1}$.

Reference	λ_{latt} (W/m K)	l_{ph} [a] (μm)	l_{ph} [b] (μm)
Ref. [87]	15	48	832
Ref. [86]	230	729	832

indicated a force $F_L = \sigma\,b$ [41, page 81] due to residual shear stresses in a direction away from the edge. However, obviously the image force $F_L = \frac{\mu\,b^2}{4\pi\,(1-\nu)\,R}$ [41, page 88] close to the free surface had the same strength in opposite direction. For this example a residual shear stress of $\sigma = 4 \times 10^6\,\text{Pa}$ was determined.

(iii) Finally, the residual shear stresses can be estimated from the bending radius of the dislocations. The bending radius $r = \frac{E_L}{\sigma\,b}$ [48, pp. 249-250] is determined by the equilibrium of stretching due to the shear stress σ and shortening for minimizing the line energy E_L. For an edge dislocation the line energy is given by $E_L = \frac{\mu\,b^2}{4\pi}\,\frac{1}{1-\nu}\,\ln(\frac{R}{r_0})$ [48, pp. 249-250], where R is half the distance between two dislocations and $r_0 \approx b$ is the dislocation core radius. For a dislocation density of $10^9\,\text{cm}^{-2}$ the line energy is about $20\,\text{eV/nm}$. The bending radius of most dislocations was larger than $100\,\text{nm}$. In summary, a residual shear stress of $\sigma < 74 \times 10^6\,\text{Pa}$ is obtained.

All three examples showed that there is a significant amount of residual shear stress in the sample. This explains, why external shear stresses had not to be applied to enable gliding. In LiF crystals the dislocation velocity varied between $10\,\text{nm/s}$ and $10\,\text{m/s}$ for an applied shear stress between $5 \times 10^6\,\text{Pa}$ and $40 \times 10^6\,\text{Pa}$ [49]. The typical dislocation velocities of free standing dislocation in Bi_2Te_3 was about $10 - 100\,\text{nm/s}$ (Table 7.2). Therefore, residual shear stresses between $5 \times 10^6\,\text{Pa}$ and $15 \times 10^6\,\text{Pa}$ are a reasonable estimation.

7.2.3 Lattice thermal conductivity

Bi_2Te_3 is known for its high thermoelectric figure of merit ZT at room temperature. One reason for this high ZT value is a low lattice thermal conductivity of about $\lambda_{\text{latt}} = 1.5\,\text{W/m}\,K$ at $300\,K$, which was attributed to a high structural disorder [19]. The dependence of the lattice thermal conductivity on structural disorder was nicely demonstrated for single crystalline Si thin films and other model materials [10]. Particularly, at low temperatures phonon scattering on crystal surfaces, grain boundaries, and on the strain field of dislocations is dominant and significantly reduces the lattice thermal conductivity. In single crystalline Bi_2Te_3, only a few measurements of the lattice thermal conductivity cover a wide temperature range [19, 86, 87]. In these measurements the small phonon mean free paths could not be explained by phonon surface-scattering, Umklapp-processes, and isotope scattering alone over the entire temperature range [19]. Therefore, it was assumed that phonon scattering on dislocations should be dominant without proving their existence [19].

The phonon mean free path in Bi_2Te_3 due to phonon scattering on the strain field of dislocations will be estimated and discussed. The measurements of the lattice thermal conductivity [86, 87] showed a peak at about $4 - 9\,K$, which is a typical feature for single crystals. For the discussion only the measurements at the lowest temperatures are of interest, e.g., at a temperature of $3\,K$ the lattice thermal conductivities were found to be $\lambda_{\text{latt}} = 15\,\text{W/m}\,K$ [87] and $\lambda_{\text{latt}} = 230\,\text{W/m}\,K$ [86] (Table 7.3). The phonon mean free path l_{ph} can be calculated as $\lambda_{\text{latt}} = 1/3\,C\,v\,l_{\text{ph}}$ according to transport theory for isotropic solids, where C is the total specific heat and v is the velocity of sound. The specific heat was calculated as $C = \frac{12\pi^4}{5}\,k_B\,z\,\frac{N}{V}\,(\frac{T}{\theta_D})^3$ according to the Debye model at low temperatures, where T is the temperature, θ_D is the Debye

temperature, z is the number of atoms per unit cell, $\frac{N}{V}$ is the number of unit cells per volume, and k_B is the Boltzmann's constant. On the other hand, the phonon mean free path l_{ph} is related to the dislocation density N_D according to $l_{ph} = 0.455\,(\gamma^2\,b^2\,k_D)^{-1}\,\frac{1}{N_D}\frac{\theta_D}{T}$ [9, page 325], where γ is the Grüneisen constant, $\mathbf{b}$ is the Burgers vector, and $k_D = \left(6\pi^2\frac{N}{V}\right)^{\frac{1}{3}}$ is the Debye radius.

Table 7.3 shows the phonon mean free paths determined by transport theory for a dislocation density of $N_D = 10^9\,\text{cm}^{-2}$. Only for a lattice thermal conductivity of $\lambda_{latt} = 230\,\text{W/m K}$ at 3 K [86] the dislocation density is large enough to explain the small phonon mean free path. For a significantly smaller lattice thermal conductivity of $\lambda_{latt} = 15\,\text{W/m K}$ at 3 K [87] the dislocation density should be one order of magnitude higher. However, in the literature only dislocation densities of $10^9\,\text{cm}^{-2}$ were reported in bulk Bi_2Te_3 [24, 25, 33].

There is no reason to assume a higher dislocation density to explain the low lattice thermal conductivity of Bi_2Te_3 reported in Reference [87] without experimental proof. Instead, other types of structural disorder found in n-type and p-type Bi_2Te_3 might explain the discrepancy. (i) Diffraction contrast experiments in the TEM yielded a displacive modulation with a wavelength of 10 nm, which was referred to as natural nanostructure (nns) [34, 63]. The displacement field of the nns is correlated to a sinusoidal strain field which should significantly scatter phonons. The nns is a more promising reason than the dislocations to explain the low lattice thermal conductivity in Bi_2Te_3. (ii) Oscillating dislocations are also known to contribute to phonon scattering and shall be discussed in more detail here.

7.2.4 Ultrasound attenuation

The dislocation resonance theory of Granato and Lücke predicts a strong interaction between phonons and dislocations acting as damped vibrating strings [50–52]. Ultrasound attenuation experiments measure the attenuation $\alpha(\omega)$ and the velocity of sound $v(\omega)$ in dependence of the frequency ω of the incident ultrasound. A related quantity is the decrement $\triangle(\omega) = 2\pi\alpha(\omega)\frac{v(\omega)}{\omega}$. Granato and Lücke derived for the decrement $\Delta(\omega) = \Omega\,\Delta_0\,N_D\,L^2\,f(\frac{\omega}{\omega_0}, D)$, where N_D is the dislocation density, L is the length of the dislocation or of its oscillating segments, $f(\frac{\omega}{\omega_0}, D) = \{\frac{\omega}{\omega_0}/D\}/\{[1 - (\frac{\omega}{\omega_0})^2]^2 + (\frac{\omega}{\omega_0}/D)^2\}$ is the frequency response which depends on the damping constant D and on the ratio of the frequency ω to the resonance frequency ω_0 of the dislocation. Ω is an orientation factor and Δ_0 is a constant. Therefore, ultrasound attenuation is strong for materials with a high density of dislocations.

The effects of dislocations on ultrasound attenuation were nicely demonstrated on HgTe [54]. Measurements on annealed samples at a temperature of 4.2 K as a function of the frequency showed a maximum at 240 MHz. A second experiment at room temperature and for constant frequency showed a hysteresis for a stress applied at right angles to the propagation of sound. Particularly, the latter measurement confirmed the dependence of the attenuation on the dislocation configuration, since the dislocation microstructure was changed.

The relatively high density and mobility of the dislocations in Bi_2Te_3 should be relevant for phonon scattering. A direct proof for the absorption of phonons by dislocations in Bi_2Te_3 was given by ultrasound absorption measurements reported by Esayan [23]. The ultrasound attenuation and the dislocation density were measured on annealed and cold worked n-type and p-type samples in a temperature range of $100 - 300\,\text{K}$ and at a frequency range of $40 - 64\,\text{kHz}$. The measurements showed an increased attenuation (i) at higher frequencies and (ii) at higher dislocation densities. At a temperature between 180 K and 210 K the absorption increased exponentially on temperature, indicating a thermally activated process. Particularly, for cold worked samples an absorption peak at about $230 - 250\,\text{K}$ has formed, which disappeared after annealing. The predictions of Granato and Lücke about the decrement $\triangle(\omega)$ were also checked and confirmed by Esayan. However, the calculations of the decrement $\triangle(\omega)$ were based on a dislocation density of $10^5 - 10^6\,\text{cm}^{-2}$ obtained from optical measurements on etched surfaces, whereas the dislocation density found in the TEM is by several orders of magnitude higher. Therefore, these calculations were reviewed here.

The decrement $\triangle(\omega)$ is determined by a product of three fitting parameters, i.e., (i) the

Table 7.4 Fundamental parameters of the Granato-Lücke theory of dislocation resonance [50, 53] applied to Bi_2Te_3. The dislocation length was assumed to be $L = 2.5 \times 10^{-4}$ cm and the temperature $T = 240$ K.

	A (g/cm)	B (dyn s/cm^2)	C (dyn)	ω_0 (1/s)	f_0 (MHz)	D	Δ_0
Formula	$= \pi \rho b^2$	$= \left(\frac{3 k_B z}{10 v_t a^2} \right) T$	$= \frac{2 \mu b^2}{\pi (1-\nu)}$	$= \frac{\pi}{L} \sqrt{\frac{C}{A}}$	$= \frac{\omega_0}{2\pi}$	$= \omega_0 \frac{A}{B}$	$= \frac{8 \mu b^2}{\pi^3 C}$
Value	4.7×10^{-14}	1.6×10^{-4}	4.4×10^{-4}	1.21×10^9	193	0.37	0.31

Ref. [16] for an overview of material parameters: Burgers vector $\mathbf{b} = [1, 1, 0]$ and $b = 0.438$ nm, mass density $\rho = 7.86$ g/cm^3, shear modulus $\mu = 2.74 \times 10^{11}$ dyn, Poisson's ratio $\nu = 0.24$, number of atoms per unit cell $z = 5$, shear wave velocity $v_t = 1650$ m/s, lattice parameter $a = 0.438$ nm, and Boltzmann's constant k_B.

dislocation length L, (ii) the dislocation density N_D, and (iii) the frequency response $f(\frac{\omega}{\omega_0}, D)$. (i) Esayan used a dislocation length of $L = 2.5 \, \mu$m. Our results support this assumption. The motion of the dislocation indicated no pinning centers and thereby a reduced length of the oscillating segments of the dislocations. Therefore, the dislocation length is limited by the grain size which was found to be $1 - 10 \, \mu$m. (ii) A dislocation density of $N_D = 10^9$ cm^{-2} found by TEM is significantly higher than a value of $10^5 - 10^6$ cm^{-2} reported by Esayan. (iii) Esayan seems to have overestimated the frequency response $f(\frac{\omega}{\omega_0}, D)$. The fundamental parameters which determine the resonance frequency $\omega_0 = 2\pi f_0$ and the normalised damping coefficient D are the effective dislocation mass per unit length A, the damping force per unit length B, and the dislocation line energy C [50, 53] (Table 7.4). The resonance frequency of dislocations in Bi_2Te_3 should be about 217 MHz (Table 7.4). This is by orders of magnitude higher than the frequencies used in the ultrasound experiments by Esayan. Therefore, in the low frequency range the frequency response can be approximated by $f(\frac{\omega}{\omega_0}, D) \approx \frac{\omega}{\omega_0}/D = B \frac{\omega}{A\omega_0^2}$. Esayan assumed for the damping force a value of $B \approx 10^{-2}$ dyn s/cm^2. We found a significantly smaller value of $B \approx 10^{-4}$ dyn s/cm^2 (Table 7.4), which is in the typical range of damping forces found in other materials [52, 54].

In summary, the decrement $\Delta(\omega)$ in the low frequency range is determined by the product of the dislocation density N_D, the damping force B, and the dislocation length L. Esayan [23] used a dislocation density being by two or three orders of magnitude too small and a damping force being by two or three orders of magnitude too large. Therefore, the Granato-Lücke theory of dislocation resonance seems still to be a good model to explain ultrasound attenuation in Bi_2Te_3.

Both, the estimations of the lattice thermal conductivity and of the ultrasound attenuation confirmed the relevance of phonon scattering on dislocations in Bi_2Te_3. However, this conclusion is still something doubtful since the calculations are not based on combined measurements of the microstructure and of the transport properties on the same sample, which would be highly recommended in future.

Chapter 8

Image simulation of strain fields

8.1   Strain field and line energy of a dislocation

In Chapter 2.5 it was pointed out that the diffraction contrast in the TEM is determined by the displacement function $\beta(z) = \frac{\partial}{\partial z}(\mathbf{g} \cdot \mathbf{u})$, where $\mathbf{g}$ is the diffracting plane, $\mathbf{u}$ is the displacement field, and $\frac{\partial \mathbf{u}}{\partial x_l}$ is the strain field of the extended crystal defect. In Chapter 2.2 the displacement field and the strain field of a dislocation in an elastically isotropic crystal was given (Eq. 2.12 and 2.13). For elastically anisotropic crystals the displacement field, the strain field, and the line energy of a dislocation with Burgers vector $\mathbf{b}$ and line direction $\mathbf{t}$ was calculated by Eshelby [43], Stroh [44, 45], and by Barnett and Lothe [46]. An overview of these more advanced theories was given in the textbook of Hirth and Lothe [41, chap. 13.7]

The displacement field $\mathbf{u}$ is determined by an equilibrium condition for the stress field (Eq. 2.6), the Burgers circuit (Eq. 2.6), and the plane strain property (Eq. 2.9). According to Stroh [45] the solution for the displacement field can be expressed in terms of orthonormal plane basis vectors $\mathbf{m}$ and $\mathbf{n}$ defined by $\mathbf{t} = \mathbf{m} \times \mathbf{n}$ (Eq. 2.7, Fig. 2.1(c)). Eshelby proposed an "Ansatz" for the displacement field of the form

$$\mathbf{u} = \mathbf{A}\, f(\mathbf{m} \cdot \mathbf{x} + p\, \mathbf{n} \cdot \mathbf{x})\,, \tag{8.1}$$

where the coefficient p and the vector $\mathbf{A}$ are determined by Equations 2.6. Using this "Ansatz", the equilibrium condition (Eq. 2.6) is transformed into a homogeneous linear equation system

$$\left\{ (mm) + p\left[(mn) + (nm) \right] + p^2 (nn) \right\} \mathbf{A} = 0\,. \tag{8.2}$$

The components of the 3×3 matrices (mm), (mn), (nm), and (nn) are defined by

$$(mm)_{jk} = m_i\, c_{ijkl}\, m_l\,, \tag{8.3a}$$

$$(mn)_{jk} = m_i\, c_{ijkl}\, n_l\,, \tag{8.3b}$$

$$(nm)_{jk} = n_i\, c_{ijkl}\, m_l\,, \tag{8.3c}$$

$$(nn)_{jk} = n_i\, c_{ijkl}\, n_l\,, \tag{8.3d}$$

where c_{ijkl} are the tensor components of the elastic constants. The equation system (Eq. 8.2) only yields non vanishing values for $\mathbf{A}$ for

$$\det \left\{ (mm) + p\left[(mn) + (nm) \right] + p^2\, (nn) \right\} = 0\,, \tag{8.4}$$

which is a six degree equation with respect to the coefficient p. Eshelby and Stroh showed, that all six p values are distinct and occur in three complex conjugate pairs. The three roots with positive imaginary part were denoted by p_1, p_2, and p_3. The three roots with negative imaginary part were denoted by $p_4 = \bar{p}_1$, $p_5 = \bar{p}_2$, and $p_6 = \bar{p}_3$.

It is possible to recast the equation system 8.2 into a six-dimensional eigenvalue problem given by

$$N\boldsymbol{\xi} = p\,\boldsymbol{\xi}\,, \tag{8.5a}$$

$$\boldsymbol{\xi} = \left\{ \begin{matrix} \mathbf{A} \\ \mathbf{L} \end{matrix} \right\}\,, \tag{8.5b}$$

$$\mathbf{L} = -\left\{ (nm) + p\,(nn) \right\}\mathbf{A}\,, \tag{8.5c}$$

$$N = -\begin{pmatrix} s & q \\ b & s^{\mathrm{T}} \end{pmatrix}\,, \tag{8.5d}$$

$$q = (nn)^{-1}\,, \tag{8.5e}$$

$$s = (nn)^{-1}(nm)\,, \tag{8.5f}$$

$$b = (mn)(nn)^{-1}(nm) - (mm)\,. \tag{8.5g}$$

The eigenvalues p_α ($\alpha = 1, 2, \ldots, 6$) are solutions of the determinental relation $\det(N - p\,I) = 0$, being identical with Equation 8.4. Particularly, the 3×3 matrices q, s, and b are of interest in the following. According to Eshelby and Stroh, for normalised eigenvectors defined by $2\,\mathbf{A}_\alpha \cdot \mathbf{L}_\alpha = 1$ (no sum on α) the displacement field and the strain field are given by

$$\mathbf{u} = \frac{1}{2\pi i} \sum_{\alpha=1}^{6} \pm \mathbf{A}_\alpha\,(\mathbf{L}_\alpha \cdot \mathbf{b})\,\ln\left(\mathbf{m} \cdot \mathbf{x} + p_\alpha\,\mathbf{n} \cdot \mathbf{x}\right)\,, \tag{8.6a}$$

$$\frac{\partial \mathbf{u}}{\partial x_l} = \frac{1}{2\pi i} \sum_{\alpha=1}^{6} \pm \mathbf{A}_\alpha\,(\mathbf{L}_\alpha \cdot \mathbf{b})\,\frac{m_l + p_\alpha\,n_l}{\mathbf{m} \cdot \mathbf{x} + p_\alpha\,\mathbf{n} \cdot \mathbf{x}}\,, \tag{8.6b}$$

where the positive sign has to be used for $\alpha = (1, 2, 3)$ and the negative sign for $\alpha = (4, 5, 6)$.

At this point, Barnett and Lothe introduced cylinder coordinates r and θ (Eq. 2.10, Fig. 2.1(c)) and the integral formalism to further simplify the expression for the strain field. The plane basis vectors $\mathbf{m}$ and $\mathbf{n}$ were expressed in terms of fixed orthonormal plane basis vectors $\mathbf{m}_0$ and $\mathbf{n}_0$ rotated by an angle θ (Eq. 2.10, Fig. 2.1(c)). Therefore, the matrices (mm), (mn), (nm), and (nn) (Eq. 8.3) and the related matrices q, s, and b (Eq. 8.5) depend on the azimuth angle θ. The components of the latter matrices were integrated over θ, yielding 3×3 matrices Q, S, and B defined by

$$Q_{jk} = -\frac{1}{2\pi} \int_0^{2\pi} q_{jk}\,d\theta\,, \tag{8.7a}$$

$$S_{jk} = -\frac{1}{2\pi} \int_0^{2\pi} s_{jk}\,d\theta\,, \tag{8.7b}$$

$$B_{jk} = -\frac{1}{2\pi} \int_0^{2\pi} b_{jk}\,d\theta\,. \tag{8.7c}$$

Barnett and Lothe showed, that the combinations of the eigenvectors $\mathbf{A}_\alpha$ and $\mathbf{L}_\alpha$ in Equation 8.6 are related to these integrals. Particularly, the strain field can be expressed in terms of the real matrices q, s, b, Q, S, and B, yielding

$$\frac{\partial \mathbf{u}}{\partial x_l}(r, \theta) = \frac{1}{2\pi}\frac{1}{r}\left(m_l\,\mathbf{s}_\mathrm{m} + n_l\,\mathbf{s}_\mathrm{n}\right)\,, \tag{8.8a}$$

$$\mathbf{s}_\mathrm{m} = -S\,\mathbf{b}\,, \tag{8.8b}$$

$$\mathbf{s}_\mathrm{n} = q\,(B\,\mathbf{b}) + s\,(S\,\mathbf{b})\,. \tag{8.8c}$$

This result is similar to the results obtained for isotropic crystals, only the vectors $\mathbf{s}_\mathrm{m}$ and $\mathbf{s}_\mathrm{n}$ had to be redefined (Eq. 2.13).

Finally, the line energy of the dislocation is given by

$$E_{\mathrm{L}} = \frac{1}{4\pi}\, \mathbf{b} \cdot (B\,\mathbf{b})\, \ln\left(\frac{R}{r_0}\right) \,, \tag{8.9}$$

where r_0 is the dislocation core radius and R is half the distance between the dislocations.

In summary, the displacement field, the strain field, the stress field, and the line energy of dislocations in elastically anisotropic crystals show following fundamental properties:

Dislocation property (i) The displacement field, the strain field, and the stress field show plain strain properties and are proportional to the Burgers vector.

Dislocation property (ii) The strain field and the stress field can be expressed in terms of cylinder coordinates r and θ, and of real matrices. Particularly, the matrices Q, S, and B only depend on the line direction and on the material constants.

Dislocation property (iii) The strain field and the stress field are inversely proportional to the radius r.

Dislocation property (iv) The strain field and the stress field can be resolved in a factor only depending on the radius r and a factor only depending on the azimuth angle θ.

Dislocation property (v) The line energy is proportional to $|\mathbf{b}|^2$. Therefore, dislocations with Burgers vectors $\mathbf{b}$ which correspond to shortest lattice vectors are energetically favourable.

Dislocation property (vi) The line energy depends on the line direction $\mathbf{t}$ and the material constants.

8.2 Principles of programming

8.2.1 Aim of image simulation, geometry, and displacement function

Burgers vector, absorption coefficient, and computing time

In Chapter 2.5 an introduction in the two-beam dynamical diffraction theory of Howie and Whelan [55, 56] and in the image simulation of strain fields was given. The diffraction contrast in the TEM was described by the Howie-Whelan equations (Eq. 2.27) for the complex amplitudes of the direct beam T and the diffracted beam S, which depend on a large part on the displacement function $\beta(z)$, the absorption coefficients A and N, the extinction distance $\xi_{\mathbf{g}}$, and the dimensionless excitation error w (Eq. 2.29).

The most import aim of the image simulation of dislocations is the determination of the Burgers vector $\mathbf{b}$. For anisotropic crystals the $\mathbf{g} \cdot \mathbf{b} = 0$ criterion for dislocations being out of contrast is not valid and useless, there will be a significant diffraction contrast also under this condition.

The absorption coefficients A and N are fundamental material parameters, which are usually assumed to be identical ($A = N$) [47, chap. 2.4]. Similar to the extinction distance $\xi_{\mathbf{g}}$, the absorption coefficients differ for each Bragg reflection $\mathbf{g}$. The aim is to get a complete table, which contains for each Bragg reflection the corresponding extinction distance and absorption coefficients. This table can then be used for image simulation of other extended crystal defects in the same material, e.g., the nns in Bi_2Te_3.

The limiting factor for the usefulness of image simulation is the computing time, which is closely related to the number of columns and slices, the complexity of the displacement function, and the efficiency of the programme and the software. For numerical integration of the Howie-Whelan equations the volume was subdivided in cells with a size of $(dx \times dy \times dz) \approx (2\,\mathrm{nm} \times 2\,\mathrm{nm} \times 2\,\mathrm{nm})$, yielding a total number of lattice sites of $(N_{\mathrm{x}} \times N_{\mathrm{y}} \times N_{\mathrm{z}}) \approx (100 \times 50 \times 100) = 500{,}000$ (Fig. 8.1(a)). Therefore, for one simulated image at least $4 \times 500{,}000$ computations are necessary, since for each cell of the volume the displacement function β (Eq.
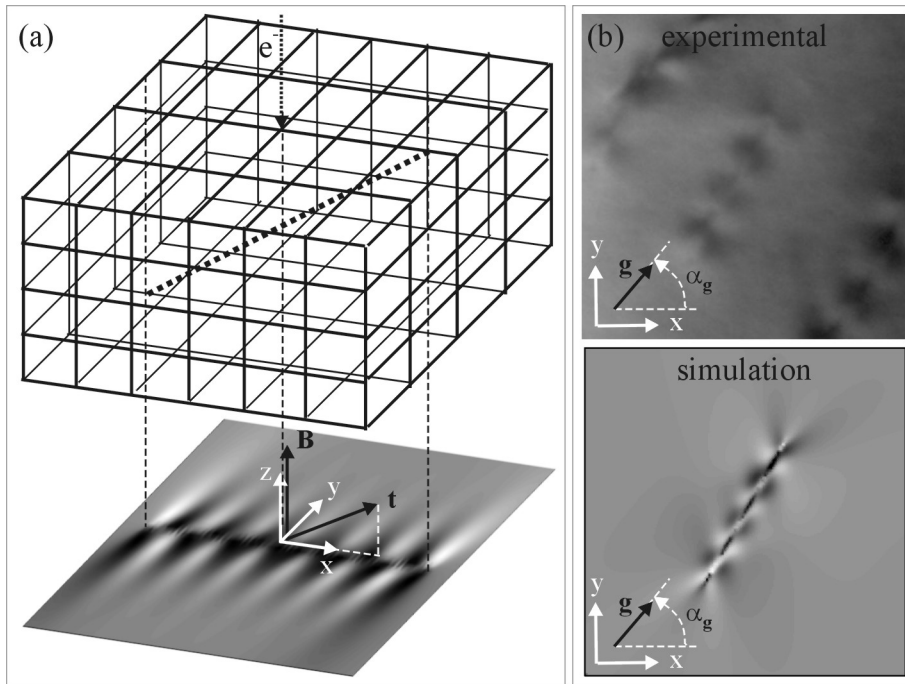
Figure 8.1 Geometries for image simulation. The beam direction **B** is parallel to the z axis and in opposite direction to the physical beam direction. (a) The line direction points towards the positive x axis. (b) The x axis was chosen such that the diffracting vector **g** in the experimental and in the simulated images have the same orientation (angle $\alpha_{\mathbf{g}}$).

2.29), the transformation matrices (K_n) for the amplitudes (Eq. 2.31), the complex amplitudes T and S (Eq. 2.31), and the intensities I_{T} and I_{S} (Eq. 2.28) of the direct beam and the diffracted beam have to be calculated. Head achieved a computing time of about $40 - 50\,\mathrm{s}$ for one image of a dislocation [47].

The aim of this work was to further reduce the computing time for one image of a dislocation, since a large number of simulations is required for stereomicroscopy experiments: In $\mathrm{Bi_2Te_3}$ there are three energetically favourable Burgers vectors, which are $[1,0,0]$, $[0,1,0]$, and $[1,1,0]$. Fortunately, the diffraction contrast is very sensitive to the Burgers vector, so that only one two-beam image might be enough to rule out the wrong Burgers vectors. However, approximately five different values for the absorption coefficient ($A = 0,\ldots,0.15$) and five different values for the excitation error ($w = -1,\ldots,1$) might be required for an unambiguous result, yielding up to 25 image simulations for each two-beam image. In Chapter 8.3.2 a stereomicroscopy experiment will be presented with 11 two-beam images of the same dislocation. Therefore, about 275 image simulations would be required only for this experiment. The total computing time for the entire experiment would be less than $1\,\mathrm{h}$ for a computing time of $10\,\mathrm{s}$ per image. In summary, a complete stereomicroscopy experiment could be surely analysed within one day.

Geometry

A fast image simulation programme for dislocations was reported by Head [47]. Head used a geometry similar to that shown in Figure 8.1 [47, chap. 4.4]. The beam direction **B** was chosen in opposite direction to the physical beam direction and the z axis was chosen to be parallel to the beam direction **B**. The orientation of the x axis was defined in two different ways. (a) The line direction **t** points towards the positive x axis (Fig. 8.1(a)). Therefore, the projection of the defect line runs from left to right in the micrograph. The defect is at the bottom of the foil at the left-hand side and at the top on the right-hand side. (b) The x axis was chosen such

that the orientation of the diffracting vector $\mathbf{g}$, i.e., its angle $\alpha_{\mathbf{g}}$ to the x axis, are identical in the experimental and in the simulated images (Fig. 8.1(b)). Particularly, experimental images as acquired can be simulated by using this definition of the x axis.

Displacement function $\beta(z)$ and singularities at the dislocation core

Two different axis systems have to be used for image simulation of dislocations. The first axis system (axes Ox, Oy, and Oz) is related to the beam direction $\mathbf{B}$ and the line direction $\mathbf{t}$ or to the diffracting vector $\mathbf{g}$ as shown in Figure 8.1, and is referred to as experimental axis system in the following. The second axis system (axes Ox_1, Ox_2, and Ox_3) is related to the crystal structure, and is referred to as crystal axis system in the following. The Howie-Whelan equations (Eq. 2.27) and particularly the displacement function $\beta(z) = \mathbf{g} \cdot \frac{\partial \mathbf{u}}{\partial z}$ (Eq. 2.29) were derived with respect to the experimental axis system. The elastic constants c_{mn} and particularly the strain field $\frac{\partial \mathbf{u}}{\partial x_l}$ (Eq. 8.8) of the dislocation were derived with respect to the crystal axis system. Therefore, $\frac{\partial \mathbf{u}}{\partial z}$ is not identical to $\frac{\partial \mathbf{u}}{\partial x_3}$ and has to be considered.

First, in the Howie-Whelan equations (Eq. 2.27) the physical beam direction is relevant, which is in opposite direction to the beam direction $\mathbf{B}$ defined here (Fig. 8.1(a)). Therefore, for the calculation of the displacement function $\beta(z)$ (Eq. 2.29) an additional negative sign had to be introduced, i.e., $\beta(z) = -\frac{\partial}{\partial z}(\mathbf{g} \cdot \mathbf{u})$. Second, the matrix $(R_{\mathbf{B}})$ transforms vector components x_i and derivatives $\frac{\partial}{\partial x_i}$ from the crystal axis system into the experimental axis system according to $x_i' = (R_{\mathbf{B}})_{ij} \, x_j$ and $\frac{\partial}{\partial x_i'} = (R_{\mathbf{B}})_{ij} \, \frac{\partial}{\partial x_j}$, and particularly $\frac{\partial}{\partial z} = (R_{\mathbf{B}})_{3j} \, \frac{\partial}{\partial x_j}$ In summary, under consideration of these transformation laws and Equation 8.8 the displacement function $\beta(z)$ is given by

$$\beta(r,\theta) = -\frac{1}{2\pi}\frac{1}{r}\,\beta_\theta(\theta)\,, \tag{8.10a}$$

$$\beta_\theta(\theta) = \mathbf{g} \cdot \left[(\mathbf{R}_{\mathrm{z}} \cdot \mathbf{m})\,\mathbf{s}_{\mathrm{m}} + (\mathbf{R}_{\mathrm{z}} \cdot \mathbf{n})\,\mathbf{s}_{\mathrm{n}} \right]\,, \tag{8.10b}$$

$$\mathbf{s}_{\mathrm{m}} = -S\,\mathbf{b}\,, \tag{8.10c}$$

$$\mathbf{s}_{\mathrm{n}} = q\,(B\,\mathbf{b}) + s\,(S\,\mathbf{b})\,, \tag{8.10d}$$

$$(\mathbf{R}_{\mathrm{z}})_j = (R_{\mathbf{B}})_{3j}\,. \tag{8.10e}$$

The transformation matrix $R_{\mathbf{B}}$ and the related transformation vector $\mathbf{R}_{\mathrm{z}}$ will be given in Appendix C.3.3.

In contradiction to Head, the number of lattice sites N_{x}, N_{y}, and N_{z} (Fig. 8.1(a)) were chosen to be odd integer numbers in this work. Therefore, the strain field and thereby the amplitudes at the dislocation core in the centre of the micrograph will also be calculated. However, close to the dislocation core at distances $r < |\mathbf{b}|$ linear elasticity theory and also numerical integration break down, since the strains and thereby the displacement function β become large. Therefore, close to the dislocation core the radius r was replaced by $|\mathbf{b}|$ in Equation 8.10 to avoid programme aborts due to the singular character of the strain field at the dislocation core (Eq. 8.8 and 8.10). Also, at the centre of the dislocation core ($r = 0$) the displacement function was assumed to be zero since the cylinder coordinates would be not defined.

$$\beta(r,\theta) = \begin{cases} -\frac{1}{2\pi}\frac{1}{r}\,\beta_\theta(\theta) & \text{for } r > |\mathbf{b}| \\ -\frac{1}{2\pi}\frac{1}{|\mathbf{b}|}\,\beta_\theta(\theta) & \text{for } 0 < r \le |\mathbf{b}| \\ 0 & \text{for } r = 0 \end{cases}\,. \tag{8.11}$$

8.2.2 Effective programming

Cylinder coordinates versus generalised cross section

In this section, the most significant differences between the software implementations of the image simulation of dislocations in this work and of Head [47] will be discussed (Table 8.1). Head achieved a computing time of $40 - 50\,\mathrm{s}$ per image by ingenious programming. Meanwhile,

Table 8.1 Principles of effective programming for image simulation.

A.K. Head et al. [a]	This work
Strain field according to the Stroh formalism [b]	Strain field according to the integral formalism of D.M. Barnett and J. Lothe [c]
Generalized cross section	Cylinder coordinates
Runga-Kutta method	"Pendellösung" method
FORTRAN	MATLAB®
Serial computing with "for"-loops	Parallel computing with matrix algebra and multi-dimensional arrays

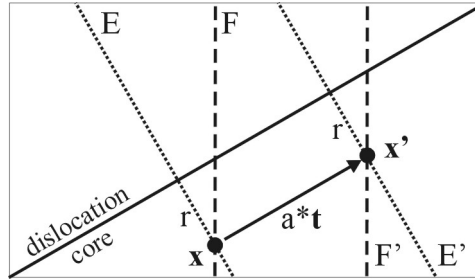[a]Ref. [47]. [b]Ref. [44, 45]. [c]Ref. [46].

Figure 8.2 Dislocation in cross section and effective programming by using generalised cross sections (planes E or F) or cylinder coordinates (r, θ). The displacement field and the strain field are identical at two points $\mathbf{x}$ and $\mathbf{x}' = \mathbf{x} + a \cdot \mathbf{t}$, where $\mathbf{t}$ is the line direction and a is an arbitrary factor.

faster personal computer are available. However, even with modern computers the computing time for one simulated image can exceed several hours for not optimised programmes. Therefore, the computing time is determined in a large part by effective programming and by the use of software specialised on solving mathematical problems.

Head used the Stroh formalism (Eq. 8.6) to calculate the strain field of the dislocation, whereas in this work the integral formalism (Eq. 8.8) of Barnett and Lothe was used (Chap. 8.1, Table 8.1). Head could reduce the computing time drastically due to the plane strain property of the strain field of the dislocation; $\frac{\partial \mathbf{u}}{\partial x_l}(\mathbf{x}) = \frac{\partial \mathbf{u}}{\partial x_l}(\mathbf{x} + a \cdot \mathbf{t})$ (Eq. 8.6) since $\mathbf{m} \cdot \mathbf{t} = 0$ and $\mathbf{n} \cdot \mathbf{t} = 0$ hold, where $\mathbf{t}$ is the line direction and a is an arbitrary factor. Figure 8.2 shows a dislocation within the sample in cross section. Planes E and E' are perpendicular to the line direction $\mathbf{t}$ of the dislocation (Fig. 8.2). Due to the plane strain property, the strain fields at a point $\mathbf{x}$ on plane E and at a point $\mathbf{x}' = \mathbf{x} + a \cdot \mathbf{t}$ on plane E' have the same values. Head showed, that for image simulation the strain field or the displacement function $\beta(z)$ have only to be precalculated on a plane E and these values can be transferred to the corresponding points on the parallel plane E'. Plane E was referred to as generalised cross section by Head [47, chap. 4.2.1]. It is also possible to choose a plane F, being parallel to the beam direction B, as generalised cross section (Fig. 8.2) and to transfer the values to the parallel plane F' under consideration of $\mathbf{x}' = \mathbf{x} + a \cdot \mathbf{t}$.

According to Barnett and Lothe the strain field can be expressed in terms of cylinder coordinates (r, θ) (Eq. 8.8). Obviously, the concept of the generalised cross section is also valid when using cylinder coordinates; $\frac{\partial \mathbf{u}}{\partial x_l}(r, \theta) = \frac{\partial \mathbf{u}}{\partial x_l}(r', \theta')$ (Eq. 8.8) since $\mathbf{m}_0 \cdot \mathbf{t} = 0$ and $\mathbf{n}_0 \cdot \mathbf{t} = 0$ and thereby $(r, \theta) = (r', \theta')$ (Eq. 2.10) hold for $\mathbf{x}' = \mathbf{x} + a \cdot \mathbf{t}$. It also turned out that the strain field (Eq. 8.8) can be resolved in a factor only depending on the radius r and factor only depending on the azimuth angle θ. The displacement function $\beta(r, \theta) = -\frac{1}{2\pi} \frac{1}{r} \beta_\theta(\theta)$ (Eq. 8.10) shows the same property. In this work, the latter factor $\beta_\theta(\theta)$ was precalculated to accelerate image simulation, i.e, the strain field or the displacement function have only to be precalculated on a unit circle around the dislocation core in the generalised cross-section plane E.

"Pendellösung" method versus Runge-Kutta method

Head used the Runge-Kutta method for numerical integration of the Howie-Whelan equations (Table 8.1), represented by the transformation matrices (K_n) (Eq. 2.31). In this work a simpler method referred to as "Pendellösung" method was used for the calculation of the transformation matrices (K_n). In Appendix C.5 derivations for the transformation matrices (K_n) will be given in detail. For both methods the transformation matrices (K_n) depend in a large part on the displacement function. The "Pendellösung" method (i) assumes a constant displacement function within each slice, (ii) the differential equations were transformed by an "Ansatz" into algebraic equations which were solved, finally (iii) the transformation matrix is a mean value of two matrices (Eq. C.25). The Runga-Kutta method is a more general method for numerical integration of first-order differential equations $\frac{\partial \mathbf{y}}{\partial z} = f(z, \mathbf{y})$. This method requires the calculation of the displacement function at the top, at the bottom, and in the center of each slice. The transformation matrix (K_n) is a mean value of four matrices (Eq. C.26). The Runge-Kutta method is slower than the "Pendellösung" method, since more calculations required.

Parallel computing versus serial computing

The calculation of multiple products of matrices and vectors are required for the strain field, the displacement function, and also for the numerical integration of the Howie-Whelan equations. Head used the programming language FORTRAN for the implementation of image simulation (Table 8.1). However, programming languages like FORTRAN are not able do matrix algebra. Products of matrices and vectors have to be solved by "for"-loops. E.g., the line energy in Equation 8.9 contains the term $\mathbf{b} \cdot (B\,\mathbf{b})$, which is identical with $b_i\,B_{ij}\,b_j$ in index notation. With FORTRAN, two "for"-loops with respect to the indices i and j would be required to calculate this sum of products element by element.

   In this work MATLAB® was used, which is a software specialised for mathematical problems and particularly for matrix algebra. With MATLAB®, expressions such as $\mathbf{b} \cdot (B\,\mathbf{b})$ can be solved with the slower "for"-loops or directly by matrix algebra. E.g., the MATALAB® code would be given by "`b'*(B*b)`". The software automatically recognises the character of the variables and adopts the operators between the variables to the problem. The operator "`'`" transposes the column vector $\mathbf{b}$ into a row vector $\mathbf{b}^{\mathrm{T}}$. The term in brackets will be treated as a product of the matrix B with a column vector $\mathbf{b}$ and yields a column vector $\mathbf{c}$. Finally, the outer product will be treated as scalar product between the row vector $\mathbf{b}^{\mathrm{T}}$ and the column vector $\mathbf{c}$. Particularly, for the calculation of the Q, S, and B matrices (Eq. 8.7) and for the angle depended term of the displacement function (Eq. 8.10) the matrix algebra is of advantage and reduced drastically the computing time.

   A second time saving feature of MATLAB® is to use multi-dimensional arrays for functions of several variables. Examples for simple arrays are vectors being one-dimensional arrays and matrices being two-dimensional arrays. For basic functions such as $\sin(x)$, MATLAB® will return at once (i) a scalar $f = \sin(x)$ for x being a scalar, (ii) a vector with components $f_j = \sin(x_j)$ for x being a vector, (iii) a matrix with components $f_{jk} = \sin(x_{jk})$ for x being a matrix, and finally (iv) a three-dimensional array with components $f_{ijk} = \sin(x_{ijk})$ for x being a three-dimensional array. Particularly, the time consuming "for"-loops can be avoided by using multi-dimensional arrays. This property can also be extended to ordinary multiplication operators "`*`" and division operators "`/`" by replacing them by the operators "`.*`" and "`./`", respectively. E.g., for two matrices A and B the expression "`C=A/B`" would yield an error and "`C=A*B`" would yield a matrix multiplication according to $C_{ij} = A_{ik}\,B_{kj}$; whereas "`C=A./B`" and "`C=A.*B`" would yield a component by component division and multiplication according to $C_{ij} = A_{ij}/B_{ij}$ and $C_{ij} = A_{ij}/B_{ij}$ (no sum on i and j), respectively. Finally, functions can be defined which are compatible with multi-dimensional arrays by using combinations of basic functions and the "`.`"-operator.

   In this work, the coordinates X, Y, and Z which address the $500,000$ cells of the analysed volume were stored in three-dimensional arrays. The definitions of the functions for the displacement function $\beta(X, Y, Z)$, the transformation matrices $K_n(\beta)$, the amplitudes (T, S), and the

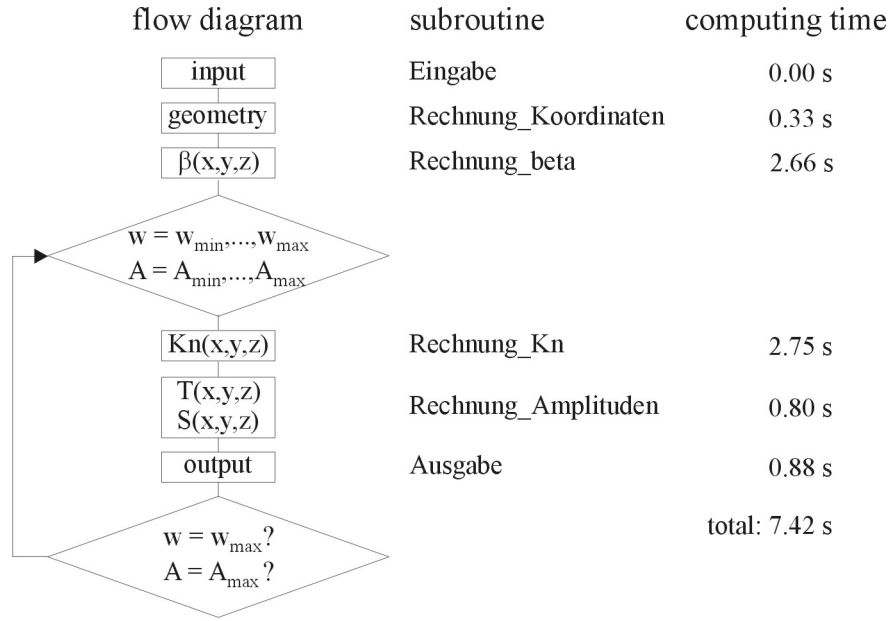| flow diagram	subroutine	computing time
input	Eingabe	0.00 s
geometry	Rechnung_Koordinaten	0.33 s
$\beta(x,y,z)$	Rechnung_beta	2.66 s
$w = w_{\min},...,w_{\max}$ $A = A_{\min},...,A_{\max}$		
$Kn(x,y,z)$	Rechnung_Kn	2.75 s
$T(x,y,z)$ $S(x,y,z)$	Rechnung_Amplituden	0.80 s
output	Ausgabe	0.88 s
		total: 7.42 s
$w = w_{\max}$? $A = A_{\max}$?		

Figure 8.3 Structure of the main programme and computing time for the various subroutines. The volume was subdivided in $125 \times 47 \times 79 = 464,125$ lattice sites.

intensities $(I_{\mathrm{T}}, I_{\mathrm{S}})$ are compatible with three-dimensional arrays. Therefore, time consuming "for"-loops could be avoided for the determination of these quantities .

8.2.3   Main programme and flow diagram

Throughout the entire programme subroutines and functions were used, which help to keep a clear structure. The entire programme is kept as simple as possible. Even a user who is not familiar with MATALB in detail can easily use the programme, since particularly only the input parameters have to be changed.

The main programme "Start" is build up by following subroutines:

(i) Subroutine "Eingabe" for defining the input parameters, which are the acceleration voltage U of the microscope, the lattice parameters (a, c) and the basis vectors $(\mathbf{a}_1, \mathbf{a}_2, \mathbf{a}_3)$ of the crystal lattice, the elastic constants c_{mn}, the diffracting vector $\mathbf{g}$, the extinction distance $\xi_{\mathbf{g}}$, the Burgers vector $\mathbf{b}$, the line direction $\mathbf{t}$, the beam direction $\mathbf{B}$, the foil normal $\mathbf{F}$, the foil thickness d_{F}, the size of the image $(L_{\mathrm{x}}, L_{\mathrm{y}})$, the size of the cells (dx, dy, dz), the dimensionless excitation error w, and the absorption coefficient A. All lengths have to entered in nanometers and all vectors in Miller indices. Particularly, the size of the simulated image can be adopted to the experimental image.

(ii) Subroutine "Rechnung_Koordinaten" for the transformation of the input parameters from the crystal axis system into the experimental axis system.

(iii) Subroutine "Rechnung_beta" for the calculation of the displacement function.

(iv) Subroutine "Rechnung_Kn" for the calculation of the transformation matrices.

(v) Subroutine "Rechnung_Amlituden" for the calculation of the amplitudes and intensities.

(vi) Subroutine "Ausgabe" for the presentation of the output parameters as contour maps and diagrams. Examples for such diagrams are the displacement function and the intensities of the direct beam and the diffracted beam in dependence of the specimen thickness at

Table 8.2 Image simulation parameters for dislocations in aluminium and β-brass shown in Figures 8.4 and 8.5.

Micro-graph	Diffracting vector $\mathbf{g}$	Beam direction $\mathbf{B}$	Extinction distance $\xi_{\mathbf{g}}$ (nm)	Excitation error w	Absorption coefficient A	$\mathbf{g} \cdot \mathbf{b}$
		aluminium [a]				
(a)	$(-2, 0, 0)$	$[0, 1, 3]$	70.2	0.45	0.07	1
(b)	$(0, 2, 0)$	$[1, 0, 3]$	70.2	0.50	0.07	-1
(c)	$(-1, 1, 1)$	$[10, 1, 11]$	58.0	0.20	0.06	0
(d)	$(1, 1, -1)$	$[1, 5, 6]$	58.0	0.15	0.06	-1
(e)	$(-2, 0, 2)$	$[8, -1, 8]$	119.2	0.33	0.09	1
(f)	$(2, -2, 0)$	$[1, 1, 8]$	119.2	0.29	0.09	0
(g)	$(-3, -1, 1)$	$[6, -1, 17]$	147.8	0.97	0.11	2
		β-brass [b]				
(a)	$(0, -1, 1)$	$[2, 3, 3]$	32.4	0.12	0.07	2
(b)	$(1, -1, 0)$	$[3, 3, 4]$	32.4	0.57	0.07	2
(c)	$(1, 0, -1)$	$[5, 3, 5]$	32.4	0.20	0.07	0
(d)	$(0, 2, 0)$	$[4, 0, 7]$	44.6	0.18	0.08	-2
(e)	$(1, -2, 1)$	$[6, 7, 8]$	57.6	0.60	0.10	4
(f)	$(2, -1, -1)$	$[6, 5, 7]$	57.6	0.90	0.10	2

[a]Ref. [47, chap. 5.2]: acceleration voltage $U = 100\,\mathrm{kV}$, lattice parameter $a = 0.406\,\mathrm{nm}$, Burgers vector $\mathbf{b} = \frac{1}{2}[-1, -1, 0]$, line direction $\mathbf{t} = [5, 2, 3]$, foil normal $\mathbf{F} = [5, 2, 8]$, foil thickness $d_{\mathrm{F}} = 258\,\mathrm{nm}$, elastic constants $c_{11} = 10.82 \times 10^{10}\,\mathrm{Pa}$, $c_{12} = 6.13 \times 10^{10}\,\mathrm{Pa}$, and $c_{44} = 2.85 \times 10^{10}\,\mathrm{Pa}$, the extinction lengths were reduced by a factor of 0.826 for consideration of n-beam systematic conditions.
[b]Ref. [47, chap. 5.3]: acceleration voltage $U = 100\,\mathrm{kV}$, lattice parameter $a = 0.294\,\mathrm{nm}$, Burgers vector $\mathbf{b} = [1, -1, 1]$, line direction $\mathbf{t} = [5, -4, 5]$, foil normal $\mathbf{F} = [2, 1, 3]$, foil thickness $d_{\mathrm{F}} = 155\,\mathrm{nm}$, elastic constants $c_{11} = 12.91 \times 10^{10}\,\mathrm{Pa}$, $c_{12} = 10.97 \times 10^{10}\,\mathrm{Pa}$, and $c_{44} = 8.24 \times 10^{10}\,\mathrm{Pa}$.

any column of the analysed volume. Examples of contour maps are the bright field and the corresponding dark field images.

The flow diagramme, the corresponding subroutines at each step of the programme, and the computing times are shown in Figure 8.3. The last three subroutines are embedded in loops with respect to the dimensionless excitation error w and the absorption coefficient A.

8.3 Results and discussion

8.3.1 Dislocations in aluminium and β-brass

In the textbook of Head [47] image simulation was carried out on dislocations in the nearly elastically isotropic aluminium (anisotropy ratio $A = 1.2$, Eq. 2.5) and the highly elastically anisotropic β-brass (anisotropy ratio $A = 8.5$, Eq. 2.5). The input parameters for the simulation of dislocations in both materials are summarised in Table 8.2. The experimental and simulated images of Head are shown in Figures 8.4 and 8.5. The simulated images of this work are also shown in these figures.

There is a good agreement between the experimental and simulated images. Particularly, the positive test results for the highly anisotropic β-brass is important. However, image simulation is also required for nearly isotropic materials such as aluminium. Dislocations were imaged with strong diffraction contrast although the $\mathbf{g} \cdot \mathbf{b} = 0$ criterion for dislocations being out of contrast was fulfilled (micrographs (c) and (f)).

The computing times were measured for a dislocation in aluminium (micrograph (d)). Head achieved a computing time of $40 - 50\,\mathrm{s}$ for a volume subdivided in 7740 columns and each column subdivided in 64 slices, yielding about $500,000$ cells [47, pp. 4, 317-318]. Our programme achieved a computing time of less than $10\,\mathrm{s}$ (Fig. 8.3) which is a highly satisfactorily result. Image simulation is no longer the most time consuming part of the entire stereomicroscopy experiment.
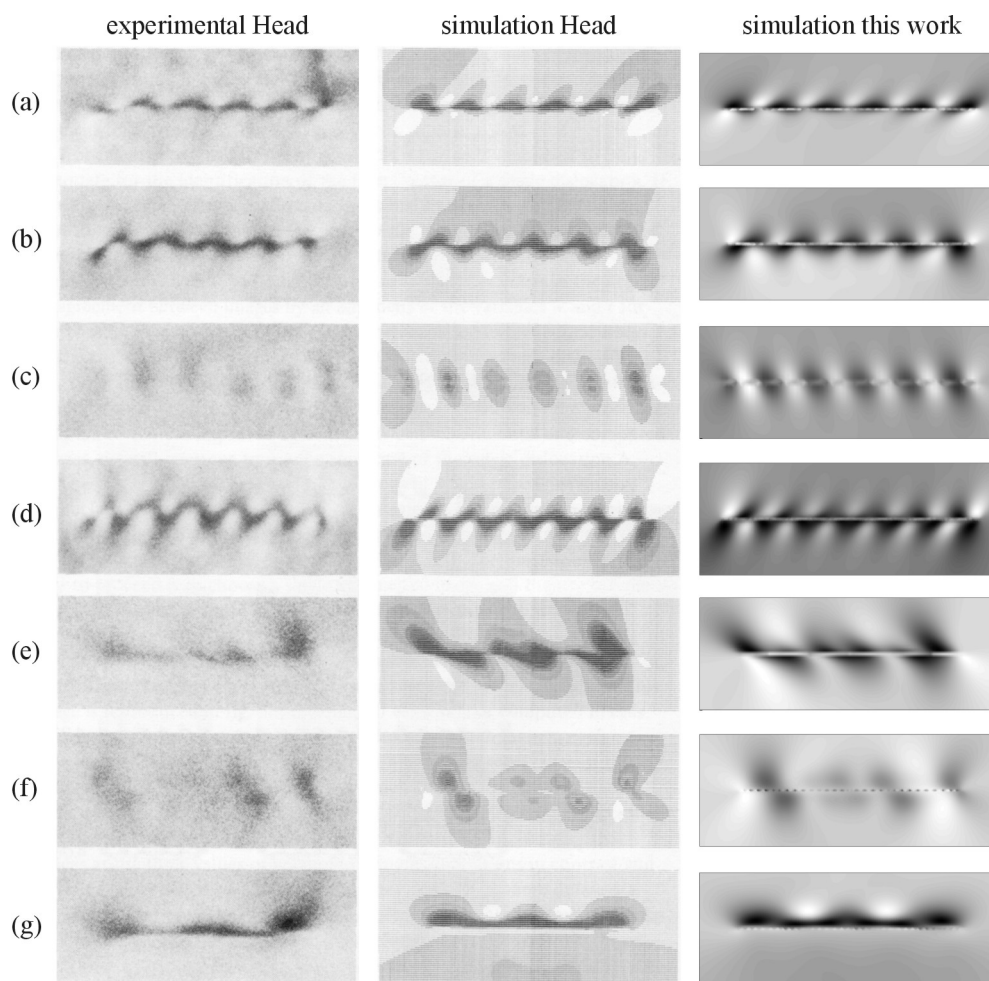
Figure 8.4 Experimental and simulated bright field images of dislocations in aluminium reported by Head [47, page 132] and comparison with simulated images of this work. The simulation parameters are given in Table 8.2.
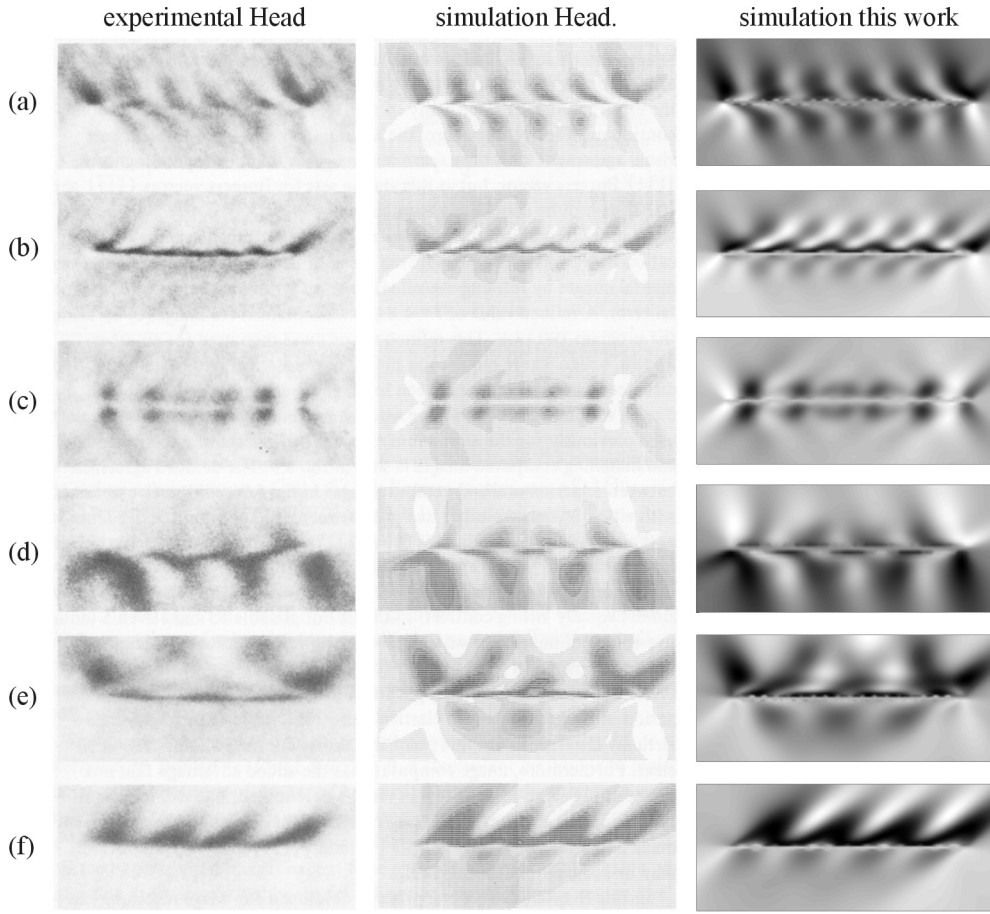
experimental Head   simulation Head.   simulation this work

Figure 8.5 Experimental and simulated bright field images of dislocations in β-brass reported by Head [47, page 142] and comparison with simulated images of this work. The simulation parameters are given in Table 8.2.

8.3.2 Dislocations in Bi$_2$Te$_3$

Bi$_2$Te$_3$ is a nearly elastically isotropic material (anisotropy ratio $A = 1.2$, Eq. 2.5). The elastic constants are given in Table 8.3 [59]. The 6×6 matrix of the elastic constants of Bi$_2$Te$_3$ (point symmetry $\bar{3}m$) differs significantly from isotropic materials (Eq. 2.4). There are 5 independent elastic constants c_{11}, c_{12}, c_{13}, c_{14}, and c_{44}, whereas $c_{66} = \frac{1}{2}(c_{11} - c_{12})$ [59, 105].

$$c_{mn} = \begin{pmatrix} c_{11} & c_{12} & c_{13} & c_{14} & 0 & 0 \\ c_{12} & c_{11} & c_{13} & -c_{14} & 0 & 0 \\ c_{13} & c_{13} & c_{33} & 0 & 0 & 0 \\ c_{14} & -c_{14} & 0 & c_{44} & 0 & 0 \\ 0 & 0 & 0 & 0 & c_{44} & c_{14} \\ 0 & 0 & 0 & 0 & c_{14} & c_{66} \end{pmatrix}. \tag{8.12}$$

The experiments on gliding dislocations in p-type bulk Bi$_2$Te$_3$ (sample P4, Chap. 7) served as basis for the image simulations. Stereomicroscopy was applied on one specific dislocation (Fig. 8.6 and 8.7). The sample was tilted from an orientation parallel to the a axis to an orientation closer to the c axis (Table 8.3, Fig. 3.3). All quantities necessary for image simulation were determined for this specific dislocation (Table 8.3), particularly yielding a dislocation in the basal plane with line direction $\mathbf{t} = [2.7, -1, 0]$.

Table 8.3 Image simulation parameters for a dislocation in p-type Bi_2Te_3 (sample P4) shown in Figures 8.6 and 8.7. The diffracting vectors $\mathbf{g}$ are specified by Miller indices (h, k, l) and an orientation angle $\alpha_\mathbf{g}$. The beam directions $\mathbf{B}$ are specified by Miller indices $[u, v, w]$ and polar coordinates (ϕ, ρ).

Micro-graph	Diffracting vector $\mathbf{g}$ $(h, k, l) / \alpha_\mathbf{g}$	Beam direction $\mathbf{B}$ $[u, v, w] / (\phi, \rho)$	Extinction distance $\xi_\mathbf{g}$ (nm)	Excitation error w	Nearest pole	Relative tilt angle	$\mathbf{g} \cdot \mathbf{b}$
(a)	$(-1, 1, 10)$ / $48°$	$[6.84, -3.16, 1]$ / $(342°, 51.8°)$	44.4	0.7	$[5, -5, 1]$	$44°$	0
(b)	$(-1, 0, 5)$ / $99°$	$[5, -3.02, 1]$ / $(338°, 45.3°)$	33.4	0.7	$[5, -5, 1]$	$51°$	-1
(c)	$(0, 1, 5)$ / $3°$	$[10.1, -5, 1]$ / $(341°, 62.4°)$	33.4	0.6	$[5, -5, 1]$	$36°$	1
(d)	$(1, 1, 0)$ / $322°$	$[3.52, -3.52, 1]$ / $(330°, 41.2°)$	42.8	0.9	$[5, -5, 1]$	$57°$	2
(e)	$(0, 0, -15)$ / $238°$	$[10.4, 1, 0]$ / $(5°, 90.0°)$	57.5	0.3	$[1, 0, 0]$	$0°$	0
(f)	$(0, 1, 5)$ / $0°$	$[59.4, -5, 1]$ / $(356°, 83.6°)$	33.4	0.3	$[1, 0, 0]$	$11°$	1
(g)	$(0, 1, -10)$ / $286°$	$[104, 10, 1]$ / $(5°, 86.0°)$	44.4	0.5	$[1, 0, 0]$	$4°$	1
(h)	$(0, -1, -5)$ / $179°$	$[-1.18, -5, 1]$ / $(287°, 33.1°)$	33.4	0.6	$[-5, -10, 2]$	$83°$	-1
(i)	$(2, -1, 0)$ / $267°$	$[-1.41, -2.81, 1]$ / $(270°, 19.3°)$	42.8	0.3	$[-5, -10, 2]$	$92°$	1
(j)	$(2, 0, 5)$ / $308°$	$[-2.5, -7.2, 1]$ / $(280°, 42.3°)$	52.0	0.5	$[-5, -10, 2]$	$87°$	2
(k)	$(2, -2, -5)$ / $239°$	$[-3.61, -6.11, 1]$ / $(264°, 37.4°)$	52.0	0.5	$[-5, -10, 2]$	$97°$	0

Acceleration voltage $U = 120\,\text{kV}$, lattice parameters $a = 0.43835\,\text{nm}$ and $c = 3.0487\,\text{nm}$, Burgers vector $\mathbf{b} = [1, 1, 0]$, line direction $\mathbf{t} = [2.7, -1, 0]$, foil normal $\mathbf{F} = [5, -2, 1]$, foil thickness $d_\text{F} = 120\,\text{nm}$, absorption coefficient $A = 0.1$, elastic constants $c_{11} = 6.847 \times 10^{10}\,\text{Pa}$, $c_{12} = 2.177 \times 10^{10}\,\text{Pa}$, $c_{13} = 2.704 \times 10^{10}\,\text{Pa}$, $c_{14} = 1.325 \times 10^{10}\,\text{Pa}$, $c_{33} = 4.768 \times 10^{10}\,\text{Pa}$, and $c_{44} = 2.738 \times 10^{10}\,\text{Pa}$, see Ref. [16] for an overview of material parameters.
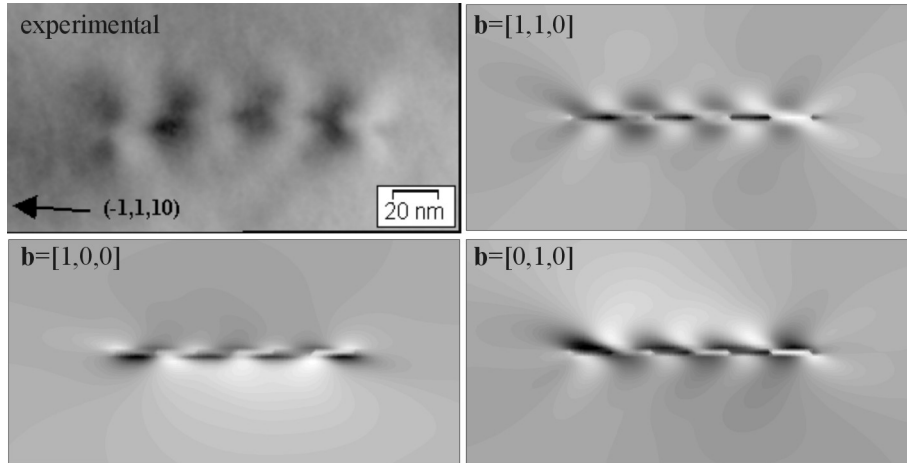

Figure 8.6 Experimental and simulated $\mathbf{g} = (-1, 1, 10)$ bright field images of a dislocation in p-type Bi_2Te_3 (sample P4) with Burgers vectors $\langle 1, 0, 0 \rangle$. The simulation parameters are given in Table 8.3, micrograph (a).
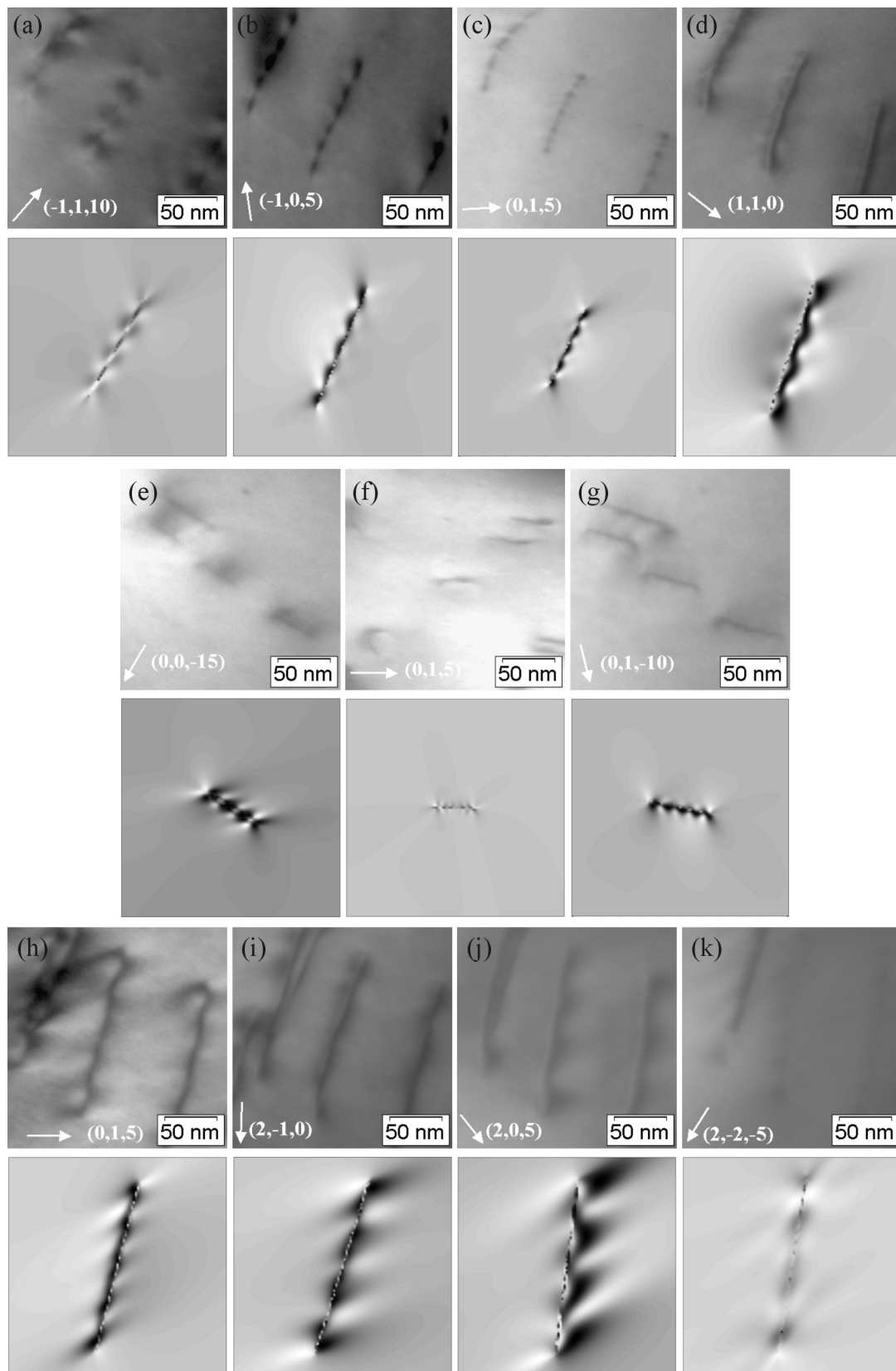
Figure 8.7 Experimental and simulated bright field images of a dislocation in *p*-type Bi$_2$Te$_3$ (sample P4) with Burgers vector [1, 1, 0]. The simulation parameters are given in Table 8.3.

First, for micrograph (a) (Table 8.3) three simulated images were calculated for the energetically most favourable Burgers vectors $\langle 1, 0, 0 \rangle$. Only for a Burgers vector $\mathbf{b} = [1, 1, 0]$ there is a good agreement in symmetry between the experimental and simulated image (Fig. 8.6). Second, the two-beam images of the dislocation acquired close to various poles and the corresponding simulated images are shown in Figure 8.7. Most of the simulated images yielded a fairly good agreement with the experimental images, although the dimensionless excitation errors w and absorption coefficients A were not optimised.

The sample and also this dislocation were not ideal for image simulation with higher accuracy for two reasons. (i) The dislocation was slightly bent (Fig. 8.6) since it was a dislocation which was able to glide before the stereomicroscopy experiments were carried out. (ii) The sample was contaminated since it was not freshly prepared. Therefore, the sample was ion-etched once again for a few minutes and stereomicroscopy experiments on straight dislocations were intended to carry out once again. However, after ion-etching a nns was found in the entire TEM sample. Image simulation of dislocations failed due to the superposition of strain fields of the dislocations and of the nns.

8.3.3   Image simulation of the nns in Bi$_2$Te$_3$

The n-type sample N4 (Chap. 5.1.3) and the p-type sample P3 (Chap. 5.1.5) were used for image simulation of the structural modulations (nns) in bulk Bi$_2$Te$_3$. Sample N4 showed two nns which were referred to as nns(1) and nns(2). Sample P3 is identical to sample P4, which was used for studies on gliding dislocations (Table 3.1, Chap. 7). However, sample P4 showed a nns in the entire sample after additional ion-etching and was therefore referred to as sample P3.

The simplest model for the nns is a sinusoidal displacement field $\mathbf{u}(\mathbf{r}) = \mathbf{u}_0 \sin(\mathbf{q} \cdot \mathbf{r})$ with displacement vector $\mathbf{u}_0$ and wave vector $\mathbf{q}$. On the basis of the experimental results the displacement field of the nns was found to be approximately a frozen lattice wave in transverse mode, i.e., the wave vector being perpendicular to the displacement vector. The direction and wavelength of the wave vector were determined by analyses of the two-beam images and diffraction patterns. The direction of the displacement vector was determined by using the $\mathbf{g} \cdot \mathbf{u} = 0$ criterion for a displacement field being out of contrast. The aim of the image simulation was (i) to determine the amplitude of the displacement vector by comparison of the diffraction contrast of the experimental and the simulated images and (ii) to verify the validity of the sinusoidal model by comparison of the orientations and wavelengths of the nns-fringes in the experimental and the simulated images for various beam directions (tilt angles).

For the analysis of nns(1) in sample N4, $\mathbf{g} = (-1, 0, 5)$ bright field images were acquired close to various poles (Table 8.4, Fig. 8.8, Fig. 3.3). Additionally, a $\mathbf{g} = (0, -1, 10)$ bright field image was acquired close to the $[10, -10, 1]$ pole. The directions of the displacement vector and of the wave vector were found to be $[-10, -5, 1]$ and $(1, 0, 10)$, respectively (Table 8.4). For the simulations the amplitude of the displacement vector and the wavelength of the wave vector were assumed to be 15 pm and 12 nm, respectively. All input parameters are summarised in Table 8.4. The experimental and simulated images agree very well with respect to the orientation and the wavelength of the nns-fringes at the various beam directions (tilt angles) (Fig. 8.8). Even, at relatively large tilt angles of about 70° (Table 8.4) the differences between the orientations of the nns-fringes in the experimental and simulated images are less than 10°. Finally, an amplitude of $10 - 20$ pm for the displacements is evident to explain a typical diffraction contrast $(I_{\max} - I_{\min})/(I_{\max} + I_{\min})$ of about 25%, where I is the intensity.

For the analysis of nns(2) in sample N4, $\mathbf{g} = (0, 1, 5)$ bright field images were acquired close to various poles (Table 8.4, Fig. 8.8, Fig. 3.3). Additionally, a $\mathbf{g} = (-1, 0, -10)$ bright field image was acquired close to the $[10, -10, 1]$ pole. The directions of the displacement vector and of the wave vector were found to be $[5, 10, 1]$ and $(0, -1, 10)$, respectively (Table 8.4). For the simulations the amplitude of the displacement vector and the wavelength of the wave vector were assumed to be 15 pm and 12 nm, respectively. All input parameters are summarised in Table 8.4. There was no agreement between experimental and simulated images with respect to the orientation of the nns-fringes at the various beam directions (tilt angles) (Fig. 8.8). A better agreement was obtained for a refined value $\mathbf{q} = (3, -4, 25)$ for the wave vector (Fig. 8.8).

Table 8.4 Parameters used for image simulation of the structural modulations (nns) in *n*-type and *p*-type Bi_2Te_3 (samples N4 and P3) shown in Figures 8.8 and 8.9. The diffracting vectors **g** are specified by Miller indices (h, k, l) and an orientation angle $\alpha_\mathbf{g}$. The beam directions **B** are specified by Miller indices $[u, v, w]$ and polar coordinates (ϕ, ρ).

Micro-	Diffracting vector **g**		Beam direction **B**		Extinction	Nearest	Relative
graph	(h, k, l)	$\alpha_\mathbf{g}$	$[u, v, w]$	(ϕ, ρ)	distance $\xi_\mathbf{g}$ (nm)	pole	tilt angle
			nns(1) in sample N4 [a]				
(a)	$(-1, 0, 5)$	$315°$	$[5, -80.1, 1]$	$(303°, 85.2°)$	33.4	$[0, -1, 0]$	$0°$
(b)	$(-1, 0, 5)$	$312°$	$[5, -6.79, 1]$	$(325°, 55.8°)$	33.4	$[5, -5, 1]$	$36°$
(c)	$(-1, 0, 5)$	$299°$	$[5, -0.42, 3]$	$(356°, 36.9°)$	33.4	$[10, 5, 2]$	$65°$
(d)	$(0, -1, 10)$	$290°$	$[4.96, -10, -1]$	$(319°, 117.8°)$	44.4	$[10, -10, -1]$	$36°$
			nns(2) in sample N4 [b]				
(a)	$(0, 1, 5)$	$210°$	$[38.7, -5, 1]$	$(354°, 80.5°)$	33.4	$[1, 0, 0]$	$0°$
(b)	$(0, 1, 5)$	$217°$	$[1.98, -5, 1]$	$(316°, 41.9°)$	33.4	$[5, -5, 1]$	$50°$
(c)	$(0, 1, 5)$	$230°$	$[-1.66, -5, 3]$	$(281°, 32.4°)$	33.4	$[-5, -10, 2]$	$73°$
(d)	$(-1, 0, -10)$	$45°$	$[10, -21.7, -1]$	$(318°, 103.9°)$	44.4	$[10, -10, -1]$	$43°$
			nns in sample P3 [c]				
(a)	$(0, -1, -5)$	$203°$	$[121.5, -5, 1]$	$(358°, 86.8°)$	33.4	$[1, 0, 0]$	$0°$
(b)	$(0, -1, -5)$	$197°$	$[3.04, -5, 1]$	$(322°, 45.3°)$	33.4	$[5, -5, 1]$	$52°$
(c)	$(0, 1, 5)$	$21°$	$[-0.75, -5, 1]$	$(292°, 33.9°)$	33.4	$[-5, -10, 2]$	$74°$
(d)	$(1, 1, 0)$	$334°$	$[25.6, -25.6, 1]$	$(330°, 81.1°)$	42.8	$[1, -1, 0]$	$28°$
(e)	$(-1, -1, 0)$	$155°$	$[7.98, -7.98, 1]$	$(330°, 63.3°)$	42.8	$[5, -5, 1]$	$36°$
(f)	$(-1, -1, 0)$	$151°$	$[0.95, -0.95, 1]$	$(330°, 13.3°)$	42.8	$[0, 0, 1]$	$75°$

[a]Displacement vector $\mathbf{u}_0$ (direction $[-10, -5, 1]$, amplitude 15 pm), wave vector **q** (directions $(1, 0, 10)$, wavelength 12 nm), foil normal $\mathbf{F} = [14, -22.5, 1]$, foil thickness $d_F = 70$ nm, excitation error $w = 0.3$, absorption coefficient $A = 0.1$.

[b]Displacement vector $\mathbf{u}_0$ (direction $[5, 10, 1]$, amplitude 15 pm), wave vector **q** (directions $(0, -1, 10)$ or $(3, -4, 25)$, wavelength 12 nm), foil normal $\mathbf{F} = [14, -22.5, 1]$, foil thickness $d_F = 70$ nm, excitation error $w = 0.3$, absorption coefficient $A = 0.1$.

[c]Displacement vector $\mathbf{u}_0$ (direction $[5, 10, 1]$, amplitude 15 pm), wave vector **q** (directions $(0, -1, 10)$ or $(-1, 0, 5)$, wavelength 17 nm), foil normal $\mathbf{F} = [7.81, -2.19, 1]$, foil thickness $d_F = 70$ nm, excitation error $w = 0.3$, absorption coefficient $A = 0.1$.

The wave vector $\mathbf{q} = (3, -4, 25)$ is also perpendicular to the displacement vector and differs by $33°$ with respect to its direction from $\mathbf{q} = (0, -1, 10)$.

For the analysis of the nns in sample P3, $\mathbf{g} = (0, 1, 5)$ and $\mathbf{g} = (1, 1, 0)$ dark field images were acquired close to various poles (Table 8.4, Fig. 8.9, Fig. 3.3). The displacement vector and wave vector were found to be $[5, 10, 1]$ and $(0, -1, 10)$, respectively (Table 8.4). A second possible direction for the wave vector would be $(-1, 0, 5)$, which was determined by analysis of two-beam images acquired close to the $[5, -5, 1]$ pole (micrographs (b) and (e)). For the simulations the amplitude of the displacement vector and the wavelength of the wave vector were assumed to be 15 pm and 17 nm, respectively. All input parameters are summarised in Table 8.4. The experimental and simulated images agree very well only for a wave vector $(-1, 0, 5)$ (Fig. 8.9). The wave vector $\mathbf{q} = (-1, 0, 5)$ is also perpendicular to the displacement vector and differs by $47°$ with respect to its direction from $\mathbf{q} = (0, -1, 10)$.

The simulations showed that the simple sinusoidal model for the displacement field is a fairly good approximation. It explains the conditions for the nns being out of contrast, the magnitude of the diffraction contrast, and the wavelength and the orientation of the nns-fringes at various beam directions. The most striking result is the determination of the amplitude of the displacement field of about $10 - 20$ pm, since it is a quantity beyond the lateral resolution of the TEM.
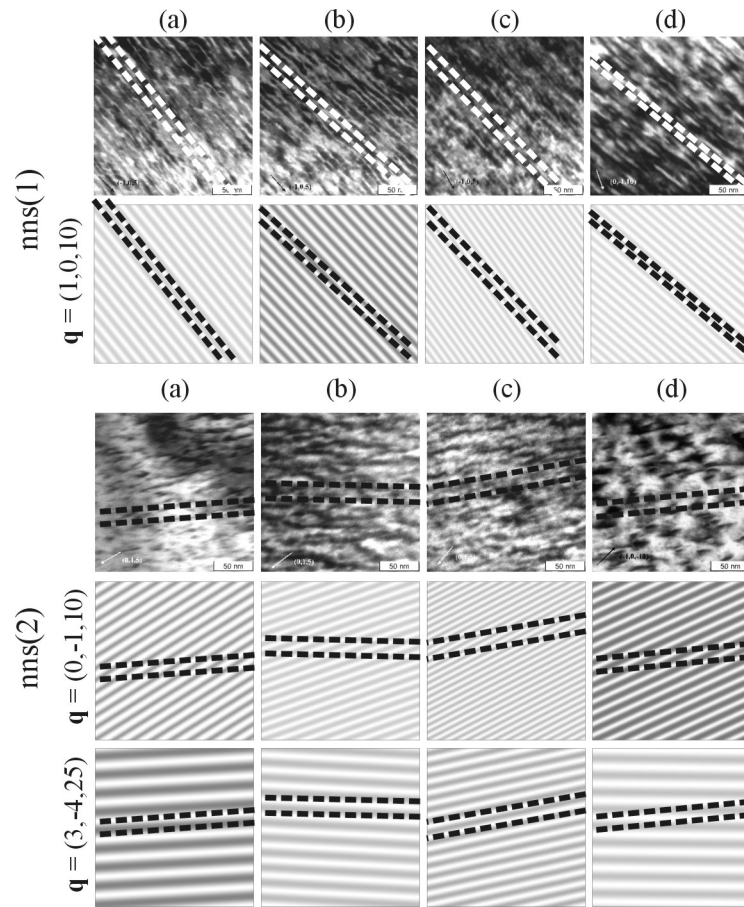
Figure 8.8 Experimental and simulated bright field images of nns(1) and nns(2) in n-type Bi_2Te_3 (sample N4). The simulation parameters are given in Table 8.4. The dashed lines indicate the orientation and the wavelength of the nns-fringes in the experimental images.
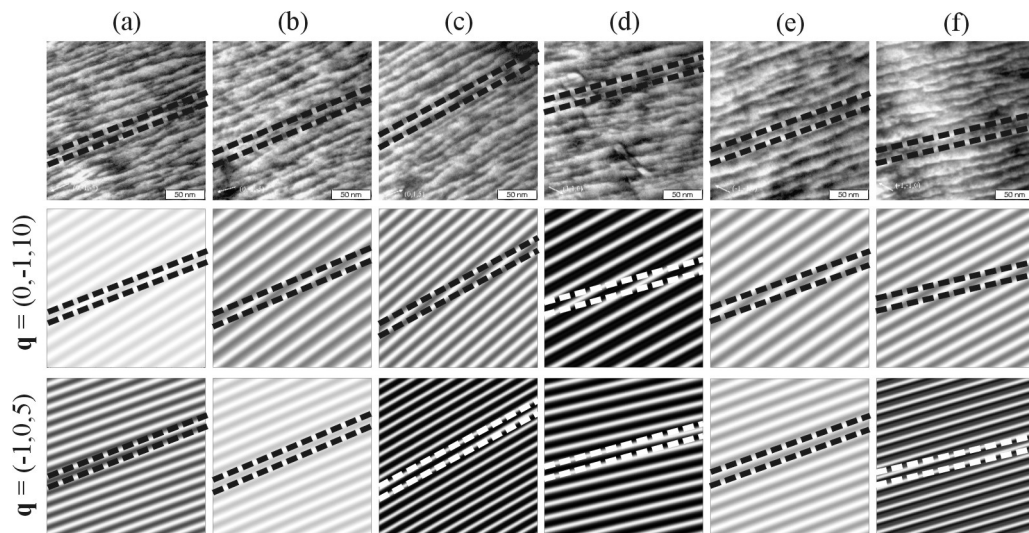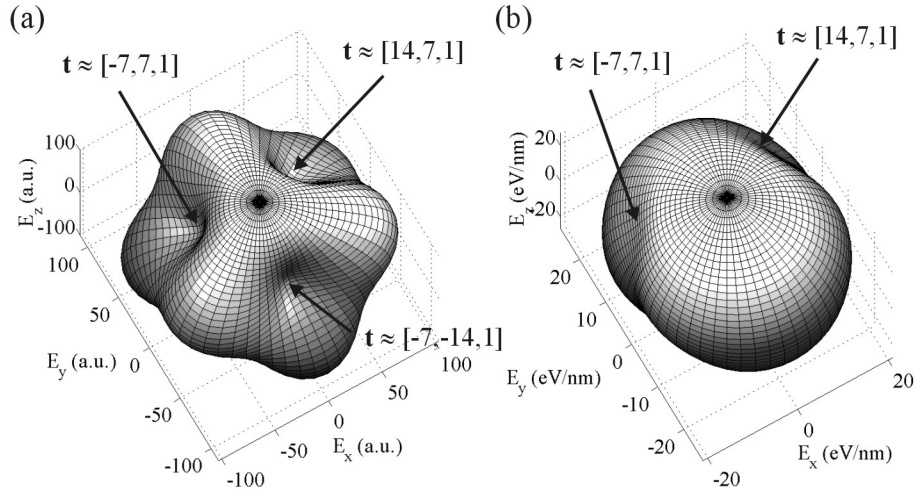

Figure 8.9 Experimental and simulated dark field images of the nns in p-type Bi_2Te_3 (sample P3). The simulation parameters are given in Table 8.4. The dashed lines indicate the orientation and the wavelength of the nns-fringes in the experimental images.

Figure 8.10 3D-Polar diagrams of the line energy E_{L} of dislocations in Bi_2Te_3 in dependence of the polar coordinates of the line direction $\mathbf{t}$ for (a) for hypothetical screw dislocations with Burgers vector $\mathbf{b} = \mathbf{t}$ and for (b) dislocations with Burgers vector $\mathbf{b} = [1,0,0]$.

8.3.4 Line energy of basal plane and nonbasal plane dislocations in Bi_2Te_3

An ordered network of dislocations a few nanometer apart was assumed to be the origin of the displacement field of the nns. An important reason to rule out this model was a closer inspection of the line energy of such dislocations (Chap. 5.2.2). It is known that in hexagonal structures dislocations with Burgers vectors $\mathbf{b} = \langle 1,0,0 \rangle$ are energetically most favourable. However, Bi_2Te_3 has a trigonal crystal structure and other dislocations might be energetically more favourable. A systematic search was carried out to determine the energetically most favourable combinations of Burger vectors and line directions in Bi_2Te_3. The line energy was calculated according to the integral formalism of Barnett and Lothe (Eq. 8.9).

The first step was to calculate the line energy for hypothetical screw dislocations ($\mathbf{b} = \mathbf{t}$) in dependence of the polar coordinates (φ, ρ) of the line direction $\mathbf{t} = [\cos(\varphi)\sin(\rho), \sin(\varphi)\sin(\rho), \cos(\rho)]$. The result is presented as a 3D-polar diagram (Fig. 8.10(a)). The energetically most favourable line directions for screw dislocations in Bi_2Te_3 are parallel to the $\langle -7,7,1 \rangle$ directions, i.e., $[-7,7,1]$, $[14,7,1]$, and $[-7,-14,1]$ (Fig. 8.10(a)). The second step was to calculate such a 3D-polar diagram of the line energy for a specific Burgers vector, e.g., $\mathbf{b} = [1,0,0]$ (Fig. 8.10(b)). The smallest line energy was found for line directions close to $\mathbf{t} = [14,7,1]$ and $\mathbf{t} = [-7,7,1]$, both having a small angle between the line directions and the Burgers vector $\mathbf{b} = [1,0,0]$ compared to $\mathbf{t} = [-7,-14,1]$ (Fig. 8.10(b), Table 8.5).

The line energy in dependence of the line direction was also calculated for other Burgers vectors and yielded similar diagrams. It turned out as general rule for Bi_2Te_3 that dislocations with (i) Burgers vectors $\mathbf{b} = \langle 1,0,0 \rangle$, (ii) line directions $\mathbf{t} \approx \langle -7,7,1 \rangle$, (iii) and a small angle between the line directions and the Burgers vectors are energetically most favourable. Particularlry, mixed nonbasal plane dislocations with Burgers vector $\langle 1,0,0 \rangle$ and line directions $\langle -7,7,1 \rangle$ are energetically more favourable than screw dislocations and edge dislocations in the basal plane (Table 8.5). However, such nonbasal plane dislocations were still not unambiguously identified by TEM in this work (App. A.2).

Table 8.5 Line energies of dislocations in Bi_2Te_3 in dependence of the Burgers vector **b**, line direction **t**, and angle β between them. The line energies were calculated assuming $R = 10\,\mu m$ and $r_0 = |\mathbf{b}|$, where R is half the distance between the dislocations and r_0 is the dislocation core radius.

Burgers vector **b**	Line direction **t**	Angle β $= \sphericalangle(\mathbf{b},\mathbf{t})$	Line energy (eV/nm)
$[1,0,0]$	$[1,0,0]$	$0°$	20.7
$[1,0,0]$	$[1,2,0]$	$90°$	26.8
$[1,0,0]$	$[14,7,1]$	$41°$	20.2
$[1,0,0]$	$[-7,7,1]$	$41°$	20.2
$[1,0,0]$	$[-7,-14,1]$	$90°$	29.9
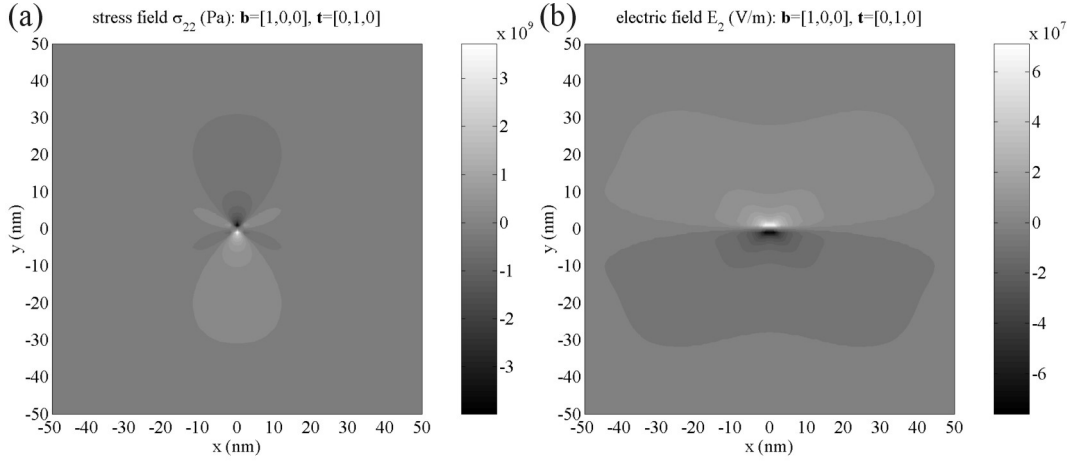
Figure 8.11 (a) Stress tensor component σ_{22} and (b) electric field component $(\mathbf{E})_2$ surrounding a dislocation in $BaTiO_3$ with Burgers vector $[1,0,0]$ and line direction $[0,1,0]$. The Burgers vector is parallel to the x axis and the line direction is parallel to the z axis, pointing out of the paper sheet.

8.3.5   Dislocations in BaTiO$_3$

$BaTiO_3$ is a ferroelectric model compound. Prepared as ceramics it reveals the Positive Temperature Coefficient Resistivity (PTCR) effect used in a large number of devices. The tetragonal phase is a multi-axes ferroelectric compound which reveals $180°$ and $90°$ domains. Imaging and reconstructing of the ferroelectric domain structure at grain boundaries is of central importance for an improved understanding of the PTCR effect. The domain boundaries can be imaged in the TEM under two-beam conditions yielding the delta-fringe contrast. The simulation of the fringe contrast by dynamical diffraction theory is used to determine the orientation of the c axis in two adjacent domains close to the domain wall. The strain fields and the electric fields of dislocations sitting at the grain boundaries can be calculated by continuum theory [106].

The integral formalism of Barnett and Lothe shown in Chapter 8.1 was also developed for the piezoelectric case so that the strain field $\frac{\partial \mathbf{u}}{\partial x_l}$, the stress field σ_{ij}, and the electrical field $\mathbf{E}$ around a dislocation can be computed simultaneously [46]. Figure 8.11 shows the stress tensor components σ_{22} and the electric field component $(\mathbf{E})_2$ surrounding a dislocation with Burgers vector $[1,0,0]$ and line direction $[0,1,0]$. The material parameters of tetragonal $BaTiO_3$ [107] required for the calculations are (i) the lattice parameters $a = 0.399\,nm$ and $c = 0.403\,nm$, (ii) the elastic constants $c_{11} = 27.5 \times 10^{10}\,Pa$, $c_{12} = 17.9 \times 10^{10}\,Pa$, $c_{13} = 15.3 \times 10^{10}\,Pa$, $c_{33} = 16.5 \times 10^{10}\,Pa$, $c_{44} = 5.43 \times 10^{10}\,Pa$, and $c_{66} = 11.3 \times 10^{10}\,Pa$, (iii) the piezoelectric constants $d_{15} = 392 \times 10^{-12}\,C/N$, $d_{31} = -34.5 \times 10^{-12}\,C/N$, and $d_{33} = 85.6 \times 10^{-12}\,C/N$, and (iv) the dielectric constants $\epsilon_1 = 36.3 \times 10^{-9}\,F/m$ and $\epsilon_3 = 1.42 \times 10^{-9}\,F/m$.

Appendix A

New results in bulk Bi$_2$Te$_3$

A.1 CBED on the structural modulation (nns)

Convergent Electron Beam Diffraction (CBED) is a TEM imaging technique which is known to be very sensitive to local changes of the lattice parameters and strain in the sample [42, chap. 21]. The sample was cooled with liquid nitrogen to $77\,\mathrm{K}$ for the CBED measurements. The energy selecting aperture ($\Delta\mathrm{E} = 20\,\mathrm{eV}$) of the OMEGA filter was used to avoid background from inelastically scattered electrons. A CBED pattern of the nns was acquired in p-type Bi$_2$Te$_3$ (sample P3, Table 3.1) under $(0,1,5)$ two-beam condition at a spot size of $10\,\mathrm{nm}$ (Fig. A.1). For an ideal crystal, within the diffraction disks parallel fringes should appear, which correspond to the rocking-curve intensity oscillations, i.e., the intensities of the direct beam $I_\mathrm{T}(w)$ and of the diffracted beam $I_\mathrm{S}(w)$ in dependence of the dimensionless excitation error w (Eq. 2.30 and C.27). However, the fringes within the diffraction disks are strongly disturbed (Fig. A.1). This indicates a strain field being correlated to the nns.
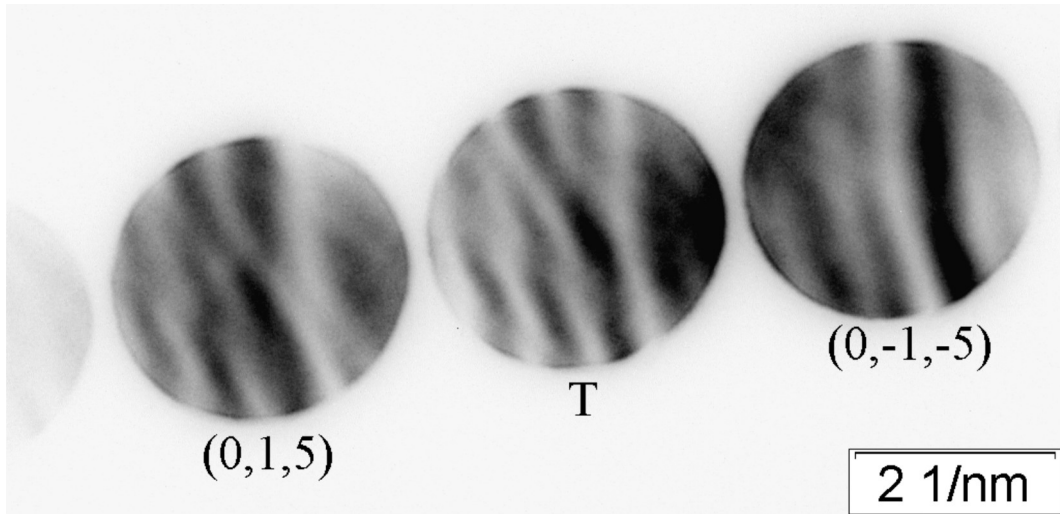

Figure A.1 CBED pattern obtained on the nns in p-type bulk Bi$_2$Te$_3$ (sample P3) under $(0,1,5)$ two-beam condition.
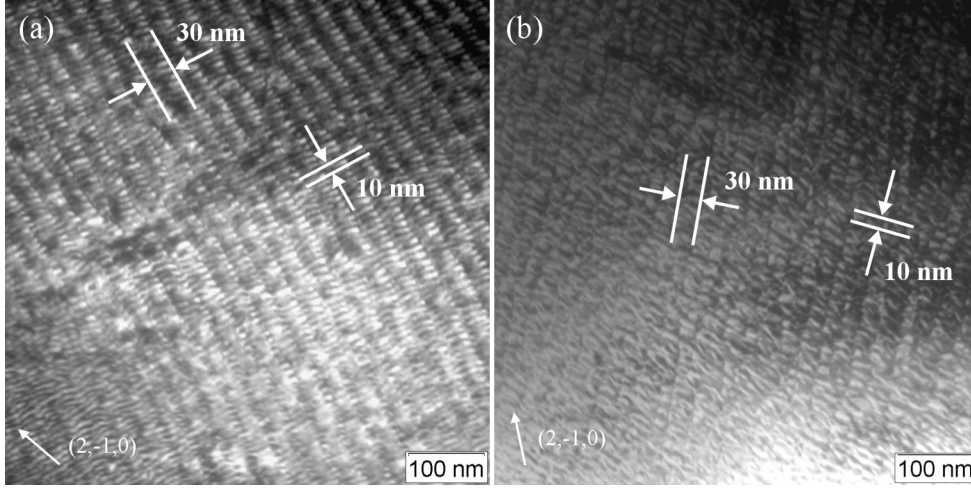
Figure A.2 $(2, -1, 0)$ two-beam images obtained in (a) *n*-type and (b) *p*-type Bi$_2$Te$_3$ bulk materials. The samples show a superposition of two structural modulations with identical wavelengths and wave vectors in both materials.

A.2 A further type of structural disorder and nonbasal plane dislocations

The TEM measurements on *n*-type and *p*-type Bi$_2$Te$_3$ bulk materials yielded in both materials gliding dislocations and the nns as common features of structural disorder. However, in both materials one more variation of structural disorder was found. Dark field images were acquired in a sample orientation close to the *c* axis (Fig. A.2). The images show the superposition of two structural modulations, which could also be imaged separately with other Bragg reflections. Stereomicroscopy yielded identical wavelengths λ, wave vectors $\mathbf{q}$, and displacement vectors $\mathbf{u}$ for both structural modulations in both samples, i.e., (i) $\lambda = 30$ nm, $\mathbf{q} = (1, 1, 0)$, $\mathbf{u} = [1, 1, 0]$ and (ii) $\lambda = 10$ nm, $\mathbf{q} = (-1, 1, 0)$, $\mathbf{u} = [5, -5, 1]$. The displacement vector was obtained from the $\mathbf{g} \cdot \mathbf{u} = 0$ criterion for displacement fields being out of contrast. Occasionally, gliding dislocations were also observed.

This new type of structural disorder on the nanometer scale in Bi$_2$Te$_3$ materials is not identical to the nns, since the two-beam images of the nns acquired in sample orientations close to the *c* axis significantly differed (Fig. 5.5(c)-(f)). Particularly, there seems to be a symbiotic relation between the 30 nm and the 10 nm structural modulations because they were only simultaneously observed. In both samples, the reflections for these structural modulations being out of contrast, their wavelengths, and their wave vectors were identical for both materials. Therefore, this new type of structural disorder is of general character for Bi$_2$Te$_3$ materials. Probably, the network of parallel "dislocations" observed in Bi$_2$Te$_3$ thin films (Fig. 6.3(b)) is identical to the structural modulations shown here.

The origin of the modulation with a wavelength of 10 nm is most likely a pure displacive modulation, because the displacement vector points out of the basal plane and dislocations with such Burgers vectors are energetically unfavourable in the highly anisotropic Bi$_2$Te$_3$. The origin of the modulation with a wavelength of 30 nm could be (i) a pure displacive modulation or (ii) a network of parallel nonbasal plane dislocations with Burgers vector $[1, 1, 0]$ and line direction $[10, -10, 3]$. However, gliding dislocations were simultaneously observed which should be blocked due to the intersection between basal plane and nonbasal plane dislocations.

Similar to the nns, this new type of structural disorder should significantly scatter phonons and reduce the lattice thermal conductivity due to the amplitude and wavelength of its displacement field. Nonbasal plane dislocations might also significantly change the thermoelectric properties. In the literature, TEM measurements on Bi$_2$Te$_3$ were reported, also yielding
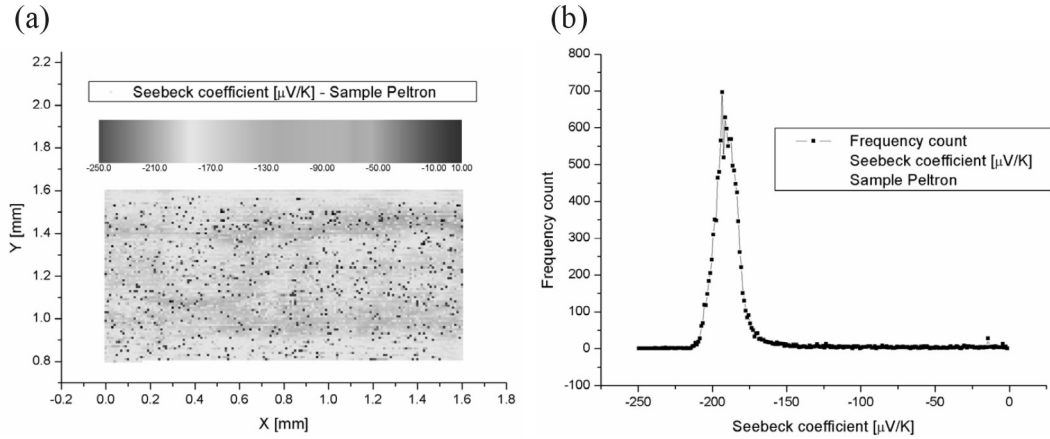
Figure A.3 (a) Thermopower distribution and (b) thermopower histogram obtained from SPM measurements on n-type Bi_2Te_3 bulk material.

nonbasal plane dislocations with a dislocation density significantly smaller compared to the dislocation density of basal plane dislocations [24]. Also, it was reported that bulk Bi_2Te_3 showed changes from p-type to n-type character and a reduction of the carrier mobility after heavy plastic deformation [108]. A reduction of the carrier mobility in cold worked samples with larger dislocation densities was also reported elsewhere [23]. These changes in cold worked materials were attributed to gliding and intersection of basal plane and nonbasal dislocations, generating an excess of electrically active Te vacancies [108].

A.3 Thermopower distribution

Recently, Seebeck scanning microprobes (SPM) are available, which are able to measure the thermopower at a lateral resolution down to $20\,\mu$m at a relative error of about 3% [109]. SPM is a surface scan technique where a probe tip heats a small area around the point of interest and the gradients of the temperature and the thermoelectric voltage are measured by two thermocouples. This technique was also applied to several high-ZT Tellurides, i.e., n-type and p-type bulk Bi_2Te_3 [110, 111] and to $AgPb_mSbTe_{2+m}$ bulk materials [112].

Figure A.3 shows the thermopower distribution and a histogram obtained from SPM measurements on our n-type Bi_2Te_3 bulk material. The measurements were carried out at the Institute of Materials Research, German Aerospace Center (DLR) [113]. The thermopower shows local changes on a length scale of $200\,\mu$m (Fig. A.3(a)) and a mean value of $-192 \pm 9\,\mu$V/K (Fig. A.3(b)). The same sample was also used for the acquisition of chemical maps by EDX in a SEM. However, the chemical maps yielded no contrast.

The local changes of the thermopower might be correlated to variations in stoichiometry by $1-2$ at. % found by WDX [33] and by EDX in the TEM (Chap. 4). The relative error of the thermopower $\sigma_S/S = 5\%$ is only slightly larger than the error of 3% found in pure homogeneous PbTe reference material [112]. Nevertheless, the SPM technique seems to be more sensitive to chemical modulations and yields distribution maps with higher contrast than the chemical maps obtained by EDX in the SEM. Therefore, SPM measurements are highly recommended for combined measurements of the microstructure and thermoelectric properties in future due its high sensitivity and lateral resolution.
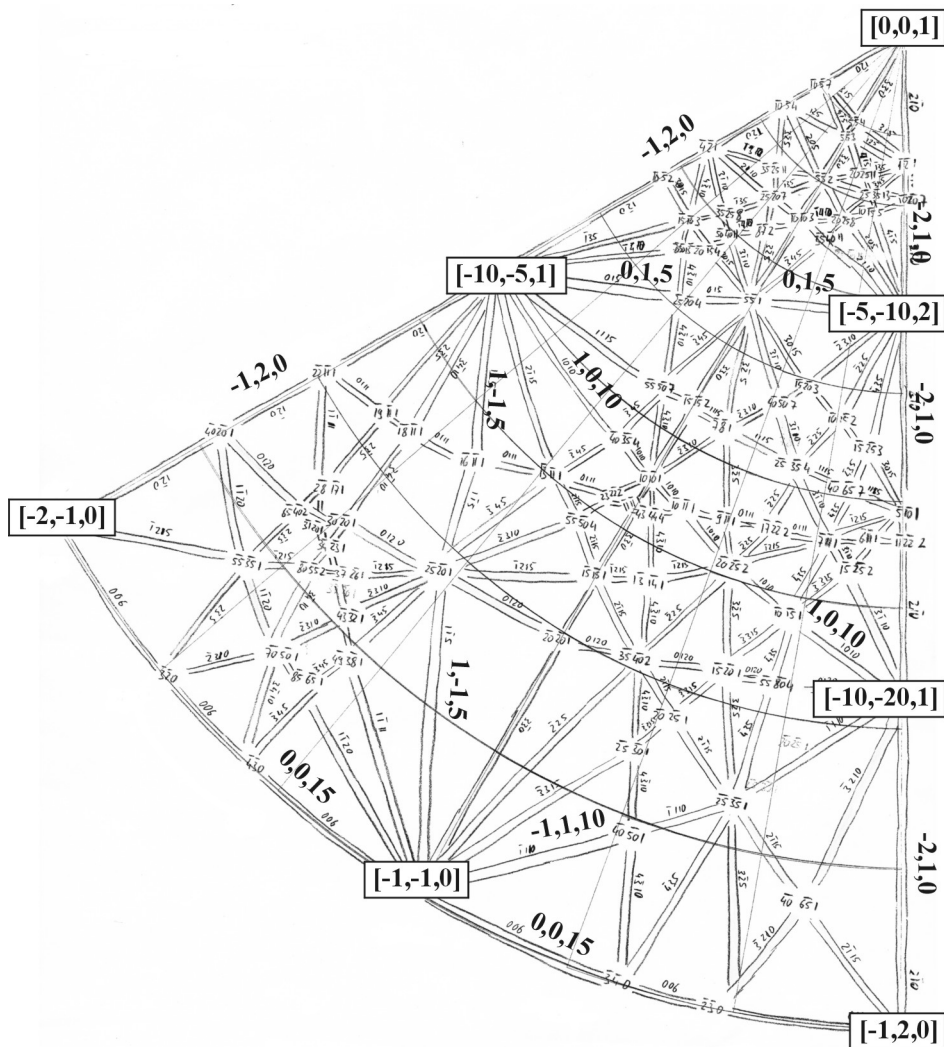
Appendix B

Detailed Kikuchi maps for Bi₂Te₃

Figure B.1 Detailed Kikuchi map for Bi₂Te₃. The most important poles and Kikuchi lines are labelled.

Figure B.2 Detailed Kikuchi map for Bi_2Te_3. The most important poles and Kikuchi lines are labelled.

Appendix C

MATLAB code for image simulation of dislocations

C.1   Main programme "Start"

The main programme "Start" is shown in the following. The operator "%" is used for comments or to deactivate the programme sequence in that line. After each subroutine the computing time spend so far is measured. The subroutine "Rechnung_Zeit" at the end of the programme calculates the total computing time and the computing time for the various subroutines. The dimensionless excitation error w and the absorption factor A can be varied by "for"-loops, a series of simulated two-beam images will be calculated and presented in separated windows on the desktop. Each window will be labelled with an identity number "Figure_No" and an automatically generated title including the dimensionless excitation error w and the absorption factor A.

```
%************************************************************************************************
%Hauptmenü Start
%************************************************************************************************
clear
time1=clock;
%Eingabe Geräte-, Material-, Versetzungs-, und Abbildungsparameter
Eingabe_Bi2Te3
time2=clock;
%Umrechnung aller Größen in experimentelles Achsensystem
Rechnung_Koordinaten
time3=clock;
%Berechnung der Gitterverbiegungsfunktion beta=g*du/dz
Rechnung_beta
time4=clock;
%Numerische Lösung der Howie-Whelan Gleichungen
global w A
Figure_No=0;
for A=A_min:A_delta:A_max      %Schleife für Absorptionskooeffzienten A=N
    for w=w_min:w_delta:w_max  %Schleife für dimensionslosen Anregungsfehler w
        Rechnung_Kn            %Berechnung der Transformationmatrizen für die Amplituden
        time5=clock;
        Rechnung_Amplituden    %Berechnung der Amplituden und Intensitäten
        time6=clock;
        Ausgabe                %Darstellung als Linienplots oder Kontourplots
        Figure_No=Figure_No+1;
    end;
end;
time7=clock;
Rechnung_Zeit
```

C.2 Input

C.2.1 Subroutine "Eingabe"

The subroutine "Eingabe_Bi2Te3" is shown in the following. Some variables are declared as "global" variables, since they are used in functions. An example of a function is "Xig_Bi2Te3(g_hkl)", which calculates the extinction distance $\xi_{\mathbf{g}}$ for a Bragg reflection "g_hkl". Besides the input parameters, there are some further options which can be preset within the subroutine "Eingabe": (i) Line scans of the intensities parallel to the line direction and in beam direction are specified by the column coordinates $x0$ and $y0$. The displacement field in the $z0$ plane can be presented. (ii) The x axis of the experimental axis system can be defined with respect to the line direction or with respect to the diffracting vector. (iii) The Runge-Kutta method or the "Pendellösung" method can be chosen for numerical integration of the Howie-Whelan equations. (iv) The simulation parameters can be additionally presented in the simulated images. (v) The contrast of the images can be optimised and the number of grey scale values can be preset. (vi) The bright field and dark field images can be saved automatically.

```
%****************************************************************************************************
%subroutine Eingabe_Bi2Te3
%****************************************************************************************************
% Beschleunigungsspannung U in kV
global U
U=120
% Gitterkonstanten in nm
a=0.43835
c=3.0487
%Basisvektoren des Realraums in nm
global a1 a2 a3
a1=[a; 0; 0]
a2=[-a/2; a/2*sqrt(3); 0]
a3=[0; 0; c]
%Eingabe der 6x6 Matrix der elastische Konstanten in 10GPa
global c_mn
c_mn=zeros(6,6);
c_mn(1,1)=6.847;
c_mn(1,2)=2.177; c_mn(2,1)=c_mn(1,2);
c_mn(1,3)=2.704; c_mn(3,1)=c_mn(1,3);
c_mn(1,4)=1.325; c_mn(4,1)=c_mn(1,4);
c_mn(2,2)=c_mn(1,1);
c_mn(2,3)=c_mn(1,3); c_mn(3,2)=c_mn(2,3);
c_mn(2,4)=-c_mn(1,4); c_mn(4,2)=c_mn(2,4);
c_mn(3,3)=4.768;
c_mn(4,4)=2.738;
c_mn(5,5)=c_mn(4,4);
c_mn(5,6)=c_mn(1,4); c_mn(6,5)=c_mn(5,6);
c_mn(6,6)=0.5*(c_mn(1,1)-c_mn(1,2));
c_mn
%Anisotropiefaktor
A_iso=c_mn(4,4)/(0.5*(c_mn(1,1)-c_mn(1,2)))
%Eingabe Versetzungs-Parameter
t_uvw=[2.7; -1; 0]  %Linienrichtung t in Millerindizes, muss nicht Länge=1 haben
b_uvw=[1; 1; 0]     %Burgersvektor b in Millerindizes
%Eingabe Abbildungs-Parameter
F_uvw=[5; -2; 1]  %Flächennormale in Millerindizes, muss nicht Länge=1 haben
g_hkl=[-1; 1; 10] %Reflex g für Zweistrahlbedingung in Millerindizes
alpha_g=48          %Winkel des Reflexes g in grad zur x-Achse, gemessen im Bild gegen Uhrzeigersinn
B_phi=342, B_rho=51.8 %Strahlrichtung in Polarkoordinaten jeweils in grad
B_uvw=[-1,0,5]      %Strahlrichtung in Millerindizes,
polar=1             %rechnen mit Strahlrichtung in (1) in Polarkoordinaten oder (0) Millerindizes
%Eingabe zum Bildausschnitt und zur Probendicke
global d_F Lx Ly dx dy dz
d_F=120      %Probendicke in Richtung der Flächennormalen in nm
dz=2         %Rasterweite in Strahlrichtung=z-Richtung
Lx=200       %Bildbreite in x-Richtung in nm
dx=2         %Rasterweite in x-Richtung in nm
Ly=100       %Bildbreite in y-Richtung in nm
dy=2         %Rasterweite in y-Richtung in nm
x0=0, y0=0  %vertikalen Linescan bei (x0,y0) und für horizontalen Linescan durch y0
```

```
z0=0          %Darstellung Gitterverbiegungsfunktion beta in der Ebene z0
%Eingabe Extinktionslänge in nm
global Xig
Xig=Xig_Bi2Te3(g_hkl)
%Eingabe Wertebereich dimensionsloser Anregungsfehler w
w_min=0.7
w_max=0.7
w_delta=0.1
%Eingabe Wertebereich Absorptionskooeffzienten A=N
A_min=0.1
A_max=0.1
A_delta=0.05
%Optionen
%Orientierung der x-Achse an (1) der Versetzungsrichtung oder (0) dem Bragg Reflex
X_Achse=1;
%Berechnung der Transformationsmatrizen (1) nach dem Runge-Kutta Verfahren
%oder (0) mit der Pendellösungs-Methode
Runge_Kutta=0;
%Automatische Bildbeschiftung (1) ein - und (0) ausschalten
Bild_Text=0;
%Einstellung des Kontrast bei den Bildern: (1) optimaler Kontrast, (0) reales Bild
Bild_Kontrast=0;
%Anzahl der Graustufen in den Bildern (20: Minimum; 50: gut; 256: sehr gut)
Graustufen=256;
%Automatische Bildspeicherung für Bilder ITxy, ISxy und ITxy_ISxy (1) ein- und (0) auschalten
Auto_Save=0;
%Bild-Formatierung
Font_Name='times';
Font_Size=10;
Line_Width=2;
```

C.2.2   Extinction distance $\xi_{\mathbf{g}}$

The function is "Xig_Bi2Te3(g_hkl)" calculates the extinction distance $\xi_{\mathbf{g}}$ corresponding to the Bragg reflection $\mathbf{g}$. For centrosymmetric crystals, the extinction distance $\xi_{\mathbf{g}}$ is given by

$$\xi_{\mathbf{g}} = \frac{\pi\, V_{\mathrm{e}} \cos(\theta_{\mathbf{g}})}{\lambda\, F_{\mathbf{g}}} \,, \tag{C.1}$$

where $F_{\mathbf{g}}$ is the kinematical structure factor, $\theta_{\mathbf{g}}$ is the Bragg angle, V_{e} is the volume of the unit cell, and λ is the wavelength of the electrons [42, chap. 13.4]. The volume of the unit cell $V_{\mathrm{e}} = \mathbf{a}_1 \cdot (\mathbf{a}_2 \times \mathbf{a}_3)$ is determined by the basis vectors $\mathbf{a}_1$, $\mathbf{a}_2$, and $\mathbf{a}_3$ of the crystal lattice. The wavelength of the electrons including relativistic corrections is given by $\lambda = 2.42\,\mathrm{pm}/\sqrt{\gamma^2 - 1}$, where $\gamma = 1 + \frac{U}{512\,\mathrm{kV}}$ is the relativistic correction factor and U is the acceleration voltage in units of "kV". The Bragg angle $\theta_{\mathbf{g}}$ is determined by Bragg's law $\sin(\theta_{\mathbf{g}}) = \frac{1}{2}\,\lambda\,|\mathbf{g}|$. The kinematical structure factor $F_{\mathbf{g}}$ is given by

$$F_{\mathbf{g}} = \sum_j f_j(\mathbf{g}) \exp[2\pi i\, \mathbf{g} \cdot \mathbf{r}_j] \,, \tag{C.2}$$

where f_j are the atomic scattering amplitudes and $\mathbf{r}_j$ are the positions of the atoms in the unit cell [42, chap. 16.2]. The atomic scattering amplitudes f were calculated by an analytical approximation

$$f(\mathbf{g}) = \gamma \sum_k a_k \exp\left[-b_k \left(\frac{1}{2}\,|\mathbf{g}|\right)^2\right] \,, \tag{C.3}$$

where a_k and b_k are fitting parameters [114, 115]. Debye-Waller factors for consideration of temperature effects were omitted.

```
%*******************************************************************************************
%function Xig_Bi2Te3(g_hkl)
%*******************************************************************************************
%Berechnung des Extiktionslänge Xig_hkl für den reziproken Vektor g_hkl
function Xig=Xig_Bi2Te3(g_hkl);
%Beschleunigungsspannung U in keV und Basisvektoren des Realraums in nm
global U a1 a2 a3
%Volumen der Elementarzelle in nm^3
V_e=a1'*(cross(a2,a3));
%reziproke Basisvektoren in 1/nm
global a1_s a2_s a3_s
a1_s=cross(a2,a3)/V_e;
a2_s=cross(a3,a1)/V_e;
a3_s=cross(a1,a2)/V_e;
%Transformationsmatrix T_hkl
%für Transformation eines reziproken Vektors g_hkl mit Millerschen Indizes
%in einen reziproken Vektor g_car mit kartesischen Koordinaten
T_hkl=[a1_s(1), a2_s(1), a3_s(1); a1_s(2), a2_s(2), a3_s(2); a1_s(3), a2_s(3), a3_s(3)];
%relativistische Wellenlänge l_rel der Elektronen in nm
%und relativistischer Korrekturfaktor g_rel
g_rel=1+U/512;
l_rel=0.00242/sqrt(g_rel^2-1);
%Parameter a in nm und Parameter b in nm^2 zur Berechnung der atomaren Formfaktoren
a_Bi=[0.38412; 0.46784; 0.31924; 0.13625];
b_Bi=[0.502608; 0.119988; 0.025598; 0.003177];
a_Te=[0.4785; 0.3688; 0.1500; 0];
b_Te=[0.27999; 0.05083; 0.00581; 0];
%reziproker Vektor unter Zweistrahlbedingung in kartesischen Koordinaten in 1/nm
g_car=T_hkl*g_hkl;
%Streuparameter s in 1/nm, und Braggwinkel theta_Bragg in Radian,
s_hkl=0.5*norm(g_car);
theta_Bragg=asin(0.5*l_rel*norm(g_car));
%atomare Formfaktoren f_Bi und f_Te in nm,
f_Bi=g_rel*sum(a_Bi.*exp(-b_Bi*s_hkl^2));
f_Te=g_rel*sum(a_Te.*exp(-b_Te*s_hkl^2));
%Translationsvektoren bzgl. hexagonalem Gitter
R1=[0; 0; 0];
R2=[2/3; 1/3; 1/3];
R3=[1/3; 2/3; 2/3];
%Atompositionen x des Metalls M=Bi und der Nichtmetalle X=Te
M=[0; 0; 0.4];
X1=[0; 0; 0.212];
X2=[0; 0; 0];
Bi1=M+R1; Bi2=M+R2; Bi3=M+R3; Bi4=-M+R1; Bi5=-M+R2; Bi6=-M+R3;
Te1=X1+R1; Te2=X1+R2; Te3=X1+R3; Te4=-X1+R1; Te5=-X1+R2; Te6=-X1+R3;
Te7=X2+R1; Te8=X2+R2; Te9=X2+R3;
%kinematischer Strukturfaktor F in nm
g=g_hkl;
F_Bi=f_Bi*(exp(2*pi*i*(g'*Bi1))+exp(2*pi*i*(g'*Bi2))+exp(2*pi*i*(g'*Bi3))+exp(2*pi*i*(g'*Bi4))
        +exp(2*pi*i*(g'*Bi5))+exp(2*pi*i*(g'*Bi6)));
F_Te1=f_Te*(exp(2*pi*i*(g'*Te1))+exp(2*pi*i*(g'*Te2))+exp(2*pi*i*(g'*Te3))+exp(2*pi*i*(g'*Te4))
         +exp(2*pi*i*(g'*Te5))+exp(2*pi*i*(g'*Te6)));
F_Te2=f_Te*(exp(2*pi*i*(g'*Te7))+exp(2*pi*i*(g'*Te8))+exp(2*pi*i*(g'*Te9)));
F_hkl=F_Bi+F_Te1+F_Te2;
%Extinktionslänge in nm
Xig=(pi*V_e*cos(theta_Bragg))/(l_rel*abs(F_hkl));
```

C.3   Geometry

C.3.1   Subroutine "Rechnung_Koordinaten"

In Chapter 8.2.1 it was mentioned that two different axis systems have to be used, the experimental axis system and the crystal axis system. With respect to the crystal axis system, Miller indices, Cartesian coordinates, and polar coordinates were used for specifying the vectors. Therefore, the names of the vector variables have suffixes "uvw" and "hkl" for indicating Miller indices and a suffix "car" for indicating Cartesian coordinates. With respect to the ex-

perimental axis system, the names of the vector variables have a suffix "B". The subroutine "Rechnung_Koordinaten" calculates (i) the components of the vectors in both axis systems and (ii) the lattice coordinates X, Y, and Z of the columns and cells. Table C.1 gives an overview on the quantities used by the subroutines and their variables names with respect to the different axis systems.

```
%***********************************************************************************************
%subroutine Rechnung_Koordinaten
%***********************************************************************************************
%-----------------------------------------------------------------------------------------------
%Basisvektoren des reziproken Raumes
%-----------------------------------------------------------------------------------------------
%Volumen der Elementarzelle in nm^3
V_e=a1'*(cross(a2,a3));
%reziproke Basisvektoren in 1/nm
global a1_s a2_s a3_s
a1_s=cross(a2,a3)/V_e;
a2_s=cross(a3,a1)/V_e;
a3_s=cross(a1,a2)/V_e;
%-----------------------------------------------------------------------------------------------
%Transformationsmatrizen T_uvw und T_hkl
%-----------------------------------------------------------------------------------------------
%Transformation eines Richtungsvektors B_uvw mit Millerschen Indizes
%in einen Richtungsvektor B_car mit kartesischen Koordinaten
T_uvw=[a1(1), a2(1), a3(1); a1(2), a2(2), a3(2); a1(3), a2(3), a3(3)];
%Transformation eines reziproken Vektors g_hkl mit Millerschen Indizes
%in einen reziproken Vektor g_car mit kartesischen Koordinaten
T_hkl=[a1_s(1), a2_s(1), a3_s(1); a1_s(2), a2_s(2), a3_s(2); a1_s(3), a2_s(3), a3_s(3)];
%-----------------------------------------------------------------------------------------------
%Umrechnung der Abbildungsparameter in kartesische Koordinaten
%-----------------------------------------------------------------------------------------------
%Flächennormale definieren mit Länge=1
F_car=T_uvw*F_uvw/norm(T_uvw*F_uvw)
[F_phi,F_rho,F_r]=car_to_spher(F_car)
%reziproker Vektor g für Zweistrahlbedingung
g_car=T_hkl*g_hkl
[g_phi,g_rho,g_r]=car_to_spher(g_car)
%Strahlrichtung B
if polar==1
    B_car=spher_to_car(B_phi,B_rho)
    [B_phi,B_rho,B_r]=car_to_spher(B_car)
    B_uvw=inv(T_uvw)*B_car
else
    B_car=T_uvw*B_uvw
    [B_phi,B_rho,B_r]=car_to_spher(B_car)
end;
%Winkel zwischen Strahlrichtung und Reflex g
alpha_gB=subspace(g_car,B_car)*180/pi
%Programmabbruch, falls Strahlrichtung nicht bis auf 0.1° genau senkrecht zu Reflex g
if abs(alpha_gB-90)>0.1
    break;
end;
%-----------------------------------------------------------------------------------------------
%Umrechnung der Versetzungs-Parameter in kartesische Koordinaten
%-----------------------------------------------------------------------------------------------
%Linienrichtung t mit Länge=1 definieren, t soll in Richtung der Flächennormale orientiert sein
global t_car
t_car=T_uvw*t_uvw/norm(T_uvw*t_uvw);
if (acos(t_car'*F_car)>=(pi/2))
    t_uvw=-t_uvw
    t_car=-t_car
end;
t_uvw
t_car
[t_phi,t_rho,t_r]=car_to_spher(t_car)
%Burgersvektor b
global b_car b_r
b_car=T_uvw*b_uvw
```

```matlab
[b_phi,b_rho,b_r]=car_to_spher(b_car)
%Schraubenkomponente bs des Burgersvoktor b
bs_car=(b_car'*t_car)*t_car
bs_uvw=inv(T_uvw)*bs_car
%Stufenkomponente be des Burgersvektors b
be_car=cross(t_car,cross(b_car,t_car))
be_uvw=inv(T_uvw)*be_car
%Orthonormalbasis bzgl. Linienrichtung t
global m0_car n0_car
if norm(be_car)>0
    m0_car=be_car/norm(be_car)  %Stufenkomponente des Burgers-Vektors gibt die x-Achse vor
    n0_car=cross(t_car,m0_car)
else
    t_phi_rad=t_phi*pi/180; t_rho_rad=t_rho*pi/180;
    m0_car=[cos(t_phi_rad)*cos(t_rho_rad); sin(t_phi_rad)*cos(t_rho_rad); -sin(t_rho_rad)]
    n0_car=[-sin(t_phi_rad); cos(t_phi_rad); 0]
end;
%-----------------------------------------------------------------------------------------------
%Koordinatentransformationen von Kristallachsensystem in experimentelles Achsensystem
%-----------------------------------------------------------------------------------------------
%Drehmatrix R_B
global R_B
if (X_Achse==1)
    %Drehmatrix R_B für Strahlrichtung parallel z-Achse und t parallel x-Achse
    ts_car=R_phi_rho(B_phi,B_rho)*t_car;
    [ts_phi,ts_rho,ts_r]=car_to_spher(ts_car);
    R_B=R_phi_rho(ts_phi,0)*R_phi_rho(B_phi,B_rho)
else
    %Drehmatrix R_B für Strahlrichtung parallel z-Achse und Reflex g wie im Bild orientiert
    gs_car=R_phi_rho(B_phi,B_rho)*g_car;
    [gs_phi,gs_rho,gs_r]=car_to_spher(gs_car);
    R_B=R_phi_rho(gs_phi-alpha_g,0)*R_phi_rho(B_phi,B_rho)
end;
%Transformationsvektor für Gitterverbiegungsfunktion beta
R_z=R_B(3,:)
%reziproker Vektor, Strahlrichtung, Flächennormale, Linienrichtung t und Burgersvektor b
%bzgl experimentellen Achsensystem
global g_B B_B F_B t_B b_B
g_B=R_B*g_car
B_B=R_B*B_car
F_B=R_B*F_car
t_B=R_B*t_car
b_B=R_B*b_car
%Orthonormalbasis bzgl. experimentellen Achsensystem
global m0_B n0_B
m0_B=R_B*m0_car
n0_B=R_B*n0_car
%-----------------------------------------------------------------------------------------------
%Bildausschnitts Berechnungen in nm
%-----------------------------------------------------------------------------------------------
%Probendicke in Strahlrichtung
d_B=d_F/F_B(3)
%Länge der Versetzung im Bild
L_d=d_F/(F_B'*t_B)*sqrt(t_B(1)^2+t_B(2)^2)
%x-Richtung
global Nx
Nx=2*ceil(Lx/dx/2)+1 %Gesamtanzahl der Rasterpunkte in x-Richtung
dx=Lx/(Nx-1)         %Endgültige Rasterweite
%y-Richtung
global Ny
Ny=2*ceil(Ly/dy/2)+1 %Gesamtanzahl der Rasterpunkte in y-Richtung
dy=Ly/(Ny-1)         %Endgültige Rasterweite
%z-Richtung
global Lz Nz
Lz=d_B
Nz=2*ceil(Lz/dz/2)+1 %Gesamtanzahl der Rasterpunkte in y-Richtung
dz=Lz/(Nz-1)         %Endgültige Rasterweite
%Rasterpunkte in xy-Ebene
Nxy=Nx*Ny
```

Table C.1 Quantities and their variable names used by the subroutines with respect to the crystal axis system and the experimental axis system.

Quantity	Symbol	Crystal axis system		Experimental axis system
		Miller indices	Cartesian coordinates	
Lattice parameters	a, c		a, c	
Basis vectors of the real lattice	$\mathbf{a}_1, \mathbf{a}_2, \mathbf{a}_3,$		a1, a2, a3	
Basic vectors of the reciprocal lattice	$\mathbf{a}_1^*, \mathbf{a}_2^*, \mathbf{a}_3^*,$		a1_s, a2_s, a3_s	
Volume of a unit cell	V_e		V_e	
Elastic constants	c_{mn}		c_mn	
Burgers vector	$\mathbf{b}$	b_uvw	b_car	b_B
Polar coordinates of $\mathbf{b}$	$(\varphi_{\mathbf{b}}, \rho_{\mathbf{b}}, r_{\mathbf{b}})$		(b_phi, b_rho, b_r)	
Screw component of $\mathbf{b}$	$\mathbf{b}_s$	bs_uvw	bs_car	bs_B
Edge component of $\mathbf{b}$	$\mathbf{b}_e$	be_uvw	be_car	be_B
Line direction	$\mathbf{t}$	t_uvw	t_car	t_B
Polar coordinates of $\mathbf{t}$	$(\varphi_{\mathbf{t}}, \rho_{\mathbf{t}}, r_{\mathbf{t}})$		(t_phi, t_rho, t_r)	
Plane basis vectors	$\mathbf{m}_0, \mathbf{n}_0$		m0_car, n0_car	m0_B, n0_B
Beam direction	$\mathbf{B}$	B_uvw	B_car	B_B
Polar coordinates of $\mathbf{B}$	$(\varphi_{\mathbf{B}}, \rho_{\mathbf{B}}, r_{\mathbf{B}})$		(B_phi, B_rho, B_r)	
Foil normal	$\mathbf{F}$	F_uvw	F_car	F_B
Polar coordinates of $\mathbf{F}$	$(\varphi_{\mathbf{F}}, \rho_{\mathbf{F}}, r_{\mathbf{F}})$		(F_phi, F_rho, F_r)	
Bragg reflection	$\mathbf{g}$	g_hkl	g_car	g_B
Polar coordinates of $\mathbf{g}$	$(\varphi_{\mathbf{g}}, \rho_{\mathbf{g}}, r_{\mathbf{g}})$		(g_phi, g_rho, g_r)	
Foil thickness	d_F			d_F
Specimen thickness in beam direction	d_B			d_B
Dislocation length in the image	L_d			L_d
Specimen size	L_x, L_y, L_z			Lx, Ly, Lz
Cell size	dx, dy, dz			dx, dy, dz
Number of lattice sites	N_x, N_y, N_z			Nx, Ny, Nz
Column coordinates for line scans	$x0, y0$			x0, y0
Plane coordinate for imaging the strain field	$z0$			z0

```
%Rasterpunkte im Volumen
Nxyz=Nx*Ny*Nz
%Raster erzeugen
ix=1:Nx;
iy=1:Ny;
iz=1:Nz;
[IX,IY,IZ]=ndgrid(ix,iy,iz);
%Koordinaten erzeugen
X=-Lx/2+dx*(IX-1);
Y=-Ly/2+dy*(IY-1);
Z=(d_F/2-F_B(1)*X-F_B(2)*Y)/F_B(3)-dz*(IZ-1);
%zusätzliche Stützpunkte für das Runge-Kutta Verfahren
if Runge_Kutta==1
    Z2=(d_F/2-F_B(1)*X-F_B(2)*Y)/F_B(3)-dz*(IZ-1/2);
    Z3=(d_F/2-F_B(1)*X-F_B(2)*Y)/F_B(3)-dz*(IZ);
end;
%Daten auslesen in der xy-Ebene an der Probenunterseite
X_xy=X(:,:,Nz);
Y_xy=Y(:,:,Nz);
%Koordinaten erzeugen für vertikalen Linescan bei (x0,y0)
%und für horizontalen Linescan durch y0
%und für Darstellung der Gitterverbiegungsfunktion beta in der Ebene z0
ix0=floor((x0+Lx/2)/dx+1);
iy0=floor((y0+Ly/2)/dy+1);
iz0=floor((z0+Lz/2)/dz+1);
Z_scan=dz*(iz'-1);
X_scan=-Lx/2+dx*(ix'-1);
```

C.3.2   Transformation between Miller indices and Cartesian coordinates

The basis vectors of the crystal lattice are referred to as $\mathbf{a}_1$, $\mathbf{a}_2$, and $\mathbf{a}_3$ and have to be entered in Cartesian coordinates. The transformation matrix T_{uvw} which converts the Miller indices (u, v, w) of a lattice vector $\mathbf{B}$ into Cartesian coordinates (B_1, B_2, B_3) is given by

$$\mathbf{B} = u\,\mathbf{a}_1 + v\,\mathbf{a}_2 + w\,\mathbf{a}_3\,, \tag{C.4a}$$

$$\begin{pmatrix} B_1 \\ B_2 \\ B_3 \end{pmatrix} = u \begin{pmatrix} (\mathbf{a}_1)_1 \\ (\mathbf{a}_1)_2 \\ (\mathbf{a}_1)_3 \end{pmatrix} + v \begin{pmatrix} (\mathbf{a}_2)_1 \\ (\mathbf{a}_2)_2 \\ (\mathbf{a}_2)_3 \end{pmatrix} + w \begin{pmatrix} (\mathbf{a}_3)_1 \\ (\mathbf{a}_3)_2 \\ (\mathbf{a}_3)_3 \end{pmatrix} = T_{\mathrm{uvw}} \begin{pmatrix} u \\ v \\ w \end{pmatrix}\,, \tag{C.4b}$$

$$T_{\mathrm{uvw}} = \begin{pmatrix} (\mathbf{a}_1)_1 & (\mathbf{a}_2)_1 & (\mathbf{a}_3)_1 \\ (\mathbf{a}_1)_2 & (\mathbf{a}_2)_2 & (\mathbf{a}_3)_2 \\ (\mathbf{a}_1)_3 & (\mathbf{a}_2)_3 & (\mathbf{a}_3)_3 \end{pmatrix}\,. \tag{C.4c}$$

The reciprocal basis vectors $\mathbf{a}_1^*$, $\mathbf{a}_2^*$, and $\mathbf{a}_3^*$ were calculated according to

$$\mathbf{a}_1^* = \frac{\mathbf{a}_2 \times \mathbf{a}_3}{V_{\mathrm{e}}}\,, \tag{C.5a}$$

$$\mathbf{a}_2^* = \frac{\mathbf{a}_3 \times \mathbf{a}_1}{V_{\mathrm{e}}}\,, \tag{C.5b}$$

$$\mathbf{a}_3^* = \frac{\mathbf{a}_1 \times \mathbf{a}_2}{V_{\mathrm{e}}}\,, \tag{C.5c}$$

where $V_{\mathrm{e}} = \mathbf{a}_1 \cdot (\mathbf{a}_2 \times \mathbf{a}_3)$ is the volume of the unit cell. The transformation matrix T_{hkl} which converts the Miller indices (h, k, l) of a reciprocal lattice vector $\mathbf{g}$ into Cartesian coordinates (g_1, g_2, g_3) is given by

$$\mathbf{g} = h\,\mathbf{a}_1^* + k\,\mathbf{a}_2^* + l\,\mathbf{a}_3^*\,, \tag{C.6a}$$

$$\begin{pmatrix} g_1 \\ g_2 \\ g_3 \end{pmatrix} = h \begin{pmatrix} (\mathbf{a}_1^*)_1 \\ (\mathbf{a}_1^*)_2 \\ (\mathbf{a}_1^*)_3 \end{pmatrix} + k \begin{pmatrix} (\mathbf{a}_2^*)_1 \\ (\mathbf{a}_2^*)_2 \\ (\mathbf{a}_2^*)_3 \end{pmatrix} + l \begin{pmatrix} (\mathbf{a}_3^*)_1 \\ (\mathbf{a}_3^*)_2 \\ (\mathbf{a}_3^*)_3 \end{pmatrix} = T_{\mathrm{hkl}} \begin{pmatrix} h \\ k \\ l \end{pmatrix}\,, \tag{C.6b}$$

$$T_{\mathrm{hkl}} = \begin{pmatrix} (\mathbf{a}_1^*)_1 & (\mathbf{a}_2^*)_1 & (\mathbf{a}_3^*)_1 \\ (\mathbf{a}_1^*)_2 & (\mathbf{a}_2^*)_2 & (\mathbf{a}_3^*)_2 \\ (\mathbf{a}_1^*)_3 & (\mathbf{a}_2^*)_3 & (\mathbf{a}_3^*)_3 \end{pmatrix}\,. \tag{C.6c}$$

C.3.3   Polar coordinates and transformation between crystal axis system and experimental axis system

With respect to the crystal axis system, polar coordinates $(\varphi_{\mathbf{x}}, \rho_{\mathbf{x}}, r_{\mathbf{x}} = |\mathbf{x}|)$ were introduced (Fig. 3.2), such that a vector $\mathbf{x}$ with Cartesian coordinates (x_1, x_2, x_3) is given by

$$\begin{pmatrix} x_1 \\ x_2 \\ x_3 \end{pmatrix} = r_{\mathbf{x}} \begin{pmatrix} \cos(\varphi_{\mathbf{x}})\,\sin(\rho_{\mathbf{x}}) \\ \sin(\varphi_{\mathbf{x}})\,\sin(\rho_{\mathbf{x}}) \\ \cos(\rho_{\mathbf{x}}) \end{pmatrix}\,. \tag{C.7}$$

The plane basis vectors $\mathbf{m}_0$ and $\mathbf{n}_0$ of a mixed dislocation are given by $\mathbf{m}_0 = \frac{\mathbf{b}_e}{|\mathbf{b}_e|}$ and $\mathbf{n}_0 = \mathbf{t} \times \mathbf{m}_0$, where $\mathbf{b}_e$ (Eqn. 2.1) is the edge component of the Burgers vector $\mathbf{b}$. However, for a screw dislocation $\mathbf{b}_e$ would be zero. Alternatively, the plane basis vectors can also be expressed in terms of the polar coordinates $(\varphi_{\mathbf{t}}, \rho_{\mathbf{t}}, r_{\mathbf{t}})$ of the line direction $\mathbf{t}$ according to

$$\mathbf{m}_0 = \begin{pmatrix} \cos(\varphi_{\mathbf{t}})\,\cos(\rho_{\mathbf{t}}) \\ \sin(\varphi_{\mathbf{t}})\,\cos(\rho_{\mathbf{t}}) \\ -\sin(\rho_{\mathbf{t}}) \end{pmatrix}\,, \tag{C.8a}$$

$$\mathbf{n}_0 = \begin{pmatrix} -\sin(\varphi_{\mathbf{t}}) \\ \cos(\varphi_{\mathbf{t}}) \\ 0 \end{pmatrix}\,. \tag{C.8b}$$

Finally, the matrix $R_{\mathbf{B}}$ for the transformation of the components of a vector from the crystal axis system into the experimental axis shall be derived. In general, the matrix $R_{\varphi\rho}(\varphi,\rho)$ for the transformation of a unit vector $[\cos(\varphi)\sin(\rho),\sin(\varphi)\sin(\rho),\cos(\rho)]$ into a vector $[0,0,1]$ being parallel to the z axis is given by

$$R_{\varphi\rho}(\varphi,\rho) = \begin{pmatrix} \cos(\varphi)\cos(\rho) & \sin(\varphi)\cos(\rho) & -\sin(\rho) \\ -\sin(\varphi) & \cos(\varphi) & 0 \\ \cos(\varphi)\sin(\rho) & \sin(\varphi)\sin(\rho) & \cos(\rho) \end{pmatrix}. \tag{C.9}$$

This transformation matrix corresponds to a rotation of the vector by an angle φ in a left-handed sense around the z axis and a subsequent rotation by an angle ρ in a left-handed sense around the y axis (Fig. 3.2).

The transformation matrix $R_{\mathbf{B}}$, for an experimental axis system where the beam direction $\mathbf{B}$ is parallel to the z axis and the line direction $\mathbf{t}$ points towards the positive x axis (Fig. 8.1(a)), is given by

$$R_{\mathbf{B}} = R_{\varphi\rho}(\varphi_{\mathbf{t}'},0)\,R_{\varphi\rho}(\varphi_{\mathbf{B}},\rho_{\mathbf{B}})\,, \tag{C.10a}$$

$$\mathbf{t}' = R_{\varphi\rho}(\varphi_{\mathbf{B}},\rho_{\mathbf{B}})\,\mathbf{t}\,. \tag{C.10b}$$

The first matrix $R_{\varphi\rho}(\varphi_{\mathbf{B}},\rho_{\mathbf{B}})$ yields the beam direction being parallel to the z-axis. The second matrix $R_{\varphi\rho}(\varphi_{\mathbf{t}'},0)$ yields a line direction pointing towards the positive x axis.

The transformation matrix $R_{\mathbf{B}}$, for an experimental axis system where the beam direction $\mathbf{B}$ is parallel to the z axis and the diffracting vector $\mathbf{g}$ deviates in its orientation by an angle $\alpha_{\mathbf{g}}$ from the positive x axis (Fig. 8.1(b)), is given by

$$R_{\mathbf{B}} = R_{\varphi\rho}(\varphi_{\mathbf{g}'} - \alpha_{\mathbf{g}},0)\,R_{\varphi\rho}(\varphi_{\mathbf{B}},\rho_{\mathbf{B}})\,, \tag{C.11a}$$

$$\mathbf{g}' = R_{\varphi\rho}(\varphi_{\mathbf{B}},\rho_{\mathbf{B}})\,\mathbf{g}\,. \tag{C.11b}$$

The first matrix $R_{\varphi\rho}(\varphi_{\mathbf{B}},\rho_{\mathbf{B}})$ yields the beam direction being parallel to the z-axis. The second matrix $R_{\varphi\rho}(\varphi_{\mathbf{g}'} - \alpha_{\mathbf{g}},0)$ yields an angle $\alpha_{\mathbf{g}}$ between the diffracting vector and the x axis.

```
%*****************************************************************************************************
%function car_to_spher(B_car)
%*****************************************************************************************************
%Berechnung der sphärischen Koordinaten phi (Winkel zur x-Achse in grad),
%rho (Winkel zur z-Achse in grad), und r (Betrag) für einen kartesischen Vektor B_car
function [phi_grad,rho_grad,r]=car_to_spher(B_car);
[phi,rho,r1]= cart2sph(B_car(1),B_car(2),B_car(3));
phi_grad=phi*180/pi;
rho_grad=90-rho*180/pi;
r=r1;


%*****************************************************************************************************
%function spher_to_car(B_car)
%*****************************************************************************************************
%Berechnung eines kartesischen Vektors B_car aus den sphärischen Koorinaten
%phi (Winkel zur x-Achse in grad) und rho (Winkel zur z-Achse in grad)
function [B_car]=spher_to_car(phi_grad,theta_grad);
phi=phi_grad*pi/180;
theta=theta_grad*pi/180;
B_car=[cos(phi)*sin(theta); sin(phi)*sin(theta); cos(theta)];


%*****************************************************************************************************
%function R_phi_rho(phi_grad,rho_grad)
%*****************************************************************************************************
%Drehmatrix, um eine Strahlrichtung B=(cos(phi)sin(rho),sin(phi)sin(rho),cos(rho))
%in einen kartesischen [0,0,1]-Vektor zu transformieren
function R=R_phi_rho(phi_grad,rho_grad);
phi=phi_grad*pi/180;
rho=rho_grad*pi/180;
R=[cos(phi)*cos(rho), sin(phi)*cos(rho), -sin(rho);
   -sin(phi),        cos(phi),          0;
   cos(phi)*sin(rho), sin(phi)*sin(rho), cos(rho)];
```

C.3.4   Coordinates

The sample widths L_x and L_y are constants, whereas the sample thickness in beam direction $d_B = L_z$ depends on the foil thickness d_F, the beam direction $\mathbf{B}$, and the foil normal $\mathbf{F}$. For an untilted sample, the beam entrance surface and the beam exit surface are parallel to the x-y plane. The foil thickness d_F and the sample thickness in beam direction d_B are identical. The beam enters the sample at $z_+ = d_F/2$ and leaves the sample at $z_- = -d_F/2$, independent of the x and y coordinates. However, for a tilted sample $z_\pm$ and thereby d_B are determined by $\pm d_F/2 = \mathbf{x} \cdot \mathbf{F}$, yielding

$$z_\pm(x,y) = \frac{1}{(\mathbf{F_B})_3} \left[\pm \frac{1}{2}\, d_F - x\,(\mathbf{F_B})_1 - y\,(\mathbf{F_B})_2 \right] , \tag{C.12a}$$

$$d_B = z_+(x,y) - z_-(x,y) = \frac{d_F}{(\mathbf{F_B})_3} , \tag{C.12b}$$

where $\mathbf{F_B}$ is the foil normal with respect to the experimental axis system. In a similar way the length L_d of the dislocation in the image can be derived and is given by

$$L_d = \frac{d_F}{\mathbf{F_B} \cdot \mathbf{t_B}} \, \sqrt{[(\mathbf{t_B})_1]^2 + [(\mathbf{t_B})_2]^2} , \tag{C.13}$$

where $\mathbf{t_B}$ is the line direction with respect to the experimental axis system.

The number of lattice sites N_x, N_y, and N_z were chosen to be odd integers, e.g., $N_x = 2\,\mathrm{ceil}\left(\frac{L_x}{2\,dx}\right) + 1$, where L_x is the sample width and dx is width of the cells in x direction. The function $\mathrm{ceil}(A)$ rounds the real number A to the nearest integer greater than or equal to A. Finally, the width of the cells had to be redefined by $dx = \frac{L_x}{N_x - 1}$.

At this point the arrays for the coordinates were defined. First, simple one-dimensional arrays $ix = (1, \dots, N_x)$, $iy = (1, \dots, N_y)$, and $iz = (1, \dots, N_z)$ were generated to address the lattice sites, e.g., by the programme sequence "`ix=1:Nx`". The colon operator " `:` " replaces the slow "for"-loops. The second step is very crucial with respect to a short computing time. Three-dimensional arrays IX, IY, and IZ were generated on the basis of the one-dimensional arrays ix, iy, and iz by the programme sequence "`[IX,IY,IZ]=ndgrid(ix,iy,iz)`". Functions of several variables can be computed very fast by using such multi-dimensional arrays. The programming code is very simple and requires no explicit "for"-loops. Finally, three-dimensional arrays X, Y, and Z were generated for the coordinates of the lattice points according to

$$X = -\frac{L_x}{2} + dx\,(IX - 1) , \tag{C.14a}$$

$$Y = -\frac{L_y}{2} + dy\,(IY - 1) , \tag{C.14b}$$

$$Z = z_+(X,Y) - dz\,(IZ - 1) . \tag{C.14c}$$

The X, Y, and Z coordinates lie in a range between $-\frac{L_x}{2}$ and $+\frac{L_x}{2}$, $-\frac{L_y}{2}$ and $+\frac{L_y}{2}$, and z_+ and z_-, respectively. For the Runge-Kutta method the Z coordinates at the centre and at the bottom of each slice have also to be calculated. For the presentation of the intensities as contour maps two-dimensional arrays X_{xy} and Y_{xy} were generated, representing the X and Y coordinates at the exit surface. For the presentation of the intensities as line scans in x-direction and in beam direction one dimensional arrays X_{scan} and Z_{scan} were generated for the coordinates, respectively.

C.4 Displacement function β

C.4.1 Subroutine "Rechnung_beta"

In Chapter 8.2.1 it was shown that the displacement function β only depends on cylinder coordinates (r, θ). Particularly, the displacement function β can be resolved in a factor only depending on r and a factor only depending on θ and is given by

$$\beta = -\frac{1}{2\pi}\frac{1}{r}\beta_\theta(\theta)\,, \tag{C.15}$$

where $\beta_\theta(\theta)$ represents the term only depending on the angle θ.

The subroutine "Rechnung_beta" can be divided in two main sections. (i) First, $\beta_\theta(\theta)$ is precalculated according to the integral formalism of Barnett and Lothe [46] (Chap. 8.1). The numerical integrations were considered to be simple by Barnett and Lothe. However, the effective and fast calculation of the strain field and thereby $\beta_\theta(\theta)$ by a programme is more demanding than the numerical integration of the Howie-Whelan equations. Therefore, the integral formalism had to be modified. The optimizations are shown in the following sections. The number of individual calculations could be reduced by a factor of 100. (ii) The displacement function β is determined by the function "beta_xyz(x,y,z)". This function accepts the three-dimensional arrays X, Y, and Z for the coordinates as arguments, and therefore β is also a three-dimensional array.

Additionally, the subroutine calculates the line energy of the dislocation. The Burgers circuit is also carried out to test if there are any errors in the code. Finally, the displacement function at the column $(x0, y0)$ and at the $z0$ plane are read out for presentation as line scans in beam direction and as colour map, respectively. Table C.2 gives an overview of the quantities used by the subroutines and their variables names or function names.

```
%*************************************************************************************************
%subroutine Rechnung_beta
%*************************************************************************************************
%Berechnung von Hilfmatrizen mn0, nm0, nn0 und mm0 nach Barnett und Lothe
global mm0 mn0 nm0 nn0
mm0=zeros(3,3); mn0=zeros(3,3); nm0=zeros(3,3); nn0=zeros(3,3);
for js=1:3
    for ks=1:3
        for is=1:3
            for ls=1:3
                mm0(js,ks)=mm0(js,ks)+m0_car(is)*c_mn_tensor(is,js,ks,ls)*m0_car(ls);
                mn0(js,ks)=mn0(js,ks)+m0_car(is)*c_mn_tensor(is,js,ks,ls)*n0_car(ls);
                nm0(js,ks)=nm0(js,ks)+n0_car(is)*c_mn_tensor(is,js,ks,ls)*m0_car(ls);
                nn0(js,ks)=nn0(js,ks)+n0_car(is)*c_mn_tensor(is,js,ks,ls)*n0_car(ls);
            end;
        end;
    end;
end;
mm0, mn0, nm0, nn0
%Q, S und B Matrizen jeweils durch Integration nach Simpson im Intervall [0,2*pi]
global Q_int S_int B_int
Q_int=-1/(2*pi)*quad_matrix(@q_theta,0,2*pi)
S_int=-1/(2*pi)*quad_matrix(@s_theta,0,2*pi)
B_int=-1/(2*pi)*quad_matrix(@b_theta,0,2*pi)
time4a=clock;
%Linienenergie in eV/nm für Versetzungsabstand R und core-Radius r0
R=10000;                                  %halber Versetzungsabstand in nm
r0=b_r;                                   %core Radius gleich Burgers-Vektor-Betrag
E_L=1/(4*pi)*log(R/r0)*b_car'*(B_int*b_car) %Linienenergie
%Burgers-Umlauf
b_circ=quad_matrix(@b_circ_theta,0,2*pi)
%Berechnung der reinen Winkelabhängigkeit der Gitterverbiegungsfunktion
%im Intervall [-180°,180°] mit Schrittweite dth_grad in grad und Anzahl der Schritte Nth
global dth_rad beta_theta
dth_grad=0.1;
dth_rad=dth_grad*pi/180;
```

```
Nth=2*ceil(pi/dth_rad)+1
beta_theta=zeros(1,Nth);
for ith=1:Nth
    theta_rad=-pi+dth_rad*(ith-1);
    m_theta=cos(theta_rad)*m0_car+sin(theta_rad)*n0_car;
    n_theta=-sin(theta_rad)*m0_car+cos(theta_rad)*n0_car;
    s_m=-S_int*b_car;
    s_n=s_theta(theta_rad)*(S_int*b_car)+q_theta(theta_rad)*(B_int*b_car);
    beta_theta(ith)=g_car'*((R_z*m_theta)*s_m + (R_z*n_theta)*s_n);
end;
time4b=clock;
%Gitterverbiegungsfunktion an den Stützpunkten (x,y,z)
beta=beta_xyz(X,Y,Z);
%Gitterverbiegungsfunktion an Stützpunkten (x,y,z+dz/2) und (x,y,z+dz) für Runge-Kutta Verfahren
if Runge_Kutta==1
    beta2=beta_xyz(X,Y,Z2);
    beta3=beta_xyz(X,Y,Z3);
end;
%Daten auslesen in der Ebene z0
beta_xy=beta(:,:,iz0);
%Daten auslesen für vertikalen Linescan bei (x0,y0)
for izh=1:Nz
    beta_zhelp(izh)=beta(ix0,iy0,izh);
end;
beta_z=beta_zhelp';
```

C.4.2   Redefinition of the matrices depending on the azimuth angle θ

The calculation of the matrices (mm), (mn), (nm), and (nn) (Eq. 8.3) first requires the conversion of the matrix c_{mn} of the elastic constants into the tensor of the elastic constants c_{ijkl}. The function "c_mn_tensor(i,j,k,l)" determines the matrix suffices m and n from the tensor suffices (i, j) and (k, l) according to Equation 2.3.

For the calculation of the matrices (mm), (mn), (nm), and (nn) a summation on the components of the tensor of elastic constants is required. This is a time consuming process and can be simplified as follows: In the definitions of these matrices (Eq. 8.3) the plane basis vectors $\mathbf{m}$ and $\mathbf{n}$ were replaced by their appropriate definitions (Eq. 2.10), e.g.,

$$
\begin{aligned}
(nn)_{jk} &= n_i \, c_{ijkl} \, n_l \\
&= [-\sin(\theta)(\mathbf{m_0})_i + \cos(\theta)(\mathbf{n_0})_i] \, c_{ijkl} \, [-\sin(\theta)(\mathbf{m_0})_l + \cos(\theta)(\mathbf{n_0})_l]. \quad \text{(C.16)}
\end{aligned}
$$

At this point new 3×3 matrices $(mm0)$, $(mn0)$, $(nm0)$, and $(nn0)$ were defined.

$$
\begin{aligned}
(mm0)_{jk} &= (\mathbf{m_0})_i \, c_{ijkl} \, (\mathbf{m_0})_l \,, &\text{(C.17a)} \\
(mn0)_{jk} &= (\mathbf{m_0})_i \, c_{ijkl} \, (\mathbf{n_0})_l \,, &\text{(C.17b)} \\
(nm0)_{jk} &= (\mathbf{n_0})_i \, c_{ijkl} \, (\mathbf{m_0})_l \,, &\text{(C.17c)} \\
(nn0)_{jk} &= (\mathbf{n_0})_i \, c_{ijkl} \, (\mathbf{n_0})_l \,. &\text{(C.17d)}
\end{aligned}
$$

Finally, the matrices (mm), (mn), (nm), and (nn) can be expressed in terms of these new matrices and are given by

$$
\begin{aligned}
(mm) &= \sin(\theta)\,\cos(\theta)\,[(mn0) + (nm0)] + \cos^2(\theta)\,(mm0) + \sin^2(\theta)\,(nn0)\,, &\text{(C.18a)} \\
(mn) &= -\sin(\theta)\,\cos(\theta)\,[(mm0) - (nn0)] + \cos^2(\theta)\,(mn0) - \sin^2(\theta)\,(nm0)\,, &\text{(C.18b)} \\
(nm) &= -\sin(\theta)\,\cos(\theta)\,[(mm0) - (nn0)] + \cos^2(\theta)\,(nm0) - \sin^2(\theta)\,(mn0)\,, &\text{(C.18c)} \\
(nn) &= -\sin(\theta)\,\cos(\theta)\,[(mn0) + (nm0)] + \cos^2(\theta)\,(nn0) + \sin^2(\theta)\,(mm0)\,. &\text{(C.18d)}
\end{aligned}
$$

For the calculation of the matrices (mm), (mn), (nm), and (nn) and their related matrices q, s, and b the excessive and time consuming summations on the tensor components of elastic constants c_{ijkl} were replaced by summations on the constant matrices $(mm0)$, $(mn0)$, $(nm0)$, and $(nn0)$.

```
%********************************************************************************
%function c_mn_tensor(i,j,k,l)
%********************************************************************************
%Berechnung der Tensorkomponeneten der elastischen Konstanten in eV/nm^3
function c_ijkl=c_mn_tensor(is,js,ks,ls);
global c_mn
im=0.5*(is+js)*(is==js)+(9-(is+js))*(is~=js);
jn=0.5*(ks+ls)*(ks==ls)+(9-(ks+ls))*(ks~=ls);
c_ijkl=c_mn(im,jn)*10^2/1.6022;


%********************************************************************************
%function q_theta(theta)
%********************************************************************************
%q-Matrix in Abhänggeit des Azimutwinkels nach Barnett und Lothe
function q=q_theta(theta_rad);
%nn-Matrix Komponenten nach Barnett-Lothe
global mm0 mn0 nm0 nn0
nn_theta=-cos(theta_rad)*sin(theta_rad)*(mn0+nm0)+cos(theta_rad)^2*nn0+sin(theta_rad)^2*mm0;
%q-Matrix
q=inv(nn_theta);


%********************************************************************************
%function s_theta(theta)
%********************************************************************************
%s-Matrix in Abhänggeit des Azimutwinkels nach Barnett und Lothe
function s=s_theta(theta_rad);
%nm und nn Matrix Komponenten nach Barnett-Lothe
global mm0 mn0 nn0
nm_theta=-cos(theta_rad)*sin(theta_rad)*(mm0-nn0)+cos(theta_rad)^2*nm0-sin(theta_rad)^2*mn0;
nn_theta=-cos(theta_rad)*sin(theta_rad)*(mn0+nm0)+cos(theta_rad)^2*nn0+sin(theta_rad)^2*mm0;
%s-Matrix
s=inv(nn_theta)*nm_theta;


%********************************************************************************
%function b_theta(theta)
%********************************************************************************
%b-Matrix in Abhänggeit des Azimutwinkels nach Barnett und Lothe
function b=b_theta(theta_rad);
%mm, mn, nm, und Matrix Komponenten nach Barnett-Lothe
global mm0 mn0 nm0 nn0
mm_theta=cos(theta_rad)*sin(theta_rad)*(mn0+nm0)+cos(theta_rad)^2*mm0+sin(theta_rad)^2*nn0;
mn_theta=-cos(theta_rad)*sin(theta_rad)*(mm0-nn0)+cos(theta_rad)^2*mn0-sin(theta_rad)^2*nm0;
nm_theta=-cos(theta_rad)*sin(theta_rad)*(mm0-nn0)+cos(theta_rad)^2*nm0-sin(theta_rad)^2*mn0;
nn_theta=-cos(theta_rad)*sin(theta_rad)*(mn0+nm0)+cos(theta_rad)^2*nn0+sin(theta_rad)^2*mm0;
%b-Matrix
b=mn_theta*(inv(nn_theta)*nm_theta) - mm_theta;


%********************************************************************************
%function b_circ_theta(theta_rad)
%********************************************************************************
%Displacement in Abhänggeit des Azimutwinkels für Burgers-Vektor-Umlauf
function b_th=b_circ_theta(theta_rad);
global Q_int S_int B_int b_car m0_car n0_car
m_theta=cos(theta_rad)*m0_car+sin(theta_rad)*n0_car;
n_theta=-sin(theta_rad)*m0_car+cos(theta_rad)*n0_car;
s_m=-S_int*b_car;
s_n=s_theta(theta_rad)*(S_int*b_car)+q_theta(theta_rad)*(B_int*b_car);
b_th=1/(2*pi)*((n_theta'*m_theta)*s_m + (n_theta'*n_theta)*s_n);
```

C.4.3 Numerical integration of the matrices Q, S, and B

The numerical integration for the matrices Q, S, and B (Eq. 8.7) since 3×9 numerical integrals would be required, corresponding to the number of matrix elements. With MATLAB numerical integrals can be solved by the function "quad(f,a,b)", where "f" is a scalar function and "a" and "b" are the limits. However, the integrands q, s, and b are matrices depending on the azimuth angle θ, and therefore the function "quad(f,a,b)" can not be used. A new function "quad_matrix(f,a,b)" was defined to overcome this problem. The numerical integration is

carried out according to the "Simpson-1/3"-method

$$F = \frac{b-a}{3\,N} \left[f(a) + f(b) + 4 \sum_{k=1}^{N/2} f(a + [2\,k - 1]\,h) + 2 \sum_{k=1}^{N/2-1} f(a + 2\,k\,h) \right] , \tag{C.19}$$

where f is the integrand, a and b are the limits, N is an even number of intervals, and $h = \frac{b-a}{N}$ is the width of the intervals [116, chap. 15.4]. The integrals in Equation 8.7 were approximated by this finite sum. The new function increases the number of intervals N by a factor of two until the relative changes are less than 10^{-4} or the number of intervals N is larger than 1000. Particularly, in Equation C.19 the integrand f can also be a matrix function. Therefore, all 9 components of the matrices Q, S, or B are calculated parallel and formally according to

$$Q = -\frac{1}{2\pi} \int_0^{2\pi} q \, d\theta \,, \tag{C.20a}$$

$$S = -\frac{1}{2\pi} \int_0^{2\pi} s \, d\theta \,, \tag{C.20b}$$

$$B = -\frac{1}{2\pi} \int_0^{2\pi} b \, d\theta \,. \tag{C.20c}$$

```
%***********************************************************************************************
%function quad_matrix(f,a,b)
%***********************************************************************************************
%Berechnung des Integrals für eine Matrix Funktion f(x)
%in den Integrationsgrenzen [a,b] mit Hilfe des Simpson 1/3 Verfahrens
function F_int=quad_matrix(f,a,b);
N1=50;                                  %minimale Anzahl an Intervallen
N_max=500;                              %maximale Anzahl an Intervallen
precision=10^-4;                        %minimale Genauigkeit der Integration
F_int_N1=quad_matrix_simpson(f,a,b,N1); %grobes Integral
weiter=1;
while weiter
    N2=2*N1;                                %Doppelte Anzahl an Intervallen
    F_int_N2=quad_matrix_simpson(f,a,b,N2); %für verfeinertes Integral
    delta=abs(F_int_N2-F_int_N1);           %Differenz-Beträge der beiden Integrale
    mean=1/2*(abs(F_int_N2)+abs(F_int_N2)); %Mittelwert-Beträge der beiden Integrale
    abbruch=(delta<=precision*mean) | (N2>=N_max); %Abbruchbedingung
    weiter=~all(all(abbruch));
    N1=N2;
    F_int_N1=F_int_N2;
end;
N2
F_int=F_int_N2;

%***********************************************************************************************
%function quad_matrix_simpson(f,a,b)
%***********************************************************************************************
%Berechnung des Integrals für eine Matrix Funktion f(x)
%in den Integrationsgrenzen [a,b] mit Hilfe des Simpson 1/3 Verfahrens
function F_int=quad_matrix_help(f,a,b,N);
N=floor(N/2)*2; %gewärleistet das mit gerader Anzahl von Intervallen gerechnet wird
h=(b-a)/N;      %Schrittweite
F_int=0;
sum1=0;
for ks=1:N/2
    x_ks=a+(2*ks-1)*h;
    sum1=sum1+feval(f,x_ks);
end;
sum2=0;
for ks=1:N/2-1
```

```
    x_ks=a+2*ks*h;
    sum2=sum2+feval(f,x_ks);
end;
f_a=feval(f,a);
f_b=feval(f,b);
F_int=h/3*(f_a+f_b+4*sum1+2*sum2);
```

C.4.4   Determination of the displacement function β

In Chapter 8.2.1 the displacement function $\beta = -\frac{1}{2\pi}\frac{1}{r}\beta_\theta(\theta)$ was given in Equation 8.10. The subroutine "Rechnung_beta" first calculated the angle depend term $\beta_\theta(\theta)$ in an interval between $-180°$ and $180°$ at an interval width of $\Delta\theta = 0.1°$. A "for"-loop has to be used since the equations contain matrix and vector products, which is not compatible with the technique using multi-dimensional arrays. Second, the displacement function β was determined by the function "beta_(x,y,z)" in dependence of the coordinates $\mathbf{x} = (X, Y, Z)$. This function determines the cylinder coordinates (r, θ) (Eq. 2.10) by using a complex number z.

$$z = \mathbf{m_{0B}} \cdot \mathbf{x} + i \cdot \mathbf{n_{0B}} \cdot \mathbf{x}, \tag{C.21a}$$

$$r = \begin{cases} |z| & \text{for } |z| > |\mathbf{b}| \\ |\mathbf{b}| & \text{for } |z| \leq |\mathbf{b}| \end{cases}, \tag{C.21b}$$

$$\theta = \begin{cases} \arg(z) & \text{for } |z| > 0 \\ 0 & \text{for } |z| = 0 \end{cases}. \tag{C.21c}$$

The advantage of the complex number z is that the programme does not break down due to the singularity of the $\tan(\theta)$-function in Equation 2.10. The singularities of the displacement function at the centre of the dislocation core for $r \leq |\mathbf{b}|$ (Eq. 8.11) and of the definition of the cylinder coordinates (r, θ) at $r = 0$ were also considered. Finally, the fixed plane basis vectors $\mathbf{m_{0B}} = R_\mathbf{B}\,\mathbf{m_0}$ and $\mathbf{n_{0B}} = R_\mathbf{B}\,\mathbf{n_0}$ (Eq. 2.11, C.8, and C.10) with respect to the experimental axis system have to be used.

```
%********************************************************************************************
%function beta_xyz(x,y,z)
%********************************************************************************************
%Berechnung der Gitterverbiegungsfunktion beta
function beta=beta_xyz(x,y,z);
global dth_rad beta_theta m0_B n0_B b_r
m0_B_x=m0_B(1); m0_B_y=m0_B(2); m0_B_z=m0_B(3);
n0_B_x=n0_B(1); n0_B_y=n0_B(2); n0_B_z=n0_B(3);
m0x=m0_B_x.*x+m0_B_y.*y+m0_B_z.*z;
n0x=n0_B_x.*x+n0_B_y.*y+n0_B_z.*z;
%Übergang in komplexe Ebene
z=m0x+i*n0x;
%Abstand zum Versetzungscore mit Betrag des Burgersvektor b als Mindestwert
r=abs(z).*(abs(z)>b_r)+b_r.*(abs(z)<=b_r);
%Berechnung des Winkels theta, direkt am Versetzungscore wird theta auf 0 gesetzt
theta_rad=angle(z+(abs(z)==0));
%Zuordnung von Winkel theta zur Zelle ith in der beta_theta gespeichert ist
ith=round((theta_rad+pi)/dth_rad+1);
%Gitterverbiegungsfunktion  beta, direkt am Versetzungscore wird beta auf 0 gesetzt
beta=-1./(2*pi*r).*beta_theta(ith).*(abs(z)~=0);
```

C.5   Transformation matrices (K_n)

C.5.1   Subroutine "Rechnung_Kn"

The amplitudes of the direct beam T and of the diffracted beam S are coupled by the Howie-Whelan differential equations (Eq. 2.27). As will be shown, the numerical integration of these equations, i.e., the calculation of the amplitudes in each slice, can be solved by subsequent matrix multiplication from slice (n) to slice $(n+1)$. The subroutine "Rechnung_Kn" calculates these transformation matrices (K_n) (Eq. 2.30) either by using the "Pendellösung" method or by the Runge-Kutta method. Both methods assume a constant displacement function $\beta(z)$ and thereby $w'(z)$ within each slice (Eq. 2.29).

$$\beta_n = \beta(z_n)\,, \tag{C.22a}$$

$$w'_n = w'(z_n) = w + \xi_{\mathbf{g}}\,\beta_n\,. \tag{C.22b}$$

```
%*********************************************************************************************
%subroutine Rechnung_Kn
%*********************************************************************************************
%Transformationsmatrizen zur numerische Lösung der Howie-Whelan-Gleichungen
%Amplituden des transmittierten Strahls T und abgebeugten Strahls S erfüllen:
%dT=(-N*T+(i-A)*S)*pi/Xig
%dS=((i-A)*T+(-N+2i*(w+Xig*beta))*S)*pi/Xig
if Runge_Kutta==0
    %mit Hilfe des Pendellösungsverfahren
    [Kn_11,Kn_12,Kn_21,Kn_22]=Kn_Pendel(beta);
else
    %mit Hilfe des Runge-Kutta-Verfahrens
    [Kn_11,Kn_12,Kn_21,Kn_22]=Kn_RungeKutta(beta,beta2,beta3);
end;
```

C.5.2   "Pendellösung" method

The Howie-Whelan equations (Eq. 2.27) can be numerically integrated by using a method, which is referred to as "Pendellösung" method in the following. For an ideal crystal ($\beta = 0$) the Howie-Whelan equations can be analytically solved since $w'(z) = w$ (Eq. 2.27) is constant. The solutions for the amplitudes are well known and are referred to as "Pendellösung" (Eq. 2.30 and C.27). The "Pendellösung" method assumes a constant strain field within each slice, i.e, $w'(z)$ is replaced by w'_n (Eq. C.22) for each slice (n). Therefore, the differential equations can be transformed by an "Ansatz" into algebraic equations and the algebraic equations can be solved. The general solutions for the amplitudes in slice $(n+1)$ have to be of the form

$$\begin{pmatrix} T_{n+1} \\ S_{n+1} \end{pmatrix} = \begin{pmatrix} C1_n \\ C3_n \end{pmatrix} \exp\left\{\alpha1_n\,\frac{\pi}{\xi_{\mathbf{g}}}\,dz\right\} + \begin{pmatrix} C2_n \\ C4_n \end{pmatrix} \exp\left\{\alpha2_n\,\frac{\pi}{\xi_{\mathbf{g}}}\,dz\right\}\,, \tag{C.23}$$

since the Howie-Whelan equations are first-order differential equations. The constants $C1_n$, $C2_n$, $C3_n$ and $C4_n$ are determined by the amplitudes (T_n, S_n) in slice (n). The dimensionless factors $\alpha1_n$ and $\alpha2_n$ are determined by the roots

$$\alpha1_n = -N + i\,w'_n + \sqrt{(i-A)^2 - w'^2_n}\,, \tag{C.24a}$$

$$\alpha2_n = -N + i\,w'_n - \sqrt{(i-A)^2 - w'^2_n}\,. \tag{C.24b}$$

Finally, the transformation matrix is given by

$$(K_n) = \frac{1}{\alpha1_n - \alpha2_n}\left[(M1_n)\exp\left\{\alpha1_n\,\frac{\pi}{\xi_{\mathbf{g}}}\,dz\right\} + (M2_n)\exp\left\{\alpha2_n\,\frac{\pi}{\xi_{\mathbf{g}}}\,dz\right\}\right]\,, \tag{C.25a}$$

$$(M1_n) = \begin{pmatrix} -[\alpha2_n + N] & [i-A] \\ [i-A] & -[\alpha2_n + N - 2\,i\,w'_n] \end{pmatrix}\,, \tag{C.25b}$$

$$(M2_n) = \begin{pmatrix} [\alpha1_n + N] & -[i-A] \\ -[i-A] & [\alpha1_n + N - 2\,i\,w'_n] \end{pmatrix}\,. \tag{C.25c}$$

```
%***********************************************************************************************
%function Kn_Pendel(beta)
%***********************************************************************************************
%Transformationsmatrizen zur numerischen Lösung der Howie-Whelan-Gleichungen
%nach der Pendellösungsmethode
function [Kn_11,Kn_12,Kn_21,Kn_22]=Kn_Pendel(beta)
global  w A Xig dz
%Absorptionskooeffzienten A=N
N=A;
dZ=pi/Xig*dz;
w_n=w+Xig*beta;
alpha1_n=-N+i.*w_n+((i-A)^2-w_n.^2).^0.5;
alpha2_n=-N+i.*w_n-((i-A)^2-w_n.^2).^0.5;
nenner=1./(alpha1_n-alpha2_n);
exp_1=nenner.*exp(alpha1_n*dZ);
exp_2=nenner.*exp(alpha2_n*dZ);
M1n_11=-(alpha2_n+N);
M1n_12=(i-A);
M1n_21=(i-A);
M1n_22=-(alpha2_n+N-2*i*w_n);
M2n_11=(alpha1_n+N);
M2n_12=-(i-A);
M2n_21=-(i-A);
M2n_22=(alpha1_n+N-2*i*w_n);
Kn_11=M1n_11.*exp_1+M2n_11.*exp_2;
Kn_12=M1n_12.*exp_1+M2n_12.*exp_2;
Kn_21=M1n_21.*exp_1+M2n_21.*exp_2;
Kn_22=M1n_22.*exp_1+M2n_22.*exp_2;
```

C.5.3   Runge-Kutta method

The Runga-Kutta method is a general method for numerical integration of first-order differential equations $\frac{\partial \mathbf{y}}{\partial z} = f(z, \mathbf{y})$, which was also used by Head [47]. Also for this method the amplitudes can be calculated by using transformation matrices due to the linear character of the Howie-Whelan equations.

To explain the principle it shall be assumed that $y(z)$ is a scalar function. Also, the simpler but less accurate Euler method shall be first explained instead of the Runge-Kutta method. The principle of the Euler method is to assume a constant slope $m_n = y' = f(x, y_n)$ within each slice (n) and to calculate iteratively $y_{n+1} = y_n + m_n\, dz$, where dz is the slice width (Fig. C.1) [116, chap. 18.12]. For linear first-order differential equations $y' = a\, y$ the Euler method can be further simplified. The slope is given by $m_n = a\, y_n$ and therefore $y_{n+1} = K_n \cdot y_n$, where $K_n = 1 + a\, dz$ might be regarded as transformation factor. For a vector function $\mathbf{y}(z)$ whose components are coupled by a linear first-order differential equation, e.g., the Howie-Whelan equations, (K_n) would be a transformation matrix.

The principle of the Runge-Kutta method is to calculate a mean slope $m_n = \frac{1}{6}(m1_n + 2\, m2_n + 2\, m3_n + m4_n)$ for each slice (n), where $m1_n$ and $m4_n$ represent the slopes at the top and the bottom of the slice, and $m2_n$ and $m3_n$ represent the slopes at the centre of the slice [116, chap. 18.12]. Finally, the transformation matrix for the Howie-Whelan equations 2.27 is given by

$$(K_n) = I + \frac{1}{6}\{(M1_n) + 2 \cdot (M2_n) + 2 \cdot (M3_n) + (M4_n)\}, \tag{C.26a}$$

$$I = \begin{pmatrix} 1 & 0 \\ 0 & 1 \end{pmatrix}, \tag{C.26b}$$

$$(M_n) = \begin{pmatrix} -N & [i-A] \\ [i-A] & [-N + 2\, i\, w'_n] \end{pmatrix} \frac{\pi}{\xi_{\mathbf{g}}}\, dz, \tag{C.26c}$$

$$(M1_n) = (M_n), \tag{C.26d}$$

$$(M2_n) = (M_{n+\frac{1}{2}}) + \frac{1}{2}\,(M_{n+\frac{1}{2}})\,(M1_n), \tag{C.26e}$$
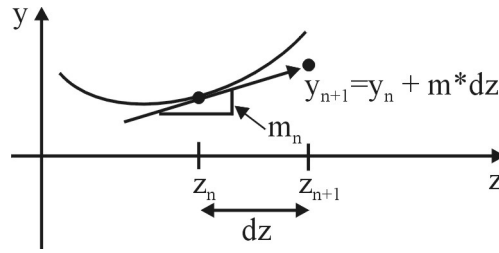
Figure C.1 Principle of the Euler method for numerical integration of first order differential equations.

$$(M3_n) = (M_{n+\frac{1}{2}}) + \frac{1}{2} (M_{n+\frac{1}{2}}) (M2_n),$$ (C.26f)

$$(M4_n) = (M_{n+1}) + (M_{n+1}) (M3_n).$$ (C.26g)

```
%**********************************************************************************************
%function Kn_RungeKutta(beta,beta2,beta3)
%**********************************************************************************************
%Transformationsmatrizen zur numerischen Lösung der Howie-Whelan-Gleichungen
%nach dem Runge-Kutta Verfahren
function [Kn_11,Kn_12,Kn_21,Kn_22]=Kn_RungeKutta(beta,beta2,beta3)
global  w A Xig dz
%Absorptionskooeffzienten A=N
N=A;
dZ=pi/Xig*dz;
w_n=w+Xig*beta;
w_n2=w+Xig*beta2;
w_n3=w+Xig*beta3;
M_11=-N*dZ;
M_12=(i-A)*dZ;
M_21=(i-A)*dZ;
M_22=(-N+2*i*w_n)*dZ;
M_22_2=(-N+2*i*w_n2)*dZ;
M_22_3=(-N+2*i*w_n3)*dZ;
M1n_11=M_11;
M1n_12=M_12;
M1n_21=M_21;
M1n_22=M_22;
M2n_11=M_11+1/2*(M_11*M1n_11+M_12*M1n_21);
M2n_12=M_12+1/2*(M_11*M1n_12+M_12*M1n_22);
M2n_21=M_21+1/2*(M_21*M1n_11+M_22_2.*M1n_21);
M2n_22=M_22_2+1/2*(M_21*M1n_12+M_22_2.*M1n_22);
M3n_11=M_11+1/2*(M_11*M2n_11+M_12*M2n_21);
M3n_12=M_12+1/2*(M_11*M2n_12+M_12*M2n_22);
M3n_21=M_21+1/2*(M_21*M2n_11+M_22_2.*M2n_21);
M3n_22=M_22_2+1/2*(M_21*M2n_12+M_22_2.*M2n_22);
M4n_11=M_11+(M_11*M3n_11+M_12*M3n_21);
M4n_12=M_12+(M_11*M3n_12+M_12*M3n_22);
M4n_21=M_21+(M_21*M3n_11+M_22_3.*M3n_21);
M4n_22=M_22_3+(M_21*M3n_12+M_22_3.*M3n_22);
Kn_11=1+1/6*(M1n_11+2*M2n_11+2*M3n_11+M4n_11);
Kn_12=1/6*(M1n_12+2*M2n_12+2*M3n_12+M4n_12);
Kn_21=1/6*(M1n_21+2*M2n_21+2*M3n_21+M4n_21);
Kn_22=1+1/6*(M1n_22+2*M2n_22+2*M3n_22+M4n_22);
```

C.6 Amplitudes and intensities

C.6.1 Subroutine "Rechnung_Amplituden"

The subroutine "Rechnung_Amplituden" calculates the complex amplitudes of the direct beam T and of the diffracted beam S according to Equation 2.31 and the related intensities I_T and I_S according to Equations 2.28. The subroutine also calculates the mean intensity and the diffraction contrast $(I_{\max} - I_{\min})/(I_{\max} + I_{\min})$, where I is the intensity. Finally, the intensities are read out at the exit surface, parallel to the line direction, and in beam directions for the presentation in contour maps and diagrams.

```
%**********************************************************************************************
%subroutine Rechnung_Amplituden
%**********************************************************************************************
%Amplituden des direkten Strahls T und des abgebeugten Strahls S
T=1+0*IX;
S=0*IX;
for izh=2:Nz
    T(:,:,izh)=(Kn_11(:,:,izh-1).*T(:,:,izh-1)+Kn_12(:,:,izh-1).*S(:,:,izh-1));
    S(:,:,izh)=(Kn_21(:,:,izh-1).*T(:,:,izh-1)+Kn_22(:,:,izh-1).*S(:,:,izh-1));
end;
%Intensitäten des direkten Strahls T und des abgebeugten Strahls S
IT=real(T.*conj(T));
IS=real(S.*conj(S));
%Daten auslesen in der xy-Ebene
ITxy=IT(:,:,Nz);
ISxy=IS(:,:,Nz);
IT_max=max(max(ITxy));
IT_min=min(min(ITxy));
IT_Kontrast=(IT_max-IT_min)/(IT_max+IT_min)*100;
IT_mean=1/2*((IT_max+IT_min));
IS_max=max(max(ISxy));
IS_min=min(min(ISxy));
IS_Kontrast=(IS_max-IS_min)/(IS_max+IS_min)*100;
IS_mean=1/2*((IS_max+IS_min));
%Daten auslesen für linescan in Strahlrichtung
for izh=1:Nz
    ITzhelp(izh)=IT(ix0,iy0,izh);
    ISzhelp(izh)=IS(ix0,iy0,izh);
end;
ITz=ITzhelp';
ISz=ISzhelp';
%Daten auslesen für Linescan in x-Richtung
ITx=IT(:,iy0,Nz);
ISx=IS(:,iy0,Nz);
%Intensitäten des direkten Strahls T und des abgebeugten Strahls S im idealen Kristall
%in Abhängigkeit der Probendicke
[ITz_ideal,ISz_ideal]=I_ideal(w,Z_scan);
%in Abhängigkeit des dimensionslosen Anregungsfehlers w im Intervall [-Lw/2,+Lw/2]
Lw=3;                   %Intervallbreite
dw=0.05;               %Schrittweite
Nw=2*ceil(Lw/dw/2+1)   %Gesamtanzahl der Rasterpunkte in x-Richtung
dw=Lw/(Nw-1)           %Endgültige Rasterweite
w_scan=-Lw/2+dw*((1:Nw)'-1);
[ITw_ideal,ISw_ideal]=I_ideal(w_scan,d_B);
```

C.6.2 Thickness fringes and rocking-curves in ideal crystals

The function "I_ideal" in the subroutine "Rechnung_Amplituden" is used to calculate the intensities of the direct beam and the diffracted beam in an ideal crystal (i) in dependence of the sample thickness z and (ii) in dependence of the dimensionless excitation error w, which represents a rocking curve. The amplitudes for an ideal crystal ($\beta = 0$) can be determined by

Equations C.24 and C.25, yielding

$$\begin{pmatrix} T(w,z) \\ S(z,w) \end{pmatrix} = \frac{1}{\alpha1 - \alpha2} \left[\begin{pmatrix} -[\alpha2 + N] \\ [i - A] \end{pmatrix} \exp\left\{ \alpha1 \frac{\pi}{\xi_{\mathbf{g}}} z \right\} + \begin{pmatrix} [\alpha1 + N] \\ -[i - A] \end{pmatrix} \exp\left\{ \alpha2 \frac{\pi}{\xi_{\mathbf{g}}} z \right\} \right] ,$$

(C.27a)

$$\alpha1 = -N + i\,w + \sqrt{(i - A)^2 - w^2} \,,$$ (C.27b)

$$\alpha2 = -N + i\,w - \sqrt{(i - A)^2 - w^2} \,.$$ (C.27c)

```
%*********************************************************************************************
%function I_ideal(w,z)
%*********************************************************************************************
%Amplituden und Intensitäten des direkten Strahls t und des abgebeugten Strahl S im idealen
%Kristall in Abhängigkeit der Probendicke t in nm und des dimensionslosen Anregungsfehlers
function [IT_ideal,IS_ideal]=I_ideal(w,z)
global A Xig
N=A;
Z=pi/Xig*z;
alpha1=-N+i*w+sqrt((i-A)^2-w.^2);
alpha2=-N+i*w-sqrt((i-A)^2-w.^2);
nenner=1./(alpha1-alpha2);
exp_1=nenner.*exp(alpha1.*Z);
exp_2=nenner.*exp(alpha2.*Z);
T=-(alpha2+N).*exp_1+(alpha1+N).*exp_2;
S=(i-A).*exp_1-(i-A).*exp_2;
IT_ideal=real(T.*conj(T));
IS_ideal=real(S.*conj(S));
```

C.7   Output

C.7.1   Subroutine "Ausgabe"

The subroutine "Rechnung_titles" in the subroutine "Ausgabe" converts the input and output parameters in "string" variables for the presentation in the contour maps and diagrams. Various contour maps and diagrams are available, e.g., the bright field and dark field images "Figure_ITxy" and "Figure_ISxy",respectively. Each of the figures can be activated by removing the comment symbol "%" at the beginning of the line.

```
%*********************************************************************************************
%subroutine Ausgabe
%*********************************************************************************************
%Erzeugt Bildbeschriftungen
Rechnung_titles;
%Darstellung der Gitterverbiegungsfunktion beta
%Figure_beta_theta         %Reine Winkelabhängigkeit um den Versetzungskern
%Figure_beta_theta_polar   %Reine Winkelabhängigkeit um den Versetzungskern als Polardiagramm
%Figure_beta_xy            %als contour map in der z0-Ebene
%Figure_beta_z             %als Linescan in Abhängigkeit der Probendicke
%Darstellung der Intensitäten als Kontourplots
%Figure_ITxy_ISxy          %Hellfeld-Bild und Dunkelfeld-Bild
Figure_ITxy                %Hellfeld-Bild
%Figure_ISxy               %Dunkelfeld-Bild
%Darstellung der Intensitäten als Linescans
%Figure_ITx_ISx            %parallel zur Versetzungslinie
%Figure_ITz_ISz            %in Abhängigkeit der Probendicke
%Figure_ITz_ISz_ideal      %in Abhängigkeit der Probendicke für Ideal-Kristall
%Figure_ITz_ISz_Vergleich  %in Abhängigkeit der Probendicke für idealen und gestörten Kristall
%Figure_ITw_ISw_ideal      %in Abhängigkeit des Anregungsfehlers w für Ideal-Kristall
```

C.7.2 Bright field image "Figure_ITxy"

The bright field and dark field images are presented as undistorted contour maps. The area between the contour isolines are filled with solid colour, whereas the isolines are shaded out. The number of contour levels (grey levels) and their absolute values can be specified in the subroutine "Eingabe". For an image with optimised contrast the range of the contour levels is identical to the range of the intensities. For an image with realistic contrast the range of the contour levels is between 0 and the maximum intensity. A file name is automatically generated and displayed in the heading of the window, specifying the dimensionless excitation error w and the absorption coefficient A. Finally, all input and output parameters can be optionally displayed in the figure.

```
%********************************************************************************************
%subroutine Figure_ITxy
%********************************************************************************************
%Darstellung des Hellfeld-Bildes
if Bild_Kontrast==0
    contour_No_IT=[0:IT_max/Graustufen:IT_max];
else
    contour_No_IT=Graustufen;
end;
%Bild erzeugen mit fortlaufender Nummer
figure_handle=figure(5000+Figure_No);
contourf(X_xy,Y_xy,ITxy,contour_No_IT);
colormap(gray);
shading flat;
axis image;
%Minimale Bildbeschriftung
title_string='';
title_string=strcat('I_T: ', IT_Kontrast_string, ', ', IT_mean_string);
title(title_string);
xlabel('x (nm)');
ylabel('y (nm)');
%Formatierung
Figure_File_Name='';
Figure_File_Name=strcat('ITxy_', w_str, '_', A_str);
set(figure_handle,'Name', Figure_File_Name, 'FileName', Figure_File_Name);
set(get(gca,'title'),'FontName',Font_Name,'FontSize',Font_Size);
set(get(gca,'xlabel'),'FontName',Font_Name,'FontSize',Font_Size);
set(get(gca,'ylabel'),'FontName',Font_Name,'FontSize',Font_Size);
set(get(gcf,'currentaxes'),'FontName',Font_Name,'FontSize',Font_Size);
%volle Bildbeschriftung
if Bild_Text==1
    Bild_dim=axis;
    text_x=Bild_dim(1);
    text_y=Bild_dim(3)+0.9*(Bild_dim(4)-Bild_dim(3));
    text_handle=text(text_x,text_y,Figure_Parameters);
    set(text_handle,'FontName',Font_Name,'FontSize',Font_Size);
end;
%Bild automatisch speichern
if Auto_Save==1
    saveas(figure_handle,Figure_File_Name,'tiffn');
end;
```

Table C.2 Quantities, their variable names, and their function names used for the integral formalism of Barnett and Lothe and for numerical integration of the Howie-Whelan equations.

Quantities and their symbols	Equation	Variable or function name
Coordinates		
Coordinates x, y, z	C.14	X, Y, Z, X_xy, Y_xy, X_scan, Z_scan
Coordinates z_n, $z_{n+\frac{1}{2}}$, z_{n+1}	C.22, C.26	Z, Z2, Z3
Integral formalism of Barnett and Lothe		
Cylinder coordinates r and θ	2.10, C.21	r and theta
Transformation matrix (R_B)	8.10, C.10, C.11	R_B
Transformation vector $\mathbf{R}_z$	8.10	R_z
Elastic constants c_{mn} and c_{ijkl}	2.2, 2.3	c_mn, c_mn_tensor(i,j,k,l)
Plane basis vectors $\mathbf{m}$ and $\mathbf{n}$	2.7, 2.10	m_theta, n_theta
Fixed plane basis vectors $\mathbf{m}_0$ and $\mathbf{n}_0$	2.10, 2.11, C.8	m0_car, m0_B, n0_car, n0_B
Matrices (mm), (mn), (nm), (nn)	8.3, C.18	mm_theta, mn_theta, nm_theta, nn_theta
Matrices $(mm0)$, $(mn0)$, $(nm0)$, $(nn0)$	C.17	mm0, mn0, nm0, nn0
Matrices q, s, b	8.5	q_theta(theta), s_theta(theta), b_theta(theta)
Matrices Q, S, B	8.7, C.19, C.20	Q_int, S_int, B_int
Vectors $\mathbf{s}_m$ and $\mathbf{s}_n$	2.13, 8.8, 8.10	s_m and s_n
Displacement function β	2.29, 8.10, 8.11	beta, beta_xy, beta_z, beta_xyz(x, y, z)
Displacement function term $\beta_\theta(\theta)$	8.10	beta_theta
Displacement function β_n, $\beta_{n+\frac{1}{2}}$, β_{n+1}	C.22, C.26	beta, beta2, beta3
Line energy E_L	2.16, 8.9	E_L
Howie Whelan equations		
Complex amplitudes T and S	2.27, 2.31, C.27	T, S
Intensity I_T	2.28	IT, ITxy, ITx, ITz, IT_max, IT_min, IT_mean, IT_Kontrast
Intensity I_S	2.28	IS, ISxy, ISx, ISz, IS_max, IS_min, IS_mean, IS_Kontrast
Intensities I_T and I_S for ideal crystal	2.30, C.27	ITz_ideal, ISz_ideal, ITw_ideal, ISw_ideal, Lideal(w,z)
Slice thickness dz	2.31, C.25, C.26	dz
Absorption coefficients A and N	2.27	A, N
Dimensionless excitation error w	2.29	w
Effective excitation error w'_n, $w'_{n+\frac{1}{2}}$, w'_{n+1}	C.22, C.26, C.26	w_n, w_n2, w_n3
Components of transformation matrix (K_n)	2.31	Kn_11, Kn_12, Kn_21, Kn_22
(K_n) according Pendellösung method	C.25	Kn_Pendel(beta)
(K_n) according Runge-Kutta method	C.26	Kn_RungeKutta(beta,beta1,beta2)
Exponential factors $\alpha 1_n$, $\alpha 2_n$, $\alpha 1$, $\alpha 2$	C.24, C.27	alpha1_n, alpha2_n, alpha1, alpha2
Components of matrix $(M1_n)$	C.25, C.26	Mn1_11, Mn1_12, Mn1_21, Mn1_22
Components of matrix $(M2_n)$	C.25, C.26	Mn2_11, Mn2_12, Mn2_21, Mn2_22
Components of matrix $(M3_n)$	C.26	Mn3_11, Mn3_12, Mn3_21, Mn3_22
Components of matrix $(M4_n)$	C.26	Mn4_11, Mn4_12, Mn4_21, Mn4_22
Components of matrix (M_n)	C.26	Mn_11, Mn_12, Mn_21, Mn_22
(2,2) components of (M_n), $(M_{n+\frac{1}{2}})$, (M_{n+1})	C.26	Mn_22, Mn_22_1, Mn_22_2

Bibliography

[1] Harvesting energy through thermoelectrics: power generation and cooling. *MRS Bulletin*, **31**:188–229, 2006.

[2] D.M. Rowe. *Thermoelectrics handbook : macro to nano*. (CRC Press, Boca Raton, FL, 2006).

[3] T.M. Tritt, R.K. Willardson, and E. Weber. *Recent trends in thermoelectric materials research*, volume **69-71** of *Semiconductors and semimetals*. (Academic Press, New York, 2000).

[4] H.J. Goldsmid. *Thermoelectric refrigeration*. (Temple Press, London, 1986).

[5] J.P. Fleurial et al. In *Proceedings of the 16th International Conference on Thermoelectrics (ICT 1997)*, Dresden, Germany, 1997. (IEEE, Piscataway, NJ, USA, 1997). page 641.

[6] H. Böttner et al. *J. Microelectromech. Syst.*, **13**:414, 2004.

[7] Micropelt GmbH. Emmy-Noether-Str. 2, D-79110 Freiburg, Germany.

[8] Fraunhofer-Institut für Physikalische Messtechnik (IPM) . Heidenhofstrasse 8, D-79110 Freiburg, Germany.

[9] J.M. Ziman. *Electrons and phonons*. (Clarendon press, Oxford, 1960).

[10] D.G. Cahill, W.K. Ford, K.E. Goodson, G.D. Mahan, A. Majumdar, H.J. Maris, R. Merlin, and S.R. Philpot. *J. Appl. Phys.*, **93**:793, 2003.

[11] R. Venkatasubramanian. *Phys. Rev. B*, **61**:3091, 2000.

[12] R. Venkatasubramanian, T. Colpitts, B. O'Quinn, S. Liu, N. El-Masry, and M. Lamvik. *Appl. Phys. Lett.*, **75**:1104, 1999.

[13] R. Venkatasubramanian, E. Siivola, T. Colpitts, and B. O'Quinn. *Nature (London)*, **413**:597, 2001.

[14] D.M. Rowe. *CRC Handbook of Thermoelectrics*. (CRC Press, Boca Raton, FL, 1995). pp. 211-237.

[15] L.D. Hicks and M.S. Dresselhaus. *Phys. Rev. B*, **47**:12727, 1993.

[16] H.H. Landolt and R. Börnstein. *Numerical data and functional relationships in science and technology, New Series*, volume **17f**. (Springer, Berlin, 1983). pp. 272-278.

[17] M.H. Francombe. *Br. J. Appl. Phys.*, **9**:415, 1958.

[18] K. Stecker, H. Süssmann, W. Eichler, W. Heiliger, and M. Stordeur. *Wiss. Z. / Martin-Luther-Universität Halle-Wittenberg / Math.-Naturwiss. Reihe*, **27**(5):5, 1978.

[19] P.A. Walker. *Proc. Phys. Soc. London*, **76**:113, 1960.

[20] J. Jaklovszky, R. Ionescu, N. Nistor, and A. Chiculita. *Phys. Status Solidi A*, **27**:329, 1975.

[21] H.G. Gatos. *Properties of elemental and compound semiconductors*. (Interscience Publishers, New York, 1960). pp. 287-293.

[22] S. Rath. *Sintermaterialien des Typs* $Bi_{2-x}Sb_xTe_{3-y}Se_y$ *und* $Bi_{1-x}Sb_x$ *für die Peltier-Kühlung bei tiefen Temperaturen*. (Liliom, München, Germany, 1999). ISBN 3-927966-95-9.

[23] V.V. Esayan, A.G. Sarkisyan, and A.A. Durgaryan. *Sov. Phys. Semicond.*, **15**:1341, 1981.

[24] P. Delavignette and S. Amelinckx. *Philos. Mag.*, **5**:729, 1960.

[25] I.V. Gasenkova and T.E. Svechnikova. *Inorg. Mater.*, **40**:570, 2004.

[26] N. Frangis, S. Kuypers, C. Manolikas, G. van Tendeloo, J. van Landuyt, and S. Amelinckx. *J. Solid State Chem.*, **84**:314, 1990.

[27] N. Frangis, C. Manolikas, and S. Amelinckx. *Phys. Status Solidi A*, **125**:97, 1991.

[28] K.F. Hsu et al. *Science*, **303**:818, 2004.

[29] E. Quarez, K.F. Hsu, R. Pcionek, N. Frangis, E.K. Polychroniadis, and M.G. Kanatzidis. *J. Am. Chem. Soc.*, **127**:9177, 2005.

[30] J. Androulakis et al. *Adv. Mater. (Weinheim, Ger.)*, **18**:1170, 2006.

[31] P.F.P. Poudeu, J. D'Angelo, A.D. Downey, J.L. Short, T.P. Hogan, and M.G. Kanatzidis. *Angew. Chem., Int. Ed.*, **45**:3835, 2006.

[32] Peltron GmbH Peltier-Technik. Flurstrasse 74, D-90765 Fürth, Germany.

[33] D. Eyidi, D. Maier, O. Eibl, and M. Westphal. *Phys. Status Solidi A*, **187**:585, 2001.

[34] D. Maier, D. Eyidi, and O. Eibl. In *Proceedings of the Sixth European Workshop on Thermoelectrics of the European Thermoelectric Society*, Freiburg, Germany, 2001.

[35] N. Peranio, O. Eibl, and J. Nurnus. In *Proceedings of the 23th International Conference on Thermoelectrics (ICT2004)*, Adelaide, Australia, 2004. (IEEE, Piscataway, NJ, USA, 2004). CDROM, Paper No. 105.

[36] N. Peranio, O. Eibl, and J. Nurnus. *J. Appl. Phys.*, **100**:114306, 2006.

[37] T.C. Harman, M.P. Walsch, B.E. Laforge, and G.W. Turner. *J. Electr. Mat.*, **34**:L19, 2005.

[38] H. Beyer, J. Nurnus, H. Böttner, A. Lamprecht, E. Wagner, and G. Bauer. *Physica E (Amsterdam)*, **13**:965, 2002.

[39] J. Nurnus et al. In *Proceedings of the 19th International Conference on Thermoelectrics (ICT 2000)*, Cardiff, UK, 2000. (Babrow Press Wales, UK, 2000). pp. 236-240.

[40] J. Nurnus, H. Böttner, H. Beyer, and A. Lamprecht. In *Proceedings of the 18th International Conference on Thermoelectrics (ICT 1999)*, Baltimore, MD, USA, 1999. (IEEE, Piscataway, NJ, USA, 1999). Cat. No. 99TH8407, pp. 696-699.

[41] J.P. Hirth and J. Lothe. *Theory of dislocations*. (Wiley, New York, 1982).

[42] D.B. Williams and C.B. Carter. *Transmission electron microscopy*. (Plenum Press, New York, USA, 1996).

[43] J.D. Eshelby, W.T. Read, and W. Shockley. *Acta Met.*, **1**:251, 1953.

[44] A.N. Stroh. *Philos. Mag.*, **3**:625, 1958.

[45] A.N. Stroh. *J. Math. Phys.*, **41**:77, 1962.

[46] D.M. Barnett and J. Lothe. *Phys. Status Solidi B*, **67**:105, 1975.

[47] A.K. Head, P. Humble, L.M. Clarebrough, A.J. Morton, and C.T. Forwood. *Computed electron micrographs and defect identification*. Defects in crystalline solids. (North Holland, Amsterdam, 1973).

[48] P. Haasen. *Physikalische Metallkunde*. (Springer, Berlin, 1974).

[49] W.G. Johnson and J.J. Gilman. *J. Appl. Phys.*, **30**:129, 1959.

[50] A. Granato and K. Lücke. *J. Appl. Phys.*, **27**:583, 1956.

[51] B.A. Bilby, K.J. Miller, and J.R. Willis. *Fundamentals of deformation and fracture: Eshelby memorial symposium, Sheffield, 3-5 April 1984*. (Cambridge University Press, Cambridge, 1982). pp. 187-202.

[52] A. Granato and K. Lücke. *J. Appl. Phys.*, **27**:789, 1956.

[53] G. Leibfried. *Z. Phys.*, **127**:344, 1950.

[54] T. Alper and G.A. Saunders. *Philos. Mag.*, **20**:225, 1969.

[55] A. Howie and M.J. Whelan. *Proc. R. Soc. London, Ser. A*, **263**:217, 1961.

[56] A. Howie and M.J. Whelan. *Proc. R. Soc. London, Ser. A*, **267**:206, 1962.

[57] N. Peranio and O. Eibl. In *Proceedings of the 23th International Conference on Thermoelectrics (ICT2004)*, Adelaide, Australia, 2004. (IEEE, Piscataway, NJ, USA, 2004). CDROM, Paper No. 72.

[58] W. Kleber, H.-J. Bautsch, and J. Bohm. *Einführung in die Kristallographie.* (Verlag Technik, Berlin, 1998).

[59] J.O. Jenkins, J.A. Rayne, and R.W. Ure. *Phys. Rev. B*, **5**:3171, 1972.

[60] N. Peranio and O. Eibl. In *Proceedings of the 23th International Conference on Thermoelectrics (ICT2004)*, Adelaide, Australia, 2004. (IEEE, Piscataway, NJ, USA, 2004). CDROM, Paper No. 73.

[61] N. Peranio and O. Eibl. *Phys. Status Solidi A*, **204**:3243, 2007.

[62] G. Cliff and G.W. Lorimer. *J. Microsc.*, **103**(2):203, 1975.

[63] N. Peranio and O. Eibl. *J. Appl. Phys.*, **103**:024314, 2008.

[64] M. Watanabe and D.B. Williams. *J. Microsc.*, **221**:89, 2005.

[65] B. Birajdar, V. Braccini, A. Tumino, T. Wenzel, O. Eibl, and G. Grasso. *Supercond. Sci. Technol.*, **19**:916, 2006.

[66] D. Eyidi, O. Eibl, T. Wenzel, K.G. Nickel, S.I. Schlachter, and W. Goldacker. *Supercond. Sci. Technol.*, **16**:778, 2003.

[67] J.I. Goldstein and D.B. Williams. *Scanning Electron Microsc.*, **1**:427, 1978.

[68] J. Bentley, N.J. Zaluzec, E.A. Kenik, and R.W. Carpenter. *Scanning Electron Microsc.*, **2**:581, 1979.

[69] C.E. Fiori and D.E. Newbury. *Scanning Electron Microsc.*, **1**:401, 1978.

[70] C.E. Fiori and D.E. Newbury. *Scanning Electron Microsc.*, **2**:251, 1980.

[71] W.A.P. Nicholson, C.C. Gray, J.N. Chapman, and B.W. Robertson. *J. Microsc.*, **125**:25, 1981.

[72] K.G. Ryan, N.E. Flower, and M.R. Presland. *J. Microsc.*, **134**:281, 1984.

[73] H. Cerva and W. Russwurm. *J. Am. Ceram. Soc.*, **71**:522, 1988.

[74] R.F. Egerton and S.C. Chang. *Ultramicroscopy*, **55**:43, 1994.

[75] J.C. Bennett and R.F. Egerton. *J. Microsc. Soc. Amer.*, **1**:143, 1995.

[76] K. Kanaya and S. Okayama. *J. Phys. D*, **5**:43, 1972.

[77] Wm.J. Veigele. *Atomic Data Tables*, **5**:51, 1973.

[78] G.H. Zschornack. *Atomdaten für die Röntgenspektralanalyse.* (Deutscher Verlag für Grundstoffindustrie, Leipzig, Germany, 1989).

[79] O. Eibl. *Micron*, **30**:527, 1999.

[80] X. Zhu, O. Eibl, L. Scheideler, and J. Geis-Gerstorfer. *J. Biomed. Mater. Res.*, **79**:114, 2006.

[81] N. Peranio and O. Eibl. "Gliding dislocations in Bi_2Te_3 materials". (unpublished).

[82] L. van Pieterson, M.H.R. Lankhorst, M. van Schijndel, A.E. T. Kuiper, and J.H.J. Roosen. *J. Appl. Phys.*, **97**:083520, 2005.

[83] M. Kaiser, L. van Pieterson, and M.A. Verheijen. *J. Appl. Phys.*, **96**:3193, 2004.

[84] O. Pages, Y. Feutelais, J.R. Didry, G. Keller, H. Jacquemin, and B. Legendre. *Mater. Res. Bull.*, **34**:1065, 1999.

[85] G. Morgant, Y. Feutelais, B. Legendre, R. Castanet, and A. Coulet. *Z. Metallk.*, **81**:44, 1990.

[86] A.D. Goletskaya, V.V. Sologub, and S.S. Shalyt. *Sov. Phys. Semicond.*, **5**:416, 1971.

[87] D.K.C. MacDonald, E. Mooser, W.B. Pearson, I.M. Templeton, and S.B. Woods. *Philos. Mag.*, **4**:433, 1959.

[88] H. Hahn, W. Seemann, and H.L. Kohn. *Z. Anorg. Allg. Chem.*, **369**:48, 1969.

[89] F. Völklein and E. Kessler. *Measurement*, **5**:38, 1987.

[90] C.M. Bhandari and D.M. Rowe. *J. Phys. D.*, **18**:873, 1985.

[91] A. Guinier. *X-Ray Diffraction in Crystals, Imperfect Crystals, and Amorphous Bodies.* (Dover, New York, 1994).

[92] N. El-Masry and J.C.L. Tarn. *Appl. Phys. Lett.*, **51**:1608, 1987.

[93] G.E. Shoemake and J.A. Rayne. *Phys. Rev.*, **185**:1046, 1969.

[94] Yu.A. Boikov, B.M. Gol'tsman, and V.A. Kutasov. *Sov. Phys. Solid State*, **20**:757, 1978.

[95] C.J. Glassbrenner and G.A. Slack. *Phys. Rev.*, **134**:A1058, 1964.

[96] P. Flubacher , A.J. Leadbetter, and J.A. Morrison. *Philos. Mag.*, **4**:273, 1959.

[97] M. Asheghi, Y.K. Leung, S.S. Wong, and K.E. Goodson. *Appl. Phys. Lett.*, **71**:1798, 1997.

[98] W. Liu and M. Asheghi. *Appl. Phys. Lett.*, **84**:3819, 2004.

[99] R.C. Zeller and R.O. Pohl. *Phys. Rev. B*, **4**:2029, 1971.

[100] K. Mori, M. Sasakawa, T. Igarashi, Y. Isikawa, K. Sato, K. Noto, and Y. Muto. *Physica C*, **162-164**:512, 1989.

[101] M. Anis-ur-Rehman and A. Maqsood. *Physica C*, **418**:121, 2005.

[102] A.D. McConnel, S. Uma, and K.E. Goodson. *J. Microelectromech. Syst.*, **10**:360, 2001.

[103] O. Eibl. *Physica C*, **168**:215, 1990.

[104] O. Eibl. *Physica C*, **175**:419, 1991.

[105] J.F. Nye. *Physical properties of crystals: their representation by tensors and matrices.* (Clarendon Press, Oxford, 1985).

[106] O. Eibl, P. Pongratz, P. Skalicky, and H. Schmelz. *Phys. Status Solidi A*, **108**:495, 1988.

[107] D. Berlincourt and H. Jaffe. *Phys. Rev.*, **111**:143, 1958.

[108] J.M. Schultz, J.P. McHugh, and W.A. Tiller. *J. Appl. Phys.*, **33**:2443, 1962.

[109] H.K. Lyeo et al. *Science*, **303**:816, 2004.

[110] T.E. Svechnikova et al. *Inorg. Mater.*, **41**:1043, 2005.

[111] T.E. Svechnikova et al. *Inorg. Mater.*, **42**:101, 2006.

[112] N. Chen et al. *Appl. Phys. Lett.*, **87**:171903, 2005.

[113] Institute of Materials Research, German Aerospace Center (DLR). D-51170 Köln, Germany.

[114] G.H. Smith and R.E. Burge. *Acta Cryst.*, **15**:182, 1962.

[115] P.A. Doyle and P.S. Turner. *Acta Cryst. A*, **24**:390, 1968.

[116] H. Stöcker. *Taschenbuch mathematischer Formeln und moderner Verfahren.* (Verlag Harri Deutsch, Frakfurt a.M., 1999). 4. Auflage.

List of Tables

List of Figures

List of Acronyms and Symbols

Acronyms	
AFM	Atomic force microscopy
ans	Artificial nanostructure
EDX	Energy dispersive X-ray spectrometry
EELS	Electron energy-loss spectroscopy
EPMA	Electron probe microanalyser
FT	Fourier transformed image
FWHM	Full width at half maximum
HRTEM	High resolution transmission electron microscopy
HRXRD	High resolution X-ray diffraction
MBE	Molecular beam epitaxy
mfp	Mean free path
MOCVD	Metallorganic chemical vapor deposition
nns	Natural nanostructure
RHEED	Reflection high-energy electron diffraction
SEM	Scanning electron microscopy
SL	Superlattice
SLR0, SLR1, SLR2	Superlattice reflections in HRXRD spectra
TEM	Transmission electron microscopy
WDX	Wavelength dispersive X-ray spectrometry
XRD	X-ray diffraction
Thermoelectric effects in Peltier devices	
Z	Thermoelectric figure of merit
ZT	Dimensionless thermoelectric figure of merit
T	Temperature
$\frac{dT}{dx}$	Temperature gradient
T_{C}, T_{H}	Cold side and hot side temperature
ΔT	Maximum temperature difference
q_{C}	Cooling power density
COP	Coefficient of performance
S, $S_{p,n}$	Total thermopower, thermopowers of the p-type and n-type leg materials
Π	Peltier coefficient
K	Thermal conductance
R	Electrical resistance
σ, $\sigma_{p,n}$	Electrical conductivity, electrical conductivities of the p-type and n-type leg materials
ρ, $\rho_{p,n}$	Electrical resistivity, electrical resistivities of the p-type and n-type leg materials
$S^2\sigma$	Power factor
λ, $\lambda_{p,n}$	Thermal conductivity, thermal conductivities of the p-type and n-type leg materials
λ_{latt}	Lattice thermal conductivity
λ_{el}	Electronic thermal conductivity
$(\perp c)/(\parallel c)$	Transport coefficient measured perpendicular/parallel to the c axis
A, $A_{p,n}$	Cross-section areas of the p-type and n-type legs
L, $L_{p,n}$	Lengths of the p-type and n-type legs
I, j	Electrical current and electrical current density
I_{Q}, j_{Q}	Heat current and heat current density
E, $\mathbf{E}$	Electric field

	Fundamental parameters of the phonon system
C, c	Total specific heat and specific heat
ρ	Mass density
v	Velocity of sound
l_{ph}	Phonon mean free path
θ_{D}	Debye temperature
z	Number of atoms per unit cell
N/V	Number of unit cells per volume
T_{M}	Melting point
A	Mean atomic weight
γ	Grüneisen parameter
k_{D}	Debye radius

	Fundamental parameters of the electron system
n	Carrier density
μ	Carrier mobility
τ, $\tau(\varepsilon)$	Relaxation time
r	Electron scattering exponent
m	Effective mass
L, L_0	Lorenz number, Lorenz number of metals
E_{L}, E_{V}	Energy at the bottom of the conduction band and at the top of the valence band
E_{G}	Band gap energy
E, ε, ξ	Energy, energy with respect to E_{L} or E_{V}, and reduced energy
E_{F}, ζ, η	Fermi energy (chemical potential), Fermi energy with respect to E_{L} or E_{V}, and reduced Fermi energy
$f^0(\varepsilon)$, $f^0(\xi, \eta)$	Unperturbed Fermi distribution function
$D(\varepsilon)$	Density of states
$F_m(\eta)$	Fermi-Dirac integrals
B	Material parameter
$E_{\mathrm{D,A}}$	Impurity level of donors or acceptors
ϵ_r	Dielectric constant
N_{V}	Number of valleys in the band structure
e	Elementary charge
k_{B}	Boltzmann's constant
$\hbar$	Heisenberg's constant

	Granto-Lücke theory of dislocation resonance
$y(x,t)$	Dislocation displacement
L	Length of an oscillating dislocation or of its oscillating segments
A	Effective dislocation mass per unit length
B	Damping force per unit length
C	Dislocation line-tension
ω	Ultrasound frequency
ω_0	Resonance frequency of a dislocation
D	Normalized damping constant
$\alpha(\omega)$	Attenuation of ultrasound
$v(\omega)$	Velocity of sound
$\triangle(\omega)$	Decrement
$f\left(\frac{\omega}{\omega_0}, D\right)$	Frequency response
ρ	Mass density
v_t	Shear wave velocity
Ω	Orientation factor
Δ_0	Constant

	ans and nns
a	Layer thickness of the $2D$-quantum well
d_{SL}	SL period
$\varepsilon(\mathbf{k})$	Energy dispersion relation
x_{av}	Average Se content of the SL
$\mathbf{q}$	Wave vector of the nns
$\mathbf{u}(\mathbf{x})$, $\mathbf{u}_0$	Displacement field and displacement vector of the nns
λ	Wavelength of the nns or fringe spacing in the image
ϕ	Phase of the displacement field of the nns

Dislocations and elasticity theory	
$\mathbf{b}$	Burgers vector
$\mathbf{b}_e$, $\mathbf{b}_s$	Edge component and a screw component of the Burgers vector
$\mathbf{t}$	Line direction of a dislocation
β	Angle between Burgers vector and Line direction
$\mathbf{G}$	Glide plane normal
N_D	Dislocation density
σ_{ij}, σ	Stress field, externally applied or residual shear stress
ϵ_{kl}, $d\epsilon_{ij}$	Strain field and differential strain
c_{mn}, c_{ijkl}	Elastic constants in matrix and tensor notation
$\mathbf{u}$, $\mathbf{u}(\mathbf{x})$	Displacement field
$\mathbf{u}_0$	Displacement vector
$\frac{\partial \mathbf{u}}{\partial x_l}$	Derivatives of the elastic displacement field, "Strain field"
μ	Shear modulus
ν	Poisson ratio
A	Anisotropy ratio
E_L, dw	Line energy, differential work
F_L	Elastic force per unit length
F_R/L, F_θ/L	Radial component and angle depended component of the elastic force between two parallel dislocations
τ_L	Line tension
r_0	Core radius
R	Half the distance between the dislocations, distance to free surface
r	Radius of a dislocation bowed out
R, $\mathbf{R}$	Distance and distance vector between two parallel dislocations
δ_{ij}	Kronecker's delta function
Integral formalism of Barnett and Lothe	
$\mathbf{m}$, $\mathbf{n}$, $\mathbf{m}_0$, $\mathbf{n}_0$	Plane basis vectors
r, θ	Cylinder coordinates
$\mathbf{A}$, $\mathbf{A}_\alpha$	Eigenvector
$\mathbf{L}$, $\mathbf{L}_\alpha$	Eigenvector
p, p_α	Eigenvalue
$\mathbf{s}_m$, $\mathbf{s}_n$	Vectors determining the strain field
(mm), (mn), (nm), (nn)	3×3 matrices
$(mm0)$, $(mn0)$, $(nm0)$, $(nn0)$	3×3 matrices
q, s, b	3×3 matrices
Q, S, B	3×3 matrices
N	6×6 matrix
$\boldsymbol{\xi}$	six-dimensional vector
det	Determinant of ...
Diffraction and image simulation	
$\mathbf{g}$	Bragg reflection
$\theta_{\mathbf{g}}$	Bragg angle
$\mathbf{B}$	Beam direction
$\mathbf{F}$	Foil normal
T, S	Amplitudes of the direct beam and the diffracted beam
I_T, I_S	Intensities of the direct beam and diffracted beam
$\xi_{\mathbf{g}}$	Extinction distance
s, s_{eff}	Excitation error, effective excitation error
w	Dimensionless excitation error
A, N	Absorption coefficients
β, $\beta(z)$, $\beta(r,\theta)$	Displacement function
$\beta_\theta(\theta)$	Angle depend term of the displacement function β
(K_n)	Transformation matrix of the slice (n)
T_n, S_n	Amplitudes of the direct beam and the diffracted beam in slice (n)
$(I_{max} - I_{min})/(I_{max} + I_{min})$	Diffraction contrast
z	Specimen thickness
d_F	Foil thickness
d_B	Total specimen thickness in beam direction
(dx, dy, dz)	Cell size
(L_x, L_y, L_z)	Specimen size
(N_x, N_y, N_z)	Number of lattice points
(X, Y, Z)	Coordinates of the lattice points
L_d	Length of a dislocation in the image
$F_{\mathbf{g}}$	Kinematical structure factor
f_j	Atomic scattering amplitude of the atom j

$\mathbf{r}_j$	Position of the atom j in the unit cell
a, b	Fitting parameters for the Atomic scattering amplitude f
U	Acceleration voltage of the microscope
λ	Wavelength of the electrons
γ	Relativistic correction factor
(φ, ρ, r)	Polar coordinates of a vector
$R_{\mathbf{B}}$, $R_{\varphi\rho}$	Transformation matrices
R_{z}	Transformation vector

Crystal structure	
a, c	Lattice parameters
$\mathbf{a}_1$, $\mathbf{a}_2$, $\mathbf{a}_3$	Basis vectors of the real crystal lattice
$\mathbf{a}_1^*$, $\mathbf{a}_2^*$, $\mathbf{a}_3^*$	Basis vectors of the reciprocal crystal lattice
V_{e}	Volume of the unit cell
(hkl)	Plane with Miller indices h, k, l
$\{hkl\}$	Equivalent plane to (hkl)
$[uvw]$	Direction with Miller indices u, v, w
$\langle uvw \rangle$	Equivalent direction to $[uvw]$
T_{uvw}, T_{hkl}	Matrices for transformation of Miller indices in cartesian coordinates

Danksagung

Eine Doktorarbeit entsteht nicht ohne die beratende, finanzielle, praktische oder moralische Unterstützung anderer. Mein besonderer Dank gilt daher

- **Prof. Dr. O. Eibl** für die Vergabe dieses sehr interessanten und interdisziplinären Themas, für die kompetente Einweisung in eine breite Palette an Mikroskopietechniken, und für die unermüdliche Unterstützung bei der Analyse der Ergebnisse hinsichtlich der vielfältigen Querbezüge zwischen der Mikrostruktur und den Transporteigenschaften.

- meinen Kollegen **B. Birajdar**, **M. Rössel**, **L. Molina-Luna**, **Dr. D. Eyidi** und **Dr. M. Eber-Koyuncu** für die angenehme Zusammenarbeit bei den vielen „kleinen" Aufgaben des Alltags an der Universität.

- unserer Laborassistentin Frau **I. Meißner** für die Geduld mit meinen „hoffnungslosen" Dünnfilm-TEM-Proben.

- **Dr. J. Nurnus** und **Dr. H. Böttner** vom Fraunhofer Institut für Physikalische Meßtechnik (IPM) in Freiburg für die gute Zusammenarbeit und die freundliche Überlassung der Dünnfilm-Proben und den Ergebnissen der Transportmessungen.

- **Carl Zeiss NTS GmbH**, insbesondere Herrn **H. Drexler**, **Dipl. Ing. B. Degel**, Frau **D. Adam** und den Mitarbeitern der Instituts-Werkstatt für die technische Unterstützung bei den Arbeiten zur EDX-Analyse und für einen reibungslosen Ablauf ohne längere Ausfälle durch eine entsprechende Wartung und Verbesserung der Geräte.

- für die finanzielle Unterstützung durch die **Deutsche Forschungsgemeinschaft (DFG)** im Rahmen eines Reisekostenzuschusses für die ICT2004 Konferenz in Adelaide, Australien.

- für die finanzielle Unterstützung durch das **Land Baden-Württemberg** im Rahmen des Projekts „Quantitative Elektronenstrahl Mikroanalyse an Hochleistungsmaterialien".

- **Prof. Dr. R. Kleiner** vom Physikalisches Institut für den Zugang an das Rasterelektronenmikroskop Jeol-6500-FEG und für die freundliche Unterstützung und Einweisung durch seine Mitarbeiter **Dr. T. Nachtrab**, **H. Eitel** und **M. Kemmler**.

- **Dr. T. Wenzel** vom Institut für Geowissenschaften für die Durchführung von EPMA-Analysen.

- **Dr. E. Müller** und Herrn **P. Ziolkowski** vom Institut für Werkstoff-Forschung des Deutschen Zentrums für Luft- und Raumfahrt (DLR) in Köln für die Messungen an der Seebeck-Mikrosonde.

- und insbesondere meinen **Eltern**, meiner **Familie** und meinen **Freunden**, denen der Löwenanteil meines Danks gebührt.

Eidesstattliche Versicherung

Ich erkläre hiermit, dass ich die zur Promotion eingereichte Arbeit mit dem Titel „Structural, chemical, and thermoelectric properties of Bi_2Te_3 Peltier materials: bulk, thin films, and superlattices" selbständig verfasst, nur die angegebenen Quellen und Hilfsmittel benutzt und wörtlich oder inhaltlich übernommene Stellen als solche gekennzeichnet habe. Ich versichere an Eides statt, dass diese Angaben wahr sind und dass ich nichts verschwiegen habe. Mir ist bekannt, dass die falsche Abgabe einer Versicherung an Eides statt mit Freiheitsstrafen bis zu drei Jahren oder mit Geldstrafe bestraft wird.

Weiterhin erkläre ich, dass bisher kein Promotionsversuch unternommen wurde.

Tübingen, den _____ _____

List of Publications

Publications during Ph.D. thesis

Original papers

1. N. Peranio and O. Eibl, "Structural modulations in Bi_2Te_3", J. Appl. Phys. **103**, 024314 (2008).

2. N. Peranio, O. Eibl, and J. Nurnus, "Structural and thermoelectric properties of epitaxially grown Bi_2Te_3 thin films and superlattices", J. Appl. Phys. **100**, 114306 (2006).

3. N. Peranio and O. Eibl, "Quantitative EDX microanalysis of Bi_2Te_3 in the TEM", Phys. Status Solidi A **204**, 3243 (2007).

4. N. Peranio and O.Eibl, "Gliding dislocations in Bi_2Te_3 materials", (unpublished).

5. B. Birajdar, N. Peranio, and O. Eibl, "Quantitative electron microscopy and spectroscopy of MgB_2 wires and tapes", Supercond. Sci. Technol. **21**, 073001 (2008).

Conference papers

1. N. Peranio, O. Eibl, and J. Nurnus, "Bi_2Te_3: Structural modulations in epitaxially grown superlattices and bulk materials", In: *Materials and Technologies for Direct Thermal-to-Electric Energy Conversion*, Boston, USA, 2005, ed. by J. Yang, T. P. Hogan, R. Funahashi, and G.S. Nolas, Mater. Res. Soc. Symp. Proc. **886**, 135 (2006).

2. N. Peranio and O. Eibl, "TEM preparation of Bi_2Te_3 thin films epitaxially grown on BaF_2 substrates", In: *Proceedings of the 23th International Conference on Thermoelectrics (ICT2004)*, Adelaide, Australia, 2004, (IEEE, Piscataway, NJ, USA, 2004), paper No. 72.

3. N. Peranio and O. Eibl, "Quantitative EDX analysis of Bi_2Te_3 in the TEM", In: *Proceedings of the 23th International Conference on Thermoelectrics (ICT2004)*, Adelaide, Australia, 2004, (IEEE, Piscataway, NJ, USA, 2004), Paper No. 73.

4. N. Peranio, O. Eibl, and J. Nurnus, "Structural analysis of Bi_2Te_3 superlattices epitaxially grown on BaF_2 by transmission electron microscopy", In: *Proceedings of the 23th International Conference on Thermoelectrics (ICT2004)*, Adelaide, Australia, 2004, (IEEE, Piscataway, NJ, USA, 2004), Paper No. 105.

Conference abstracts

1. N. Peranio and O. Eibl, "Quantitative EDX analysis of Bi_2Te_3 in the TEM", In: *Microscopy conference 2005*, Davos, Switzerland, 2005, page 79.

2. N. Peranio, O. Eibl, and J. Nurnus, "Bi_2Te_3: Superlattices and structural modulations in bulk materials", In: *Microscopy conference 2005*, Davos, Switzerland, 2005, page 277.

3. N. Peranio and O. Eibl, "Direct observation of gliding dislocations in Bi_2Te_3 materials", In: *Microscopy conference 2005*, Davos, Switzerland, 2005, page 308.

Publications during diploma thesis

Original papers

1. N. Peranio, A. Rosenauer, D. Gerthsen, S.V. Sorokin, I.V. Sedova, and S.V. Ivanov, "Structural and chemical analysis of CdSe/ZnSe nanostructures by transmission electron microscopy", Physical Review B **61**, 16015 (2000).

2. D. Gerthsen, A. Rosenauer, D. Litvinov, and N. Peranio, "Structural and chemical analysis of CdSe islands in a ZnSe matrix by transmission electron microscopy", Journal of Crystal Growth **214/215**, 707 (2000).

Curriculum vitae

Personal data	Mr. Nicola Peranio Date and place of birth: 15/01/1973, Rottweil/Germany Nationality: Italy
School	
1979-1989	Grund- und Realschule / Dunningen
1989-1992	Technisches Gymnasium / Rottweil
Studies	
10/1992-10/2000	Physics at the University of Karlsruhe Prof. Dorman, Prof. v. Löhneysen, Prof. v. Baltz, Prof. Schimmel, Prof. Pilkuhn, Prof. Hollik, Prof. Klingshirn, Prof. Kampert, Prof. Weddingen, Dr. Jüngst, Dr. Würfel, Prof. Schindewolf, Prof. Heuser, Prof v. Renteln
10/1997-06/1999	Diploma thesis at the Laboratorium für Elektronenmikroskopie, Prof. D. Gerthsen "*Transmissionselektronenmikroskopische Untersuchung von CdSe/CdS- und CdSe/ZnSe-Quantenpunktstrukturen*"
Casual jobs	
10/2000-10/2002	Casual jobs
Ph.D. thesis	
10/2002-08/2007	Institute of Applied Physics, Prof. O. Eibl, Eberhard-Karls-University of Tübingen "*Structural, chemical, and thermoelectric properties of Bi_2Te_3 Peltier materials: bulk, thin films, and superlattices*"

Tübingen, den _____ _____